Transactions of the ASME

Transactions

of The American Society of Mechanical Engineers

Published on the tenth of every month, except March, June, September, and December

---

A New Type of Radiant Tubular Heater

By T. F. KREIPE,[1] PHILADELPHIA, PA.

The advantages of applying direct radiant heat to both sides of heating coils in tubular furnaces, as compared to the more customary direct application of radiant heat from one side only, is discussed. The operation, construction, and application of a novel radiant-type burner is described which embodies many desirable features. Use of the burner in tubular heaters is discussed and operating data are presented.

INTRODUCTION

CONSIDERABLE progress has been made in the past 10 years in development of an improved design for high-temperature process heaters in which a vapor, liquid, or mixtures thereof are raised to operating temperatures during flow through tubes. Application of the improved design to thermal-cracking and high-temperature catalytic reforming in the petroleum-processing field, for example, has met the requirements of severe operating conditions with improved results. The development has been directed along the lines of perfecting the burners and, also, of changing relative positions of tubes and burners from those normally encountered in conventional heaters.

Because previous operation of burners has been comparatively poor, heater design for the past 20 years has been based on firing a heater from the center of the floor or from a single row of burners on one or more of the walls. If fired from the floor, the tubes usually were placed on opposite walls of the heater structure and, if the structure permitted, tubes also were placed along the roof. If fired from a side wall or from the end, tubes usually were placed above the fire on the wall and along the roof. In some cases, floor tubes were used with side-wall firing. The general characteristic of these heaters was that the fire was placed near the center of the heater with the tubes on at least two sides of the heat source. As a result, the major portion of heat transferred to the process fluid was through the tubes on the side facing the fire, with only a relatively small amount entering the side of the tubes away from the fire and facing the refractories.

RADIANT-HEAT-TRANSFER THEORY

It has been shown[2] that with a single row of tubes spaced on tube centers equal to twice the tube diameters and heated from one side by direct radiant heat and from the other side by reradiation from the refractory wall, the total direct-radiant-heat absorption from the products of combustion by the tubes is 65.8 per cent of the total radiant heat released, and the absorption by reradiation from the hot refractories amounts to 22.5 per cent of the total radiant heat released. This relationship is based on the assumption that all of the radiant heat which falls on a furnace refractory is reradiated to the tubes, whereas a small amount is lost by conduction through the refractory wall. The flux distribution, such as that shown in Fig. 1, will occur, with the rate on the

fire side being about equal to three times that on the refractory side and the average rate will be 56.2 per cent of the maximum rate. Thus, far greater amounts of heat will be transferred through one side of the furnace tubes, with a much smaller amount of heat moving through the furnace-wall side.

Now consider some of the factors involved in any furnace design:

1 For a fixed-flow rate, tube size will be selected to obtain a reasonable fluid velocity and pressure drop.

2 Based on properties of the material flowing and the mass velocity, a fluid-film coefficient will be calcuated.

3 Allowable flux densities will be calculated based on the fluid-film coefficient, which will result in a safe operating fluid-film temperature; i.e., a temperature above which excessive reaction or decomposition will occur.

4 For the allowable absorption rate from the foregoing, the temperature at the outside face of the tube may be calculated. This temperature and operating pressure are taken into account in the selection of tube materials for the heating coil.

From the foregoing, it is apparent that design of a heater employing wall tubes must be based on conditions that exist on the fire side where most severe conditions prevail. If, for example, a maximum rate of 15,000 Btu/sq ft is determined to be allowable, this rate must be set up on the fire side, while only about 5000 Btu/hr/sq ft will be developed on the refractory side. The resulting average will be about 8430 Btu/hr/sq ft.

When the furnace structure is rearranged so that heat can be applied to the tubes from both sides directly, it has been shown[2] that the heat distribution is developed according to the pattern in Fig. 2, and the average will be 87 per cent of the maximum rate. If, as in the previous hypothetical case, the maximum allowable rate is 15,000 Btu/hr/sq ft from maximum film-temperature considerations, the over-all average will be increased effectively to 13,050 Btu/hr/sq ft without exceeding specified limitations. Thus, the duty has been increased almost 55 per cent per sq ft of exposed radiant surface. Moreover, the large differences in the tube-wall temperature that exist, with unequal application of
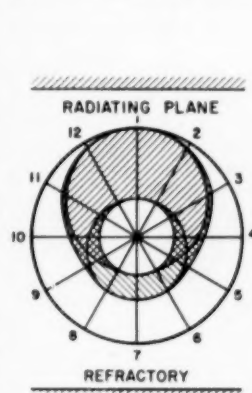
FIG. 1 FLUX DISTRIBUTION ON SINGLE ROW OF TUBES HEATED FROM ONE SIDE BY DIRECT RADIANT HEAT AND FROM OPPOSITE SIDE BY RERADIATION
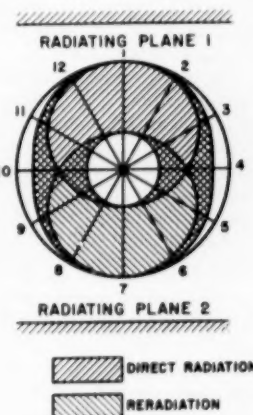

FIG. 2 FLUX DISTRIBUTION ON SINGLE ROW OF TUBES HEATED FROM BOTH SIDES BY DIRECT RADIANT HEAT

heat, have been eliminated, thereby minimizing the extent to which uneven stresses are set up on the two halves of the tube.

The principle of heating from both sides, though accepted previously, could not be used to advantage because of prohibitive flame length, which resulted in relatively large furnace chambers. There now has been a development of burners with flames so short that they have been referred to as "flameless" burners, and this has led to a design where the principle of adding heat evenly to both sides can be used in a reasonably sized heater structure.

New process developments have the general tendency toward increased temperatures and/or pressures, which often require better material of construction for the process equipment. The superior materials which have been developed for tubular-heater service permit higher operating temperatures and higher operating pressures with more safety than enjoyed previously. These superior materials also allow the design engineer to use, within accepted safety standards, higher heating rates than previously were allowed.

In order for burner development to keep pace with the strides made in metallurgy, besides providing a burner with no protruding flame so that advantage of the improved tube arrangement could be realized, it also was desirable to incorporate as many other advantageous features as possible to provide optimum utilization of radiant heat.

One variable which has a pronounced effect on radiant-heat-transfer rates is the source temperature and is the factor T_R in the Stefan-Boltzmann equation

$$Q_R = 0.173 \, FA \left[\left(\frac{T_R}{100} \right)^4 - \left(\frac{T_2}{100} \right)^4 \right]$$

where

Q_R = radiant heat absorbed, Btu/hr
0.173 = Stefan-Boltzmann constant
T_R = temperature of radiating surface, deg R
T_2 = temperature of heat-absorbing surface, deg R
F = relative emissivity of actual absorbing surface
A = absorbing-surface area

As can be seen by analysis of the equation, any increase in T_R will increase heat transferred as the difference of the fourth power of the absolute temperature of the source and the absorbing surface. An increase of 10 per cent or 300 deg F at 3000 F in T_R will increase Q_R or the total radiant heat transferred to an absorbing surface at 950 F by approximately 40 per cent, and an increase of 10 per cent or 150 deg F at 1500 F in T_R will increase Q_R by approximately 56 per cent when transferring heat to an absorbing surface at 950 F.

The most practical approach to increasing the radiating temperature is that of perfecting the burner operation to a point at which complete combustion is effected with a minimum of excess air, since air dilution decreases theoretical flame temperature more than any other single factor. For example, observations of maximum flame temperature when burning a gas of 1110 Btu/cu ft gross heating value (containing 85.48 per cent methane, 13.85 per cent ethane, and 0.67 per cent inerts) with various amounts of excess air, were reported[3] as follows:

Observed temperature with no excess air = 3470 F
Observed temperature with 10 per cent excess air = 3380 F
Observed temperature with 30 per cent excess air = 3024 F

This is occasioned by the fact that only the heteropolar gases, CO_2, H_2O, and SO_2, which are the products of complete combustion, emit and absorb radiation while the symmetrical gases, O_2,

[3] "Flame Temperatures and Vertical Gradients in Natural Gas Flames," by H. H. Kaveler and Bernard Lewis, *Chemical Reviews*, vol. 21, 1937, pp. 421–429.

N_2, and CO are nonradiant, and thus any excess air causes dilution of combustion products and decreases their heat-radiating capacity. The effect of 100 per cent excess air on radiant-heat transfer, as is sometimes experienced with common burners, is apparent.

NOVEL RADIANT BURNERS

The new-type radiant burner, which has been developed successfully, deals with the problem of maintaining minimum excess air so that maximum radiant-heat transfer can be utilized. It also produces a very short flame with complete combustion. In the new-type burner, all of the air required for combustion is inspirated by an orifice in the gas supply feeding through a venturi throat to the burner tip as shown in Fig. 3. Additional
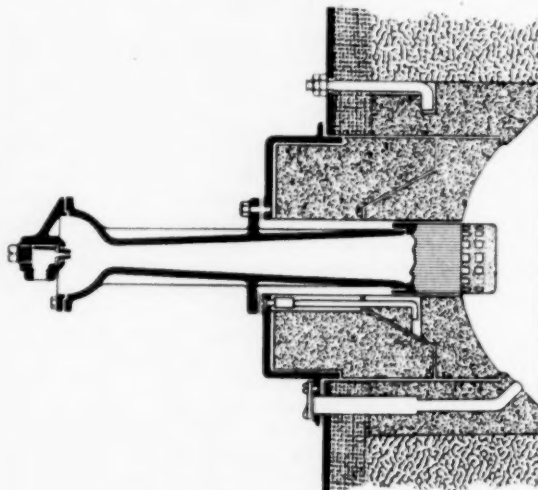
FIG. 3   RADIANT BURNER CROSS SECTION
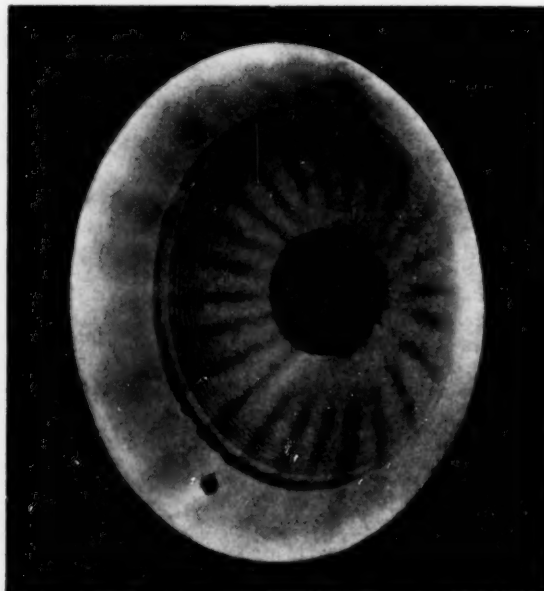
FIG. 4   RADIANT BURNER IN OPERATION

mixing of the gas and air takes place in the burner ports and on the ceramic burner cup. There are no moving parts in the burner and the flame is confined within the burner cup. Proper sizing of the gas orifice insures that maximum excess air does not exceed 10 per cent and is usually between 0 and 5 per cent. No secondary air is required. The burner in operation is shown in Fig. 4.

These developments have allowed a change in basic design of furnaces, whereby the heating coil is placed in the center of the structure, using horizontal tubes either as a single row or in a zigzag pattern with double rows of tubes. The burners are placed in the opposing side walls for the full height and length of the radiant section. In a heater of this type with an average temperature of 1750 F and with the tubes at 1200 F wall temperature, they receive 84 per cent of their heat from wall radiation and 7 per cent from gas radiation, according to research data as yet unpublished. Thus a high percentage of the heat released within the furnace is utilized immediately, resulting in more efficient transfer of heat. When refractories of low specific heat

FIG. 7 INTERNAL VIEW OF HEATER WITH RADIANT BURNERS
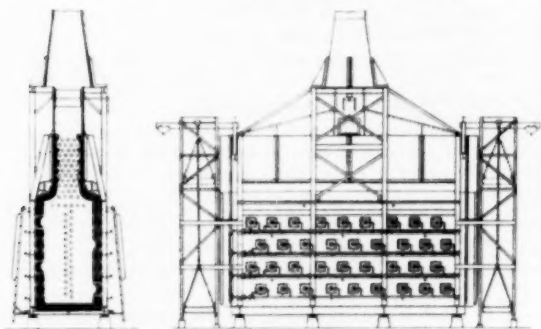
FIG. 5 TYPICAL CROSS SECTION OF FURNACE WITH RADIANT BURNERS

are used in this type heater, response to temperature control is rapid.

Since combustion is complete in a short distance, the burners may be placed near the heat-absorbing surface without danger of flames touching the tubes. Heat is applied from burners on each side of each tube for the entire length of the furnace. Furthermore, the narrow construction requires less ground area than similar-duty heaters of conventional design.

A typical cross-sectional view is shown in Fig. 5. An operating unit is shown in Fig. 6, and an interior view of the radiant section before installing the tubes is shown in Fig. 7.

Since excess air is not required for assurance of complete combustion, the operation of these heaters at high-heat-input rates does not result in oxidation of tubes, even though the metal temperature is exceedingly high, because oxygen is absent and the atmosphere in the firebox is neutral.

Some types of process heating will require that the heating be rapid at the beginning of

FIG. 6 OPERATING UNIT WITH RADIANT BURNERS

the temperature profile and much slower toward the end of the heating period. Other processes, particularly those involving a catalytic reaction after heating, require that the latter part of the heating be done as rapidly as possible to avoid product degradation before the catalytic reaction. That is, after a predetermined temperature is reached, the time to reach final temperature must be kept to a minimum to suppress undesirable reactions. In conventional-type heaters, it is necessary to change heater structure or relative tube positions to effect a major change in the shape of the heating curve, because the heat-source area is small compared to the total surface which receives heat. In this newly developed heater, heat-input rates may be changed in the various zones by the operator as required by the process without affecting the other zones. Separate heating coils may be placed in each heating zone, with independent control for each zone, because the heat-source area is spread over the entire area of the two walls of the heater opposing the tubes.

Since higher average heat-input rates can be tolerated when firing from both sides, the total heat transferred per foot of tube will be increased without exceeding a predetermined outside metal-wall temperature or a prescribed inside film temperature. This results in requiring less tube surface for a particular heater service and may be translated into shorter-length heating coils or smaller tubes. Either of these factors, the shorter-length coil or the smaller tubes, will result in savings of capital investment for tubes. The shorter-length coil also will result in less pressure drop in the coil, which is measurable as an operating saving, and will result in less residence time within the coil, which is advantageous in all high-temperature process heating.

APPLICATION OF RADIANT BURNERS

Burners which embody this radical departure from accepted methods of high heat release and resultant high percentage of radiant heat have had wide acceptance in the ferrous and nonferrous-metal forming and heat-treating industries, the glass forming, annealing, and tempering fields, and in textile and paper processing industries. Although the development of burners for the refining and chemical industries has been somewhat slower than for those industries cited, at the present time this principle is used in approximately 110 refineries, laboratories, and chemical plants by about 15 different independent companies and governmental agencies.

A major petroleum refiner[4] has reported data comparing operating results from a heater with high radiant-heat inputs to results from a conventional heater, both charging the same material, a catalytic-recycle oil as shown in Table 1.

The explanation for the lower coil-outlet temperature on the box-type furnace was that 920 F was the maximum temperature which could be reached without excessive coil-coking.

This same refiner[5] also describes a mild cracking or visbreaking operation on a crude vacuum-tower bottom product which represented 13.3 per cent liquid volume of the crude. This stock had an API gravity of 20.3, a 500 SSF viscosity at 122 F, and a Ramsbottom carbon residue of 10.5 per cent. The material had an extremely high boiling range. Only 20 per cent boiled below 1100 F. It was so unstable that it was not considered possible to process it without excessive coking, yet it was handled in a high-radiant-heat furnace with calculated rates as high as 30,000 to 40,000 Btu/hr/sq ft of tube surface on the last tube, and with an average rate of 17,000 Btu/hr/sq ft in the entire radiant

[4] "High Destruction Thermal Cracking of Catalytic Cycle Oil," by D. M. Little and G. E. Merryfield, *Oil and Gas Journal*, vol. 48, March 29, 1951, pp. 242, 246, 247, 249.

[5] "Visbreaking High Vacuum Residua," by J. G. Allen, D. M. Little, and P. M. Waddill, *Petroleum Processing*, vol. 6, June, 1951, pp. 612–615.

TABLE 1   COMPARISON OF RESULTS IN THERMAL-CRACKING A CYCLE OIL IN A RADIANT-TYPE AND A BOX FURNACE

	Radiant furnace	Box furnace
Coil outlet, deg F	1025	920
Pressure, psig	700	1100
Charge rate, bbl/hr	100	300
Aniline-point reduction, deg F	50	35
Yields, LV per cent of charge:		
Gasoline	30	22
Gas oil	44	57
Fuel oil	10	12

Conversion of gas oil to other products, liquid vol per cent of charge:		Diff	
Gas	28.6	+7.7	20.9
Gasoline	53.4	+2.3	51.1
Fuel oil	18.0	−10.0	28.0
	100.0		100.0
Gasoline octane number:			
F-1 clear	73		66
+3 cc TEL[a]/gal	86		80

[a] Tetraethyl lead.

TABLE 2   THERMAL-EFFICIENCY TEST DATA FOR A RADIANT FURNACE

	Top	Bottom
Firebox temperatures, deg F:		
Maximum	1490	1580
Minimum	1390	1575
Average	1425	1580
Stack temperature, deg F	712	
Coil temperatures:		
Inlet	117 F at 790 psig	
Outlet	1020 F at 500 psig	
Fuel gas-fired	39,400 cfh	
Heat balance:		
Heat released by flame	32.6×10^6 Btu/hr	
Heat pickup by oil in furnace	29.5×10^6 Btu/hr	
Over-all efficiency (net heating value)	81.5 per cent	
Heat pickup by oil in radiant section	22.2×10^6 Btu/hr	
Average radiant-heat-transfer rate	17,000 Btu/hr/sq ft	
Per cent useful heat	75.3	
Heat pickup by oil in convection bank	7.28×10^6 Btu/hr	
Average convection-heat-transfer rate	4920 Btu/hr/sq ft	
Per cent useful heat	24.7	

section. This was made possible by designing the furnace for low residence time and obtaining the desired cracking by increasing the outlet temperature, thus obtaining better operation by increased temperature and decreased residence time.

On a thermal-efficiency test, the operating conditions were noted by a major refiner[6] as shown in Table 2. It will be noted that an over-all thermal efficiency of 81.5 per cent was realized and that 75.3 per cent of the total heat transferred occurred in the radiant section.

CONCLUSION

The development of gas burners which will produce a high-temperature radiant source with negligible excess air and with relatively short flames has made possible a radical change in tubular-furnace construction which economically and safely utilizes high radiant-heat-transfer rates. The application to tubular heaters is not limited by any known charge-stock characteristic and presents many operating advantages paramount among which are (a) lower pressure drop, (b) neutral furnace atmosphere, (c) independent control of various heating zones, and (d) complete combustion at the burner with minimum flame length.

Discussion

L. A. MEKLER.[7] The author has interpreted erroneously two important items in the article, "Evaluation of Radiant Heat Absorption Rates in Tubular Heaters,"[8] which he uses as a refer-

[6] C. C. Tate, address to Western Petroleum Refiners Association, April, 1951.

[7] Consulting Engineer, New York, N. Y. Mem. ASME.

[8] Footnote reference 2 of the paper

ence to explain the superiority of the heater as covered by the text and illustrations of his paper.

The first error is in using Fig. 2 of his paper, which is Fig. 5B of the reference article,[5] to show the flux distribution around the tubes of the heater described. As stated in the caption of Fig. 5 of the reference article, this flux distribution applies to tubes in "single-row tube banks" irradiated from both sides. While there are some heaters with single-row tube banks irradiated from both sides, the heater covered by the text and illustrations of the present paper and as supplied by the author's company to date to the industry, has "double-row" banks irradiated from both sides. Therefore the flux-distribution diagram which would apply to the heater covered by the paper is that shown in Fig. 7B of the reference article,[5] if the tubes were on a spacing of 2.63 times the diameter, and is identical with Fig. 5A of the reference article, or Fig. 1 of the present paper, if the tubes are on a spacing of two diameters.

Similarly, in the heater as described in the article,[5] the average heat-input rates, with a maximum rate of 15,000 Btu/hr at point No. 1, would be identical with those of a single-row tube bank irradiated from one side, that is, 8430 Btu instead of the 13,050 Btu given in the paper, or exactly the same as for tubes in a single row irradiated on one side.

The second error is in the interpretation of the symbols in the Stefan-Boltzmann equation and numerical examples given in the paper which show possible 40 and 56 per cent increases in heat-transfer rates with decreases of excess air. The T_R of the equation is not the flame-burst temperature, but the theoretical equilibrium temperature of the radiating surface. While the flame-burst temperature may be increased as much as 500 deg F by reducing the excess air from 50 per cent (the maximum used in commercial tubular heaters) to 10 per cent, the maximum variation in the equilibrium temperature in any given heater with any given load would be not more than 45 deg F.

For example, using Fig. 3 of the reference article[5] with 17,000 Btu/hr/sq ft of circumferential surface, which with a two-to-one spacing, is equivalent to 29,000 Btu/hr/sq ft of effective area, the required liberation is approximately 50,000 Btu. With this liberation the equilibrium temperatures will be 1725 F or 2185 R with 10 per cent excess air, 1700 F or 2160 R for 30 per cent excess air, and 1680 F or 2140 R with 50 per cent excess air. Substituting these values and the value of 1410 R for the metal temperature in the equation, the terms in the large bracket become, respectively, 188,600, 178,200, and 170,900, which gives a total difference of approximately 11 per cent between the 10 and the 50 per cent excess air and approximately 5.5 per cent between the two extremes and 30 per cent air, which is most commonly used in the better-operated tubular heaters. While these figures are significant they certainly are far removed from the 40 per cent and the 56 per cent mentioned in the paper.

A serious misstatement of fact occurs early in the paper. There are many heaters with double-row tube banks irradiated from both sides in successful operation where this principle of heating is used to advantage. Over 2,000,000 bbl of charge per day are processed through UOP's Equiflux heaters. Some of the heaters are over 20 years old and have been operating with average rates of 17,000 to 20,000 Btu/hr/sq ft of circumferential surface, processing "black" oils down to (—) 2° API cracked residues, and distillates up to light naphtha. Per unit throughput, the UOP heaters are not appreciably larger than the heater covered by the author, and the UOP heaters are being fired with either oil or gas or both.

The thermal-efficiency data showing 81.5 per cent over-all efficiency based on the net value of the fuel, while quite high, is not particularly impressive. With an inlet-oil temperature of only 170 F and a stack temperature of 712 F, this gives an approach of 595 F between the inlet oil and the stack temperature. A great number of tubular heaters in operation have a much lower approach.

The heater described by the author represents a contribution to the art, particularly by the introduction of zonal firing, so that the rates of heat input to the various sections of the radiant tubes can be varied to obtain the desired heating curve without structural changes to the heater. This is particularly valuable in new processes where the optimum heating curve is not known definitely, and where the ability to change this curve would improve the operating results of the unit. In established processes where the desired heating curve and the time-temperature relationships are known, this characteristic of the heater is not so important because several other types of heaters with tubes irradiated from one or both sides of the banks can be used to obtain the desired heating curve with enough flexibility for normal variations in charging stocks and processing requirements.

AUTHOR'S CLOSURE

Mr. Mekler is mistaken in asserting that the heaters as supplied by the author's company to the industry to date have only double-row banks of tubes irradiated from both sides. In those applications where uniformity of heat distribution is essential, this type heater has also been supplied with single rows of tubes. The radiant heat flux distribution on these tubes will be according to Fig. 2 of my paper as stated therein, with an average of 13,050 Btu/hr/sq ft while maintaining a maximum of 15,000 Btu/hr/sq ft on point No. 1, Fig. 5, described in the reference.[5]

We have found in commercial applications that the actual total heat transferred to a double-row bank of tubes including convection heat, when spaced on two diameters and irradiated from both sides by the new type burners, is sufficiently uniform to discourage the use of single rows of tubes and the attendant larger settings required except for very special heating applications.

The findings to date on these commercial units indicate that on double rows irradiated from two sides, an average input rate of 12,750 Btu/hr/sq ft is normally realized without exceeding 15,000 Btu/hr/sq ft on point No. 1. Expressed another way, this means that the average circumferential rate is approximately 85 per cent of the maximum rate at point No. 1.

The author is indebted to Mr. Mekler for his correction to the interpretation of the symbols in the Stefan-Boltzmann equation, however, his statement that 50 per cent excess air is the maximum used in commercial tubular heaters and that 30 per cent is more commonly used in the better-operated tubular heaters is open to question. It is not uncommon to find heaters operating with excess air up to 100 per cent and in some cases even with 150 per cent excess air. Furthermore, with a given heat load and heat-input rate, the refractory equilibrium temperature is independent of a given amount of excess air; therefore, the statement that the maximum variation in equilibrium temperatures in any given heater with any given load would not exceed 45 F bears no significance since the equilibrium temperature must remain constant and actually the liberated heat must be increased sufficiently to maintain equilibrium temperature after heat losses to the excess air.

The discusser's example using Fig. 3 of the reference article[5] with 17,000 Btu/hr/sq ft of circumferential surface which is equivalent to 29,000 Btu/hr/sq ft of effective area assumes a constant required heat liberation of approximately 50,000 Btu/hr. The discusser's reference Fig. 1 and Fig. 3 show that with an effective rate of 29,000 and no excess air in a gaseous fuel, the resulting equilibrium temperature will be 1710 F for an absorbing surface at 950 F and that the required liberation will be 45,000 Btu/hr instead of 50,000 Btu/hr. Admitting 10 per cent excess

air at the same equilibrium temperature and effective rate will require a liberation of 47,000 Btu/hr while 30 per cent excess air will require a liberation of 51,000 Btu/hr and 50 per cent excess air will require a liberation of 56,000 Btu/hr. This indicates that the actual increases in fuel consumption are 4.45 per cent for 10 per cent excess air, 13.3 per cent for 30 per cent excess air and 24.4 per cent for 50 per cent excess air. Thus, the increase in fuel requirements for changing the excess air from 10 per cent to 30 per cent becomes 8.85 per cent instead of 5.5 per cent as stated by the discusser and becomes approximately 20 per cent increase for changing the excess air from 10 per cent to 50 per cent. For 100 per cent excess air, the heat liberation requirement is increased 121 per cent over that required for 10 per cent excess air.

The significant feature is that all of the increased heat which must be liberated is absorbed by the excess air and must be re-absorbed by additional convection surface to equal the efficiency of those heaters which utilize lower excess air.

Mr. Mekler's example which shows that 17,000 Btu/hr/sq ft of circumferential area will require a heat liberation of approximately 50,000 Btu/hr/sq ft indicates a thermal efficiency of 34 per cent. The author's reference Table 2 shows that on an actual operating heater 22.2×10^6 Btu/hr were absorbed in the radiant section which required only 32.5×10^6 Btu/hr of total heat liberation or an actual thermal efficiency of 67 per cent with the same average rate of 17,000 Btu/hr/sq ft as used by Mr. Mekler in his example. While it is recognized that some convection heat will be transferred to the heating coil by the products of combustion, our experimental data does not indicate that more than about 10 per cent of the total heat will be transferred by this method. Therefore, it must be concluded that the Selas Heater will perform with a higher thermal efficiency in the radiant section than Mr. Mekler's considerations indicate. Furthermore, these heaters operate satisfactorily on very low excess air which has been shown to have a pronounced effect on thermal efficiency.

Study of Cubic Characteristic Equation by Root-Locus Method

By YAOHAN CHU[1] AND V. C. M. YEH[2]

It is shown in this paper that all possible roots of a cubic characteristic equation lie on a portion of a hyperbola and of its axis. This hyperbola may be sketched readily from the values of the coefficients of the cubic equation. Hence the change of the roots of the cubic equation due to any change in its coefficients may be visualized. The discussion of the transient response in relation to possible root configurations is included. A root-locus chart is provided for "universal" use. Results from an analog computer are shown to be agreeable with those in this paper.

Introduction

THE behavior of a linear system, whether it be a feedback control system (1),[3] a lumped-parameter network, the dynamics of an aircraft (linearized), or the like, may be described by a linear ordinary differential equation with constant coefficients. The complementary solution of this differential equation gives the transient response of the system. If Laplace transformation is employed, this equation becomes a complex algebraic one. Its transient response is determined by the roots of this complex algebraic equation, which often is called the characteristic equation of the system.

For the cases of first and second-order equations, their results (2) are well known and serve as the fundamentals for those who are working in this field. For the case of third-order equations, methods (3, 4) for extracting roots are available, and charts (5) for choosing the values of constant coefficients for certain desirable roots also are available. However, the existing technique does not provide a clear picture about the influence of each constant coefficient of the cubic equation upon its roots, as one would have for the cases of first and second-order equations.

This paper attempts to demonstrate that all the three kinds of information are obtainable by means of the root-locus method, thus providing a better approach for synthesis of third-order systems. Emphasis will be laid on the third one, which is the influence of each constant coefficient upon the roots. Once the values of these constant coefficients are related to the parameters of the system, one will be able to visualize the nature of response and to know which coefficients of the cubic characteristic equation should be modified in order to achieve a desired response. It is hoped that this paper will present to the reader a view such as one would obtain by merely examining the values of the constant coefficients of the first and second-order equations.

Types of Responses

A cubic characteristic equation has three roots. It may be (a)

FIG. 1 (left) ROOT CONFIGURATIONS OF THREE TYPES OF RESPONSES ON COMPLEX s-PLANE

FIG. 2 (right) TYPES A, B, AND C RESPONSES

three simple roots, or (b) one simple root and a pair of complex roots. These are shown on the complex s-plane as in Fig. 1 (s being the complex variable). It is noted there that two possible root configurations exist for the case (b), depending on whether the time constant of the real root (i.e., the reciprocal of the real root) is larger or smaller than that of the complex root (i.e., the reciprocal of the real part of the complex roots). Their corresponding transient responses to a step input with zero initial conditions are shown in Fig. 2. For convenience, systems which possess root configuration and have an associated transient response of Fig. 2(a) are called type A, Fig. 2(b) type B, and Fig. 2(c) type C. Type A is widely accepted as the desired response for servomechanisms and other dynamic systems. Type B is sometimes desired for certain applications. Type C is generally regarded as undesirable, owing to its slow response. The patterns of these root configurations and their corresponding shapes of responses will serve as a basis for later discussions.

Study by Root-Locus Method

A cubic characteristic equation which is stable by Routh's criterion may be written as an equation of the form

$$s^3 + 2cw_n s^2 + w_n^2 s + k = 0 \dots \quad [1]$$

where $s\,(=v+jw)$ is the complex variable. This equation is a complex algebraic one, which may be written as

$$\frac{k}{s(s^2+2cw_ns+w_n^2)}=-1 \qquad\qquad [2]$$

By equating the phase angle and magnitude on each side of this equation, respectively, one obtains the phase-angle equation

$$\text{Ang } s+\text{Ang }(s^2+2cw_ns+w_n^2)=\pm180°\pm2n(180°).\quad[3]$$

where $n=0,1,2,\dots$
and the magnitude equation

$$k=|s|\cdot|s^2+2cw_ns+w_n^2| \qquad\qquad [4]$$

The plot of the phase-angle Equation [3] on the complex s-plane is known as the root locus (6, 7), and the value of k on each point of the locus is determined by the magnitude Equation [4]. Every point on the locus is a possible root of Equation [1], as it fulfills both Equations [3] and [4].

The cubic characteristic equation has three parameters: w_n, c, and k as shown in Equation [1]. The associated root locus is completely determined by the first two parameters (w_n and c), whereas the parameter k determines a set of three specific roots on the locus. There are five possible shapes of the root locus for the cubic equation which are shown in Fig. 3 (circles, squares, and triangles indicate the location of the corresponding set of three roots for the three types of responses). These five possible shapes are classified according to the values of c in Table 1. The shapes

TABLE 1   ROOT-LOCUS SHAPES

Case	c	Types of response[a]
(a)	$c<\sqrt{3}/2$	A, C
(b)	$c=\sqrt{3}/2$	A, B,[b] C
(c)	$\sqrt{3}/2<c<1$	A, B, C
(d)	$c=1$	A, B
(e)	$c>1$	A, B

[a] To be discussed later.
[b] Only at one specific point on this shape of locus.

of the root locus for these five cases are all portions of a hyperbola or its degenerated form in addition to a certain portion of the real axis. The analytic derivation of the equation of root-locus is shown in the Appendix.

The value of k corresponding to the points where root locus crosses the imaginary axis (points D and D' in Fig. 3) is called "stability limit," as unending oscillation will not occur for any value of k smaller than this limit. It can be shown that the value of stability limit for the cubic equation is equal to $2cw_n^3$ which, of course, agrees with the result from Routh's criterion.

The shapes of the locus are gradually changing from Fig. 3(a to e) from one type of hyperbola to the other as c is being increased. Since the hyperbola can be drawn accurately, the roots can be determined accurately for any given value of k. Furthermore, these locus shapes show how the three coefficients will effect all possible solutions of the cubic characteristic equation.

Case (a): $c<\dfrac{\sqrt{3}}{2}$

Fig. 3(a) shows the locus shape of case (a). There are only two possible types of response, type A and type C. Thus there is always a pair of complex roots, and the system possesses inherent oscillation regardless of the value of k. The value of undamped natural frequency of the chosen complex roots will be in the order of magnitude of the given w_n and will not be affected greatly by various values[*] of k. When k is large $\left[k>\dfrac{2}{27}\right.$

[*] For discussion hereafter, the values of k are all smaller than the stability limit.

(a) CASE A $c<\sqrt{\frac{3}{2}}$
(d) CASE D $c=1$
(b) CASE B $c=\sqrt{\frac{3}{2}}$
(e) CASE E $c>1$
(c) CASE C $\sqrt{\frac{3}{2}}<c<1$
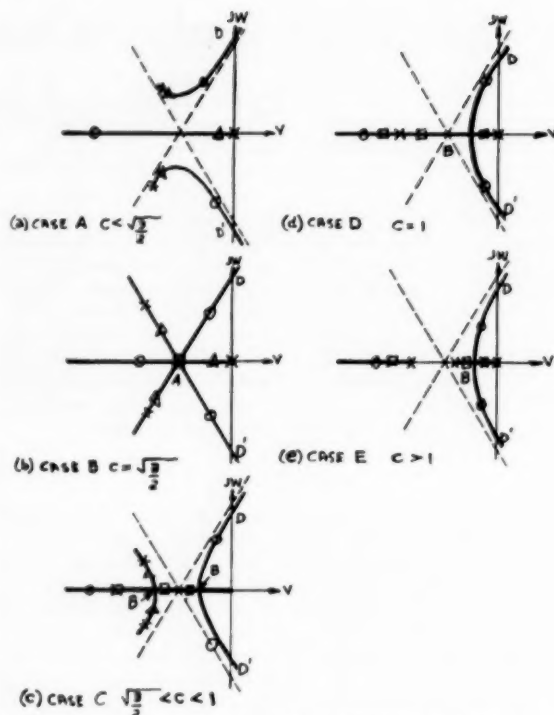
FIG. 3   FIVE POSSIBLE SHAPES OF ROOT LOCUS FOR CUBIC CHARACTERISTIC EQUATION—ALL ARE HYPERBOLAS

$(9-8c^2)cw_n^3\Big]$ the response is of type A. When k is small $\left[k<\dfrac{2}{27}(9-8c^2)cw_n^3\right]$ the response is of type C. Since type C is regarded as undesirable, small k is to be avoided. It is obvious that the damping ratio of the chosen complex roots will always be smaller than the given c. Consequently, the change of value of k renders little help in the stabilization of the system. A sufficient value of c is necessary before the selection of k.

Case (b): $c=\dfrac{\sqrt{3}}{2}$

Fig. 3(b) shows the locus shape of case (b). This is the case of demarcation for the cases (a) and (c); note that three roots for k equal to zero lie on the apex of an equilateral triangle. When k is large, the roots configuration shows a response of type A. When k is decreasing to the value at point A, the three roots are equal. The multiple roots usually give a longer response time, because, as the present case of a triple root, the transient solution will involve such an expression as

$$e^{-\tau t}(C_1+C_2t+C_3t^2)$$

where C's are constants. When k is further decreased, the root configuration shows that the system has a type C response. Thus there is always a pair of complex roots except at the point A. The value k at point A can be shown as $[2cw_n/3]^3$. It is desirable to have k larger than this value so that type A response prevails.

Case (c): $\dfrac{\sqrt{3}}{2}<c<1$

Fig. 3(c) shows the locus shape for case (c). The response is of type A for the large values of k and of type B when k is becoming smaller and of type C for small values of k. For k at point B the chosen roots are a simple and a double root. Therefore

too small a value of k is to be avoided, as otherwise type C response occurs.

Case (d): c = 1

Fig. 3(d) shows the locus shape of case (d). This is the case of demarcation for cases (c) and (e). The response is of type A for large k and becomes of type B when k is becoming smaller. No type C response will occur. If k is the value corresponding to point B, the chosen roots will be a simple and a double root.

Case (e): c > 1

Fig. 3(e) shows the locus shape of case (e). The behavior is similar to that of case (d).

Sketching the Root Locus

The roots of the cubic characteristic equation are related to its constant coefficients by means of the root locus, which is a hyperbola. When this hyperbola is sketched, their relation is clearly shown. If the cubic Equation [1] is rewritten as

$$s^3 + as^2 + bs + k = 0 \dots\dots\dots\dots\dots [5]$$

the root locus may be sketched (from the results shown in the Appendix) according to the following procedure:

Step (a) Test Equation [5] by Routh's criterion, stable if $k < ab$.

Step (b) Find c by the relation $c = a/(2\sqrt{b})$. This determines the locus shape as shown in Fig. 3.

Step (c) Find the location of the point of intersection of the asymptotes, which lies on the negative real axis and is at a distance (called as v_0) $a/3$ from the origin, Fig. 4. This asymptote always makes an angle ± 60 deg with the negative real axis. Draw the asymptotes.

Step (d) Find the location of the vertex of the hyperbola. It may be determined by (see Appendix)

$$y_0 = \sqrt{3b - a^2}/\sqrt{3} \text{ for case } (a)$$

$$x_0 = \sqrt{a^2 - 3b}/3 \text{ for cases } (b), (d), (e)$$

where y_0 and x_0 are the distances as shown in Fig. 4. Note that the hyperbola degenerates into the asymptotes for case (c).

Step (e)[5] The locus may now be readily sketched as shown in Fig. 4.

The reader is reminded that k is not involved in the sketching of the locus. In actual application, the values of a and b may not be known yet. Nevertheless, the previous four quantities

$$\left. \begin{array}{ll} c = a/(2\sqrt{b}) & v_0 = a/3 \\ x_0 = \sqrt{a^2 - 3b}/3 & y_0 = \sqrt{3b - a^2}/\sqrt{3} \end{array} \right\} \dots [6]$$

determines the shape and the location of the locus in the s-plane, and thus show its relation with the coefficients a and b.

The Root-Locus Chart

The cubic characteristic Equation [1] has three parameters; however, only the parameters c and w_n actually determine the exact shape of the root locus. If the following is defined

$$\left. \begin{array}{l} k' = k/w_n{}^3 \\ s' = s/w_n \end{array} \right\} \dots\dots\dots\dots\dots\dots\dots [7]$$

and these are substituted into Equation [2], Equation [2] becomes

$$\frac{k'}{s'(s'^2 + 2cs' + 1)} = -1 \dots\dots\dots\dots [8]$$

---

[5] Another point of the locus can be easily determined. This is the point D or D' in Fig. 3 at which gain limit lies. Its location is $v = 0$ and $w = \pm\sqrt{b}$.

The exact shape of the root locus (the hyperbola) is then determined by the value of c alone. By using the analytical expression for the root locus as shown in the Appendix, a family of root loci is plotted on the complex s'-plane for various values of c. This family of root loci as shown in Fig. 5 is called the "root-locus chart." All possible roots of a cubic characteristic equation can be extracted from this chart. It is noted there that $v'_0 (= v_0/w_n)$ is chosen as the center. The actual location of the imaginary axis $jw' (= jw/w_n)$ must be determined relative to this center for a

S- PLANE

$$X_0 = \sqrt{\frac{a^2 - 3b}{3}}$$

(a) FOR $C > \sqrt{\frac{3}{2}}$

$$y_0 = \sqrt{\frac{3b - a^2}{3}}$$

(b) FOR $C < \sqrt{\frac{3}{2}}$
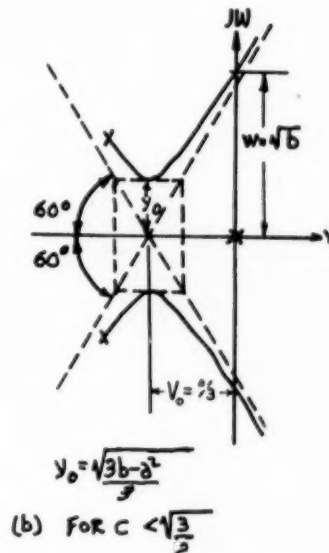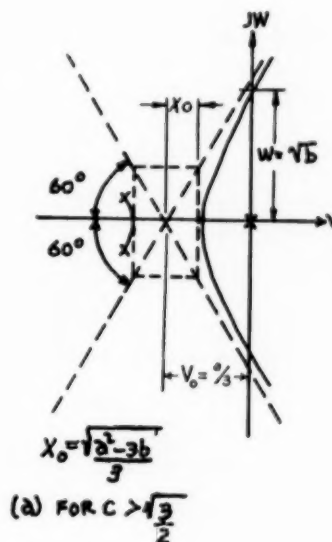
Fig. 4 Sketching Root Locus for a Cubic Characteristic Equation

$$s^3 + as^2 + bs + k = 0$$
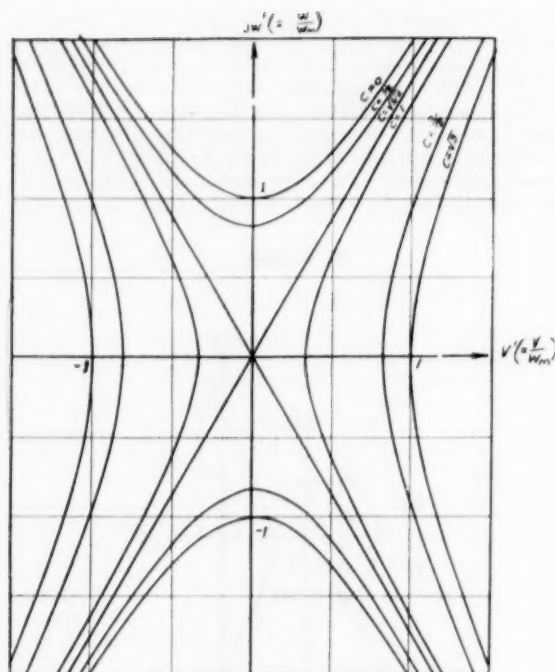
FIG. 5   ROOT-LOCUS CHART

given problem.   Once a cubic characteristic equation has been normalized in the form of Equation [8], the use of the root-locus chart is evident.

Referring to Equation [1] and the root-locus chart, the following properties may be observed:

(a) Change in the scale of root locus corresponds to a change in the value of w_n.

(b) Roots moving along one locus correspond to changes in the value of k.

(c) Roots moving from one locus to another on the root-locus chart correspond to changes in the values of c.

RESULTS FROM ANALOG COMPUTER

The transient response of a cubic characteristic equation to a step input is studied on an electronic analog computer.   The results agree with the previous discussion.   Figs. 6 to 10 are presented as demonstrations.   Fig. 6 shows the three types of response.   Figs. 7, 8, and 9 show the responses for the cases (a), (c), and (e), respectively, with various values of k of Equation [5].   It agrees with the known result that the speed of response can, in general, be improved by increasing the value of k (without exceeding the stability limit).   However, as previously stated for
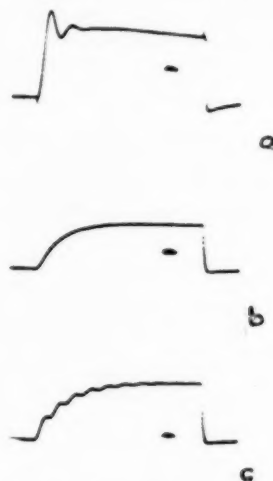
FIG. 6   THREE TYPES OF RESPONSES FROM AN ANALOG COMPUTER
(Compare with Fig. 2.   a, Type A response;   b, type B response;   c, type C response.)
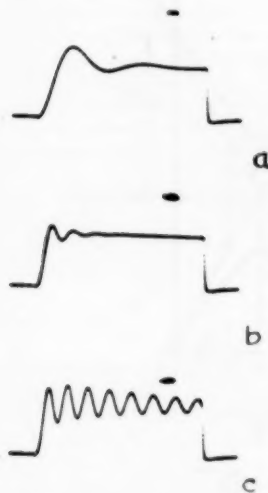
FIG. 7   RESPONSES FROM ANALOG COMPUTER CORRESPOND TO CASE OF FIG. 3(a), WITH NOT TOO SMALL VALUE OF c OF EQUATION [1]
(Compare with Fig. 10.   Value of k increases in order from a to c.)
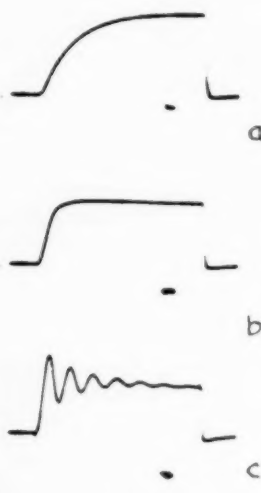
FIG. 8   RESPONSES FROM ANALOG COMPUTER CORRESPOND TO CASE OF FIG. 3(c)
(Value of k increases in order from a to c.)
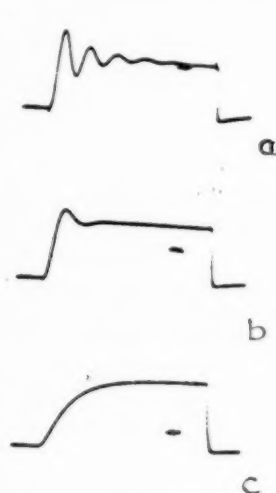
FIG. 9   RESPONSES FROM ANALOG COMPUTER CORRESPOND TO CASE OF FIG. 3(e)
(Value of k increases in order from c to a.)

the case (a), the response becomes undesirable if the value of a of Equation [5] is too small. This is demonstrated in the responses
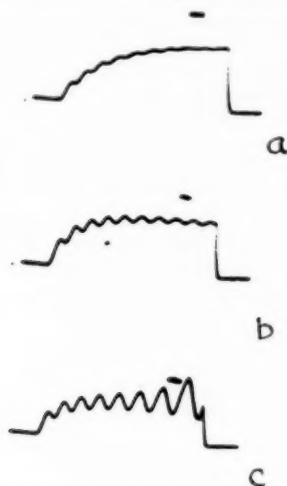
FIG. 10 RESPONSES FROM ANALOG COMPUTER CORRESPOND TO CASE OF FIG. 3(a) WITH SMALL VALUE OF c OF EQUATION [1] (Compare with Fig. 7. Value of k increases in order from a to c.)

of Fig. 10 in which all responses are of type C. This cannot be improved by changing the value of k alone.

CONCLUSION

The complexity of the possible roots of the cubic equation is nothing more than the relations involved for a hyperbola. The coefficients a and b of the cubic characteristic Equation [5] determine one of five possible shapes, and their exact location may be sketched by figuring out the quantities of Equations [6]. k is to be selected according to the desired type of response.

Type A response is possible in all the five cases. Type B response occurs in cases (c), (d), and (e), in addition to one specific point in case (b). Type C response is possible only in cases (a), (b), and (c). Thus the often desired type A response may be obtained in any stable third-order system by merely adjusting k to a proper value.

Type A response will be too oscillatory, if the value of c of Equation [1] is too small, and the change of k gives no help. Its response becomes faster, if the undamped natural frequency of the chosen complex roots is made larger. This in turn requires to a great extent a larger value of a (or v_0) and depends to a small extent on the value for the vertex distances x_0 and y_0. No type A response will occur in any of the five cases if k is too small.

ACKNOWLEDGMENT

BIBLIOGRAPHY

1 "Principles of Servomechanism," by G. S. Brown and D. P. Campbell, John Wiley & Son, New York, N. Y., 1948.
2 "Design Factors Controlling the Dynamic Performance of Instruments," by C. S. Draper and G. P. Bentley, Trans. ASME, vol. 62, 1940, pp. 421–432.
3 "Method of Successive Approximations of Evaluating the Real and Complex Roots of Cubic and Higher-Order Equations," by Shih-Nge Lin, Journal of Mathematics and Physics, vol. 20, August, 1941, pp. 231–242.

Appendix

ANALYTICAL EXPRESSION OF SHAPE OF ROOT LOCUS FOR A CUBIC EQUATION

If the Relation [2] is rewritten as

$$\frac{k}{s(s + s_1)(s + s_2)} = -1 \quad \quad \quad [9]$$

then the root locus (or phase-angle equation) is

$$\text{Ang}\,(1/s) + \text{Ang}\,[1/(s + s_1)] + \text{Ang}\,[1/(s + s_2)] = \pm 180 \deg \quad [10]$$

Letting $s = v + jw$, $s_1 = v_1 + jw_1$, and $s_2 = v_2 + jw_2$, and substituting them into Equation [10], one obtains by trigonometric relations

$$\frac{w}{v} + \frac{w + w_1}{v + v_1} + \frac{w + w_2}{v + v_2} = \frac{w(w + w_1)(w + w_2)}{v(v + v_1)(v + v_2)} \cdots [11]$$

For cases (a), (b), and (c) in Fig. 3, then

$$w_2 = -w_1 \quad \text{and} \quad v_1 = v_2 \quad \quad \quad [12]$$

By combining Equations [11] and [12], one obtains by simplification

$$w = 0 \quad \quad \quad [13a]$$

$$(w/\sqrt{3})^2 - (v + v_0)^2 = x_0^2 \quad \quad \quad [13b]$$

where $v_0 = 2v_1/3$ and $x_0 = w_1^2/3 - v_1^2/9$.

Case (a). If $w_1^2/3 > v_1^2/9$. Equations [13] become

$$w = 0 \quad \quad \quad [14a]$$

$$(w/y_0)^2 - [(v + v_0)/x_0]^2 = 1 \quad \quad \quad [14b]$$

where

$$y_0 = \sqrt{3}\,x_0 = w_n\sqrt{3 - 4c^2/3} \quad \quad \quad [15]$$

as

$$w = w_n\sqrt{1 - c^2} \quad \text{and} \quad v_1 = cw_n$$

w_n and c are from Equation [1]. Equation [14a] shows the real axis is the locus. By testing on the real axis, only negative real axis fulfills Equation [10]. This is due to the fact that tan $0° = \tan \pm 180° = 0$ and that this is introduced in Equation [11]. Equation [14b] shows the locus is a hyperbola; only that portion which fulfills Equation [10] is the locus. The locus is shown as Fig. 3(a).

Case (b). If $w_1^2/3 = v_1^2/9$, Equations [13] become

$$w = 0 \quad \quad \quad [16a]$$

$$(w_1/\sqrt{3})^2 - (v + v_0)^2 = 0 \quad \quad \quad [16b]$$

These are the two asymptotes and are shown as Fig. 3(b).

Case (c). If $\left(w_1/\sqrt{3}\right)^2 < v_1^2/9$, we have from Equations [13]

$$w = 0 \quad \quad \quad [17a]$$

$$[(v + v_0)/x_0]^2 - [w/\sqrt{3}\, x_0]^2 = 1 \ldots \ldots [17b]$$

where $x_0 = v_1^2/9 - w_1^2/3 = w_n\sqrt{4c^2 - 3}/3 \ldots [18]$

the locus is shown as Fig. 3(c).

For cases (d) and (e) of Fig. 3, then

$$w_1 = w_2 = 0 \ldots \ldots \ldots \ldots \ldots \ldots [19]$$

By combining Equations [11] and [19], one obtains after simplification

$$w = 0 \ldots \ldots \ldots \ldots \ldots \ldots \ldots [20a]$$

$$[(v + v_0)/x_0]^2 - [w/\sqrt{3}\, x_0]^2 = 1 \ldots \ldots [20b]$$

where

$$x_0 = (1/3)\sqrt{(v_1 + v_2)^2 - 3v_1v_2} = (w_n/3)\sqrt{4c^2 - 3} . \; [21]$$

as $v_1 + v_2 = 2cw_n$ and $v_1v_2 = w_n^2$.

Case (d). If $v_1 = v_2$, Equations [20a, b] is the locus and is shown as Fig. 3(d).

Case (e). Equation [20] is the locus and is shown in Fig. 3(e). It can be shown that in the Relation [21], $(v_1 + v_2)^2$ is always greater than $3v_1v_2$; therefore there exists no other shapes of the root locus. Equations [14b], [16b], [17b], and [20b] show that the two asymptotes make an angle ± 60 deg with the negative real axis. The coefficients of Equations [1], [5], and [9] are related as follows

$$\left. \begin{array}{l} a = 2cw_n = v_1 + v_2 \\ b = w_n^2 = v_1v_2 - w_1w_2 \end{array} \right\} \ldots \ldots \ldots [22]$$

from which Relation [6] is obtained.

The Study of Transients in Linear Feedback System by Conformal Mapping and the Root-Locus Method[1]

By VICTOR C. M. YEH,[2] NEW YORK, N. Y.

The correlation between frequency and transient analysis of linear feedback systems, either degenerative or regenerative, through conformal mapping is pointed out. The root locus is a special case of the conformal mapping obtained by transforming the real axis of the inverse $Y(s)$-plane onto the s-plane. A method for deriving the equations of root loci is presented, and the basic shapes of root loci are shown. The shifting and reshaping of root locus by means of controller adjustments are discussed.

Introduction

THE technique of conformal mapping has provided a powerful tool in modern engineering; this is especially true in the analysis and synthesis of linear feedback systems. It will be shown that the frequency and transient-response methods are based on two conformal transformations—a direct and a reverse transformation. The transfer locus on the one hand, and the root locus on the other, are the most useful items of information obtainable through the two-way transformation. The information yielded from one transformation tends to complement that of the other. Only by performing the two-way tranformation may one obtain complete information regarding the dynamic behavior of a linear feedback system.

Since Nyquist's paper (1)[3] the frequency-response method and its relevant transfer locus have received great attention. Draper and Bentley (2), on the other hand, have systematically introduce l the fundamentals in the transient-response method. However, the subsequent difficulty in extracting roots from a higher-order characteristic equation makes the method inadequate for synthesis. This difficulty was overcome partially when Evans (3) introduced the root-locus method.

The value of this method as a new approach to the transient analysis and synthesis of linear control systems has been fully demonstrated by Evans (3) and Bollay (4). In this paper, an analytic method for the determination of the root locus is presented, thus eliminating trial-and-error constructions.

Root-locus equations offer the possibility of systematic synthesis of control systems. By means of these equations one may observe movements of the roots of a characteristic equation along a locus when the system gain is varied; one may also notice the shifting and reshaping of the entire root locus when one of the open-loop roots (poles and/or zeros) is altered.

The Characteristic Equation

Consider the basic feedback system shown in Fig. 1 where $g_1(s)$ and $g_2(s)$ are, respectively, the dynamic representations of the controller and the plant to be controlled. Combining the

r, reference input
c, controlled variable
e, actuating signal
  $e' = r - c$ error (degenerative feedback)
  $e'' = r + c$ sum (regenerative feedback)
m, manipulated variable
u, disturbance
n, net plant input
$g_1(s)$, control element
$g_2(s)$, plant (controlled system)

FIG. 1 BLOCK DIAGRAM OF A BASIC CLOSED-LOOP SYSTEM

controller and the plant dynamics, one obtains the open-loop transfer function $KY(s)$

$$KY(s) = c/e = g_1(s)g_2(s) \dots \dots [1]$$

where K, the gain or sensitivity, is a positive real constant. The closed-loop transfer function is defined as the ratio of the controlled variable c to the reference input r; and it is given by

$$KZ(s) = c/r = \frac{KY(s)}{1 \pm KY(s)} \dots \dots [2]$$

The choice of plus or minus sign in the denominator of Equation [2] depends on whether the feedback is negative (degenerative) or positive (regenerative).

For linear systems the open-loop transfer function may be written as

$$KY(s) = \frac{K \prod_{i=1}^{m}(s + z_i)}{\prod_{i=1}^{n}(s + p_i)} \dots \dots [3]$$

where z_i and p_i are, respectively, zeros and poles of the open-loop transfer function; their total is $h = m + n$ of which there are m zeros and n poles. A transfer function having n poles and m zeros shall be referred to as $T(n, m)$; for example, a "three pole-one zero-transfer function" is designated by $T(3, 1)$. It should be noted that all systems having multiple loops can be reduced to the basic block diagram shown in Fig. 1; thus what has been mentioned will be applicable to multiple-loop systems.

The characteristic equation of the feedback system may be obtained by setting the denominator of Equation [2] equal to zero

$$1 \pm KY(s) = 0 \quad \dots \dots \dots [4]$$

This equation determines both the absolute and the relative stability of a control system as well as its transient response; it is independent of external disturbances. For physically realizable systems, $n \geq m$; substituting Equation [3] into Equation [4] yields

$$\prod_{i=1}^{n} (s + p_i) \pm K \prod_{i=1}^{m} (s + z_i) = 0 \quad \dots \dots [5a]$$

or

$$\prod_{i=1}^{n} (s + q_i) = 0 \quad \dots \dots \dots [5b]$$

where q_i are the roots of the characteristic equation, or the closed-loop poles. The locus of q_i in the s-plane is known as the root locus.

For comparison, both the open-loop and the closed-loop transfer functions are as follows:

Open-loop transfer function   Closed-loop transfer function

$$KY(s) = \frac{K \prod_{i=1}^{m} (s + z_i)}{\prod_{i=1}^{n} (s + p_i)} \qquad KZ(s) = \frac{K \prod_{i=1}^{m} (s + z_i)}{\prod_{i=1}^{n} (s + q_i)}$$

$$p_i \rightarrow q_i$$

It is seen that the zeros do not move upon the closure of the feedback loop; and p_i and q_i have one-to-one correspondence in that q_i generates the root locus which starts from p_i when the loop is open ($K = 0$). Transplanting poles from p_i to q_i constitutes the most important function of a feedback loop.

Complete determination of the closed-loop poles can be made only after the gain is specified. For a given configuration of the open-loop roots in the s-plane, however, all possible locations of the closed-loop poles regardless of gain value are confined to the root locus. It is this striking feature that provides a technique for extracting roots (both real and complex) from an algebraic equation with varying coefficients. As a result, the analysis and synthesis of higher-order linear feedback systems by the transient-response method is simplified.

Once the roots of the characteristic equation are found, the transient response to a known disturbance can be determined. If the reference input r is subjected to a step function and if there are no repeated roots, then

$$c(t) = \sum_{i=0}^{n} R_i e^{-q_i t} \quad \dots \dots \dots [6]$$

where R_i is the residue of the closed-loop poles and $q_o = 0$ is the excitation-pole at the origin. Oscillation will occur if the characteristic equation possesses a pair of conjugate complex roots. For systems with load disturbances or having elements (other than unity) in the feedback path, the same method may be used to obtain the transient response provided that the transfer function is properly modified. For systems having multiple loops a successive application of the method for each loop is necessary.

CONFORMAL MAPPING

It is interesting to note that the frequency and the transient-response methods are related through a direct and a reverse con-

formal transformation. The relevant complex planes to be used in the mapping are the s-plane, Y-plane, and the inverse Y-plane.

The direct mapping of co-ordinates of s-plane into the Y-plane with respect to a given $Y(s)$ has provided the basis for the development of the frequency-response method. The Nyquist diagram is a special case of such a mapping by transforming the imaginary axis alone. The curve in the Y-plane so obtained is known as the transfer locus. Indeed, this is the only curve needed for steady-state analysis. The stability of a system depends on whether or not its transfer locus encircles the critical points, $(\pm 1/K + jO)$, as the case may be. This transformation, $s \rightarrow Y$, is single-valued for most commonly employed transfer functions in linear feedback systems. That is to say, for each point in the s-plane there corresponds one and only one point in the Y-plane.

The reverse mapping of co-ordinates of the inverse Y-plane onto the s-plane, on the other hand, provides the foundations for the transient analysis and synthesis. The mapping of the real axis of the inverse Y-plane is identified as the root locus of the system. The reverse transformation, however, is, in general, multiple-valued. The multiplicity is the same as the order of the transfer function, that is, of the order of the relevant differential equation governing the dynamic behavior of the system.

Before carrying out any mapping, the following system of co-ordinates is defined

$$s = -\sigma + j\omega \quad \dots \dots \dots [7a]$$

$$\frac{1}{Y(s)} = K e^{j\phi} \quad \dots \dots \dots [7b]$$

where σ is a positive quantity in the left-half s-plane, K and ϕ are the magnitude and phase angle of $1/Y(s)$. The time constant τ associated with a real root or a pair of complex roots in the s-plane is the reciprocal of σ.

For first and second-order systems, the $Y^{-1}(K, \phi) \rightarrow s$ transformation may be performed by simply substituting a given value of gain K or phase angle ϕ into $Y(s)$ and solving for s. The plots of gain and angle loci may be obtained; these form two families of mutually orthogonal trajectories. As will be seen, the root locus (both for degenerative and regenerative feedback) is a special angle locus whose phase angle ϕ is an integral multiple of π.

Conformal mappings are shown in Fig. 2: (a) a reverse mapping and (b) a direct mapping with respect to $T(1, 1)$ which is given by

$$KY(s) = K(s - 1)/(s + 1)$$

The original planes are not shown.

It is recognized that a pole of $Y(s)$ is analogous to a line source of ideal fluid of unit strength, whereas a zero of $Y(s)$ resembles a line sink of ideal fluid of unit strength. There then follows that the gain and angle loci correspond, respectively, to streamlines and equipotentials. Hence the existing knowledge in the study of potential fields will be applicable here.

Fig. 3(a) shows the mapping of the inverse Y-plane onto the s-plane with respect to a $T(2, 0)$ transfer function. For this system the gain loci form a family of Cassinian ovals. There is a specific value of gain corresponding to the critically damped condition, for which case the gain locus becomes a lemniscate. Moreover, the double point of the lemniscate is also a saddle point; so that at this point the rate of change of gain along the direction joining the two poles is a maximum and that along its perpendicular direction is a minimum. The root locus of this system consists of the real axis and the perpendicular bisector of the segment between the two open-loop poles.

(a)   s-plane

(b)   Y-plane

Fig. 2   Conformal Mapping of Type $T(1, 1)$
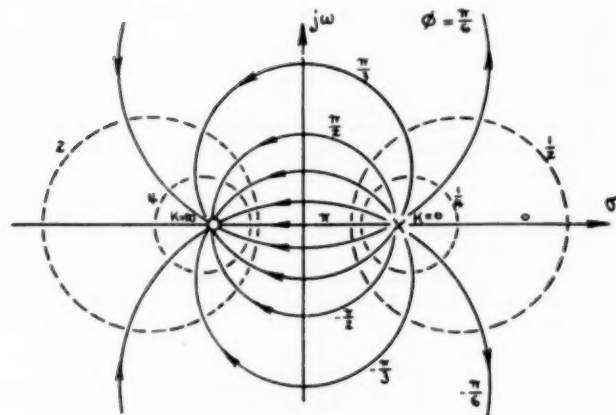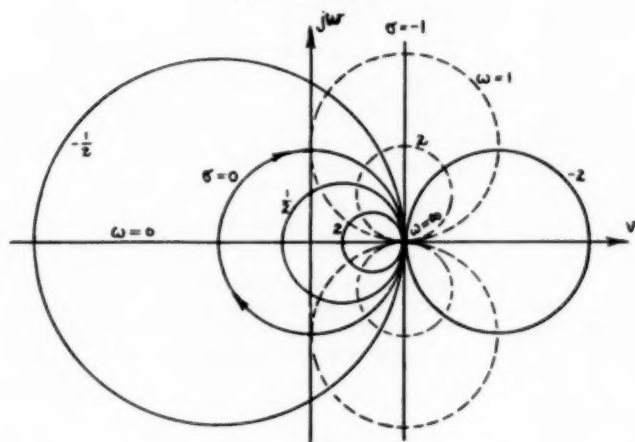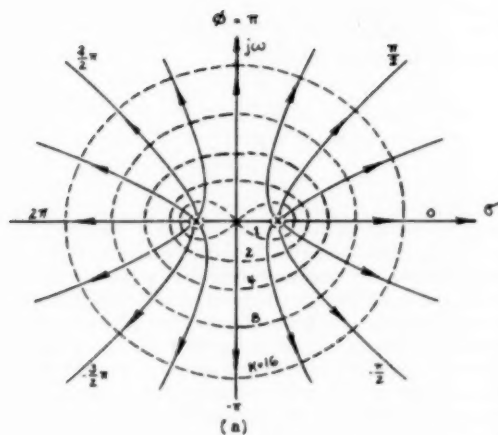
(a)
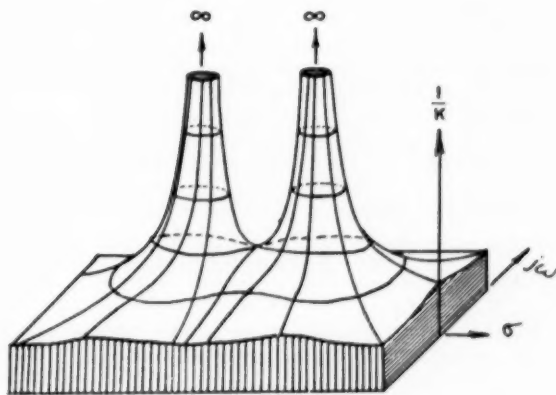
(b)

Fig. 3   Type $T(2, 0)$ System

(a, Angle loci and gain loci in s-plane.   b, Three-dimension potential surface erected on s-plane.)

Fig. 3(b) represents a three-dimensional model of the same $T(2, 0)$ erected on the s-plane, the third co-ordinate being the reciprocal of the gain. The open-loop poles represent the point at infinity in Fig. 3(b). This is analogous to potential-field theory where the point at infinity is taken as zero gain. Decreasing in height from these points means increasing gain; thus $\nabla \Phi = -K$.

THE ANGLE AND MAGNITUDE CRITERIA

In order to determine the root locus the characteristic equation is rewritten in the form

$$\frac{1}{Y(s)} = Ke^{jl\pi} = K\ \underline{/l\pi} \dots \dots \dots [8]$$

where l is an integer. Odd values of l correspond to degenerative feedback whereas even values correspond to regenerative feedback. Equation [8] states that the magnitude of the $Y^{-1}(s)$ is K and its phase angle ϕ is an integral multiple of π. In order to free the gain as a varying parameter in the characteristic equation only the angle criterion of Equation [8] need be satisfied on a root locus.

O — open-loop zero
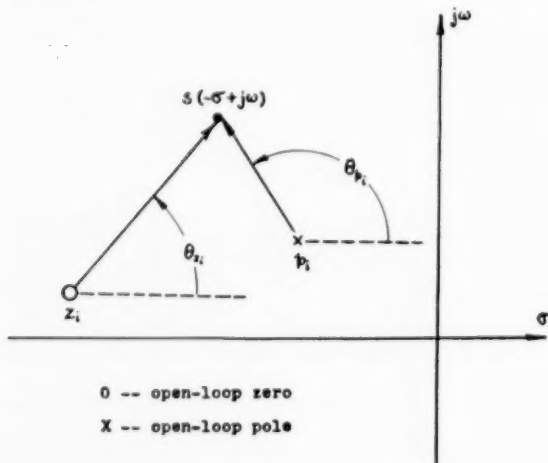
X — open-loop pole

FIG. 4   PHASE ANGLE OF A COMPLEXOR IN s-PLANE

In Fig. 4, $(\theta_i)_p$ and $(\theta_i)_z$ are the respective phase angles of a complexor formed from a pole or a zero of $Y(s)$ to an exploratory point in the s-plane. The open-loop poles are $p_i = -\sigma_i + j\omega_i$, whereas the open-loop zeros are $z_i = -\alpha_i + j\beta_i$ where $\sigma_i, \omega_i, \alpha_i$, and β_i are real constants. The tangent of these angles may be expressed as

$$\tan(\theta_i)_p = \frac{\omega - \omega_i}{\sigma_i - \sigma} \quad \text{and} \quad \tan(\theta_i)_z = \frac{\omega - \beta_i}{\alpha_i - \sigma} \dots [9]$$

For convenience, define

$$\sum_{r=1}^{h} \theta_r = \sum_{i=1}^{n} (\theta_i)_p - \sum_{i=1}^{m} (\theta_i)_z \dots \dots [10]$$

where $r = 1, 2, 3, \dots h$.

Since $h = m + n$, θ_r is either a particular $(\theta_i)_p$ or the negative of a particular $(\theta_i)_z$. Noting that the angle criterion of Equation [8] requires that

$$\sum_{r=1}^{h} \theta_r = l\pi \dots \dots \dots \dots [11]$$

the tangent of both sides of the foregoing equation gives

$$\tan\left(\sum_{r=1}^{h} \theta_r\right) = 0 \dots \dots \dots \dots [12]$$

When the tangent is expanded analytical expressions of the root locus may be obtained. Repeatedly making use of the trigonometric relation

$$\tan(x + y) = \frac{\tan x + \tan y}{1 - \tan x \tan y}$$

and setting the numerator of the expanded form of the left-hand side of Equation [12] equal to zero, one arrives at the following general expression

$$\sum_{\substack{b=1 \\ b=\text{odd}}}^{\hat{h}} \left(\sin \frac{b\pi}{2}\right) \sum_{\lambda=1}^{{}_hC_b} (\Pi_b \tan \theta_r) = 0 \dots \dots [13]$$

where $\hat{h}$ is defined as

$$\hat{h} = h, \text{ when } h \text{ is odd}$$
$$= h - 1, \text{ when } h \text{ is even}$$

and ${}_hC_b = h!/b!(h - b)!$, is the number of combinations of h things taken b at a time; $\lambda = 1, 2, 3, \dots {}_hC_b$ is an individual combination. The symbolism

$$\sum_{\lambda=1}^{{}_hC_b} (\Pi_b \tan \theta_r)$$

is defined as the sum of each combination product. This generalized form is valid for nth-order roots provided they are counted as n simple roots. The following set of equations for different values of h are obtained when substituting in Equation [13]

$$h = 1, \tan \theta_1 = 0 \dots \dots \dots \dots \dots \dots [14a]$$

$$h = 2, \tan \theta_1 + \tan \theta_2 = 0 \dots \dots \dots \dots [14b]$$

$$h = 3, \tan \theta_1 + \tan \theta_2 + \tan \theta_3 - \tan \theta_1 \tan \theta_2 \tan \theta_3 = 0$$
$$\dots [14c]$$

Substituting Equation [9] into [13] the root-locus equations may be obtained for systems of various orders, Table 1.

Once the root locus of a feedback system is obtained, the specific roots corresponding to a given value of gain may be determined from the magnitude condition. Substituting Equation [3] into [8] gives the magnitude condition

$$K = \frac{\prod_{i=1}^{n} |s + p_i|}{\prod_{i=1}^{m} |s + z_i|} \dots \dots \dots \dots [15]$$

where s may now be considered as a variable point restricted on the root locus. Equation [15], therefore, suggests the following graphical method for locating specific roots: (a) Select a point on the root locus and measure the distance from this point to all open-loop roots. (b) Obtain the product of all distances from this point to open-loop poles, and do the same for zeros. Dividing the former by the latter we obtain the gain associated with the point in question by virtue of Equation [15]. If there is no zero in the transfer function, the denominator of Equation [15] is unity. Alternatively, the analytic expression of the magnitude condition may be substituted into the root-locus equation yielding

(a) n = 1

(b) n = 2

(c) n = 3

(d) n=4
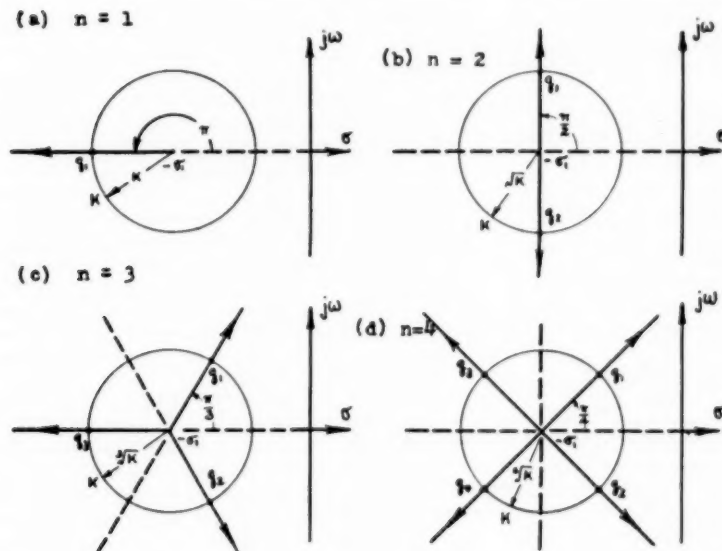
FIG. 5   ROOT LOCI OF TYPE $T(N, O)$ in s-PLANE

(a) n = 3

(b) n = 4
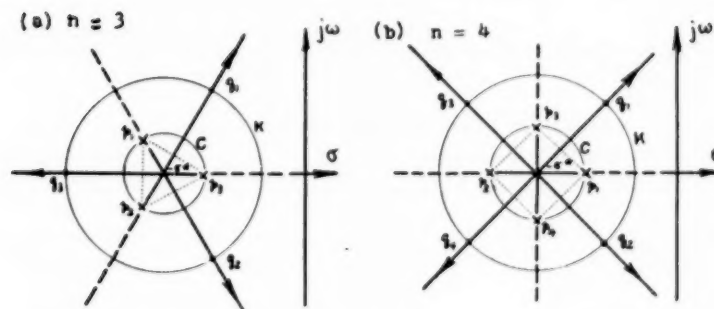
FIG. 6   ROOT LOCI OF GENERALIZED $T(N, O)$ IN s-PLANE

a pair of parametric equations having gain as a parameter. The separation of the angle criterion from the magnitude criterion is the key to the solution of higher-degree algebraic equations.

ROOT LOCUS OF TYPE $T(N,O)$

The type $T(N,O)$ transfer function is defined as a special case of $T(n,O)$, where all n open-loop poles are concentrated at a single point—an nth-order pole.

Fig. 5 shows root loci for positive and negative feedback for n having values of 1 through 4. The locus corresponding to degenerative feedback is shown by heavy solid lines whereas heavy dash lines represent the regenerative-feedback locus; constant-gain lines are shown as concentric circles. The direction of increasing gain along the degenerative-feedback locus is indicated by an arrow; for regenerative feedback it is in the opposite direction; closed-loop roots q, corresponding to gain K are marked on the locus. It is seen that the root locus is composed of different branches of a multiple-valued function. There are n branches for the degenerative-feedback locus and n complementary branches for the regenerative-feedback locus.

It should be noted that if the multiple-order pole is located at

the origin the method reduces to DeMoivre's theorem for extracting the n roots of the gain K. Note, however, that the root locus is independent of K; whereas the closed-loop poles are definitely determined by K.

More generally, if the open-loop poles form an n-sided equilateral polygon which is symmetrical with respect to the real axis, the root locus is again composed of straight lines. Two such cases are shown in Fig. 6 for a third-order and a fourth-order system. In such cases it may be stated that the n roots of K are taken with respect to the datum circle C—a circle passing through the open-loop poles having its center at $-\sigma^*$, where σ^* is the centroid of the polygon and of the open-loop poles. It is found to be

$$\sigma^* = \frac{1}{n} \sum_{i=1}^{n} p_i \dots \dots \dots \dots \dots [16]$$

It can be shown that for $n - m \geq 2$, the centroid is an invariant of the system regardless of whether or not the feedback loop is closed; thus

$$\sum_{i=1}^{n} q_i = \sum_{i=1}^{n} p_i \quad \text{for } n - m \geq 2 \dots \dots [17]$$

This is a useful property of the root locus; for if $n - m \geq 2$ the movements of q_i with a varying gain are not only restricted along root locus but also limited in such a manner that the centroid remains unchanged.

Similarly, it also can be shown that if $n - m = 1$, the closed-loop and the open-loop centroids are related with the gain as follows

$$\sigma_c^* = \sigma^* \pm \frac{K}{n} \quad \text{for } n - m \geq 1 \quad \ldots \ldots [18]$$

where σ_c^* is the closed-loop centroid.

A closely related property of the root locus is the "asymptotic center" σ_∞—the point where all linear asymptotes intersect on the real axis. It can be shown that

$$\sigma_\infty = \left[\sum_{i=1}^{n} p_i - \sum_{i=1}^{m} z_i \right] / (n - m) \quad \ldots \ldots [19]$$

if $m = n$, σ_∞ is undefined. Note that for $n - m \geq 2$, the closed-loop asymptotic center coincides with that of open-loop by virtue of Equations [16] and [19]. Moreover, if the transfer function has no zero in the finite s plane, then the expression of asymptotic center reduced to that of the centroid.

Along a root locus, for large gain values, all phase angles approach the asymptotic angle which is given by

$$\theta_\infty = \pm \frac{l\pi}{n - m}, \quad [l = 0, 1, 2, \ldots, (n - m)] \ldots [20]$$

Thus all linear asymptotes intersect at $-\sigma_\infty$ having a slope of $\tan \theta_\infty$.

BASIC SHAPES OF ROOT LOCUS

The root-locus equations for systems having up to four open-loop roots with all possible combinations of poles and zeros are tabulated in Table 1 ($n > m$). For these simple systems the root loci consist of straight lines, circles, hyperbolas, and various third-degree algebraic curves, such as the conchoid of Nicomedes, the cissoid, the strophoid, and more generally, the semiparabolic curves, and so on, or combinations thereof.

A thorough familiarity with the basic shapes of root loci are valuable in the design of control systems. The following examples are chosen to show not only how the roots may vary along a locus when gain is changed but also how the entire root locus is re-shaped when one of the controller time constants is being adjusted. Such systematic studies of the movements of roots with a varying gain in the s-plane enable the designer to achieve a desired end result.

$T(1, 0)$ and $T(1, 1)$ Types. Root loci of first-order systems are shown in Fig. 7. They consist of the entire real axis. The $T(1, 0)$ locus is divided into two parts at the open-loop pole. That part to the left of the open-loop pole is for degenerative feedback, whereas the part to the right is for regenerative feedback. Degenerative feedback reduces the characteristic time, thus speeding up the dynamic response; the system always remains stable regardless of gain value. Regenerative feedback, on the other hand, gives slower dynamic response, and the system becomes unstable when $K \geq \sigma_1$. For $T(1, 1)$ there are two possibilities as seen in Fig. 7 (b and c). The degenerative-root locus is restricted between the open-loop pole and zero thus limiting the characteristic time between $(1/\sigma_1)$ and $(1/\alpha_1)$. For regenerative feedback the system is conditionally stable.

TABLE 1   ROOT-LOCUS EQUATIONS FOR $\Lambda = m + n \leq 4$

Type	Λ	Root-locus equations (not including real axis)	Constants in root-locus equations
$T(1, 0)$	1		
$T(1, 1)$	2	None	None
$T(2, 0)$	2	Line $\sigma = \frac{1}{2}(\sigma_1 + \sigma_2)$	Perpendicular bisector or segment between open-loop poles
$T(2, 1)$	3	Circle	$\sigma_0 = \alpha_1 \quad R^2 = (\sigma_1 - \alpha_1)(\sigma_2 - \alpha_1) + \omega_{12}^2$
$T(2, 2)$	4	$(\sigma - \sigma_0)^2 + \omega^2 = R^2$	$\sigma_0 = \dfrac{\Omega_{12}^2 - B_{12}^2}{(\sigma_1 + \sigma_2) - (\alpha_1 + \alpha_2)}$, $R^2 = \sigma_0^2 + \dfrac{(\sigma_1 + \sigma_2)B_{12}^2 - (\alpha_1 + \alpha_2)\Omega_{12}^2}{(\sigma_1 + \sigma_2) - (\alpha_1 + \alpha_2)}$
$T(3, 0)$	3	Hyperbola $\left(\dfrac{\sigma - \sigma^*}{a}\right)^2 - \left(\dfrac{\omega}{b}\right)^2 = 1$	$a = \frac{1}{3}\sqrt{(\sigma_1 + \sigma_2 + \sigma_3)^2 - 3(\sigma_1\sigma_2 + \sigma_2\sigma_3 + \sigma_3\sigma_1 + \omega_{12}^2)}$ $b = \sqrt{3}\,a \quad c = \sqrt{a^2 + b^2} = 2a$
$T(3, 1)$	4	Third-degree curves $\omega^2 = (-1)^n \dfrac{\sigma^3 - a_2\sigma^2 + a_1\sigma - a_0}{\sigma - \sigma_\infty}$	$a_0 = \frac{1}{2}[(\sigma_1 + \sigma_2)\alpha_1\sigma_3 + (\sigma_1 + \sigma_3)\Omega_{12}^2]$ $a_1 = \alpha_1(\sigma_1 + \sigma_2 + \sigma_3)$ $a_2 = \frac{1}{2}(\sigma_1 + \sigma_2 + \sigma_3 + 3\alpha_1)$
$T(4, 0)$	4		$a_0 = \frac{1}{4}[(\sigma_1 + \sigma_2)\Omega_{34}^2 + (\sigma_3 + \sigma_4)\Omega_{12}^2]$ $a_1 = \frac{1}{2}[(\sigma_1 + \sigma_2)(\sigma_3 + \sigma_4) + \Omega_{12}^2 + \Omega_{34}^2]$ $a_2 = \frac{3}{4}(\sigma_1 + \sigma_2 + \sigma_3 + \sigma_4) = 3\sigma^*$

Centroid	Asymptotic center	Open-loop roots	Natural frequency
$\sigma^* = \frac{1}{n}\sum_{i=1}^{n} p_i$,	$\sigma_\infty = \frac{1}{n-m}\left[\sum_{i=1}^{n} p_i - \sum_{i=1}^{m} z_i\right]$,	$p_1 = \sigma_1 + j\omega_{12}, \; p_2 = \sigma_2 - j\omega_{12}, \; \Omega_{12}^2 = \sigma_1\sigma_2 + \omega_{12}^2$ $z_1 = \alpha_1 + j\beta_{12}, \; z_2 = \alpha_2 - j\beta_{12}, \; B_{12}^2 = \alpha_1\alpha_2 + \beta_{12}^2$	
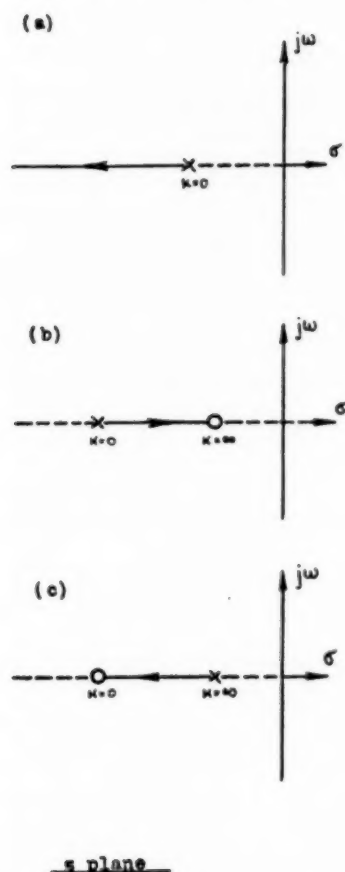
FIG. 7   ROOT LOCI FOR TYPES $T(1, 0)$ AND $T(1, 1)$
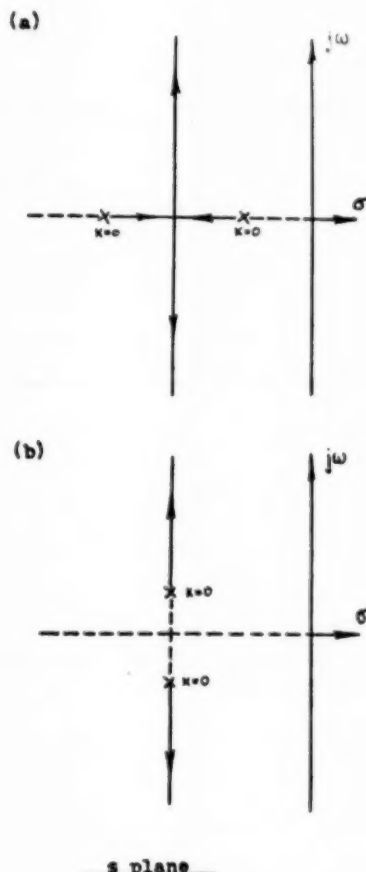
FIG. 8   ROOT LOCI FOR TYPE $T(2, 0)$

Type $T(2, 0)$.   The root locus of a common second-order system is shown in Fig. 8.   In addition to the real axis, the locus consists of the perpendicular bisector of the segment between the open-loop poles or consists of a line containing them.   The two possible configurations depending on whether the open-loop roots are over or under-damped are shown in Figs. 8(a and b).   For degenerative feedback, Fig. 8(a), increasing the gain causes the roots to come closer to each other until at critical damping the roots are equal;   further increase in gain caused the roots to separate and an increasing natural frequency and lowering damping ratio are evident.   Thus a faster response is usually associated with a larger overshoot.

Types $T(2, 1)$ and $T(2, 2)$.   Six possible configurations of root locus for a type $T(2, 1)$ transfer function are shown in Fig. 9.   Note that if the open-loop poles and zeros are alternated along the real axis as in Fig. 9(b), the circular part of the locus is suppressed and the system will not oscillate.   Of course, if the zero coincides with a pole, the system degenerates to a first-order system.   Systems having regenerative feedback are conditionally stable.   Root loci for type $T(2, 2)$ transfer functions are similar to those of type $T(2, 1)$; the root-locus equation is given in Table 1.

Fig. 10(a) shows a family of root loci of a transfer function having a pair of complex open-loop poles ($-\sigma_1 \pm j\omega_1$).   Originally, the locus consists of a vertical line and the real axis.   When a finite zero is introduced along the negative real axis, the locus

bends toward the left and forms a circle having the zero as its center.   The introduction of a finite zero may be accomplished by employing a proportional-plus-derivative controller, for example.   As the derivative time constant is increased, i.e., the zero is being moved toward the origin, the circle becomes smaller and smaller.   When the zero is in line with the open-loop complex poles the circle has its minimum radius of ω_1.   Further increase in the derivative time constant will again increase the radius of the circle.   Similarly, Fig. 10(b) shows root loci for an initially over-damped system of type $T(2, 1)$.

Type $T(3, 0)$.   For a third-order system the root locus consists of a hyperbola (or its degenerated forms) and the real axis as shown in Fig. 11.   From Table 1 the root-locus equation is

$$3(\sigma - \sigma^*)^2 - \omega^2 = a^2$$

For a pair of complex open-loop poles ($-\sigma_1 \pm j\omega_1$) and third pole σ_2 lying within the limits

$$(\sigma_1 + \sqrt{3}\omega_1) > \sigma_2 > (\sigma_1 - \sqrt{3}\omega_1)\ldots\ldots\ldots[21]$$

that is, $a < 0$, the root locus is a hyperbola having foci in the complex plane.   If the Condition [21] is not met, the hyperbola will have their foci on the real axis; if $\sigma_2 = \sigma_1 \pm \sqrt{3}\omega_1(a = 0)$, the root locus degenerates into three straight lines (including the real axis) passing through a common point and equally spaced 120

FIG. 9   ROOT LOCI FOR
TYPE $T(2, 1)$ IN s-PLANE
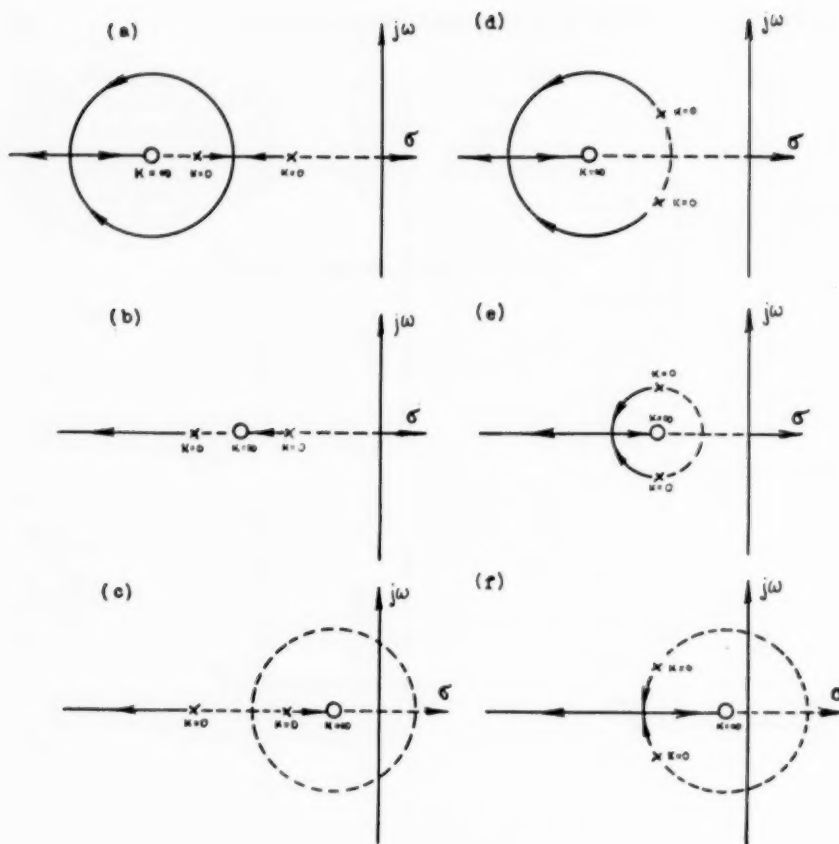
DEGENERATIVE ⟷ | ⟶ REGENERATIVE
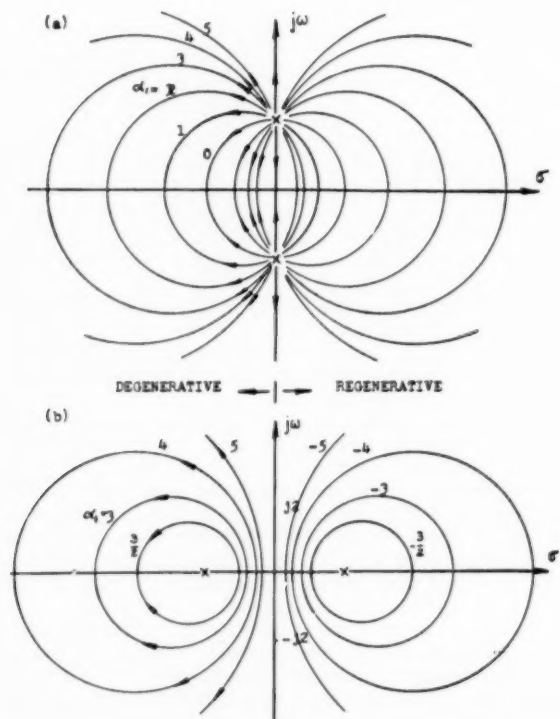
FIG. 10   ROOT LOCI FOR
TYPE $T(2, 1)$ IN s-PLANE

s plane

Fig. 11   Root-Locus Chart for Type $T(3, 0)$

Fig. 12   Root Loci for Type $T(3, 1)$ in s-Plane
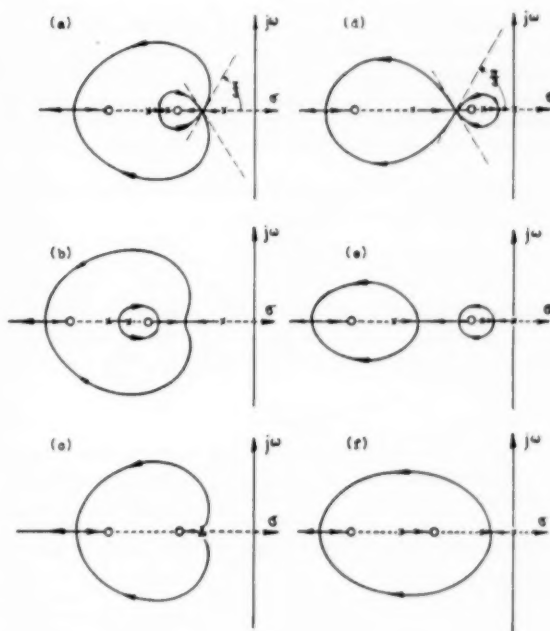
Fig. 13   Root Loci for Type $T(3, 2)$ in s-Plane

deg apart   Fig. 11 is a composite root-locus chart for type $T(3, 0)$. Note that the centroid σ^* is taken as the center; the $j\omega$-axis may be located relative to the centroid. By calculating a for a given transfer function, the root locus of the system may be obtained immediately from Fig. 11. It is seen that the loci for $a = k$ and $a = jk$, where k is a real constant, form conjugate hyperbolas.

Type $T(3, 1)$. Fig. 12 shows how the $T(3, 0)$ locus of Fig. 11 is modified by placing a zero on the negative real axis and translating it toward the origin; this is similar to increasing the time constant of a proportional-plus-derivative controller. All three poles meet at a common point for a particular gain; tangents to the curves at this point form 60-deg angles with the real axis. Notice that the asymptotic angles are ± 90 deg, and that the root locus is shifted away from the origin as the zero is translated toward the origin.

Type $T(3, 2)$. In addition to the real axis the root loci consist of closed curves only, Fig. 13. Depending on the configuration of the open-loop roots the locus may be a two-loop or one-loop curve. If the open-loop poles and zeros are alternated along the real axis, the root locus consists only of the real axis, and the system is incapable of oscillation; in all cases the real axis serves as the only asymptote.

Type $T(4, 0)$. Four out of eight possible configurations of $T(4, 0)$ locus are shown in Fig. 14. The asymptotic angles are $\pm \frac{1}{4} \pi$ and $\pm \frac{3}{4} \pi$ for degenerative feedback, and $0, \pm \frac{1}{2} \pi$ and

π for regenerative feedback. In Fig. 14(d) it is seen that with regenerative feedback the system will be stable for all values of gain.

In Figs. 7 through 14 all open-loop roots are shown in the left-half s-plane. It is clearly possible, however, that open-loop roots
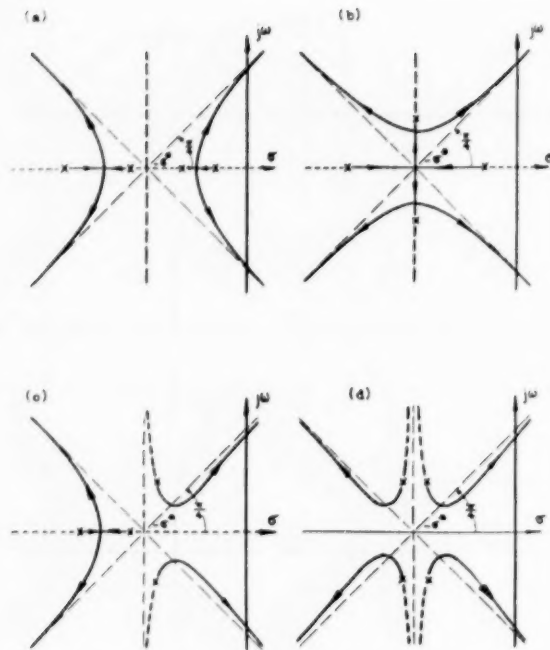
FIG. 14   ROOT LOCI FOR TYPE $T(4, 0)$ IN s-PLANE

may lie in the right-half s-plane; in such cases degenerative-feedback systems are conditionally stable whereas regenerative-feedback systems are always unstable. Although regenerative feedback is seldom used in the major loop of a control system (it is encountered in minor loops) it is mentioned here because of its usefulness in feedback amplifiers and in oscillators.

For fifth and sixth-order systems the root-locus equations are quadratic equations of ω^2 of the form

$$\omega^4 + f_2(\sigma)\omega^2 + f_4(\sigma) = 0$$

where $f_2(\sigma)$ and $f_4(\sigma)$ are, respectively, a second and fourth-degree polynomial in σ. Similarly, for seventh and eighth-order systems the root-locus equations are cubic equations in ω^2.

SUMMARY

The correlation between frequency and transient response of a linear feedback system through conformal mapping is summarized in Table 2.

TABLE 2   CORRELATION BETWEEN FREQUENCY AND TRANSIENT RESPONSE

Direction of transformation	$s \to Y$	$Y^{-1} \to s$
Information	Frequency-response	Transient-response
Analytical nature	Single-valued	Multiple-valued
Important locus in original plane	Imaginary axis ($\sigma = 0$)	Real axis ($\phi = l\pi$)
Important locus in transformed plane	Transfer locus	Root locus
Stability criterion	Nyquist	Routh-Hurwitz
Frequency or gain at stability limit	Transfer locus crosses real axis	Root locus crosses $j\omega$-axis
Gain at "aperiodic" limit	Transfer locus crosses imaginary axis	root locus crosses σ-axis

The properties of root locus are summarized as follows:

1   The entire real axis is a part of the locus; the root locus is always symmetrical about the real axis.

2   The system will become unstable when the root locus enters the right-half s-plane (Routh-Hurwitz criterion).

3   A branch (or its complement) always starts from an open-loop pole where $K = 0$ and terminates at a zero where $K = \infty$.

4   There are as many branches (or complementary branches) as the number of energy storages; that is, the number of branches equals the order of the system.

5   There are $(n - m)$ branches (or complements) which terminate at the $(n - m)$ zeros located at infinity.

6   A branch and its complement form alternate segments along the real axis; the segments are degenerative-feedback loci if they have an odd number of open-loop roots to their right; the remaining segments are regenerative-feedback loci.

7   The shape of root locus depends only on the relative separation of the open-loop roots; the absolute location of these roots determines the transient response; the shape is entirely independent of the forcing function.

8   The centroid σ^* is an invariant of the system if $n - m \geq 2$; it will shift by an amount equal to $\pm K/n$ if $n - m = 1$

$$\sigma^* = \frac{1}{n} \sum_{i=1}^{n} p_i, \quad \sigma_c^* = \frac{1}{n} \sum_{i=1}^{n} q_i$$

9   The asymptotic center is the intersection of linear asymptotes. This occurs on the real axis and is given by

$$\sigma_\infty = \frac{1}{n - m} \left[\sum_{i=1}^{n} p_i - \sum_{i=1}^{m} z_i \right]$$

The asymptotic angle θ_∞ has $2(n - m)$ distinct $\theta_\infty = \pm (l\pi)/(n - m)$ values equally spaced over 2π radians. If $n = m$, both σ_∞ and θ_∞ are undefined.

10   At a junction point the tangents to the locus are equally spaced over 2π radians.

11   Along the locus, the phase angle of an exploratory point moving to the left increases by π when passing through an open-loop pole and decreases by π when passing through a zero.

CONCLUSION

The frequency and transient-response of linear feedback systems are formally correlated through the two-way conformal transformation. Either the transfer locus in the Y-plane or the root locus in the s-plane may be used for synthesis of control systems; the two methods complement each other. The energy storages in a linear system may be treated as a number of ideal sources and sinks in the s-plane; thus potential field analogy may be used as a basis for further development.

ACKNOWLEDGMENT

BIBLIOGRAPHY

1   "Regeneration Theory," by H. Nyquist, Bell Telephone System Technical Journal, vol. 11, January, 1932, pp. 126–147.

2   "Design Factors Controlling the Dynamic Performance of Instruments," by C. S. Draper and G. P. Bentley, Trans. ASME, vol. 62, 1940, pp. 421–432.

3   "Servo-Analysis by Locus of Root Method," by W. R. Evans, Report AL-787, North American Aviation, Inc., Los Angeles, Calif., November, 1948.

4 "Aerodynamic Stability and Automatic Control," by W. Bollay, *Journal of the Aeronautical Sciences*, vol. 18, September, 1951, pp. 569–617.
5 "The Analysis and Synthesis of Linear Servomechanisms," by A. C. Hall, The Technology Press, M.I.T., 1943.
6 "Theory of Servomechanisms," by H. M. James, N. B. Nichols, and R. S. Phillips, McGraw-Hill Book Company, Inc., New York, N. Y., 1947.
7 "Servomechanism-Charts for Verifying Their Stability and for Finding the Roots of Their Third and Fourth Degree Characteristic Equations," by Y. J. Liu, M.I.T., 1941.
8 "Method of Successive Approximations of Evaluating the Real and Complex Roots of Cubic and Higher Order Equations," by S. N. Lin, *Journal of Mathematical Physics*, vol. 20, August, 1941.

Discussion

A. NOMOTO.[4] Importance of this study seems to consist in correlating the root locus to the conformal mapping, which enables to give methodical procedure to scrutinize analytical properties of the loop transfer function. It should be added that root locus can be geometrically understood as a steepest descent line of the gain surface. The author's Equations [7a] and [7b] are rewritten

$$\log K + j\phi = -\log Y(-\sigma + j\omega)$$

which expresses that $\log K + j\phi$ is a rational function of $-\sigma + j\omega$. In the direction of the root locus on which $d\phi/ds = 0$, preceding rational relation leads to that $|d \log K/ds|$ has maximum value due to the Cauchy-Riemann relations.

In studying the transient response, not only poles $(-q_i)$ of closed-loop transfer function but magnitude of each response term (R_i) is required. The writer found that root-locus method can be advantageously utilized to calculate R_i in virtue of its mapping relation. Considering the unity feedback system without any repeated poles, R_i of the author's Equation [6] or residue of $Z(s)/s$ at $s = -q_i$ is

$$R_i = \lim_{s \to -q_i} \frac{Z(s)(s + q_i)}{s} = \lim_{s \to -q_i} \frac{KY(s)}{1 + KY(s)} \frac{s + q_i}{s}$$

Differentiating the numerator and the denominator with respect to s and putting $s = -q_i$

$$R_i = \frac{Y(s)}{s \, dY(s)/ds}\bigg|_{s = -q_i} \quad\quad\quad [22]$$

If the direction of the differentiation is chosen along root locus, $Y(s)$ takes always real values $\pm(1/K)$, so that

$$R_i = -\frac{d \log s}{d \log K} = -\frac{d \log |s|}{d \log K} - j \frac{d \angle s}{d \log K}$$

When the gain is measured in db along a root locus, terms of R_i can be calculated as ratios of differences, $20\Delta \log_{10}|s|$ and $0.1516\Delta \angle s$ (deg), to that of loop gain ΔK (db).

P. S. CREAGER.[5] This paper discloses an important advance in the tools available for the study of closed-loop systems. The author is to be congratulated for the contribution he has made.

Other studies of the correlation between frequency and transient response have been made.[6,7,8]

[4] Assistant Professor, Central University, Tokyo, Japan.
[5] Associate Professor of Electrical Engineering, Rutgers University, New Brunswick, N. J.
[6] "Graphical Determination of Transfer Function Loci," by E. C. Easton and C. H. Thomas, Trans. AIEE, vol. 68, 1949, p. 307.
[7] "Transient Performance From Decibel-Log Frequency Plots," by H. Harris, Jr., M. J. Kirby, and E. F. Von Arx, Trans. AIEE, vol. 70, 1951, p. 1452.
[8] "Approximating Transient Response; Chapt. 2—Principles of Servomechanism," by G. S. Brown and D. P. Campbell, John Wiley & Sons, Inc., New York, N. Y., 1948.

Generally, these involve considerable approximation. The scheme disclosed in this paper seems to be capable of much greater accuracy.

The paper appears to divide naturally into two parts: (a) A general basic exposition of the method, and (b) application to a number of specific-type systems. This discussion will be confined to part (a) and reflects some experiences of the writer in teaching automatic control.

Fig. 1 and Equation [2] of the paper both indicate that the feedback signal may subtract or may add to the input signal. It may be worth-while to emphasize this. In general, controls use the subtractive connection but some internal loops are additive.

The systematic representation of transfer-function type by $T(n, m)$ symbol is especially worthy of note. This should be very helpful when it is realized that n and m are, respectively, the number of poles and zeros in the transfer function or alternately the same as the order of the algebraic expression in the denominator and numerator.

In the second paragraph below Equations [7a] and [7b], the paper states that poles and zeros of $Y(s)$ are analogous, respectively, to line sources and sinks. The writer requests that the author expand this point, as he suspects that many readers will have difficulty with the concepts involved.

C. H. DAWSON.[9] The author is to be congratulated for having extended our understanding of the relations between transient and frequency response; specifically, by giving the root loci in analytical form and by including the loci for the regenerative case.

Possibly because of the long time interval between submission and presentation of this paper, much of the material has now been published elsewhere. Representative is a paper by Yaohan Chu[10] which brings out the hydraulic analogy and presents a graphical approach to root loci which leads to much faster though possibly slightly less accurate results than the author's equations while keeping the effect of parameter changes more clearly in view.

In the discussion of the direct mapping onto the Y-plane, the author also might have mentioned the curvilinear square method presented by Russell and Weaver.[11]

The author states in discussing the $T(N, O)$ system that "the closed-loop roots are branch points which are determined for a given value of gain." Consider such a system having an Nth-order pole at $s = s_1$

$$KY(s) = K/(s - s_1)^N \quad\quad\quad [23]$$

$$(s - s_1)^N = 1/Y(s) = Ke^{j\phi} \quad\quad\quad [24]$$

$$s = K^{1/N} e^{j\phi/N} + s_1 \quad\quad\quad [25]$$

The branch point, as usually defined, is the origin in the $Y^{-1}(s)$-plane and is independent of the gain. However the N-branches of the root locus in the s-plane do meet at $s = s_1$.

The treatment of the case where the poles form an equilateral polygon symmetrical with respect to the real axis seems of little practical interest since such a pole arrangement in a physical system is highly unlikely.

The fact that an alternate arrangement of poles and zeros along the real axis leads to a nonoscillatory system is especially interesting. Possibly this phenomenon is related to the condi-

[9] University of Rochester, Rochester, N. Y.
[10] "Synthesis of Feedback Control System by Phase-Angle Loci," by Yaohan Chu, Trans. AIEE, vol. 71, part 2, 1952, pp. 330–339.
[11] "Synthesis of Closed Loop Systems Using Curvilinear Squares to Predict Root Location," by D. W. Russell and C. H. Weaver, Trans. AIEE, vol. 71, part 2, 1952, pp. 95–104.

tion of alternate poles and zeros along the imaginary axis which is necessary for physical realizability of passive reactive networks.

H. I. TARPLEY.[13]   The author is to be congratulated on his concise and well-prepared paper on a very difficult subject to "sell" to practical-system designers.   His reference to the vast amount of attention devoted to the frequency-response transfer-locus method is certainly not exaggerated.   That so much study would be concentrated on the db-log frequency method of system synthesis was quite natural, when one considers the ease of computation that this method affords.   Designers biased in favor of the frequency-response method have found certain difficulties in the control of transient response, but experience soon taught them how to avoid undesirable transients to a somewhat satisfactory extent.   The obvious great advantage of the db-log frequency or frequency-response synthesis approach is that the higher order systems may be handled with great ease.

The author in studying analytical methods for the determination of root loci for feedback systems has made a noteworthy contribution to the transient method of analysis and synthesis demonstrated by Evans and Bollay.   The increasing use of analog computers in the past few years has made extensive calculations economically possible.   It is quite possible that analytical expressions for root loci may lead to improved computer methods for linear-system synthesis by the elimination of much of the "hunt" and "peck" computer methods that exist today.

AUTHOR'S CLOSURE

The author wishes to thank all discussers sincerely for their constructive contributions.   He also wishes to point out that Professor Nomoto has written a paper[13] on the same topic at about the same time when the present paper was written (fall, 1951).

The method for evaluating residues R_i suggested by Professor Nomoto is welcome.   His method, however, requires the determination of several values of gain along a root-locus.   The following is a simpler graphical method for evaluating these residues.   Rewrite Equation [22] in a more explicit form

$$R_i = \frac{K \prod_{r=1}^{m} (z_r - q_i)}{\prod_{r=1}^{n} (q_r - q_i)} \Bigg|_{(q_r \neq q_i)} = K_i e^{j\phi_i}$$

where K_i and ϕ_i are, respectively, the absolute value and phase angle of the residue R_i.

With a given set of closed-loop roots and excitation-poles K_i and ϕ_i may be obtained as follows:

1.   To obtain K_i: Measure the distance from q_i to all other closed-loop roots as well as excitation-poles.   Obtain the product of distances from q_i to all poles (excluding the q_i in question), and do the same for the zeros.   Divide the former by the latter yielding the ratio K_i/K.

2.   To obtain ϕ_i: First measure the phase angle of all complexors drawn from every excitation-pole and every closed-loop root (excluding the q_i in question) to q_i.   Then sum up these angles yielding ϕ_i, calling the angles from poles positive and those from zeros negative.

It is noted that this graphical method for determining residue is the inverse of the procedure for finding the closed-loop roots with

[13] Pennsylvania State College, State College, Pa.

[13] "Contribution to the Root-Locus Analysis of the Feedback Control System," by Akira Nomoto, Proceedings of the Second Japan National Congress for Applied Mechanics, 1952, pp. 359-62.
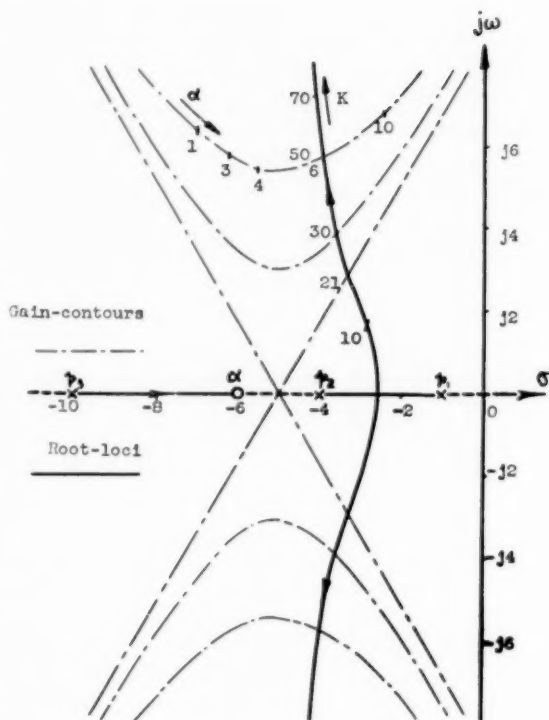
FIG. 15   ROOT-LOCI AND GAIN-CONTOURS OF $T(3, 1)$

a given value of K (Cf. the paragraph below Equation [15]).
The following useful properties should be observed:

(a)   The residue of a pole located on the real axis is $R_i = (-1)^b K_i$ where b is the total number of closed-loop roots (both poles and zeros) to the right of the pole under consideration.

(b)   For common control systems ($n > m$), the following relation holds

$$\sum_{i=0}^{n} R_i = 0$$

In reply to Professor Creager's request, it may be clarified that the analogy between pole-zero of $Y(s)$ and the line source-sink of ideal fluid (or point source-sink in two-dimension flow) is due to the existence of the orthogonal conditions between angle and gain loci, on the one hand, and streamlines and equipotentials, on the other hand.

Professor Dawson is right in pointing out that the branch point, as usually defined, is the origin in the $Y^{-1}(s)$-plane and is independent of gain.   The cases where the poles form an equilateral polygon symmetrical with respect to the real axis serve as demarkations among distinct types of transient response.   For example, for a third-order system, Fig. 6(a), if the real open-loop pole is inside the equilateral triangle, the system is always oscillatory regardless of gain value, whereas if it is outside, the system may be so adjusted that it will not oscillate.[14]

Professor Tarpley's comment is fully appreciated.   In this connection, as well as in answering Professor Dawson's remark, the author wishes to bring out the following point.   The value of the

[14] "Study of Cubic Characteristic Equation by Root-Locus Method," by Yaohan Chu and V. C. M. Yeh, published in this issue, pp. 343-348.

present analytical approach will again be brought into light when one considers the problem in which a time constant (i.e. an open-loop pole or zero) is being varied. In Fig. 15 a root-locus of Type $T(3, 1)$ transfer function is shown (heavy lines); it is a third-degree algebraic curve in addition to the real axis. When the location of the zero is being varied along the real axis, such as by adjusting the derivative time constant, a family of gain-contours are generated along each of which the closed-loop gain of the system is a constant. It can be shown analytically the gain-contours of $T(3, 1)$ are parabolas; and the location of the zero (α) is a varying parameter along the parabola. The equations of gain-contour, however, can only be obtained through the use of the root-locus equations. The determination of these gain-contours, on the other hand, by trial-and-error method or graphical construction would be extremely laborious—much more difficult than the construction of root-loci. This example illustrates the comparative advantages of the analytic approach. For further discussions the readers are referred to a paper entitled, "Synthesis of Feedback Systems by Gain Contours," to be published shortly by the author.

Static-Flow Characteristics of Single and Two-Stage Spring-Loaded Gas Pressure Regulators

By A. S. IBERALL,[1] WASHINGTON, D. C.

A theoretical investigation of greater completeness than is usually presented has been made of gas pressure regulators. Emphasis has been placed on the application to their design. The analysis is summarized in graphical form in which the characteristics of the regulator may be obtained by ruler and compass constructions. Brief attention is given to the errors inherent in the simplifications made in the analysis.

NOMENCLATURE

THE following nomenclature is used in this paper; in addition, symbols also are defined the first time they are used:

A = area
A_c = control surface area
A_m = metering orifice area (valve seat area)
A_z = effective metering orifice area, valve displaced distance X
D_1 = valve stem diameter
D_c = control surface diameter
D_m = metering orifice diameter
E = elastic modulus
F = spring force
H = a parameter
K = spring rate
M = mass flow
P = gas pressure
ΔP = pressure drop across orifice
Q = volumetric flow
R = linkage ratio
S = limiting flow for metering orifice
T = absolute temperature
V_j = velocity of metering orifice jet
W = work
X = valve displacement from closed position
X_0 = valve displacement when minimum annulus area equals metering orifice area
X = valve displacement at uncompressed position of control spring
Y = control surface displacement
a = metering orifice area per unit control surface area
c = constant
d = depth of surface irregularities of valve and seat
f = spring force per unit control surface area

k = spring rate per unit control surface area
l = axial length of softer material in valve or seat
n = coefficient of a Bernoulli suction
p = spring force per unit control surface area per atmosphere
q = unit ntp volume flow
r = regulated gage pressure per atmosphere
s = supply gage pressure per atmosphere
w = width of annular contact area of seat
x = unit valve displacement
γ = ratio of specific heats
ϵ = a displacement ratio (X_0/X)
θ = semiangle of a conical valve
λ = a parameter
μ = gas viscosity
ρ = gas density

The following subscripts are used:

g = gage pressure
r = quantities measured at regulated pressure
s = quantities measured at supply pressure

0 (for fluid parameters) signifies quantities measured at normal temperature and pressure.

INTRODUCTION

Although the gas pressure regulator is a widely used instrument, its theoretical exposition has received incomplete attention. It is the purpose of this paper to provide a somewhat more complete elucidation of the characteristics of the spring-loaded gas pressure regulator.

THEORY OF A SINGLE-STAGE PRESSURE REGULATOR

Derivation of Relations. The description of a pressure-regulating stage may be followed by reference to Fig. 1. A supply pressure P_s (the added subscript g will be utilized whenever gage pressure is intended) is applied to an entrance port of the stage. Distinction must be made between two possible elementary regulators; i.e., in one, the supply pressure acts to open the metering valve, while in the other, the supply pressure acts to close the valve. The supply pressure acts on a constant area A_m, equal to the metering orifice (valve seat) in applying a force on the metering valve. The metering valve, depicted for generality as a cone of semiangle θ, is coupled

PRESSURE ACTS TO OPEN STAGE

PRESSURE ACTS TO CLOSE STAGE

Fig. 1 Elementary Single-Stage Regulator

to a pressure-responsive surface of effective control area A_c.

For generality, the valve stem may be considered as coupled to the control surface by a linkage. For simplicity, the linkage will be taken as a linear lever with ratio R of control-surface displacement to valve displacement. The spring force of the pressure-responsive surface (depicted as a bellows) may be augmented either by a fixed or adjustable spring. The composite spring force of the system in the linkage directly coupled to the control surface at the point at which the valve is closed is denoted by F. As the valve opens, the spring force changes by an amount KY, where Y is the displacement of the control surface from its position when the valve is closed, and K, the spring rate. The displacement Y is thus also measured in the displacement of the same linkage as is the force F. The displacement of the metering valve as measured from its closed position will be taken as X, so that $Y = RX$. The other side of the pressure-responsive surface will be considered as open to atmospheric pressure P_0.

The action of the stage is as follows: The spring force holds the metering valve open when no supply pressure exists at the regulator inlet. As pressure is applied, with the regulator outlet closed off, the pressure in the regulator chamber acts on the control area A_c gradually to close the valve against the spring force so that a regulated outlet pressure P_r is obtained in the regulator chamber. As varying flows or supply pressures are demanded from or supplied to the regulator, there are small changes in the regulated pressure which spoil its ideal regulation. This may be understood by writing the static force equation for the system.

Equating the forces acting on the valve stem, when in equilibrium, there results for a "pressure acts to open" type regulator

$$A_m P_s + RA_c P_0 + RF = A_m P_r + RA_c P_r + R^2 KX \ldots [1]$$

and for a pressure acts to close type regulator

$$A_m P_s + RA_c P_r + R^2 KX = RF + RA_c P_0 + A_m P_r \ldots [2]$$

These may be rearranged to

$$P_{rg} = \frac{F}{A_c \pm A_m/R} \pm \frac{P_{sg} A_m/R}{A_c \pm A_m/R} - \frac{RKX}{A_c \pm A_m/R} \ldots [3]$$

for the two cases, where the upper sign refers to the pressure acts to open type.

The area $A_r \pm A_m/R$, which may be regarded as the net control area, may be utilized to define three specific parameters: f, the spring force per unit control area; a, the effective unbalanced metering area per unit control area; and k, the effective spring rate per unit control area. The regulation equation thus becomes

$$P_{rg} = f \pm a P_{sg} - kX \ldots [4]$$

This equation may then be interpreted as follows: The spring force per unit control area supplies a balance to determine the regulated pressure. The unbalanced metering area per unit control area left open to the supply pressure raises or lowers the regulated pressure. This may be referred to as the "supply-pressure effect." The spring rate per unit control area reduces the net spring force as the metering valve balances at a more open position to admit more flow. This results in a drop of the regulated pressure with flow and may be referred to as the "regulating characteristic."

Much invention has gone into balanced-valve arrangements to eliminate the supply pressure effect. In this paper, however, this term will not be neglected but will be carried along to give the designer or user an idea of its effect in simple regulator design and to indicate where recourse must be had to balanced-valve arrangements. A similar situation exists with respect to the regulating characteristic. This term also will be carried along.

For completeness, brief attention will be given to one more term to account for a device which the designer may sometimes add with considerable design simplicity in an attempt to improve the flow-regulating characteristic. Without the addition of moving elements, it is possible to obtain a Bernoulli suction from the metering orifice jet which will act on the control surface and give rise to a term which partially compensates for the drop in regulating pressure arising from the spring rate. The order of magnitude of this term is given by $\rho_r V_j^2/2$, where ρ_r is the gas density at the regulating pressure, and V_j is the velocity of the jet at the vena contracta of some entrainment section at which the absolute pressure of the jet is exposed to the control area. Thus the term can be written as $(Q_r/A_1)^2 \rho_r/2$, where Q_r is the volume flow at regulating pressure density and A_1 is some effective area of the jet. The meaning of the area A_1 and the precise value of the coefficient of the term is left vague because, in general, it is sensitive to the particular arrangement and means of producing the jet. As a rough measure, the area A_1 will be interpreted as the metering orifice area A_m, and an experimental coefficient n will be added. The more complete regulating equation becomes

$$P_{rg} = f \pm a P_{sg} - kX + \frac{n}{2} \rho_r \frac{Q_r^2}{A_m^2} \ldots [5]$$

where n is of the order of unity and may vary somewhat with flow. A second advantage of carrying this term along is that its form (although the sign is negative) is representative of minor pressure losses that may be encountered in specific regulator design. The net value of n is thus further reduced by these minor losses.

The problem may be completed by relating the metering valve displacement to flow. The following approximate treatment is utilized: The discharge of an orifice for both subcritical and critical flow may be approximated closely by what may be referred to as the mean density approximation, namely

$$M = 0.6A \sqrt{2\bar{\rho}\Delta P} \ldots [6]$$

where

M = mass flow through orifice

A = orifice area

0.6 = orifice discharge coefficient (for nonstandard thin-plate orifice shapes, this quantity may be somewhat larger)

ΔP = pressure drop across orifice

$\bar{\rho}$ = mean arithmetic density of gas upstream and downstream under equal enthalpy ideal gas assumption that temperatures downstream and upstream are the same

The density may be expressed as

$$\bar{\rho} = \frac{\rho_0}{P_0} \frac{T_0}{T} \bar{P} \ldots [7]$$

where

$\bar{P}$ = mean arithmetic pressure

T = absolute upstream gas temperature

0 subscripts refer to normal or ambient temperature and pressure conditions

The flow for ntp conditions thus becomes

$$Q_0 = \frac{0.6A}{\sqrt{P_0 \rho_0}} \sqrt{P_1^2 - P_2^2} \sqrt{\frac{T_0}{T}} \ldots [8]$$

where

Q_0 = volumetric flow at ntp conditions

P_1, P_2 = upstream and downstream pressures, respectively

Assuming that the regulator is used at normal temperature (or that the normal flow is measured at $T = T_0$ conditions), the flow equation becomes

$$Q_0 = \frac{0.64}{\sqrt{P_0 \rho_0}} \sqrt{P_1{}^2 - P_2{}^2} \dots \dots \dots \dots [9]$$

As the valve opens, it will be assumed that the flow restricting orifice is the minimum annulus between the valve and valve seat and becomes constant at valve displacement at which the annular area is equal to the valve seat area. This is known to be both a theoretical and an experimental approximation, but it is not a bad one. The actual magnitude of the error resulting from this assumption will be discussed further on.

The area of the minimum annulus is given by $\pi D_m X \sin \theta \left(1 - \frac{X}{2D_m} \sin 2\theta\right)$, where D_m is the diameter of the valve seat. The limiting displacement of the valve X_0 (when the area of the annular and metering orifice are equal) is given by $D_m \left(1 - \sqrt{1 - \cos \theta}\right)/\sin 2\theta$. The flow equation of the annulus thus becomes

$$Q_0 = \frac{0.6\pi D_m X \sin \theta \left[1 - \frac{X}{2D_m} \sin 2\theta\right]}{\sqrt{P_0 \rho_0}} \sqrt{P_s{}^2 - P_r{}^2} \dots [10]$$

and its fixed restriction flow (equivalent to the valve wide open) becomes

$$Q_0 = \frac{0.6\pi D_m{}^2}{4 \sqrt{P_0 \rho_0}} \sqrt{P_s{}^2 - P_r{}^2} \qquad \dots \dots [11]$$

The effect of the cone semiangle θ is to cause some extra droop in the flow characteristic which, in general, may be neglected in all except needlelike control valves. This, and other minor nonlinear sources of droop which exist, will be neglected.

The approximate area of the minimum annulus for relatively blunt valves may then be taken as $\pi D_m X \sin \theta$, the approximate limiting displacement X_0 may be taken as $D_m/4 \sin \theta$, and the approximate flow equation becomes

$$Q_0 = \frac{0.6\pi D_m X \sin \theta}{\sqrt{P_0 \rho_0}} \sqrt{P_s{}^2 - P_r{}^2} \dots \dots \dots [12]$$

while the fixed-restriction flow (equivalent to valve wide open) is given by Equation [11].

The regulating Equation [5] thus becomes

$$P_{rg} = f \pm aP_{so} - \frac{k \sqrt{P_0 \rho_0}}{0.6\pi D_m \sin \theta} \frac{Q_0}{\sqrt{P_s{}^2 - P_r{}^2}}$$
$$+ \frac{n \, \rho_0 Q_0{}^2 \, P_0}{2 \, A_m{}^2 \, P_r} \dots \dots \dots [13]$$

where the ideal-gas law was used to eliminate Q_r and ρ_r.

This result will be taken as expressing the regulating equation for an elementary ideal regulating stage. It is somewhat in error near the point at which the valve ceases to regulate. It is also somewhat in error in assuming that limiting flow accurately follows the law that the flow is proportional to $\sqrt{P_s{}^2 - P_r{}^2}$. A final source of error in this description, which makes itself evident in actual regulators, is the creep of regulated pressure at or near zero flow. This often seriously limits the application of simple regulators to dead-end service. It arises from the imperfect seal made by the valve at the point at which the valve is nominally closed and from the change in flow regime to laminar flow for very small openings. This will be discussed later on.

Graphical Solution. The regulating and flow equations may be transformed into dimensionless form by the following definitions and substitutions: Let

$\bar{X} = f/k$ (if the composite spring of the system is not restrained, $\bar{X}$ would be that valve displacement corresponding to the amount which the "free" spring length is compressed)

$S = 0.64_m \sqrt{(P/\rho)_0}$ (the limiting volumetric flow at atmospheric pressure that would be obtained if full vacuum were applied to the metering orifice with the upstream pressure at atmospheric pressure)

$r = P_{rg}/P_0 \qquad\qquad P_r = P_{rg} + P_0$
$p = f/P_0$
$s = P_{so}/P_0 \qquad\qquad P_s = P_{so} + P_0$
$q = Q_0/S$
$\epsilon = X_0/\bar{X}$
$X_0 = D_m/4 \sin \theta$
$x = X/X_0$

The regulating equation becomes

$$r = p \pm as - \frac{p\epsilon q}{\sqrt{(1 + s)^2 - (1 + r)^2}} + \frac{0.18 \, nq^2}{1 + r} \quad [14]$$

The flow equation becomes

$$q = x \sqrt{(1 + s)^2 - (1 + r)^2} \dots \dots \dots [15]$$

Whenever x exceeds unity physically, the value unity is to be used in Equation [15].

This pair of equations may be displayed graphically so as to present a complete family of regulation characteristics. In the construction of the graph, each regulation curve will, in general, be a plot of the regulated pressure r against the flow q for a selected constant value of the supply pressure s.

The construction will be given in detail for a "pressure acts to open" regulator.

First neglecting the Bernoulli term, the fundamental equations become

$$r = p + as - \frac{p\epsilon q}{\sqrt{(1 + s)^2 - (1 + r)^2}} \dots \dots [16]$$

$$q = x \sqrt{(1 + s)^2 - (1 + r)^2} \dots \dots \dots [15]$$

The graphical construction of the constant-supply pressure curves and boundaries of regimes of regulation may be followed by reference to Fig. 2. Let the point of view taken be that of the designer of a regulator.

A grid is chosen, Fig. 2(a), in which r is taken as the ordinate and q as the abscissa. The unit interval for r is chosen small enough so that the approximate value of the desired regulated pressure p falls well upon the grid. The $r = -1$ ordinate is included on the grid as a reference (this pressure corresponds to the absolute zero of pressure). The unit q interval is chosen to have the same value as the unit r interval.

The Salient Points. In the vicinity of the desired regulated pressure ordinate p, Fig. 2(b), at $q = 0$, the designer may choose three arbitrary or salient points, Fig. 2(c). As the graphical construction is developed, the significance and interpretation of these three points will become clear. In increasing value, these points are labeled, respectively, $p(1 - \epsilon) - a$; $p(1 - \epsilon)/(1 - a)$; $p/(1 - a)$.

The No-Regulation Boundary. If for given arbitrarily chosen supply pressures, the flow demand is increased, a flow is reached
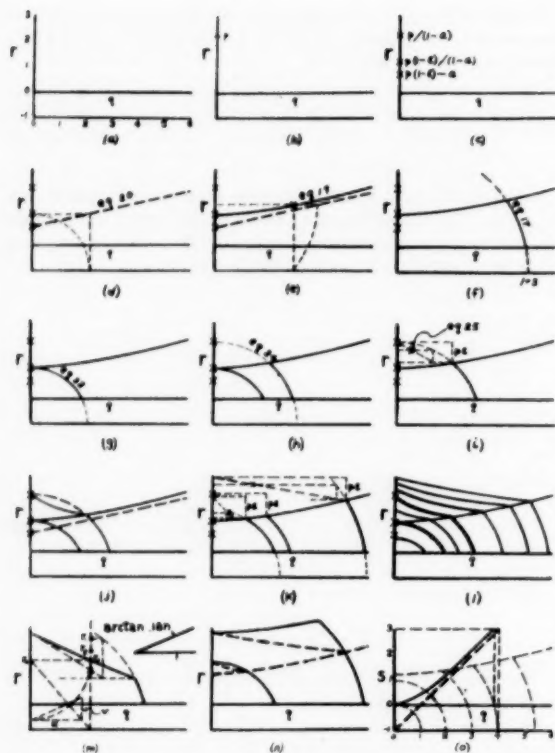
FIG. 2 CONSTRUCTION OF CHARACTERISTICS OF SINGLE-STAGE REGULATOR

(Pressure acts to open stage.)

at which x becomes unity. While physically the valve may open wider, the flow equation remains

$$q = \sqrt{(1 + s)^2 - (1 + r)^2} \qquad [17]$$

The regulating equation becomes

$$r = p(1 - \epsilon) + as \qquad [18]$$

If the supply pressure s is eliminated between these two equations the curve results, which is the boundary between the upper region in which the valve is still regulating and the lower region in which it is not. This will be referred to as the "no-regulation boundary." Its equation is

$$r = a \sqrt{q^2 + (1 + r)^2} + p(1 - \epsilon) - a \qquad [19]$$

At $q = 0$, $r = p(1 - \epsilon)/(1 - a)$, the middle salient point.

At large q, the equation becomes

$$r = p(1 - \epsilon) - a + aq \qquad [20]$$

This line, which is asymptotic to the true curve, may be easily constructed. At $q = 0$, $r = p(1 - \epsilon) - a$, the lower salient point. At $q = 1 + p(1 - \epsilon)/(1 - a)$, $r = p(1 - \epsilon)/(1 - a)$. These two points on the asymptotic line may be constructed and the asymptotic line may then be drawn, as shown in Fig. 2(d).

If now flows q_t on the true no-regulation boundary, and flows q_a on the asymptotic no-regulation boundary, are related for an identical value of r

$$r - p(1 - \epsilon) + a = a \sqrt{q_t^2 + (1 + r)^2} \qquad [19]$$

$$r - p(1 - \epsilon) + a = aq_a \qquad [20]$$

the result holds that

$$q_a = \sqrt{q_t^2 + (1 + r)^2} \qquad [21]$$

The construction of the true curve is shown for a typical point in Fig. 2(e) (in which a hyperbolic construction is used) and for the complete curve in Fig. 2(f).

The Circles of No Regulation. For points below the no-regulation boundary where no regulation occurs, the valve acts as a fixed-area restriction so that the flow equation is given by

$$q = \sqrt{(1 + s)^2 - (1 + r)^2} \qquad [17]$$

For arbitrary supply pressure s, this is a family of circles which intersect the $r = -1$ axis at $q = 1 + s$. A typical circle is shown in Fig. 2(f).

The Salient Circles. If with no flow through the valve, the supply pressure is increased above the regulated pressure, the valve (at first wide open) gradually closes until a supply pressure is reached at which $x = 1$ (the valve has closed to a degree where it is just on the point of no regulation). The supply pressure at which this occurs determines a circle of no regulation which is tangent to the no-regulation boundary. It is shown in Fig. 2(g) and it will be referred to as the "last circle of no regulation."

Its equation is given by

$$q = \sqrt{\left[1 + \frac{p(1 - \epsilon)}{1 - a}\right]^2 - (1 + r)^2} \qquad [22]$$

If the supply pressure at no flow is increased further, then the valve closes further. Finally a supply pressure is reached at which the valve just seals ($x = 0$). This is the last point at which the supply pressure and regulated outlet pressure are still equal at no flow. This point is given by

$$r = s = \frac{p}{1 - a} \qquad [23]$$

the third salient point. The circle of no regulation corresponding to this supply pressure is given by

$$q = \sqrt{\left(1 + \frac{p}{1 - a}\right)^2 - (1 + r)^2} \qquad [24]$$

It is shown in Fig. 2(h) and it will be referred to as the "first circle with complete regulation at no flow."

First Curve of Complete Regulation. As the supply pressure is increased to $s = p/(1 - a)$ at no flow, the valve gradually closes and finally closes completely. As flow is increased, the valve is regulating, and the portion of the regulating curve above the no-regulation boundary is not a circle.

Its equation is given by

$$r = \frac{p}{1 - a} - \frac{p\epsilon q}{\sqrt{\left(1 + \frac{p}{1 - a}\right)^2 - (1 + r)^2}} \qquad [25]$$

At $q = 0$, $r = p/(1 - a)$, so that this curve intersects its circle of no regulation at $q = 0$ as well as at the no-regulation boundary.

Intermediate points for this curve may be constructed by comparison with its circle. Let q_a stand for values of flow on the circle and q_t stand for values of flow on the curve, at some identical value of r. Then

$$q_c = \sqrt{\left(1 + \frac{p}{1-a}\right)^2 - (1+r)^2} \qquad [24]$$

$$r = \frac{p}{1-a} - \frac{p\epsilon q_i}{\sqrt{\left(1 + \frac{p}{1-a}\right)^2 - (1+r)^2}} \qquad [25]$$

Comparison leads to the result that

$$\frac{q_i}{q_c} = \frac{\dfrac{p}{1-a} - r}{p\epsilon} \qquad [26]$$

This construction may be made simply if the length $p\epsilon$ is known. It is easy to show that the difference in the r-ordinate between the intersection of the circle with the r-axis, and with the no-regulation boundary, is $p\epsilon$. A geometrical construction for a selected value of r using Equation [26] then will determine the required value of q_i. The construction of a typical point on the curve is shown in Fig. 2(i).

This complete curve (including its no-regulation circle below the no-regulation boundary) will be referred to as the "first curve of complete regulation."

The salient curves and circles for a regulator are shown in Fig. 2(j).

Remaining Regulating Curves. Inside or below the last circle of no regulation, the regulator characteristics are represented by concentric arcs of circles.

The curves for constant s between the last circle of no regulation and the first curve of complete regulation are designated curves of incomplete or no-flow regulation. They are so named because at zero flow the valve has not yet closed; however, regulation commences as soon as there is a finite flow and of course ceases as the regulation curve crosses the no-regulation boundary. Below the no-regulation boundary these curves are arcs of circles. Above the boundary the remainder of the curve may be constructed as follows: The equation of the curve is

$$r = p + as - \frac{p\epsilon q}{\sqrt{(1+s)^2 - (1+r)^2}} \qquad [16]$$

At $q = 0$, $r = s$ (at this supply pressure the valve is still open), so that this point is the intersection of its nonregulating circular arc extended to the $q = 0$ axis.

The remainder of the curve can be constructed from the relation

$$\frac{q}{\sqrt{(1+s)^2 - (1+r)^2}} = \frac{p + as - r}{p\epsilon} \qquad [27]$$

if the length $p + as$ is known. It can be shown that the difference in the r-ordinate on the curve between its intersection with the no-regulation circle and with the no-regulation boundary is $p + as - p\epsilon$. Adding the value of $p\epsilon$, which was obtained previously, thus gives the desired value. The construction of a typical point of a typical curve is shown in Fig. 2(k), using the relationships given in Equation [27].

The complete regulation curves lie above the first curve of complete regulation. They consist of two parts: (a) of circular arcs of no regulation below the no-regulation boundary, and (b) of curves defined by Equation [16] above the boundary. At $q = 0$ in this region, the valve is closed so that the intercept r is $p + as$. The difference in ordinate of the desired curve at $q = 0$ and at the intersection of the no-boundary curve is $p\epsilon$. The construction of a typical point on a typical complete regulation curve is also shown in Fig. 2(k).

A family of complete characteristics is shown in Fig. 2(l).

Limiting Flow. It is of use to have a plot of the limiting flow,

that is, the flow obtained when there is no flow restriction at the regulator outlet. In this case $r = 0$. The relation between flow and pressure drop becomes

$$q = \sqrt{(1+s)^2 - 1} \qquad [28]$$

The asymptotic line (at high supply pressures) is given by

$$q = 1 + s \qquad [29]$$

This is shown in Fig. 2(o) against a background of circles of no regulation. The geometric relationship between the true curve and the intercepts of the circles is also shown for a typical point.

The Bernoulli Term. An approximate construction can now be added for the Bernoulli term. The fundamental equations are

$$r = p + as - \frac{p\epsilon q}{\sqrt{(1+s)^2 - (1+r)^2}} + \frac{0.18\,nq^2}{1+r} \qquad [14]$$

$$q = x\sqrt{(1+s)^2 - (1+r)^2} \qquad [15]$$

All curves that were circles of no regulation remain so. The no-regulation boundary is modified to

$$r - a\sqrt{q^2 + (1+r)^2} = p(1-\epsilon) - a + \frac{0.18\,nq^2}{1+r} \qquad [30]$$

The no-regulation boundary is higher than before by a term which increases approximately quadratically with flow. The circles of no regulation are thus extended a bit, and the main effect of the Bernoulli term is in the regulating region away from $q = 0$.

The construction of a typical point of the regulating characteristic of a regulator with a Bernoulli term is shown in Fig. 2(m). It is based on correcting the characteristic of a regulator without a Bernoulli term. If the value of r is taken as r_0 for a regulator without a Bernoulli term for a given supply pressure s, then the regulating equation for a regulator with a Bernoulli term at the same supply pressure may be written approximately as

$$\frac{p + as + \dfrac{0.18\,nq^2}{1+r_0} - r}{p\epsilon} = \frac{q}{\sqrt{(1+s)^2 - (1+r)^2}} \qquad [31]$$

In this expression, the only approximation lies in using $q^2/(1+r_0)$ instead of $q^2/(1+r)$. The initial steps to reduce the foregoing expression to graphical form follow: First choose a flow q on some r_0 characteristic. Determine $q^2/(1+r_0)$ [$=u$ in Fig. 2(m)] by a proportional triangle construction as shown in Fig. 2(m). Lay off an angle equal to arc tan $0.18\,n$. The quantity $0.18\,nq^2/(1+r_0)$ [$= v$ in Fig. 2(m)] may then be constructed. To secure a first approximation of r corresponding to the selected q requires that the regulating curves for r_0 previously obtained be available. Add $0.18\,nq^2/(1+r_0)$ to r_0 at the same flow. This represents the first estimate of r [marked r_1 in Fig. 2(m)]. A proportional triangle construction is then used to secure a closer approximation to the value of r. Extend the r_1 ordinate to intersect the nonregulating circle [which determines an abscissa equal to $\sqrt{(1+s)^2 - (1+r_1)^2}$]. Drop a perpendicular from this point to the ordinate determined by the intersection of the nonregulating circle and the no-regulation boundary. Connecting this intersection with the point on the r_0-characteristic at which $q = 0$ thus locates a point on the abscissa q, marked by x in Fig. 2(m).

Note in Fig. 2(m) that the ordinate length of the large triangle equals $p\epsilon$, its abscissa, or base length, is $\sqrt{(1+s)^2 - (1+r_1)^2}$, and that the base of a smaller similar triangle terminating at x is q, from which the numerator of the first term of Equation [31] is determinable by proportion as the ordinate distance from the point of the r_0-characteristic at which $q = 0$ ($r = p + as$) to the

point x. From the relationship $p + as + 0.18\, nq^2/(1 + r_0) - r_2$ $= p + as - r_s$ it follows that $r_2 = r_s + 0.18\, nq^2/(1 + r_0)$. Therefore a new point [r_2 in Fig. 2(m)], a closer approximation to r, is obtained by laying off $0.18\, nq^2/(1 + r_0)$ above point x.

The procedure is repeated until the estimated r obtained converges to the estimate from the step before. A further refinement which is generally not worth the added effort, is to use the new value of r in constructing $q^2/(1 + r)$ and following the method of successive approximations through again. A typical family of curves with a Bernoulli term is shown in Fig. 2(n).

Pressure Acts to Close Regulator. The characteristics of a pressure acts to close regulator may be similarly constructed. The basic equations are

$$r = p - as - \frac{peq}{\sqrt{(1 + s)^2 - (1 + r)^2}} + \frac{0.18\, nq^2}{1 + r} \quad [14]$$

$$q = x \sqrt{(1 + s)^2 - (1 + r)^2} \quad\quad\quad [15]$$

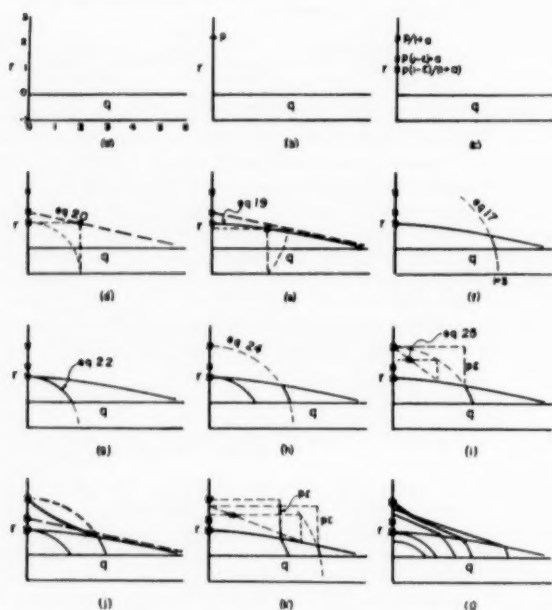The corresponding constructions are shown in Fig. 3.

FIG. 3 CONSTRUCTION OF CHARACTERISTICS OF SINGLE-STAGE REGULATOR
(Pressure acts to close stage.)

ERRORS IN ELEMENTARY THEORY OF SINGLE-STAGE REGULATOR

List of Errors. The previous theory represents the "real" characteristics of regulators in the sense that measured characteristics nominally will superimpose on the theoretically derived characteristics. From the point of view of the designer this may often be adequate and, at least in most cases, would represent the first step in real regulator design, since the general nature of the regulating characteristics is shown. However, for a precise description many detailed errors will be found. In this section it is proposed to discuss briefly some alternative analytic representations that correct these errors. It is not suggested that these alternatives will work for all cases. Their value is to indicate to the designer at least some order of magnitude of the deviations that might be expected from the elementary theory.

As was discussed previously, the errors in the analytic representation of the performance of the single-stage regulator arise from five major sources, as follows:

1. The assumed mean density flow law.
2. The flow resistance of the metering valve.
3. The assumed supply pressure effect.
4. Minor pressure drops.
5. Flow regulation at low flows.

Mean Density Flow Law. The mean density flow law is an approximation for flow through an orifice particularly with negligible velocity of approach. A closer approximation can be shown to be given by

$$Q_0 = \frac{0.6A}{\sqrt{P_0\rho_0}} \sqrt{\frac{T_0}{T}} \sqrt{P_1^2 - P_2^2} \frac{2 + P_2/P_1}{3} \sqrt{\frac{2}{1 + P_2/P_1}} \quad\quad [32]$$

instead of Equation [8].

At normal temperature, the flow equation becomes

$$q = \frac{A_X}{A_m} \sqrt{(1 + s)^2 - (1 + r)^2}\, \frac{2 + (1 + r)/(1 + s)}{3} \sqrt{\frac{2}{1 + \dfrac{1 + r}{1 + s}}} \quad [33]$$

where A_X/A_m is the ratio of the effective area of the valve, when opened to a displacement X, to the area of the metering orifice. This relationship may be used to replace Equation [15]. This result differs from Equation [15] by a factor that ranges from 1 to 0.943 as $(1 + r)/(1 + s)$ ranges from 1 to 0.

For an ideal nozzle metering restriction, the adiabatic flow law is applicable, which for small velocity of approach becomes

$$Q_0 = \frac{A}{\sqrt{P_0\rho_0}} \sqrt{\frac{2\gamma}{\gamma - 1}} \left(\frac{P_2}{P_1}\right)^{\frac{1}{\gamma}} \sqrt{1 - \left(\frac{P_2}{P_1}\right)^{\frac{\gamma-1}{\gamma}}} \sqrt{\frac{T_0}{T}}\, P_1 \quad [34]$$

where γ is the ratio of specific heats.

The limiting flow S at $P_1 = P_0$ is

$$S = \frac{A_m}{\sqrt{P_0\rho_0}} \sqrt{\gamma \left(\frac{2}{\gamma + 1}\right)^{\frac{\gamma+1}{\gamma-1}} P_0} \quad\quad [35]$$

so that the flow equation becomes

$$q = \frac{A_x}{A_m} \frac{\left(\dfrac{1 + r}{1 + s}\right)^{\frac{1}{\gamma}}}{\left(\dfrac{2}{\gamma + 1}\right)^{\frac{1}{\gamma-1}}} \frac{\sqrt{1 - \left(\dfrac{1 + r}{1 + s}\right)^{\frac{\gamma-1}{\gamma}}}}{\sqrt{\dfrac{\gamma - 1}{\gamma + 1}}} (1 + s) \quad [36]$$

instead of Equation [15]. Equation [36] applies for $(1 + r)/(1 + s)$ lying between 1 and $[2/(\gamma + 1)]^{\gamma/(\gamma-1)}$. For values of $(1 + r)/(1 + s)$ less than $[2/(1 + \gamma)]^{\gamma/(\gamma-1)}$, Equation [36] applies where the constant $[2/(\gamma + 1)]^{\gamma/(\gamma-1)}$ is substituted for $(1 + r)/(1 + s)$. While this is a possible metering relation, it is not believed that many nozzlelike metering valves have ever been built for regulators.

Flow Resistance of Metering Valve. As a rough test of the validity of the minimum annulus flow restriction assumption, some crude experiments were performed using thin and thick-plate orifices, closed by small (i.e., same diameter as the orifice) and large-diameter flat plates, and a 45-deg semiangle cone. For a thin orifice with flow in either direction with flat plate valves, the flow-displacement curve was about 30 per cent lower at $X = D_m/4$ than the minimum annulus result with an error falling off

rapidly for smaller or larger displacement. The same result held for the cone, when assessed by the first order $D_m/4 \sin \theta$ approximation. Using the more exact approximation, the error was reduced to about 20 per cent. The same results held for the thick-plate metering orifice with flow in the valve-to-orifice direction. For a thick-plate metering orifice with flow in the orifice-to-valve direction, greater flow than the approximation obtained. As the displacements were increased from closed to open, the flow error increased from about 10 per cent high at one half of the $D_m/4 \sin \theta$ point to about 20 per cent high at the $D_m/4 \sin \theta$ point, dropping off rapidly for larger displacements.

The maximum deviation in the flow-displacement law from the minimum annulus approximation and, in particular, from the first-order approximation, thus occurs near the fixed-restriction point, and, independent of valve configuration, does not exceed ±30 per cent. This results only in a percentage error in the droop of the flow-regulating characteristic occurring near the end of regulation. Since there are other possible sources of error near this point, the minimum annulus approximation is a good first-order approximation. More exact design must take into account the precise valve-orifice configuration which affects both the form of the flow-displacement variation as well as the discharge coefficient.

However, in lieu of more exact theoretical or experimental results, the following models represent some measure of the expected deviation from the minimum annulus approximation:

For thin plate orifices with flow in either direction, and with thick plate orifices with flow in the valve-to-orifice direction (pressure acts to close valves), the valve restriction acts as if the minimum annulus was in series with a fixed restriction equal to the metering orifice.

This can be represented by

$$q = \frac{\sqrt{(1 + s)^2 - (1 + r)^2}}{\sqrt{1 + \left(\frac{A_m}{A_X}\right)^2}} \quad \ldots \ldots \ldots [37]$$

where A_X is to be taken as the minimum annulus area.

Substituting in the exact minimum annulus area leads to the result

$$\frac{A_X}{A_m} = x \left(1 - \frac{x \cos \theta}{4}\right) \quad \ldots \ldots \ldots [38]$$

or the spring rate term takes on the value

$$\frac{kX}{P_0} = p\epsilon \frac{2}{\cos \theta} \left[1 - \sqrt{1 - \frac{q \cos \theta}{\sqrt{(1 + s)^2 - (1 + r)^2 - q^2}}}\right] \\ \ldots \ldots \ldots [39]$$

while the flow equation becomes

$$q = \frac{\sqrt{(1 + s)^2 - (1 + r)^2}}{\sqrt{1 + \dfrac{1}{x^2 \left(1 - \dfrac{x}{4} \cos \theta\right)^2}}} \quad \ldots \ldots \ldots [40]$$

Here x varies from 0 to infinity.

For flattish valves, the approximation holds that

$$\frac{kX}{P_0} = \frac{p\epsilon q}{\sqrt{(1 + s)^2 - (1 + r)^2 - q^2}}$$

$$\left[1 + \frac{q \cos \theta}{4 \sqrt{(1 + s)^2 - (1 + r)^2 - q^2}} + \ldots\right] \quad [41]$$

$$x = \frac{q}{\sqrt{(1 + s)^2 - (1 + r)^2 - q^2}}$$

$$\left[1 + \frac{q \cos \theta}{4 \sqrt{(1 + s)^2 - (1 + r)^2 - q^2}} + \ldots\right] \quad [42]$$

The first-order terms of these expressions are constructable into graphs and represent possible modification in the form of the regulating curves.

For thick plate valves in the opposite flow direction, it is difficult to obtain a simple analytic representation.

Supply Pressure Effect. There also exists an error with respect to the supply pressure effect. It was assumed as an approximation that the supply pressure acted on a projected area of the valve equal to the metering orifice. A better approximation is that it acts on a circular area whose equivalent diameter is $D_m(1 - X \sin 2\theta/2D_m)$.

Minor Pressure Drops. Minor pressure drops make themselves evident at two major points; (a) the drop in supply pressure to the inlet of the valve, and (b) the drop in the outlet port of the valve. If the characteristics are considered from pressure taps at the valve inlet and in the regulating chamber they may be neglected in describing the regulator characteristics and separately superimposed.

Flow Regulation at Low Flows. At small openings (leakage openings) the valve becomes essentially a laminar flow element. Its resistance may be estimated by the laminar flow resistance of parallel plates. This is given by

$$\Delta P = \frac{12\mu_0 w Q}{\pi D_m d^3} \quad \ldots \ldots \ldots \ldots [43]$$

where

ΔP = pressure drop across valve

μ_0 = gas viscosity at upstream temperature

Q = volumetric flow at mean pressure and upstream temperature

w = width of annular contact area

D_m = diameter of metering valve

d = effective separation of valve and seat at displacement at which it is nominally closed

For valves and seats that are not warped with respect to each other, d may be assumed to be of the order of magnitude of the composite mean surface irregularities of both valve and seat.

For designs which involve a definite contact area, w is of the order of magnitude of the width. For so-called line-contact designs, w is not quite as meaningful. It is at least of the order of magnitude of d.

The foregoing equation may be transformed into

$$q = \frac{1}{3.6} \frac{\sqrt{P_0 \rho_0}}{\mu_0} \frac{d^3}{D_m w} [(1 + s)^2 - (1 + r)^2] \quad \ldots [44]$$

noting that $Q = Q_0 P_0/P$.

This represents the order of magnitude of the maximum leakage flow that might be obtained from an imperfectly sealing seat.

The added pressure above that at which the valve should seal may be estimated by equating the work done in elastically deforming the surface irregularities to the work done by the added pressure on the control area.

The maximum possible amount of elastic work W is given by

$$W = \frac{\pi}{2} \frac{D_m w d^2}{l} E \quad \ldots \ldots \ldots [45]$$

where

l = depth of softer material (of either valve or seat)

E = elastic modulus of softer material

w = width of sealed annular contact area

The work done by the gas pressure W (with a one-to-one multiplication) is given by

$$W = \frac{1}{2} A_c d \Delta P_r \quad\quad [46]$$

where

ΔP_r = extra regulating pressure required to seal, neglecting slight variation in spring force, and A_c is control-surface area

Equating these and transforming, the result is obtained that

$$\Delta r = \pi \frac{E}{P_0} \frac{w}{l} \frac{D_m d}{A_c} \quad\quad [47]$$

where Δr = extra regulating pressure required to seal the valve.

Except for numerical coefficients, these two results give the order of magnitude of the leakage region, which may be imagined as a triangular area superimposed on the regulating characteristic whose height (at no flow) is given by Equation [47], and whose base measured along the regulating characteristic is given by Equation [44].

THEORY OF A TWO-STAGE PRESSURE REGULATOR

Construction of Performance Curves. In the two-stage regulator the regulated pressure of the first stage becomes the supply pressure of the second stage. The equations thus become:

For first stage

$$r_1 = p_1 + a_1 s - \frac{p_1 \epsilon_1 q_1}{\sqrt{(1+s)^2 - (1+r_1)^2}} + \frac{0.18\, n_1 q_1^2}{1+r_1} \quad [48]$$

$$q_1 = x_1 \sqrt{(1+s)^2 - (1+r_1)^2} \quad\quad [49]$$

For second stage

$$r_2 = p_2 + a_2 r_1 - \frac{p_2 \epsilon_2 q_2}{\sqrt{(1+r_1)^2 - (1+r_2)^2}} + \frac{0.18\, n_2 q_2^2}{1+r_2} \quad [50]$$

$$q_2 = x_2 \sqrt{(1+r_1)^2 - (1+r_2)^2} \quad\quad [51]$$

$$\frac{q_1}{q_2} = \frac{S_2}{S_1} \quad\quad [52]$$

The subscripts 1 and 2 denote first and second-stage quantities, respectively. The value of a in this context may be either positive or negative.

The primary result of adding a second stage is to reduce the supply pressure effect, and the secondary result is to modify the form of the limiting flow.

In what follows only two aspects of the two-stage regulator will be discussed—the geometric construction of the regulator characteristics and the limiting flow characteristic.

The construction is illustrated in Fig. 4. Construct the characteristics of the first-stage regulator, Fig. 4(a). Replot the characteristics by reducing the flow variable q_1 to the value $q_2 = q_1 S_1 / S_2$, Fig. 4(b). On the same grid construct the limiting flow

equation for the second stage (Equation [51] with $x_2 = 1$, and $r_2 = 0$). The intersection of this line with the regulating curves of the modified first-stage-regulator characteristics, Fig. 4(b), determines the limiting flow for each of the supply pressures that it has intersected.

If now the second-stage characteristics are constructed with the same flow axis, then the composite characteristics of the two-stage regulator can be constructed, Fig. 4(c). Choose a given supply pressure characteristic of the first stage. Transfer the flow intersection with the second-stage limiting flow equation to second-stage graph at $r_2 = 0$. This determines the limiting flow for the regulator at that supply pressure. Now choose some higher point on the same first-stage supply-pressure characteristic. Transfer the flow to the second-stage graph to that regulating characteristic whose supply pressure has the same value as the first-stage outlet pressure r_1. This characteristic may be determined from the fact that at $r_2 = -1$ the intercept has the value $1 + r_1$, Fig. 4(c). This determines a second point on the regulating characteristic of the two-stage regulator. By choosing other points the complete regulating characteristic for that supply pressure can be constructed. The construction is illustrated in Fig. 4(c) for a typical point. The complete characteristics can then be similarly constructed. A typical family is shown in Fig. 4(c). The limiting-flow curve for the two-stage regulator is shown in Fig. 4(d).

Limiting Flow. A geometric study of the limiting-flow characteristics shows that it falls into two regions. For all supply pressures when limiting flow obtains for the two-stage regulator, the second-stage regulator acts as a fixed restriction. In the first region of low supply pressures, the first stage also acts as a fixed restriction. At higher supply pressures the first stage may still be regulating [typically q_2 greater than $(q_2)_1$], Fig. 4(b). Rarely, at still higher pressures, the first stage may again become a fixed restriction. The condition for the existence of the transitions is whether the limiting flow equation for the second stage

$$q_2 = \sqrt{(1+r_1)^2 - 1} \quad\quad [53]$$

intersects the no-regulation boundary of the first stage defined by

$$r_1 = p_1(1 - \epsilon_1) + a_1 s + \frac{0.18\, n_1 q_1^2}{1 + r_1} \quad\quad [54]$$

$$q_1 = \sqrt{(1+s)^2 - (1+r_1)^2} \quad\quad [55]$$

which when the supply pressure s is eliminated becomes

$$r_1 = p_1(1 - \epsilon_1) - a_1 + a_1 \sqrt{q_1^2 + (1+r_1)^2} + \frac{0.18\, n_1 q_1^2}{1 + r_1} \quad [56]$$

By eliminating the first-stage outlet pressure r_1 the possible intersections are given by the roots of the equation

$$
\begin{aligned}
&[1 + q_2^2]\left[1 - a_1 \sqrt{1 + \left(\frac{S_2}{S}\right)^2} - 0.18\, n_1 \left(\frac{S_2}{S_1}\right)^2\right] - \sqrt{1 + q_2^2} \\
&\qquad\qquad \left[1 + p_1(1 - \epsilon_1) - a_1\right] + 0.18\, n_1 \left(\frac{S_2}{S_1}\right)^2 \\
&= a_1 \sqrt{1 + q_2^2}\left[\sqrt{\left[1 + \left(\frac{S_2}{S_1}\right)^2\right]\left[1 + q_2^2\right]} - \left[\frac{S_2}{S_1}\right]^2 \right. \\
&\qquad\qquad \left. - \sqrt{1 + \left[\frac{S_2}{S_1}\right]^2} \sqrt{1 + q_2^2}\right]
\end{aligned} \quad [57]
$$

If the following substitutions are made

$$z = \sqrt{1 + q_2^2} \quad\quad\quad \infty > z \geq 1$$

FIG. 4 CONSTRUCTION OF CHARACTERISTICS OF TWO-STAGE REGULATOR

$$c_1 = \frac{1 - a_1 H - 0.18\, n_1 \left(\frac{S_2}{S_1}\right)^2}{H^2} \qquad 2 > c_1 > -1$$

$$c_2 = \frac{1 + p_1(1 - \epsilon_1) - a_1}{H^2} \qquad \infty > c_2 > 0$$

$$c_3 = \frac{0.18\, n_1 \left(\frac{S_2}{S_1}\right)^2}{H^2} \qquad \frac{1}{2} > c_3 \geq 0$$

$$c_4 = \frac{a_1}{H} \qquad 1 > c_4 > 0$$

$$c_5 = \frac{\frac{S_2}{S_1}}{H} \qquad 1 > c_5 > 0$$

where

$$H = \sqrt{1 + \left(\frac{S_2}{S_1}\right)^2}$$

then

$$c_1 z^2 - c_2 z + c_3 = c_3 z \left[\sqrt{z^2 - c_5^2} - z\right] \dots \dots [58]$$

The question of interest is the existence of roots for z in the range greater than or equal to 1.

The right-hand side of Equation [58] is a function of z/c_5 that varies from $-c_4 c_5^2$ at $z/c_5 = 1$ to $-c_4 c_5^2/2$ at $z/c_5 = \infty$. For $z/c_5 > 2$, the function is very close to $-c_4 c_5^2/2$. Therefore the equation may be put in the convenient form

$$c_1 z^2 - c_2 z + (c_3 + \lambda c_4 c_5^2) = 0 \dots \dots [59]$$

where

$$\lambda = \frac{z}{c_5}\left[\frac{z}{c_5} - \sqrt{\left(\frac{z}{c_5}\right)^2 - 1}\right] \dots \dots [60]$$

For large values of z/c_5, λ may be expanded to

$$\lambda = \frac{1}{2}\left[1 + \frac{1}{4}\left(\frac{c_5}{z}\right)^2 + \frac{1}{8}\left(\frac{c_5}{z}\right)^4 + \dots\right] \dots \dots [61]$$

The roots of Equation [59] are

$$z = \frac{c_2 \pm \sqrt{c_2^2 - 4 c_1(c_3 + \lambda c_4 c_5^2)}}{2 c_1} \qquad [62]$$

It can be shown that there may exist 0, 1, or 2 roots for $z \geq 1$ depending on the relative values of c_1, c_2, c_3, c_4, c_5, and λ.

These roots may be determined by a method of successive approximations by determining the effect of various values of λ from $1/2$ to 1 in changing the condition for existence of roots. For c_5 less than $1/2$, the assumption of $\lambda = 1/2$ may be made, and Equation [62] solved to find out whether roots for $z \geq 1$ exist. For c_5 greater than $1/2$, λ may be assumed to be $1/2$ or 1, Equation [62] solved to find out whether there are roots for z, and then λ may be re-estimated by Equation [61] successively until convergence is obtained.

Consider, in general, the situation where two roots exist, in increasing order $(q_2)_1$, $(q_2)_2$. Below $(q_2)_1$, both stages act as fixed restrictions whose equations are given by

$$q_1 = \sqrt{(1 + r_1)^2 - 1} \dots \dots [53]$$

$$q_1 = \sqrt{(1 + s)^2 - (1 + r_1)^2} \quad \ldots \ldots \ldots [55]$$

$$\frac{q_1}{q_2} = \frac{S_2}{S_1} \quad \ldots \ldots \ldots \ldots \ldots \ldots [52]$$

The limiting flow equation is thus

$$1 + \left[1 + \left(\frac{S_2}{S_1}\right)^2\right] q_2^2 = [1 + s]^2 \quad \ldots \ldots \ldots [63]$$

up to the first root $(q_2)_1$.

The form of the low supply pressure limiting-flow curve is thus identical with that for the single stage, Equation [28].

Above the second root $(q_2)_2$, the same result holds.

For the region between the two roots, the limiting flow equation is given by

$$q_2 = \sqrt{(1 + r_1)^2 - 1} \quad \ldots \ldots \ldots \ldots \ldots [53]$$

$$r_1 = p_1 + a_1 s - \frac{p_1 \epsilon_1 q_1}{\sqrt{(1 + s)^2 - (1 + r_1)^2}} + \frac{0.18 \, n_1 q_1^2}{1 + r_1} \quad \ldots [48]$$

The limiting flow equation is thus

$$\sqrt{1 + q_2^2} = 1 + p_1 + a_1 s - \frac{\dfrac{S_2}{S_1} p_1 \epsilon_1 q_2}{\sqrt{(1 + s)^2 - (1 + q_2^2)}}$$

$$+ \frac{0.18 \, n_1 \left(\dfrac{S_2}{S_1}\right)^2 q_2^2}{\sqrt{1 + q_2^2}} \quad \ldots \ldots \ldots [64]$$

Analytically, the form of this equation is quite complicated. Its general characteristics are that q_2 is a slowly varying function of s which ultimately would vary linearly with s with a slope approaching $a_1/[1 - 0.18 \, n_1(S_2/S_1)^2]$.

Thus, while the limiting flow for a single-stage regulator tends to climb linearly with supply pressure, the limiting flow for a two-stage regulator tends to be more constant.

DESIGN ILLUSTRATION

There are so many design problems that can be taken as illustration that it is considered more desirable to leave these to detailed study for a particular application. Instead, as a very simple illustration, the characteristics will be described of a number of commercially available high-pressure-cylinder pressure regulators that are used for welding purposes. Characteristic among this group are single-stage pressure acts to close, no Bernoulli term, adjustable regulators which reduce cylinder pressures in the range 50 to 2000 psi to an outlet pressure in the range 50 to 1000 psi.

Some characteristic dimensions on these regulators are as follows:

$D_m = 0.05$ in.
$D_1 = 0.03$ in. (valve stem rides through seat and reduces effective metering restriction. D_1 is stem diameter)
$\theta = 45$ deg
$D_e = 0.7$ in. (a slack diaphragm is used as control area, effective diameter of which D_e is taken as 0.9 of actual diameter)
$K = 2400$ lb/in.
$\overline{X} = $ range of adjustable control spring $= 0 - \frac{3}{16}$ in.
$P_0 = 14.7$ psi
$\rho_0 = 0.0012$ gram/cm³ (normal temperature and pressure air)

From these quantities the dimensionless parameters may be computed to be

$$a = \frac{A_m}{A_c - A_m} = 0.005$$

$$p\epsilon = \frac{kD_m\left[1 - \left(\dfrac{D_1}{D_m}\right)^2\right]}{4[A_c - A_m]P_0 \sin\theta} = 4.8$$
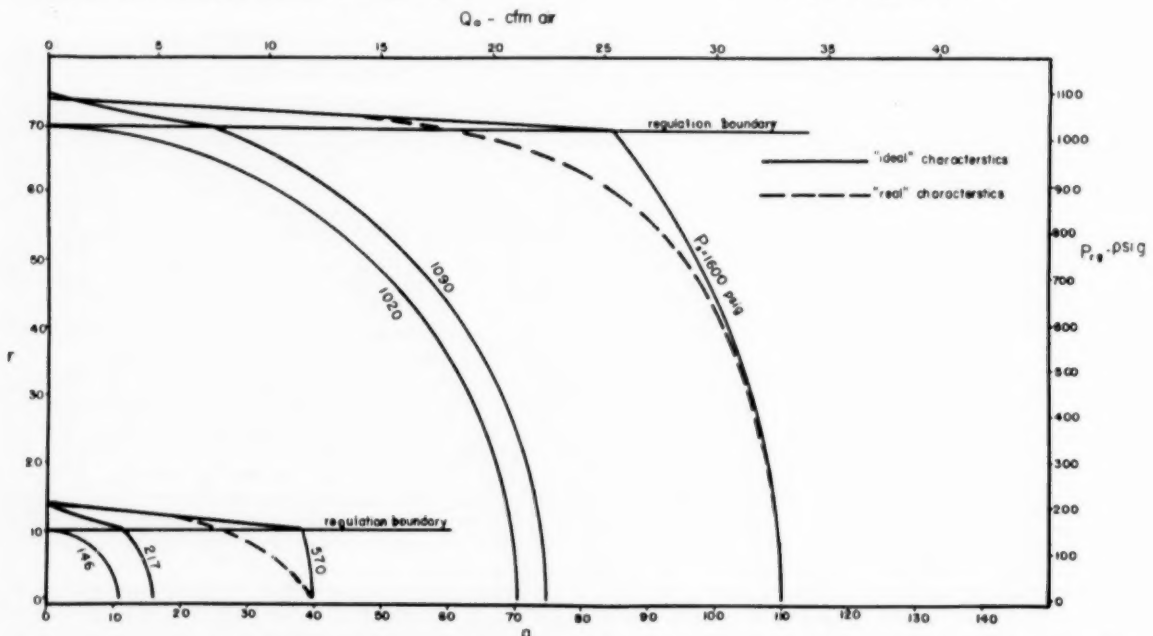
FIG. 5 THEORETICAL CHARACTERISTICS OF COMMON COMMERCIAL SINGLE-STAGE ADJUSTABLE-PRESSURE REGULATOR SHOWN AT TWO SETTINGS OF REGULATED PRESSURE

$$q = \frac{Q_0}{0.6\,A_m\left[1 - \left(\dfrac{D_1}{D_m}\right)\right]}\sqrt{\frac{\rho_0}{P_0}} = \frac{Q_0(\text{cfm})}{0.30}$$

$$p_{max} = \frac{K\bar{X}_{max}}{(A_c - A_m)P_0} = 80$$

$$X_0 = \frac{D_m}{4\sin\theta}\left[1 - \left(\frac{D_1}{D_m}\right)^2\right] = 0.11\text{ in.}$$

In these computations the elementary theory was corrected to take into account the fact that the valve stem emerges through the metering orifice.

The regulator equations are thus

$$r = p - 0.005\,s - \frac{4.8\,q}{\sqrt{(1 + s)^2 - (1 + r)^2}}$$

$$q = x\sqrt{(1 + s)^2 - (1 + r)^2}$$

These are plotted in Fig. 5 for two adjustments, $p = 74.8$ and $p = 14.8$, values corresponding to the usual range of use. The physical values also are indicated. These are computed from

$$P_{rg} = 14.7\,r,\text{ psi}$$
$$P_{sg} = 14.7\,s,\text{ psi}$$
$$Q_0 = 0.30\,q,\text{ cfm}$$

The effect of utilizing the probably more exact metering resistance relationship of Equations [41] and [42] which leads to

$$r = p - 0.005\,s - \frac{4.8\,q}{\sqrt{(1 + s)^2 - (1 + r)^2 - q^2}}$$

is also shown in Fig. 5 as the "real characteristic."

An experiment performed on a regulator of this kind and tested at the supply pressures and settings shown in Fig. 5 resulted in data which agreed with the "real" characteristics shown in the figure to within the experimental errors, except in the low flow-leakage region.
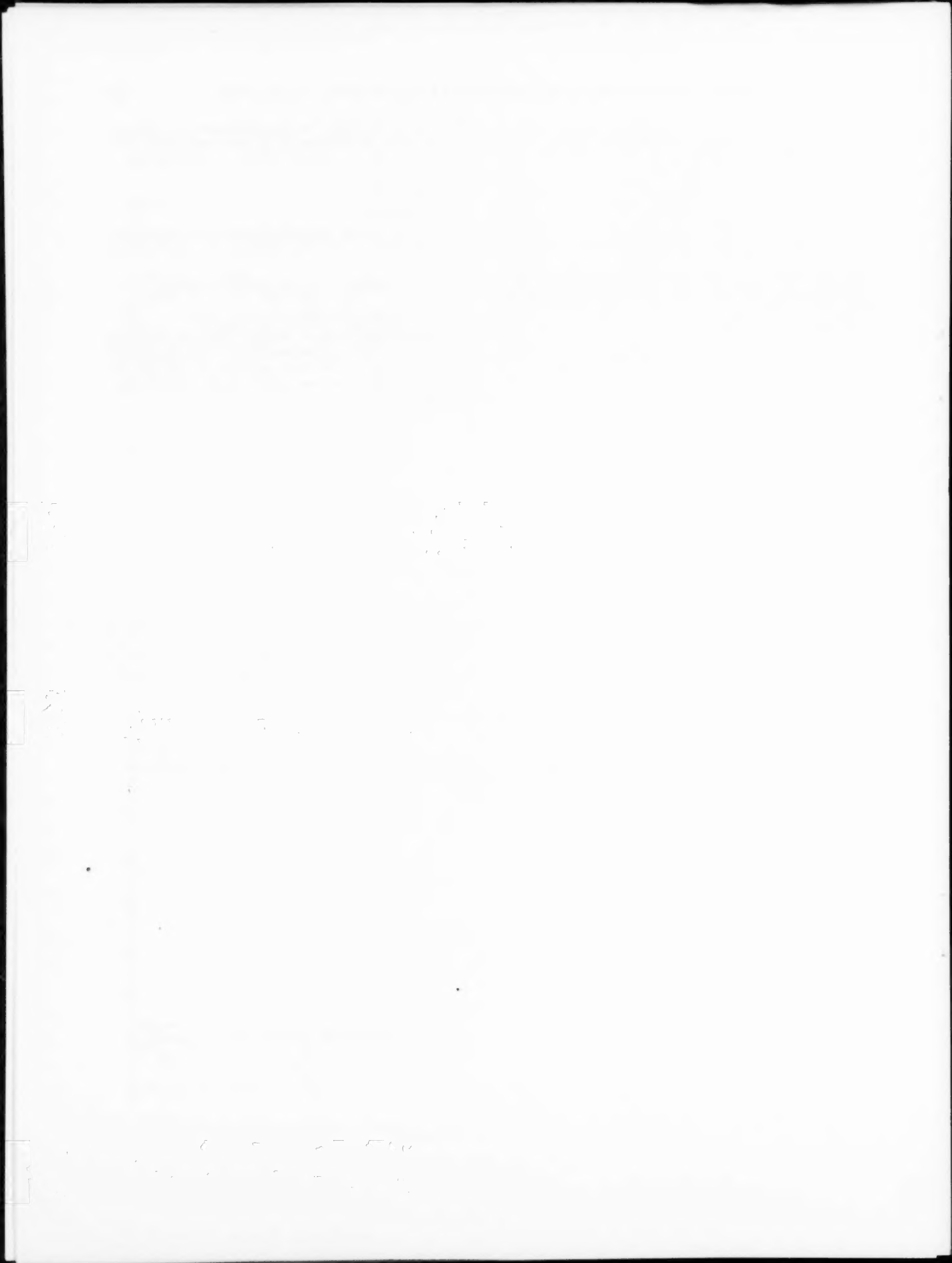
Properties of Residual Petroleum Fuels

By W. SACKS,[1] MONTREAL, QUEBEC, CANADA

Although fuels derived from petroleum process residues have been used extensively for many years, considerable confusion still exists as to their characteristics. As essentially cheap by-product fuels, they have not received a great deal of attention in the past. In recent years their use in gas turbines and diesel engines has emphasized the need for a better understanding of their properties and behavior in combustion chambers. It is the aim of the present paper to bring together the published information on the nature of residual petroleum fuels, widely scattered in petroleum and engineering journals. It will be seen that these fuels generally exhibit a more complex behavior in comparison with heavy-distillate fuels.

SOURCES OF RESIDUAL FUELS

THE principal sources of residua that form the basis of residual petroleum fuels are the crude-oil distillation towers operating at atmospheric or reduced pressure, and the fractionating towers after thermal or catalytic cracking. Catalytic processes yield considerably smaller amounts of residual fuel than do thermal processes, and coking operations may be used to bring about a further reduction of yield (1).[2] Frequently the residua in a given fuel are obtained from more than one crude oil and straight-run or cracked heavy distillates may be added to reduce their viscosity.

Three types of residual fuel may be distinguished as follows:

1 Fuels containing only straight-run residua.
2 Fuels containing only cracked residua.
3 Fuels containing both straight-run and cracked residua.

Type 1 is probably least common, but it may be noted that the amount of cracked residuum from catalytic fractionating towers is small so that fuels from this process may be considered as approximating the straight-run type.

COLLOIDAL NATURE OF RESIDUAL FUELS

The properties of residual fuels probably can be best interpreted if these fuels are regarded as colloidal dispersions of high-molecular-weight substances in an oil medium. The high-molecular-weight constituents are brown-black to black solids at room temperature and are found in other organic substances which comprise the asphaltic bitumen colloids (34).

These dispersed solids can be separated from the oils by the use of common solvents. The major portion, insoluble in light paraffins such as pentane, form the "asphaltene" group. The asphaltenes can be dissolved by aromatic solvents and by carbon tetrachloride. The remaining portion of these solids can be grouped into two classes, the "carbenes," soluble in benzene but insoluble in carbon tetrachloride, and the "carboids," which are insoluble in both benzene and carbon tetrachloride (35).

These solids probably represent thermal decomposition intermediates between aromatic hydrocarbons and coke (39)

aromatics → asphaltenes → carbenes → carboids → coke

The molecular size probably increases in this order and accounts for the differing behavior toward solvents.

Straight-run residua do not contain any appreciable amounts of carbenes or carboids (21) but may contain considerable amounts of asphaltenes. Cracked residua are distinguished by their content of carbenes and carboids and this property may be used in the analysis of residua. Thus Batchelder and Wellman (5) have proposed the use of the cyclohexane insolubles less the benzene insolubles (a measure of the carboid content) for the estimation of the cracked-residuum content of fuels.

Chemically, the asphaltenes (12), and very likely the carbenes and carboids as well, are polycyclic in structure and are stabilized in the oil medium by structurally similar lower-molecular-weight compounds of the medium. Aromatic hydrocarbons have the highest peptizing power, naphthenic hydrocarbons somewhat less, while paraffin hydrocarbons have little ability in this respect (36). Since the stabilizing or peptizing action of the medium is an equilibrium process, changes in both the nature and quantity of medium present may alter the amount of solids which are dispersed by it.

In blending residual fuels it is important to prevent the precipitation of the solids. Generally, both straight-run and cracked residua contain considerable amounts of peptizing hydrocarbons and the solids are readily dispersed. When distillate fractions are added to the residua, a portion of these solids may precipitate. If only dispersed asphaltenes are present (straight-run residua) the precipitating ability of a petroleum fraction can be related to the surface tension (33, 37) and, in general, only those fractions with a surface tension below about 24 dynes/cm (25 C) will precipitate asphaltenes. There is an approximate relationship between the surface tension and the viscosity of petroleum
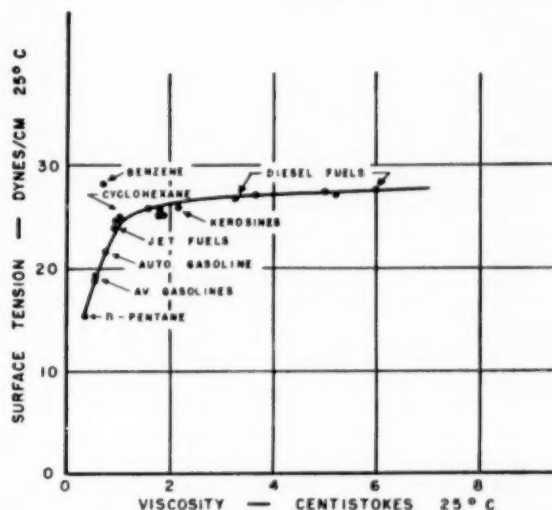

FIG. 1 VISCOSITY–SURFACE TENSION RELATION FOR PETROLEUM FUELS

fractions as shown in Fig. 1. It will be seen that kerosenes and higher-viscosity fractions can be blended with straight-run residua without asphaltene precipitation.

With cracked residua the carbenes and carboids are more difficult to peptize and blending distillates should contain a high proportion of aromatic hydrocarbons; i.e., only cracked distillates should be used. As blending aids, the "xylene equivalent" (8, 10), or the cyclohexane insolubles less benzene insolubles, may be used to characterize a given residuum, and the aniline point to characterize the distillate (4).

LABORATORY EVALUATION OF STABILITY AND COMPATIBILITY

After blending, the fuel may be tested for stability in storage and in preheaters and for compatibility with similar fuels. The substances in the fuel that may yield deposits or "sludge" are the unpeptized organic solids and inorganic compounds such as silica and salts suspended in the fuel. Deposits of this type have been designated as "dry-sludge" as distinguished from sludges that are water-emulsions (50).

The content of suspended solids in the fuel may be evaluated by a number of methods. Hot filtration of the fuel through asbestos filters (8, 23) or filter paper (50) may be used. Broom (8) found some correlation between his filtration test and sedimentation during storage while van Kerkvoort and Nieustad (50) report good correlation between their method and the amount of water-free sludge obtained in large-scale hot-centrifuging.

There is some objection to hot filtration since the filter may absorb constituents of the oil medium. An alternative method (51) uses a dilution curve for the fuel (the amount of precipitate obtained with varying amounts of a gasoline fraction) extrapolated to zero dilution. However, this method is difficult to apply to routine work. Good correlation with sedimentation in storage has been reported with a "supercentrifuge" test (19).

The more common "water and sediment" (ASTM D96-50T) and "sediment by extraction" (ASTM D473-48) tests employ benzene which may alter the amount of undispersed solids originally present in the fuel and give only a rough indication of deposition during storage.

Heat and oxidation may increase the amount of undispersed solids yielding heater deposits. Several thermal-stability tests have been devised which simulate preheating practice. Batchelder (4) determined the amount of benzene insoluble deposit on a heater tube as a measure of the thermal stability of the fuel. In the Naval Boiler and Turbine Laboratory Test (NBTL) (44) deposits on a heater tube are evaluated visually and the fuel is rated as "stable," "borderline," or "unstable." The equipment for these heater tests is not readily available. Good reproducibility has been reported for the NBTL method (8).

The hot filtration test (filter paper), before and after the fuel is heated, has been used to determine the thermal behavior of residual fuels. Good agreement with the NBTL test has been reported although the results of a limited number of tests are given (50).

Compatibility of blending components or of different fuels may be evaluated by the filtration tests or by the heater tests just described. Martin (31) has reviewed the problem of stability and compatibility recently. He considers that thermally unstable fuels are rare at present and that incompatibility is steadily being overcome by modern refinery processes (catalytic cracking).

RESIDUAL FUEL-WATER EMULSIONS

Stable emulsions are produced frequently when residual fuels are agitated with water. Emulsion formation may be particularly troublesome on ships because of sea-water contamination of the fuel. These emulsions have been shown to be of the water-in-oil type (43). A number of methods of breaking them have

been investigated and some success has been achieved using surface-active agents (43, 28).

Little is known about the fuel characteristics which govern the stability of these emulsions but there is some evidence that the nitrogen content of the fuel may be important in this respect (6).

FLOW PROPERTIES OF RESIDUAL FUELS

The dependence of viscosity on the volume concentration of the dispersed phase is characteristic of colloidal solutions. If a series of fuels are treated with a paraffin solvent such as n-pentane using a fixed ratio of solvent to fuel, the precipitation obtained (asphaltenes, carbenes, carboids, as well as suspended solids) can be taken as a measure of the dispersed-solid content of the fuels. In Fig. 2 the "n-pentane solids" content for a number of different types of residual fuel is plotted against the kinematic viscosity at 100 F. The general increase in viscosity with increasing amounts of dispersed solids is evident.
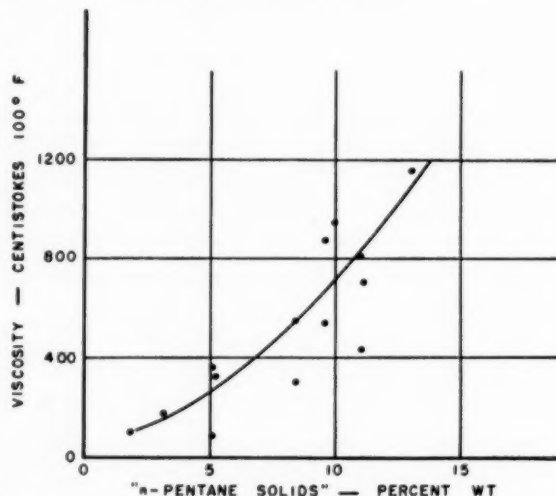
FIG. 2 VISCOSITY AND "PENTANE SOLIDS" CONTENT OF RESIDUAL FUELS

At low temperatures wax fractions of the medium may separate from solution and the viscosity depends not only on temperature but on the temperature to which the fuel has been heated before cooling (26). According to Moerbeek and van Beest (32), this behavior is caused by asphaltenes which prevent the formation of a wax-crystal network and perhaps inhibit crystallization to some extent.

Because of this property, laboratory flow tests can give only an approximate indication of the flow characteristics that may be encountered in practice. If the preheating temperature before cooling is defined, it is possible to obtain reproducible results in laboratory tests. In the "pour-point" method (gravity flow ASTM D97-47) two different preheating temperatures are specified for residual fuels and the results are reported as the "upper" and "lower" pour points. The difference between these values may be considerable and the upper pour-point temperature is not necessarily a maximum for the fuel.

A number of other methods of determining "flow-limit" temperatures for residual fuels have been devised (26, 32, 52, 46). These generally apply a small fixed pressure to the fuel in a tube. The "cold test" (32) is reported to give a good indication of the behavior to be expected in practice.

Asbach and Tegethoff (2) have proposed a "pumpability"

test. This determines the fuel temperature at which there is a break in the pressure-temperature curve, indicating a limit for normal pumping.

BEHAVIOR OF RESIDUAL FUELS IN COMBUSTION CHAMBERS

Much progress has been made in recent years in understanding the mechanism of fuel-droplet combustion. The process may be regarded as evaporation from the droplet surface followed by combustion of the vapors at a flame front surrounding the droplet. The burning rate depends on the heats of combustion and vaporization of the fuel rather than fuel-vapor pressure (18).

Residual fuels, however, contain a considerable portion of high-molecular-weight, nonvolatile constituents. Laboratory residue tests such as the Conradson (ASTM D189-46) and the Ramsbottom (ASTM D524-51T) procedures are essentially fuel evaporations. Consequently the residues in these tests should be functions of the solids in the fuel. This is shown in Fig. 3 where the Ramsbottom residues are plotted against the n-pentane solids content for a wide range of residual fuels.

FIG. 3 RELATION BETWEEN RAMSBOTTOM RESIDUE AND PENTANE SOLIDS

Experiments have shown that residual-fuel droplets yield cokelike residues on combustion (29, 48). The combustion rate of these residues is determined by oxygen diffusion to the residue surface, a much slower process (29, 45) than combustion of fuel vapors. This factor is important in combustion-chamber design, particularly in the gas turbine, since more residence time must be allowed and flame lengths tend to be greater than with distillate fuels.

METALLIC CONSTITUENTS

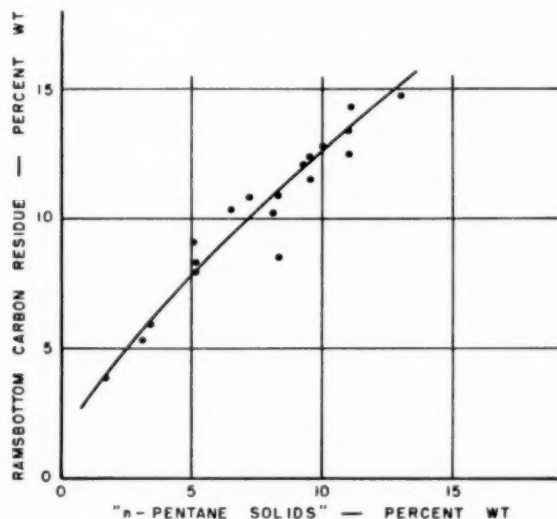The major portion of the ash-forming constituents in residual fuels are generally vanadium, sodium, iron, and nickel compounds. Considerable amounts of calcium and aluminum compounds are often present as well as relatively small amounts of many other metallic compounds (47).

Vanadium, nickel, and iron have been shown to exist as porphyrin complexes (nitrogen compounds related to chlorophyll) dissolved in many crude oils (49, 17, 42), a discovery of great importance in connection with the origin of petroleum. The changes that take place in these substances in refinery processes are not known at present but they are unusually stable com-

pounds and probably are not degraded to compounds no longer soluble in the oil.

Vanadium occurs in relatively high concentration in fuels from Venezuelan, Arabian, and certain United States crude oils. A high vanadium content is generally associated with a high sulphur content. Fig. 4 shows the vanadium-sulphur relationship for a number of fuels from Canadian refineries while recent data on United States fuels (25) support this relationship.
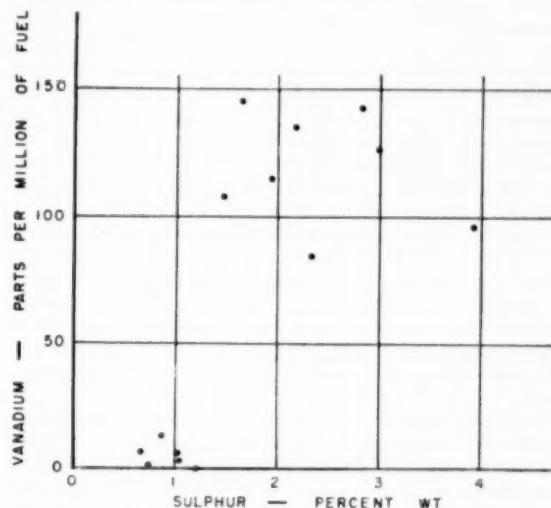
FIG. 4 ASSOCIATION OF VANADIUM WITH SULPHUR IN RESIDUAL FUELS

The formation of sulphur trioxide from sulphur dioxide on combustion is of considerable importance because of acid corrosion by exhaust gases. Vanadium oxide is an efficient industrial catalyst for the reaction and it has been suggested that this catalysis also occurs in burning residual fuels (13, 3). There is evidence (47) that this process does occur to some extent but other mechanisms may be more important. Corbett (11) found no relation between sulphur-trioxide formation in a boiler and the sulphur or vanadium content of the fuel.

Physical methods such as centrifuging and filtering have no appreciable effect on the vanadium compounds of the fuel. Vanadium can be removed by coprecipitation with the asphaltenes using solvents (40). According to a recent patent (38) asphaltenes in residual fuels also may be removed by heating with compounds such as antimony trichloride. However, economic considerations limit the application of such processes and the removal of asphaltenes has an undesirable effect on the pour point of many fuels.

The other metallic compounds probably are present mainly as salts suspended in the fuel. Of this group the sodium salts are most important and in fuels are found largely as the sulphate and the chloride (42). These suspended compounds can be removed by filtration or centrifuging (42, 13, 24). According to Lamb (27) the successful use of residual fuels in marine diesel engines depends to a large degree on removing this group since they are responsible for serious cylinder wear.

ASH DEPOSITION AND ASH CORROSION

Usually no attempt has been made to remove these metallic constituents and serious difficulties have been encountered with ash deposition and ash corrosion in both boilers and gas-turbine plants. In the gas turbine in particular, ash problems have be-

come the major obstacle in development. These problems have been attributed mainly to sodium and vanadium compounds, which yield low-melting ash components.

Little is known of the compounds that may be formed in petroleum ash. The usual chemical methods of analysis generally report the metallic compounds as oxides or sulphates. More complex physical methods (x-ray diffraction) are required to identify the actual compounds present in the ash. A complex sodium vanadate has been reported (3). Sodium and vanadium compounds which may be present have been considered by Lloyd (29).

The published results of laboratory and plant observations frequently have been conflicting. This is not surprising since operating conditions, temperature, the nature of the gas atmosphere, and construction materials would be expected to be important factors. In addition, the concentrations of vanadium and sodium in fuels may vary over a wide range and deposits at different points in a system may not be identical (29, 9).

The problems of ash deposition and ash corrosion that have been encountered in naval and industrial boilers have been discussed by Tibbetts, Wood, Douglass, and Estcourt at a recent symposium (47). Sodium and vanadium compounds were considered to be the source of most of the difficulties. Most promising solutions were felt to lie in design to avoid flame impingement on metal surfaces, in the control of other combustion conditions, and in the use of additives.

A number of papers on ash-deposition problems in gas-turbine engines have appeared in the past several years (3, 29, 22). Again, the main difficulties have been attributed to sodium and vanadium compounds. Laboratory-deposition experiments have shown that the amount of deposition depends not only on the total concentrations of sodium and vanadium in the fuel but on the sodium/vanadium ratio (42). Further, both the amount and composition of deposits have been found to depend on temperature (3).

The accelerated corrosion of steels in contact with residual fuel ashes (41, 14, 3, 16), sodium sulphate (47), and vanadium pentoxide (41, 15) has been the subject of a number of recent investigations, and the effect of variation of ash composition, nature of the alloy (3), temperature and gas atmosphere has been studied.

There is some evidence that ash-deposition and corrosion effects may be reduced by blanketing the ash particles with sufficient carbon (3, 30, 7). This probably will require very careful control of combustion conditions (droplet size, mixing) and may not be practical in many cases. The oxides of calcium, aluminum, titanium, iron, and other metals have been found to retard corrosion in laboratory tests and probably act by preventing the formation of molten ashes (47, 14). The problem of introducing metallic additives is not a simple one if good contact with the ash particles is to be maintained, without the use of large amounts of these substances. If introduced as inorganic compounds in suspension in the fuel, difficulties in handling and wear of atomizer and pump parts would be likely. If introduced by separate means directly to the flame, contact with the ash is not likely to be satisfactory. The alternative of using more expensive metallo-organic compounds in solution in the fuel may offset much of the economic advantage gained in using residual fuels.

Variation in Residual-Fuel Properties—Specifications

Residual-fuel specifications for general use such as those for Nos. 5 and 6 fuel oils (Canada and United States) usually limit only such properties as viscosity, flash point, and water and sediment in No. 6 fuels and ash, and sometimes sulphur in the No. 5 grade. Several compilations of data on U. S. No. 6 fuels have been published recently (20, 25). These are compared with the

variation found in the author's laboratory for representative fuels from Canadian refineries in Table 1. It will be seen that the extent of variation is generally similar in each case.

TABLE 1   VARIATION IN PROPERTIES OF NO. 6 RESIDUAL FUELS

Property	Canadian fuels	Data by Kottcamp and Crockett (25)	Data by Heath and Albat (20)
Specific gravity (60 F)...	0.945-1.046	0.959-0.990	0.92-1.02
Flash point PM (F)......	175-300	150-285	160-410
Viscosity, centistokes:			
100 F...............	201-1150	...	260-750
122 F...............	105-420	140-400	85-650
210 F...............	14.5-34.5	...	...
Pour point (F).........	+10-+65	0-+50	+15-+85
Water and sediment, per cent...............	...	0.02-0.50	0.05-2.0
Water by distillation, per cent...............	Nil-0.2	Trace-0.2	...
Sediment by extension, per cent...............	0.01-0.29	0.04-0.10	...
Carbon residue, per cent..	5.86-14.3 (R)	7.27-13.7 b	5-13 b
Ash, per cent...........	0.01-0.12	0.0041-0.086	0.01-0.50
Sulphur, per cent........	0.67-3.00	0.75-3.61	0.7-3.0
Heat of combustion, gross Btu/lb...............	...	18,200-18,740	18,329-18,993
n-pentane solids, per cent..	3.5-13	...	...
Vanadium, ppm.........	Nil-146	2-144	...
Vanadium, per cent ash[a]..	...	0.8-62.8	...
Sodium ppm (24)........	1.6-290	...	...
Ash fusion temp (F)......	...	1085-1330	...

[a] Tibbetts (47) gives nil-63.9 per cent.
[b] Method not stated.

Specifications for use in naval boilers are more restrictive and in addition to the properties listed in the foregoing, may limit pour point, specific gravity, and carbon residue, and may require thermal stability and compatibility tests.

No specifications for gas-turbine residual fuel have been published as yet. Much research is in progress and a good deal more operating experience is required. These specifications probably will resemble those for naval fuel with additional restrictions on vanadium and sodium contents.

BIBLIOGRAPHY

1 "Control of the Production of Residual Fuel Oil," by G. Armistead, Oil and Gas Journal, vol. 48, 1949, pp. 57–58, 73–75.

2 "Determination of the Pumpability of Fuel Oils," by H. R. Asbach and J. Tegethoff, Brennstoff-Chemie, vol. 24, 1943, p. 67.

3 "The Gas Turbine and Its Fuels," by E. L. Bass, I. Lubbock, and C. G. Williams, Shell Aviation News, No. 156, June, 1951.

4 "The Stability of Residual Fuels," by A. H. Batchelder, Refiner, vol. 15, 1936, pp. 485–492.

5 "Identification and Properties of Straight-Run and Cracked Residua," by A. H. Batchelder and H. B. Wellman, Refiner, vol. 17, 1938, pp. 280–282, 312.

6 "Fuel Oil Research at the Naval Research Laboratory," by P. Borgström, R. D. Norton, and O. I. Lewis, Journal of the American Society of Naval Engineers, vol. 46, 1934, pp. 173–185.

7 "Problem of Burning Residual Oils," by A. T. Bowden, Oil Engine and Gas Turbine, vol. 18, 1950, p. 234.

8 "Stability of Fuel Oil," by W. E. J. Broom, Journal of the Institute of Petroleum, vol. 31, 1945, pp. 347–352.

9 "Gas Turbines," by B. O. Buckland, Petroleum Engineer, vol. 22, 1950, pp. C-37–C-42.

10 "The Stability of Fuel Oil-Gas Oil Blends," by D. G. Butlin, Journal of the Institute of Petroleum, vol. 36, 1950, pp. 43–55.

11 "The Deleterious Effects of Sulphur in Fuels," by P. F. Corbett, British Coal Utilization Research Association, vol. 15, 1951, pp. 169–181.

12 "The Colloidal Structure of Asphalt," by H. Eilers, Journal of the Physical and Colloid Chemistry, vol. 53, 1949, pp. 1195–1211.

13 "Erosion and Corrosion Damage Through Use of Heavy Heating Oils As Fuels for Engines, Boilers and Gas Turbines," by B. Engel, Erdöl und Kohle, vol. 3, 1950, pp. 321–327.

14 "Oil Ash Corrosion of Metals at Elevated Temperature," by C. G. Evans, paper at Symposium on Corrosion and Erosion of Gas Turbine Materials, ASTM meeting, June, 1950.

15 "Metals and Alloys Containing Vanadium or Exposed to Vanadium Oxide Are Subject to Rapid Oxidation," by M. G. Fontana, Industrial and Engineering Chemistry, vol. 42, 1950, pp. 66–66A.

16 "Surface Corrosion of Heat-Resisting Materials Under Action of Bunker Oil Ashes Containing Sodium, Sulphur and Vanadium," by F. Gallmann, J. Friedly, and W. Epprecht, *Petroleum Times*, vol. 55, 1951, p. 713.

17 "Spectra of Porphyrins in Petroleums and Bitumen," by A. Glebovskaya and M. V. Volkenshtein, *Journal of General Chemistry* (USSR), vol. 18, 1948, pp. 1440–1451.

18 "The Combustion of Droplets in a Fuel Spray," by G. A. E. Godsave, *Nature*, vol. 164, 1949, p. 708.

19 "The Tendency of Cracked Fuel Oils to Form Deposits in Fuel Oil Heaters," by R. R. Gurley and J. G. O'Neill, *Journal of the American Society of Naval Engineers*, vol. 46, 1934, pp. 186–198.

20 "Properties and Characteristics of Fuel Oils for Industrial Gas-Turbine Usage," by D. P. Heath and E. Albat, Trans. ASME, vol. 72, 1950, pp. 331–340.

21 "An Analytical Method Used in the Study of the Composition of Asphalts and Cracked Fuels," by E. S. Hillman and B. Barnett, *Refiner*, vol. 18, 1939, pp. 533–538.

22 "Some Considerations Dealing With the Formation of Deposits in Gas Turbine Plants," by D. F. Hughes and R. G. Voysey, *Journal of the Institute of Fuel*, vol. 22, 1949, pp. 197–201.

23 "Determining the Sediment Content of Fuel Oil," by S. H. Hulse and H. L. Thwaites, *Industrial and Engineering Chemistry*, Analytical Edition, vol. 10, 1938, pp. 678–680.

24 "Unpublished Report," by F. G. Kitson, National Research Council of Canada, No. MP-8, December, 1951.

25 "Some Aspects of the Application of Residual Oils As Fuel for the Gas Turbine," by C. F. Kottcamp and L. O. Crockett, ASME Paper No. 50—A-131.

26 "The Temperature Sensitivity of Viscous Oils," by D. J. W. Kreulen, *Journal of the Institute of Petroleum*, vol. 24, 1938, pp. 441–452.

27 "The Burning of Boiler Fuels in Marine Diesel Engines," by J. Lamb, Trans. of the Institute of Marine Engineers, vol. 60, February, 1948, pp. 1–25.

28 "Emulsions of Sea-Water in Admiralty Fuel Oil With Special Reference to Their Demulsification," by A. S. C. Lawrence and W. Killner, *Journal of the Institute of Petroleum*, vol. 34, 1948, pp. 821–856.

29 "The Problem of Burning Residual Oils in Gas Turbines," by P. Lloyd and R. P. Probert, Proceedings of The Institution of Mechanical Engineers, vol. 163, 1950, pp. 206–220.

30 "Discussion at a Symposium on Combustion Reactions in Relation to Gas Turbine Practice," by J. J. Macfarlane, *Journal of the Institute of Petroleum*, vol. 37, 1951, pp. 573, 575.

31 "The Stability and Compatibility of Fuel Oils," by C. W. G. Martin, *Petroleum Times*, vol. 55, 1951, p. 428.

32 "Cold Test for Fuels," by B. H. Moerbeek and A. C. van Beest, *Journal of the Institute of Petroleum*, vol. 21, 1935, pp. 155–168.

33 "The Surface Tension Rule for Asphaltic Bitumen," by F. J. Nellensteyn and M. Baart, *Journal of the Institute of Petroleum*, vol. 35, 1949, pp. 302–305.

34 "The Properties of Asphaltic Bitumen," by J. P. Pfeiffer, Elsevier Publishing Company, Inc., New York, N. Y., 1950, pp. 1–9.

35 "The Properties of Asphaltic Bitumen," by J. P. Pfeiffer, ibid., p. 15.

36 Ibid, p. 43.

37 Ibid, pp. 28–29.

38 "Refining Residual Fuels," by G. H. Reman, U. S. Patent No. 2,493,596 to Shell Development Company, January, 1950.

39 "Conversion of Petroleum," by A. N. Sachanen, Reinhold Publishing Corporation, New York, N. Y., 1940, pp. 124–134.

40 "Reduction of the Vanadium Content of Residual Petroleum Fuels by Solvent Precipitation," by W. Sacks, *Canadian Journal of Technology*, vol. 29, 1951, pp. 492–495.

41 "Attack on Heat Resistant Steels of Vanadium-Containing Oil Ashes," by P. Schapfer, P. Amgwerd, and H. Preis, *Schweizer Archiv für Wissenschaftliche Technische*, vol. 15, 1949, pp. 291–299.

42 "Fuels for Aviation and Industrial Gas Turbines," by M. O. Scott, R. Stansfield, and T. Tait, *Journal of the Institute of Petroleum*, vol. 37, 1951, pp. 487–509.

43 "The Formation and Properties of Emulsions of Oil Fuel and Water," by H. J. Sharp and J. F. R. Ince, *Engineering*, vol. 167, 1949, pp. 361–364.

44 "Blending Residual Fuel Oil," by F. L. Smith, *Refiner*, vol. 24, 1945, pp. 135–138.

45 "The Combustion of Fuel Particles," by D. B. Spalding, *Fuel*, vol. 30, 1951, pp. 121–130.

46 "Standard Methods for Testing Petroleum and Its Products," Institute of Petroleum, London, England, 1949, pp. 399–402.

47 "Problems Encountered in Burning Heavy Fuel Oil As Related to Attack of Metals at High and Low Temperatures and the Fouling of Tube Banks," by E. F. Tibbetts, O. L. Wood, D. Douglass, and V. F. Estcourt, ASME Paper No. 50—A-136.

48 "An Experimental Study of the Evaporation and Combustion of Falling Droplets," by J. E. C. Topps, *Journal of the Institute of Petroleum*, vol. 37, 1951, pp. 535–553.

49 "Chlorophyll and Hemin Derivatives in Organic Minerals," by A. Treibs, *Zeitschrift für angewandte Chemie*, vol. 49, 1936, pp. 682–686.

50 "Determination of Dry-Sludge Content of Fuel Oils; Development of the Shell Hot Filtration Test," by W. J. van Kerkvoort and A. J. J. Nieustad, *Journal of the Institute of Petroleum*, vol. 37, 1951, pp. 596–604.

51 "Sludge and Sludge Formation in Cracked Residues," by J. Voskuil and I. Robu, *Journal of the Institute of Petroleum*, vol. 24, 1938, pp. 181–206.

52 "The Science of Petroleum," by P. Woog, Oxford University Press, New York, N. Y., vol. 2, 1938, pp. 1118–1124.
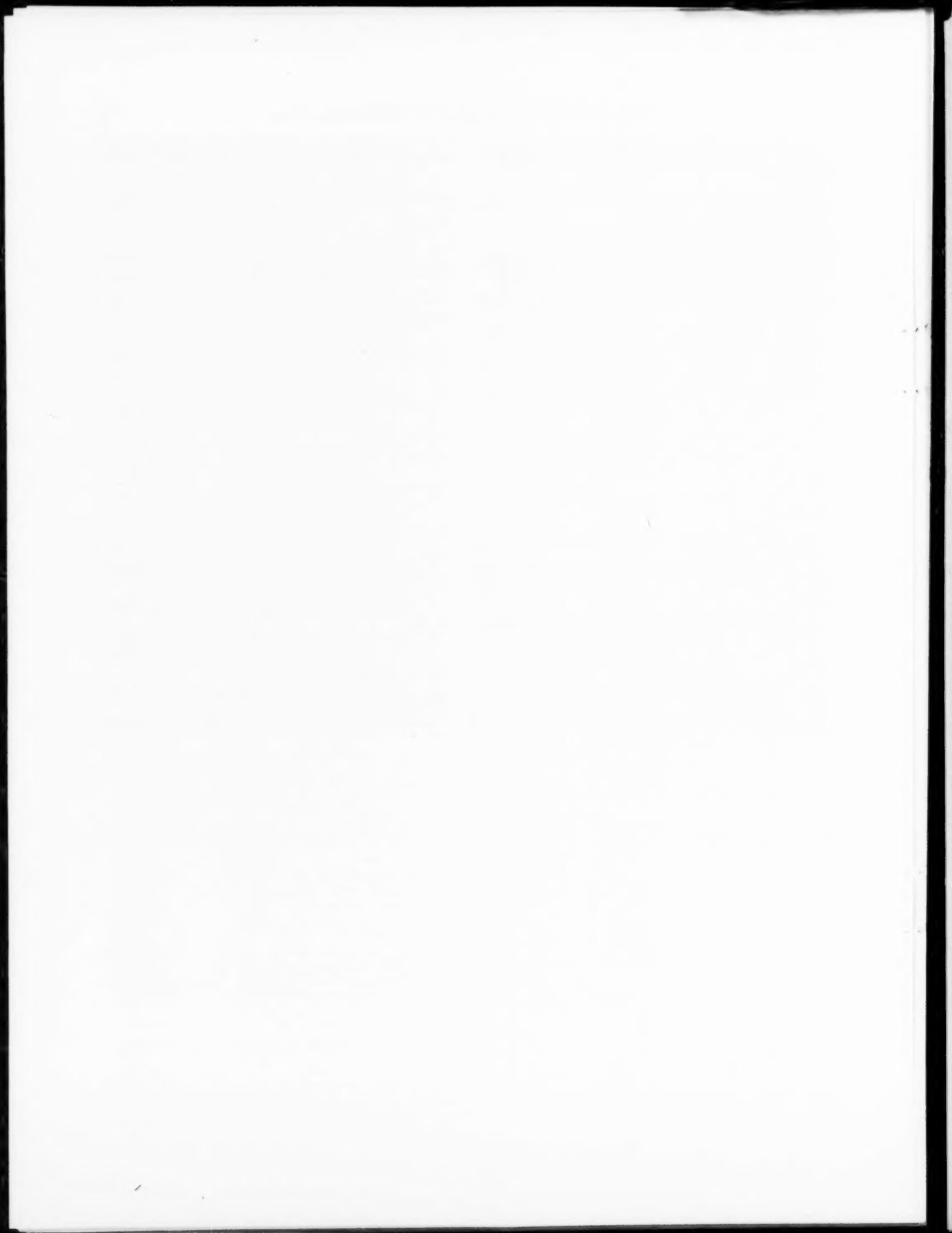
Mechanical Aspect of Seizing in Metal Wear

By HARRY CZYZEWSKI,[1] PORTLAND, ORE.

Alloys of the class called "self-lubricated" alloys have a resistance to "accelerated mechanical abrasion" which it has not been possible to duplicate by external lubrication. Alloys in this class include gray cast iron (graphite lubricant), oil-impregnated powder-metal compositions (oil lubricant) and leaded copper-base and iron-base alloys (lead lubricant). It is the purpose of this paper to present the mechanical aspect of seizing in metal wear which accounts in a qualitative manner for the observed phenomena in accelerated mechanical abrasion. The mechanical analysis also explains the failure of externally lubricated alloys to equal the performance of self-lubricated alloys.

MECHANICAL ABRASION

WHEN a particle abrades a surface, there is a definite relationship between the dimensions of the abrading particle and the track, or furrow, left on the abraded surface. The mechanical abrasion may be classified in two general categories, (a) normal, (b) accelerated. In normal mechanical abrasion, the track left by the abrader has a profile the same (except for elastic recovery) as the profile of the contacting part of the abrader. There is little difference in response to normal mechanical abrasion between self-lubricated and homogeneous (externally lubricated) alloys. An example of normal mechanical abrasion on steel is shown in Fig. 1; the abrading medium in this case was metallographic emery paper of 1-0 grade. In accelerated mechanical abrasion, the track left by the abrader has a larger profile than the profile of the contacting part of the abrader.

For the purpose of this paper, "seizing" is defined as the state in which the relative motion of the opposing metal parts is stopped, because the track (or tracks) increases in profile to the extent that further propagation of the track requires more translational energy than is available in the system. An example of incipient seizing of a steel bushing is given in Fig. 2. "Galling" may be defined as arrested seizing; i.e., the increased track profile becomes constant or decreases with continued propagation of the track. An example of galling of a steel shaft is shown in Fig. 3 in which the track decreases in width, then remains constant for a short distance before disappearing rapidly as the contact pressure is reduced.

Self-lubricated alloys vary markedly from homogeneous alloys, having less tendency to seize and suffering less damage when galling does take place. For example, gray cast iron (which is sometimes referred to as steel plus graphite) may show a pattern such as that in Fig. 4, when galling occurs. The extent of damage from the galling of cast iron is restricted sharply compared to the damage to steel. The superiority of self-lubricated alloys for this purpose generally has been attributed to the phenomenon of lubrication. However, most efforts by external lubrication fail to duplicate the resistance of the self-lubricated alloys to the incipience of galling, and especially the decreased damage from galling.

FIG. 1 EXAMPLE OF NORMAL MECHANICAL ABRASION OF STEEL BY EMERY PAPER; ×150

FIG. 2 EXAMPLE OF INCIPIENT ACCELERATED MECHANICAL ABRASION OF STEEL BUSHING

(Increase in profile of paths of abrading particles is evident in lower part of bushing; ×3.)

MECHANICAL ASPECT OF SEIZING

When seizing is initiated in metal-to-metal wear, it is evident that a change has occurred from normal to accelerated mechanical
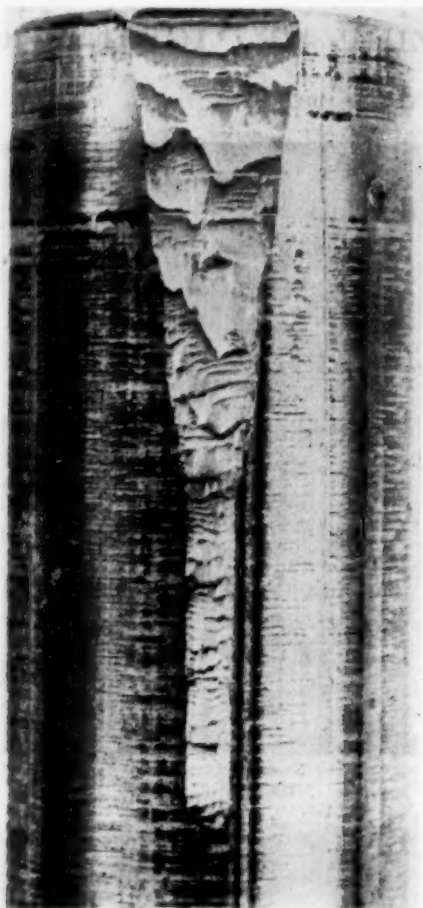
FIG. 3   EXAMPLE OF GALLING OF STEEL SHAFT IN WHICH TRACK
WIDTH DECREASES, THEN BECOMES CONSTANT FOR SHORT DISTANCE
(Galled portion terminated when contact pressure was removed in that
area; ×3.)

FIG. 4   EXAMPLE OF ACCELERATED MECHANICAL ABRASION OR
GALLING IN GRAY CAST IRON SHOWING THAT ABRASION TRACKS
RETAIN A COMPARATIVE NARROW WIDTH AND DEPTH: ×50
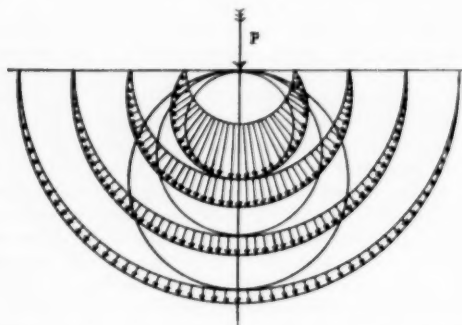
FIG. 5   DISTRIBUTION OF PRINCIPAL STRESSES FOR POINT CONTACT
ON PLANE IN ELASTIC DEFORMATION OF HOMOGENEOUS ISOTROPIC
MEDIUM
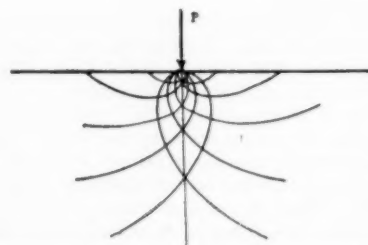
FIG. 6   SCHEMATIC DIAGRAM OF THEORETICAL SHEARING-STRESS
TRAJECTORIES FOR CONDITION OF POINT PRESSURE ON PLANE

abrasion. This change may be analyzed qualitatively in terms
of stress distribution at the point of contact being considered.

The stress distribution for a point contact on a plane for the
elastic case of a homogeneous isotropic medium is well known.
The distribution of principal stresses is shown in Fig. 5. The
shearing-stress trajectories are shown in Fig. 6. The shearing
stress is equal to

$$\tau_{xy} = \frac{-2P \sin \theta \cos^2 \theta}{\pi y} = \frac{-2Pxy^2}{\pi(x^2 + y^2)^2}$$

where P is the normal force on the surface and acts along the
y-axis, and x and y are the co-ordinates of the point at which
τ_{xy} is being determined.   The point of contact is at the origin of
the rectangular-co-ordinate system.

In the metal-to-metal wear being considered, the metal parts
are in relative motion; thus the effect of a translational force
component on the contact-pressure distribution must be evalu-
ated.   In effect, the translational force component causes higher
shear stresses on the side of the point of contact opposite the
translational force.   Also, in metal-to-metal wear the contacting
asperities (high spots) do not make point contacts but actually
make contact over a certain area. Such a case can be treated

crudely as a problem of point contact, in which the resultant of
the normal force and the translational force is considered as the
new point force.

Then too, in the case of metal-to-metal wear, plastic deforma-
tion occurs. However, the stress distribution for plastic defor-

mation may be considered similar to that for elastic deformation, since the metals used industrially in metal-to-metal wear applications are generally of the cubic-crystal systems, which have available many slip planes for plastic flow. Thus, as a first approximation, the elastic modulus may be replaced by the work-hardening modulus in quantitative studies.

Normal mechanical abrasion may be interpreted as in Fig. 7 in which two surfaces are shown schematically with a contact between asperities (high spots) on opposing surfaces. The effect of the upper asperity on the lower asperity at the point of contact O, is indicated by the two force components, i.e., the normal force component P and the translational force component F. In this case the normal force P is comparatively low, and the resultant R of these two forces is at a low acute angle to the surface (x-axis). Since R is comparatively small, the shearing stresses will be small. In addition, the low ac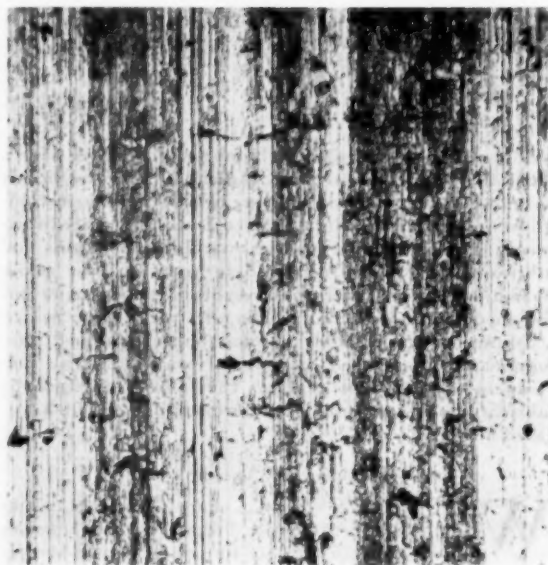ute angle at which R acts will cause a deflection of the shearing-stress trajectories in the direction of the x-axis. There is, also, a large strain component perpendicular to the xy-plane in Fig. 7. The net result is that the metal of the lower asperity will tend to flow around the upper asperity, i.e., perpendicular to the xy-plane. The ideal case of normal mechanical abrasion would occur if the upper asperity were completely rigid.
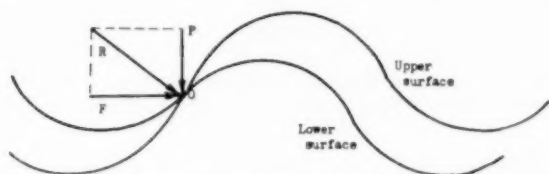
FIG. 7 SCHEMATIC ILLUSTRATION OF FORCE SYSTEM DUE TO ASPERITY OF UPPER SURFACE ACTING ON ASPERITY OF LOWER SURFACE, WHEN NORMAL PRESSURE P IS COMPARATIVELY LOW
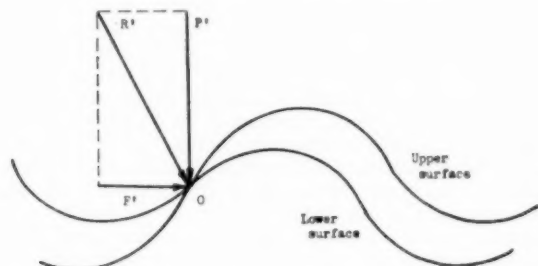
FIG. 8 SCHEMATIC ILLUSTRATION OF FORCE SYSTEM DUE TO ASPERITY OF UPPER SURFACE ACTING ON ASPERITY OF LOWER SURFACE, WHEN NORMAL PRESSURE P' IS COMPARATIVELY HIGH

Accelerated mechanical abrasion then can be interpreted as shown in Fig. 8. In this case the normal force P' is much greater than P in the preceding case, but the translational force F' is the same as F. Thus the new resultant force R' is larger in magnitude than R and acts at a larger angle to the x-axis than does R. In such a case the shearing stress will be higher, and the shearing-stress trajectories will not be deflected as greatly in the direction of the x-axis, as shown in Fig. 10. There will be a pronounced tendency for the lower asperity to flow up in front of the upper asperity; i.e., the shearing strain will be high in the xy-plane and parallel to the surface of the upper asperity.

Only one point of contact of the opposing surfaces thus far has been considered. There are, of course, many points of contact between the two surfaces. As the lower asperity rises above the

x-axis, it will have the effect of disengaging other asperity contacts in its vicinity, and the share of the total load is increased on the particular asperity considered. In the terms of Fig. 8, P' will increase, and R' will increase in magnitude and tend toward a direction normal to the x-axis. This is a case of increasing instability since the reaction to the incident force serves to increase the incident force.

As the incident force on the lower asperity increases, the volume of metal of the lower surface, which is plastically deformed, also increases to exceed the deformation which occurs in normal mechanical abrasion. Thus accelerated mechanical abrasion may be considered analogous to machining with a cutting tool having a built-up edge, where, in accelerated mechanical abrasion, the built-up edge becomes much larger than the incident asperity. In accord with this concept, the surface in accelerated mechanical abrasion, Fig. 2, appears similar to a machined surface in which the tool has a built-up edge.

The increase in normal force can continue until the translational force component is comparatively negligible, and relative translation of the two opposing surfaces stops (seizing occurs).
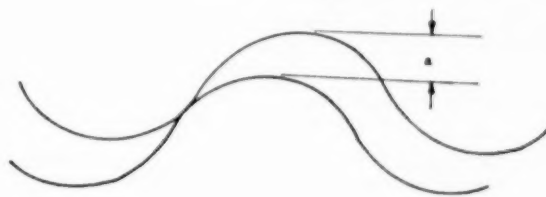
A. Comparatively rough surfaces in contact.

B. Comparatively smooth surfaces in contact.

FIG. 9 SCHEMATIC ILLUSTRATION OF EFFECT OF SURFACE SMOOTHNESS

(Amount of permissible deformation is approximately proportional to vertical distances, a and b, as indicated. Rougher surfaces have greater permissible deformation before seizing begins than do smooth surfaces.)

CORRESPONDENCE WITH EMPIRICAL DATA

The mechanical analysis of accelerated mechanical abrasion agrees qualitatively with the published empirical data on metal wear.

(a) *Effect of Normal Pressure.* The literature is prolific in stating that galling and seizing are incurred with increase in the normal pressure between the opposing metal surfaces. The accepted relationship is consistent with the role of the normal force described previously. Moreover, the mechanical analysis illustrates that accelerated mechanical abrasion is a "go or no-go" type of reaction in homogeneous alloys. (A discussion of self-lubricated alloys is given subsequently.) Lubricants ordinarily are considered to alleviate the tendency to seize by separating the opposing metal surfaces so that high local concentrations of load are not incurred.

(b) *Effect of Surface Finish.* The lubrication theory predicted that the separation of the opposing metal surfaces would be accomplished more easily if the surface finish was improved, i.e., if all the asperities were removed. Now it is known, however,

that a high order of surface finish increases the tendency for galling and seizing. The mechanical analysis of accelerated mechanical abrasion indicates, as shown in Fig. 9, that a low-order surface roughness tends to gall because the amount of deformation that will cause instability is reduced so much. This correspondence of the theory with empirical data is one of the principal contributions of the mechanical analysis.

(c) *Effect of Work-Hardening Modulus.* It is known that the critical shearing stress for plastic deformation increases with strain, i.e., work-hardening occurs. The metal with highest work-hardening modulus, therefore, would be expected to have
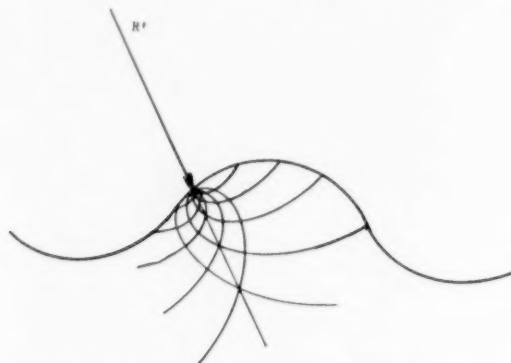

FIG. 10 SCHEMATIC DIAGRAM SHOWING THEORETICAL SHEARING-STRESS TRAJECTORIES FOR CONDITIONS SHOWN IN FIG. 8

the greatest resistance to galling, all other factors being the same. In general, the "softer" alloys gall more readily than hard alloys.

(d) *Effect of Temperature.* The tendency to gall increases with a rise in temperature. This also is consistent with the mechanical interpretation, since the critical shearing stress and the work-hardening modulus decrease as the temperature increases.

(e) *Effect of Velocity.* In the literature, an increase in velocity is credited with increasing the tendency to gall. Since the shearing stress and work-hardening modulus are increased slightly by nominal increases in velocity, the mechanical analysis does not verify the observed relationship. However, galling tests usually are conducted so that the surfaces receive repeated contacts from which the surface temperatures increase considerably. The increase in temperature more than compensates for the increase in velocity, and the mechanical analysis accounts for the observed results in this manner.

(f) *Effect of Foreign Particles.* It is easy to see that the mechanical aspect of seizing accounts for the tendency of close-fitting moving parts to gall and seize when a foreign particle is introduced between the parts. The galling of powder-metallurgy die parts and of press-fitted parts are well-known examples of galling caused by presence of foreign particles. Foreign particles produce high localized loads which start the seizing reaction.

SELF-LUBRICATED ALLOYS

The most widely accepted metal characteristic to reduce the tendency to gall is self-lubrication. Self-lubrication is exemplified by porous powder metals (oil-impregnated), gray cast irons and graphitic steels (graphite-lubricated), and leaded bronzes (lead-lubricated). The mechanical aspect of seizing provides an additional reason for the success of self-lubricated metals which is suggested to account for the failure of externally lubricated metals to equal self-lubricated metals in resistance to seizing. For example, if the lower surface in Fig. 8 were that of a powdered metal (or graphitic or leaded metal), cavities (or soft

phases) would be present at such sites as below or to the right of the point of contact O. If a cavity lies below the point of contact, the load P' will not be resisted as rigidly, point O will drop, and part of the load P' will be distributed to the other neighboring points. Thus, in such a case, the phenomenon of seizing is not initiated. If the cavity is to right of point O, the asperity will be less able to resist the translational force F' and, therefore, will tend to move toward the cavity rather than up; i.e., the shearing-stress trajectories are deflected into the cavities, as shown in Fig. 11. In such a case, any incipient seizing will be terminated rapidly.
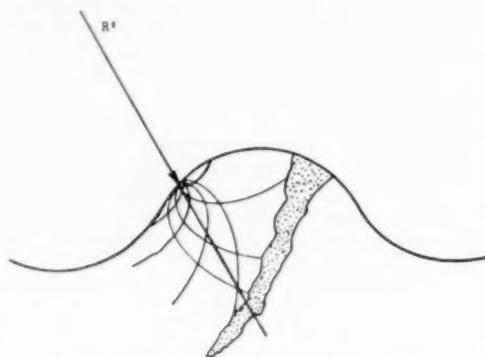
FIG. 11 SCHEMATIC DIAGRAM SHOWING DEFLECTION OF SHEARING-STRESS TRAJECTORIES BY PRESENCE OF SOFT PHASE OR CAVITY—DOTTED AREA—IN AFFECTED FIELD

Thus both facts, namely, that self-lubricated alloys are known to have a greater resistance to incipience of galling and to have a lower extent of damage from galling, are accounted for in the mechanical aspect of accelerated mechanical abrasion. On this basis, porous alloys without a lubricating agent would be expected to gall less than nonporous alloys, also unlubricated.

The mechanical interpretation of accelerated mechanical abrasion would provide a principle upon which to design surfaces of "engineered roughness." It is evident that the "roughness" must be on a scale comparable with the asperity size, i.e., the microscopic scale. Many instances of the significance of such engineered roughness are known in practice. The importance of graphite-flake size, shape, and distribution in gray cast-iron applications is well known. From the standpoint of self-lubrication, the dimensions of the "lubricant reservoir" would not be too critical. Yet, in practice, the graphite-flake classification is controlled closely for such parts as piston rings, cylinders, and other wearing-surface applications.

Talbot and Kozlik[2] have reported on the gall resistance of ductile iron compared to flake gray iron. They found that for equal graphite contents and similar matrix structures, the gall resistance of the flake-graphite iron was superior to that of the ductile iron. The ductile iron was equal in gall resistance to gray iron in which the flake-graphite content is lower than the nodular-graphite content. These results correspond to predictions from the mechanical analysis of seizing.

Porous chromium-plated surfaces are superior to the nonporous surfaces in resistance to galling. The effect of size, shape, and distribution of porosity again was found to be more critical than would be predicted from lubrication theory, since channel porosity of the chromium plate is superior to round-pit-type porosity.

[2] "Investigations Into the Gall Resistance of Metals," by A. M. Talbot and R. A. Kozlik, presented at the Rotary Pump Section Meeting of the Hydraulic Institute, December 5 1949, New York, N. Y.

For proper "wearing-in" of many metal parts, it is necessary to have good resistance to accelerated mechanical abrasion. Chemically pitted surfaces are known to be superior to "super-finished" surfaces in many such applications for wearing-in characteristics.

In most industrial applications the mechanical effect is complementary to the lubrication-film effect of separating the surfaces but somewhat decreases the importance accorded to the lubrication effect alone. There is ample evidence that empirical methods have determined in many cases the importance of microscale engineered roughness, which is predicted (qualitatively, at this time) from the mechanical analysis of accelerated mechanical association. In future surface engineering such interpretations undoubtedly will get tested for quantitative validity.

Discussion

J. W. PENNINGTON.[3] The author's interesting analysis of the mechanical aspect of seizing in metal wear is an additional contribution to our concept of one of the phases of the very complicated and intricate phenomenon which we call wear. To get an understanding of this problem, we certainly must follow the author's example and analyze what is happening at the actual points of contact.

In the comparison of this analysis with empirical data, the author points out that a very smooth surface finish leads more readily to seizing than a rougher finish. The writer believes that this should be restricted to borderline or dry-lubrication conditions. Smooth surfaces make more easily possible the formation of a fluid film which will separate the moving surfaces completely. However, if the film is ruptured and contact does occur, galling or seizing will occur more readily with smooth surfaces than with rough surfaces. The nature of the surface finish, whether roughness is due to hills or valleys, is also important.

The analogy of a cutting tool with a built-up edge seems to be a good one and makes it easier to visualize the mechanism by which the accelerated damage from seizing occurs.

The discussion of self-lubricating alloys is interesting and it is well to compare this with T. L. Oberle's analysis of the effect of hardness and modulus on wear.[4] The giving-way or yielding of asperities in a porous material, whether or not the pores are filled with a lubricant, seems to tie in directly with Oberle's analysis. Certainly, the ready yielding of the asperities in an open material indicates a low effective modulus of elasticity.

Although the diagrams which the author presents are relatively simple, a very concentrated study is necessary to reveal the thinking that is behind such an analysis.

[3] Chief Engineer, Metal Products Division, Piston Ring Department, Koppers Company, Baltimore, Md. Mem. ASME.

[4] "Hardness, Elastic Modulus and Wear of Metals," by T. L. Oberle, SAE Transactions, July, 1952, pp. 511–515.
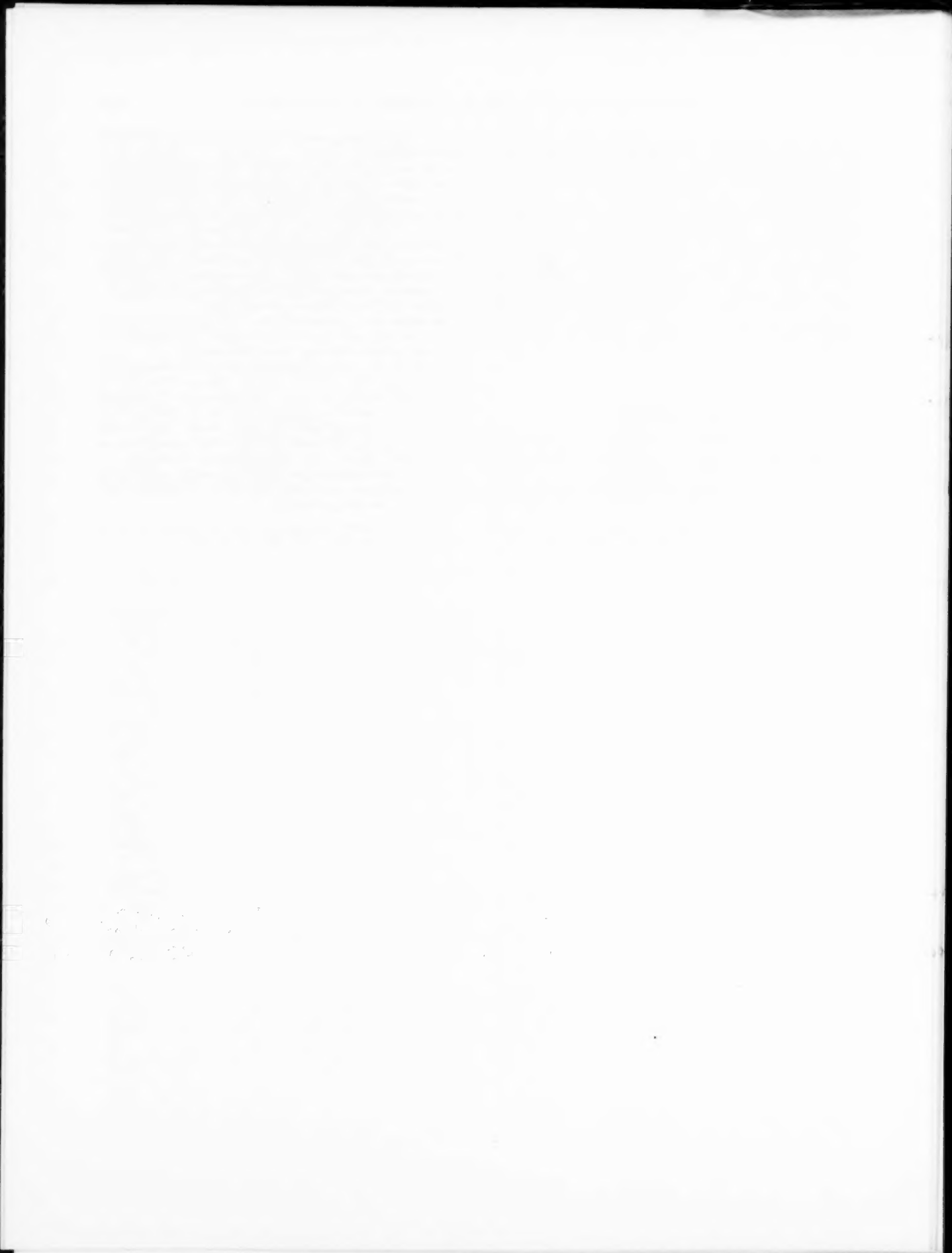
Heat-Transfer and Friction Characteristics for Gas Flow Normal to Tube Banks— Use of a Transient-Test Technique

By W. M. KAYS,[1] A. L. LONDON,[2] AND R. K. LO[3]

Heat-transfer and flow-friction design data are presented for flow normal to circular tube bundles for the Reynolds-number range, 500 to 20,000 (based on tube diameter). Six staggered circular tube patterns and one in-line arrangement were tested. Tentative correlations are presented for the staggered arrangements allowing interpolation of the test results to obtain design data partially covering a transverse pitch-ratio range from 1.25 to 2.50, and a longitudinal pitch-ratio range from 0.75 to 1.50. Data also are provided so that the influence of the number of tube rows on the mean coefficient may be estimated accurately. These results are of interest in applications involving small-diameter tubes and low-density fluids, as, for example, the gas-turbine regenerator. They supplement the high Reynolds-number data of Pierson, Huge, and Grimison, and the low Reynolds-number viscous-flow-range data of Bergelin, Colburn, et al., by providing needed information for the intermediate range. A transient-test technique was employed in obtaining these data. Several tests employing a conventional steady-state technique also were made to demonstrate the validity of the transient method. The advantages and limitations of the transient method are considered in detail.

NOMENCLATURE

The following nomenclature is used in the paper:

A = heat-transfer area, sq ft
A_c = minimum free-flow area, the smaller magnitude of either the transverse or diagonal openings, sq ft
C = thermal capacitor cylinder heat capacity, Btu/deg F
C_f = coefficient for friction correlation defined in Fig. 13, dimensionless
C_h = coefficient for heat-transfer correlation, defined in Fig. 12, dimensionless
c_p = specific heat at constant pressure, Btu/(lb deg F)
D = tube diameter, ft
f = friction factor defined by Equation [2], dimensionless
f''' = friction factor defined by Equation [3], dimensionless
G = mass velocity based on minimum free-flow area, A_c, lb/(hr ft²)
g_c = proportionality in Newton's second law, 32.2 (lb/#) (ft/sec²)

h = unit convective heat-transfer conductance, Btu/(hr ft² deg F)
k = thermal conductivity, Btu/(hr ft² deg F/ft)
L = effective flow length of a tube bank, defined by Equation [4], ft
n = number of tube rows in direction of flow, dimensionless
P = static pressure, #/ft²
q = heat-transfer current — Btu/hr
r_h = hydraulic radius defined by Equation [1], ft
t = temperature, deg F
t^* = nondimensional temperature of thermal-capacitor cylinder, Equation [7]
V = velocity, fps
w = mass-flow rate, lb/hr
X_l = longitudinal pitch ratio, longitudinal tube spacing divided by tube diameter, dimensionless
X_t = transverse pitch ratio, transverse tube spacing divided by tube diameter, dimensionless
μ = viscosity, lb/(hr ft)
ρ = fluid density, lb/ft³
θ = time, hr, sec
N_{St} = Stanton number, $h/(Gc_p)$, a heat-transfer modulus
N_{Pr} = Prandtl number, $\mu c_p/k$, a fluid-properties modulus
N_R = Reynolds number, $4r_hG/\mu$, a flow modulus
N_{RD} = Reynolds number based on tube diameter, DG/μ
lb = denotes pounds mass in distinction to
# = denoting pounds force

INTRODUCTION AND OBJECTIVES

At present there is a considerable body of data in the literature on both the convective heat-transfer and flow-friction characteristics for flow normal to banks of circular tubes. In fact, along with flow inside circular tubes, this class of flow geometry probably has received more experimental attention than any other. The most commonly accepted design data are those of Pierson (1),[4] Huge (2), and Grimison (3), presented in 1937, all concerned with gas flow at high Reynolds numbers, and the more recent work of Bergelin, Colburn, and Hull (4) with oils at very low Reynolds numbers. The work to be presented here is likewise concerned with gas flow normal to tube banks, but in the intermediate N_R range, supplementing the earlier results. Some overlap of the Reynolds-number test range allows a direct comparison with the Pierson, Huge, and Grimison data. After the present program was started, Bergelin, et al. (5), published some test results, again using oils, also covering the intermediate region, and a comparison with their results is of interest.

The recent interest in the use of small-diameter tubes (of the order of ⅛ in.) and low-density gases in such heat-exchanger applications as the gas-turbine regenerator has resulted in a Reynolds-number range of interest on the tube bank side that extends somewhat below the 2000 minimum (N_R based on tube

[1] Assistant Professor of Mechanical Engineering, Stanford University, Stanford University, Calif. Assoc. Mem. ASME.
[2] Professor of Mechanical Engineering, Stanford University. Mem. ASME.
[3] Case Institute of Technology, Cleveland, Ohio.

[4] Numbers in parentheses refer to the Bibliography at the end of the paper.

diameter) reported by Pierson, Huge, and Grimison, although probably not down into the viscous-flow region considered by Bergelin (4). Therefore it was felt that test data should be obtained in this region, since little or nothing has been known of the effect or extent of flow transition for tube banks, and design outside of the range of available test data is thus quite speculative. It was further felt that more attention should be devoted to the very compact tube-bank arrangements, and that some additional arrangements, not tested previously, should be considered.

Another incentive for this work was provided by the desire to investigate the applicability of a transient heat-transfer test technique (6) which holds many advantages over the more commonly employed steady-state methods and which, it is believed, in many cases yields more adequate heat-exchanger design data. It is hoped that the transient technique will find use in the future in many other types of experiments with tube banks, as, for example, the determination of the effects of baffles on individual tubes, the effects of part cross, part longitudinal flow, and so on.

The specific objectives of this paper are as follows:

1 To demonstrate the validity, simplicity, and power of the transient technique for determination of the heat-transfer characteristics of tube banks, and to indicate its limitations.

2 To present, as determined by this method, the heat-transfer and flow-friction characteristics of six compact staggered circular tube-bank patterns in the approximate Reynolds-number range, 500–10,000.

3 To show the variation of heat-transfer performance of individual tubes in the rows near the entrance and exit of a finite tube bank.

TEST SURFACES AND METHOD OF PRESENTATION OF RESULTS

The tube patterns tested are designated according to their transverse and longitudinal pitch ratios, X_t and X_l, respectively. (The definition of the pitch ratios is shown in the diagrams, Figs. 3 to 11.) With the exception of the pitch ratios, all of the transient-test cores were identical. The following staggered patterns were investigated:

| X_t | 1.25 | 1.50 | 1.50 | 1.50 | 2.00 | 2.50 |
| X_l | 1.25 | 1.00 | 1.25 | 1.50 | 1.00 | 0.75 |

Experiments with two steady-state steam-to-air test cores were conducted also. Both of these had $X_t = 1.50$ and $X_l = 1.25$, but one was a staggered and the other an in-line pattern. These tests were used to support the validity and to demonstrate the limitations of the transient method.

The first four of the staggered patterns listed were also tested by Pierson (1); the last two have not been reported upon before. $X_t = 2.00$, $X_l = 1.00$, Fig. 10, is a square staggered layout. Both $X_t = 1.50$, $X_l = 1.25$ (Fig. 3), and $X_t = 2.50$, $X_l = 0.75$, Fig. 11, have very close to equilateral triangular layouts. These two are identical except for a 90-deg difference in orientation with respect to the air-flow direction.

The steady-state test cores were constructed from $1/_8$-in. brass tubes soldered into $1/_8$-in-thick brass tube sheets. The core was 15 rows deep (direction of flow) with 26 tubes in a row. The tubes were $9^3/_4$ in. long.

All of the transient test cores were constructed of $3/_8$-in. aluminum "dummy" tubes which fitted into $1/_2$-in. plastic tube sheets so as to be readily removable. Again, the tubes were $9^3/_4$ in. long. The outsides of the tube-to-sheet joints were sealed with Scotch tape so as to prevent air leaks, and at the same time allow for ready removal as desired. The number of rows varied from 13 to 26, and the number of tubes per row from 10 to 20. For each transient arrangement the same aluminum dummy tubes were used, as well as the same over-all shell. The only difference was that a new pair of plastic tube sheets was drilled for each pattern. Any of the aluminum dummy tubes could be withdrawn and replaced with the thermal-capacity cylinder (to be described) which is the "active" test element of the transient method.

Detailed descriptions of the various patterns are contained in Table 1 and also on the graphs giving the basic heat-transfer and flow-friction design data, Figs. 5, 7 to 11.

The heat-transfer and friction test data are presented in the form

$$N_{St}N_{Pr}{}^{2/3} = \phi(N_R)$$

$$f = \phi(N_R)$$

The mass velocity G, lb/(hr ft^2), is in all cases evaluated on the basis of the minimum free-flow area A_c, regardless of whether the minimum occurs in the transverse or diagonal passages. The length dimension employed in the Reynolds number has been chosen arbitrarily as a hydraulic diameter defined as follows

$$4r_h = 4A_cL/A \quad \quad \quad [1]$$

This dimension was selected to provide a treatment consistent with the previous work accomplished on the Stanford-Navy research project on compact surfaces, and because it is a more convenient design parameter (8). For comparison with the results of other workers a conventional tube-diameter Reynolds number will be employed. The friction factor also is defined consistent with this previous work

$$dP_f/dL = f(\rho V^2)/(r_h 2g_c) \quad \quad [2]$$

Since the pressure drops and then rises through each tube row, the friction pressure gradient, dP_f/dL, can be interpreted as the gradient between any two points in the core an integer number of rows apart. Hence this friction factor can be handled in an identical manner as the friction factor for flow "through" a tube, and it is directly proportional to the conventionally employed tube-bank friction factor, f''', defined as follows

$$\Delta P/\rho = 4f'''nV^2/2g_c \quad \quad [3]$$

The effective flow length of the tube bank is

$$L = nDX_l \quad \quad \quad [4]$$

Combining Equations [2], [3], and [4]

$$f''' = (DX_l/4r_h)f$$

Since all tests have been run with air the Prandtl number has not been a test variable. However, Prandtl number to the $2/_3$

TABLE 1   STAGGERED-TUBE-BANKS GEOMETRICAL DATA, TRANSIENT TESTS

	$X_t = 1.25$ $X_l = 1.25$	$X_t = 1.50$ $X_l = 1.00$	$X_t = 1.50$ $X_l = 1.25$	$X_t = 1.50$ $X_l = 1.50$	$X_t = 2.00$ $X_l = 1.00$	$X_t = 2.50$ $X_l = 0.75$
Tube diameter, ft	0.0313	0.0313	0.0313	0.0313	0.0313	0.0313
Hydraulic diameter, $4r_h$, ft	0.0125	0.0196	0.0256	0.0298	0.0327	0.0271
Minimum free-flow area	transverse	transverse	transverse	transverse	diagonal	diagonal
Free-flow: Frontal area	0.200	0.333	0.333	0.333	0.414	0.366
Area per unit of volume, ft^2/ft^3	64.4	67.1	53.6	44.8	50.3	53.6
No. of rows in test core	13	15	15	15	19	26

power has been introduced into the results so that they may be employed for fluids with differing Prandtl numbers. The use of $N_{Pr}^{2/3}$ probably will yield fairly accurate results in the Prandtl-number range of gases. Although $N_{Pr}^{2/3}$ is commonly employed over a very wide range of Prandtl numbers, it is at best only a moderately good approximation.

Transient Heat-Transfer Test Technique

The transient method for determining the unit heat-transfer conductance between a body immersed in a fluid stream, and that stream, was proposed 12 years ago by London, Nottage, and Boelter (6). Determination of the unit heat-transfer conductance by this method is based upon the fact that it is often possible to design the immersed body so as to permit the idealizations, (a) the entire resistance to heat transfer is "lumped" at the solid-fluid interface, and (b) all of the thermal capacity of the system is lumped within the solid. If these parameters are thus essentially separate, the surface conductance can be evaluated by a simple analysis of the experimentally established transient response of the solid when first heated (or cooled) relative to the stream temperature, and then immersed in the stream.

Description of Apparatus. For the tests described here, the heated solid body, which will be called the thermal-capacitor cylinder, consists of a 4-in. length, $3/8$-in-diam solid copper rod mounted between plastic end pieces as shown in Fig. 1. This cylinder can be fitted in place of any of the aluminum cylinders of the test cores just described.

same circuit as used for the steady-state tests, and the air temperature was measured upstream of the test core by the same shielded thermocouple as employed for the steady-state tests. All thermocouple emf's were determined by an electronic, continuous-balance potentiometer. The maximum cooling rate of the capacitor was at all times less than 5 per cent of the response speed of this instrument, so it is believed that any transient measurement error introduced by instrument lag is negligible.

The air-flow rate through the test core was determined by the same orifice-metering system as employed for the steady-state tests. The same instrumentation also was employed for the core pressure-drop data that were needed for the friction-factor evaluation.

Test Procedure. The capacitor cylinder was removed from the test core and heated in a small electric oven to 50–60 deg F above ambient. Thus the plastic end sections also were heated which helped to minimize end-leakage heat transfer from the copper capacitor. The capacitor cylinder was next placed in its position in the core and during the initial cooling period the duct-air temperatures, orifice temperature, pressure, and pressure drop were recorded. When the capacitor had cooled to a predetermined approach to duct-air temperature, 10 millivolts (about 30 deg F), time recording was started for each of five 1-millivolt intervals in thermocouple response (about 3 deg F). Two $1/10$-sec least-count stop watches were employed, one starting and one stopping at each interval. At the conclusion of the test all of the other nontransient data again were recorded.
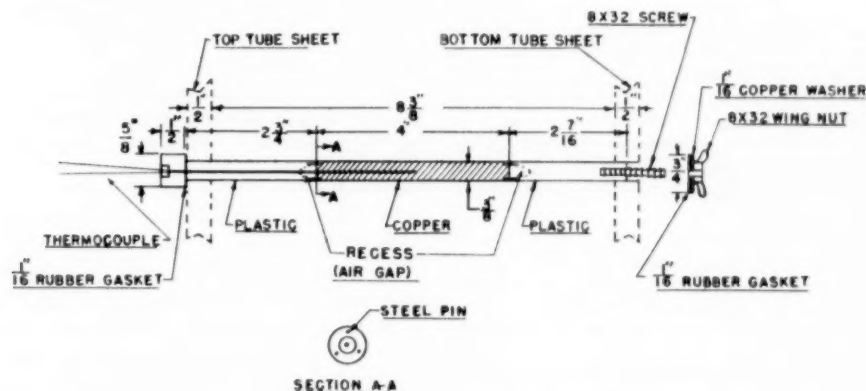
Fig. 1   Transient-Test Thermal-Capacitor Cylinder

At the juncture between the copper and plastic cylinders both are slightly recessed to minimize thermal contact and to isolate the copper portion effectively. A rigid connection is effected at each end by small steel pins. The test method is founded upon maintaining negligible end-leakage heat transfer between the copper and the plastic relative to the convection heat transfer from the copper cylinder surface. An iron-constantan thermocouple is soldered in the center of the copper section at the bottom of a small-diameter hole drilled from one end.

The capacitor was made of pure electrolytic copper, the unit heat capacity for which is accurately known. Prior to assembly it was carefully weighed, and likewise, the relatively small mass of steel end pins and solder. From these data the total effective thermal capacity of the copper cylinder could be determined.

All tests were performed in an air duct with $8^3/4 \times 9^3/4$-in. throat which previously had been used for steady-state steam-to-air tests, and which is fully described in an earlier paper (7). The thermocouple leads from the capacitor were connected into the

For each tube arrangement a complete series of tests were run with the capacitor cylinder inserted near the center line of the core, a minimum of 11 rows from the in-flow face and 4 rows from the exit-flow face. Twenty to twenty-five runs were taken for each core, covering approximately the Reynolds-number range 500 to 10,000 with 15 per cent flow-rate increments. After this sequence of tests, at a Reynolds number near the middle of the range, a series of runs were taken by inserting the capacitor in each row, starting at the entrance face row, thus obtaining the row-to-row variation in the convection conductance. As the $X_t = 1.50$, $X_l = 1.25$ geometry was employed to compare the steady-state and transient techniques, for this transient test core, the row-to-row variation was determined for three different Reynolds numbers, and also the transverse variation was checked to determine the nature of the wall effects. In all of the test cores split tubes were used at the walls and the variation of the conductance from tube-to-tube transverse to the flow direction was found to be less than 1 per cent.

Analysis of Data. An energy balance on the cooling thermal capacitor yields for the rate of change of temperature

$$q = -C \frac{dt}{d\theta} \quad \quad \quad \quad \quad [5]$$

Assuming that heat is transferred from the capacitor cylindrical surface only, i.e., no end leakage, that the capacitor is at all times at a uniform temperature, i.e., no internal resistance, and employing a mean unit thermal conductance with respect to heat-transfer area, the heat-transfer-rate equation for convection becomes

$$q = hA(t - t_a) \quad \quad \quad \quad \quad [6]$$

Combining Equations [5] and [6]

$$hA(t - t_a) = -C \frac{dt}{d\theta} \quad \quad \quad [7a]$$

C, A, and t_a are constants. The mean unit conductance h is a function of the fluid properties, the flow conditions, and the geometry. For only small variations of t and constant flow it will be essentially a constant. This equation can then be integrated from $\theta = 0$, $t = t_0$ to $\theta = \theta$, $t = t$, yielding

$$t^* = \frac{t - t_a}{t_0 - t_a} = e^{-\frac{hA}{C}\theta} \quad \quad \quad [7b]$$

where t^* is the nondimensional temperature defined by the left equal sign.

A plot of $-\log_e t^*$ as a function of θ should yield a straight line with slope equal to hA/C. The analysis of the experimental data is further simplified if the system is operated over a small temperature range, for in this case the temperature-emf response of the thermocouple is close to linear. Then it is only necessary to plot the logarithm of the emf ratios directly rather than convert to temperature. It also is apparent that the calibration of the potentiometer is of secondary importance and is only needed to demonstrate a linear scale.

Fig. 2 is a data plot for a typical test and demonstrates the expected straight-line relationship. Departures from linearity would reflect combinations of end leakage, variation of h, and possibly instrument lag effects, all presumed negligible.

The reduction of the remainder of the data, and the calculations leading to the determination of $N_{St}N_{Pr}^{2/3}$ and f versus N_R, are identical to the procedures described for steady-state tests (7).

Experimental Accuracy. Space permits only a brief consideration of this important point. The three main sources of error are the following: (a) Those arising from the idealizations postulated for the development of Equations [7a] and [7b]; (b) errors introduced by the measuring instruments; and (c) uncertainties existing in current data on the air physical properties and the capacitor system.

Errors associated with the idealizations of the analysis which were considered specifically are in connection with the following:

1 Lumped-parameter behavior of the resistance associated with the boundary layer and the capacitance of the copper cylinder.

2 Heat transfer by forced convection alone; i.e., radiation is negligible, free-convection effects are small, and end leakage is small.

3 Mixing between the heated boundary layer of the capacitor and the boundary layer of the plastic end pieces which, in general, are at a moderately different surface temperature.

4 The fact that in steady-state tests, and most design applications of tube banks, the cylinder surface temperature at a circumferential section is normally both isothermal and constant with
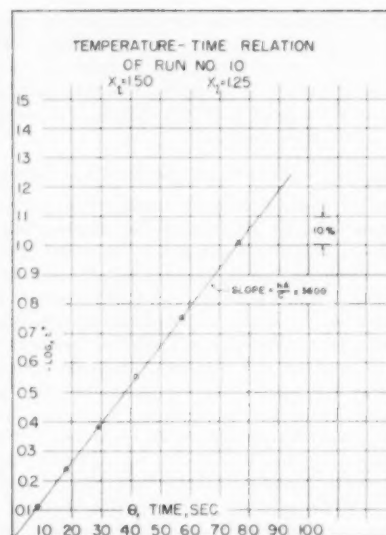
FIG. 2 TEMPERATURE-TIME PLOT TRANSIENT-TEST RUN

time. In the transient-test technique, however, although the surface temperature is essentially isothermal at an instant, it is varying continuously with time. Consequently, a boundary element of flow is exposed to a variable temperature surface in passage over the tube.

The probable magnitude of all of these errors can be estimated, and for the conditions of the tests reported here, are believed to have only a negligible effect.

The instrumentation errors that need to be considered are listed as follows:

1 Temperature-measurement accuracy and instrument lag, estimated uncertainty, ±4 microvolts.

2 Measurement of time, ±1 per cent uncertainty.

3 Air-flow rate, ±1 per cent uncertainty (7).

Physical-properties errors are estimated as follows:

1 Capacitor constant, C/A, ±0.5 per cent uncertainty.

2 Prandtl number for air, ±2 per cent uncertainty (10, 11).

3 Air specific heat, c_p, ±0.5 per cent uncertainty (10).

The following summarizes the expected uncertainties discussed in the foregoing:

	Maximum expected error, per cent
$d \log_e t^*/d\theta$	±2
w	±1
C/A	±0.5
c_p	±0.5
N_{Pr}	±2
Miscellaneous	±2

Note that a miscellaneous error of ±2 per cent is included to cover the accumulated uncertainties associated with departures from the idealizations of the analysis. On this basis the final maximum expected error associated with the heat-transfer modulus $N_{St}N_{Pr}^{1/3}$ is ±5 per cent, with the probability that the maximum error will be well within this magnitude as demonstrated by the excellent repeatability of the test results.

For Reynolds numbers and friction factors the conclusions reached in (7) are applicable here, and the maximum expected

uncertainties are ± 2 per cent in N_R and ± 5 per cent in f. It should be noted, however, that the neglect of entrance and exit-flow effects for cores of only 13 to 26 rows may introduce a slight uncertainty into the f-characteristic presumably representative of a core with an infinite number of rows.

The steady-state tests were conducted by the methods described in (7), and the expected maximum uncertainty in both $N_{St}N_{Pr}^{2/3}$ and f is ± 5 per cent, and for N_R, ± 2 per cent.

Comparison With Steady-State Tests. The foregoing analysis for the transient technique is concerned with the accuracy of the $N_{St}N_{Pr}^{2/3}$ versus N_R determination for a single tube within a large bank of tubes. There remains the question as to whether data determined for a single tube can be employed to predict performance for a bank of tubes, all of which are heated, or cooled. This is an important question because the single tube of the transient tests is exposed to air which is initially at a uniform temperature, whereas any one tube in a totally heated tube bank (except one in the first row) is exposed to a stream of fluid which may not be uniform in temperature because of the thermal boundary layer which is built up and shed from the preceding tubes in the bank. How well the single-tube results apply to totally heated tube banks depends, then, upon the thoroughness of mixing from row to row. For staggered tube-bank arrangements it is believed that the mixing is sufficient, and for in-line tubes with turbulent main stream flow it is also probably sufficient. However, it has been found that for viscous main stream flow there is a very marked difference between transient single-tube test results and steady-state over-all tube-bank data. Consequently, all of the transient-test results to be presented in this paper are for staggered arrangements only, the in-line data being from steady-state steam-to-air tests.

In order to substantiate the foregoing assertions the steam-to-air core (staggered, $X_t = 1.50$, $X_l = 1.25$) described previously, with a pattern identical to one of the transient cores, was tested. The results of these tests for both heat transfer and friction are presented in Fig. 3 and are summarized in Table 2. In Fig. 4 these data are compared with that of Grimison (3), with Jakob's equation for friction factor based on Grimison's data (12), with an equation of Colburn's as given in (13), and with some data of Bergelin's (5). It will be noted here that the Reynolds number is based on the conventional tube diameter rather than the flow hydraulic diameter. Both the heat-transfer and friction curves lie below the Grimison data by about 15 and 20 per cent, respectively. Surprisingly, the heat-transfer test data are much better approximated by Colburn's equation, which was proposed before the Grimison data were available. The Bergelin heat-transfer data lie high relative to the present data, but it should be noted that these were obtained with oils at very much higher Prandtl numbers.

The transient-test data for the same staggered pattern are presented in Fig. 5 for a central location of the capacitor cylinder
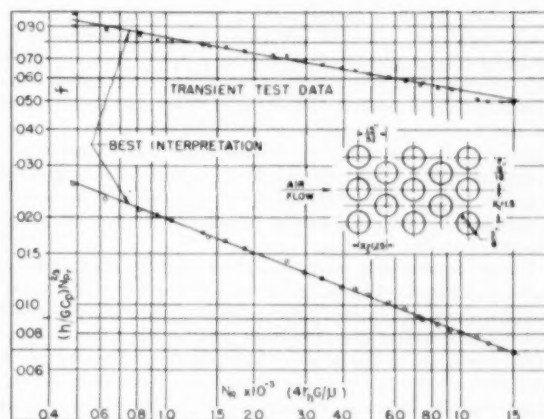
Fig. 3 Steady-State Tests, Heat-Transfer and Flow-Friction Characteristics Staggered, $X_t = 1.50$, $X_l = 1.25$

Tube outside diameter, 0.25 in.
Flow hydraulic radius, r_h, 0.00415 ft
Minimum free-flow area, transverse spacings
No. of tube rows deep, 15
Free-flow/frontal area, 0.333
o, Hot-core test points. Heat-transfer data evaluated on basis of zero steam-side resistance
x, Cold-core friction factors
Best interpretation of friction data based on cold-core tests
Best interpretation of heat-transfer data based on allowance for steam-side resistance
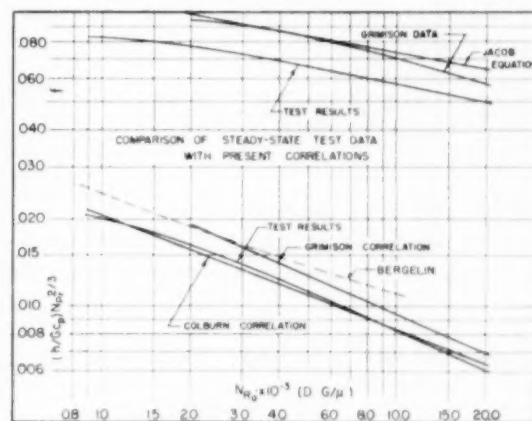
Fig. 4 Comparison of Correlations From Literature With Steady-State Test Results, $X_t = 1.50$, $X_l = 1.25$

TABLE 2 SUMMARY OF BASIC HEAT-TRANSFER AND FRICTION DATA, STEADY-STATE TESTS

	Staggered tubes $X_t = 1.50$, $X_l = 1.25$			In-line tubes $X_t = 1.50$, $X_l = 1.25$		
N_R	$N_{St}N_{Pr}^{2/3}$	f	$N_{St}N_{Pr}^{2/3}$	f	N_R
800	0.0200	0.0827	0.00790	0.0265	800
1000	0.0188	0.0812	0.00750	0.0281	1000
1200	0.0178	0.0800	0.00778	0.0331	1200
1500	0.0165	0.0780	0.00960	0.0410	1500
2000	0.0148	0.0750	0.0108	0.0497	2000
2500	0.0136	0.0725	0.0110	0.0535	2500
3000	0.0126	0.0702	0.0108	0.0554	3000
4000	0.0111	0.0670	0.0102	0.0562	4000
5000	0.0100	0.0640	0.00958	0.0558	5000
6000	0.00924	0.0614	0.00900	0.0549	6000
8000	0.00810	0.0578	0.00820	0.0525	8000
10000	0.00730	0.0559	0.00752	0.0505	10000
12000	0.00670	0.0530			12000
15000	0.00603	0.0508			15000

in the tube bundle. Before making the comparison with the steady-state core, extensive row-to-row traverses were made in the transient-test core. The results of these traverses are presented and discussed in a later section of this paper. It is sufficient to state here that, in general, the first two or three tube rows, and also the last, have a significantly lower unit film conductance for turbulent flow than the tube rows in the interior of the tube bundle. In order to compare steady-state tests of an entire tube bundle with transient tests of individual tubes in a bundle it is necessary to evaluate the integrated average of tube-to-tube variations in h from the transient-test data.

The comparison of transient and steady-state technique results is shown in Fig. 6. Two transient-test curves are presented—one from the direct test results for the central location of the capacitor, and the other the integrated average behavior for a 15-row core.

The curvature in the integrated transient heat-transfer line is attributable to the fact that the behavior of the first four and last tube rows with N_R do not exactly parallel the behavior of the internal tube rows. The excellent agreement obtained demonstrates convincingly that for staggered tube banks the transient technique yields accurate data for steady-state heat-exchanger design.

The friction factors for both cores were obtained by the same

technique, so this comparison demonstrates no more than the self-consistency of the test methods and the foregone conclusion that the principles of similitude are valid.

Test Results

One of the expressed objectives of this paper is to present tube-bundle heat-transfer and flow-friction design data. The various tube-bank patterns studied have been described. Six staggered patterns were tested by the transient method, one was checked by a steady-state method and, in addition, one in-line pattern was tested by a steady-state method.

The basic heat-transfer and flow-friction characteristics for the staggered patterns (transient tests) are summarized in Table 3 and presented graphically in Figs. 5, 7 to 11. In all cases $N_{St}N_{Pr}^{2/3}$ and f are presented as functions of N_R, the latter based on a flow hydraulic diameter. Although the desired test range of Reynolds numbers was 500 to 10,000, the limitations of various parts of the apparatus made this range impossible in some cases. The heat-transfer characteristics presented are taken from a tube well removed from the entrance and exit-flow faces of the tube bank, and thus represent the characteristics of an "infinite" bank. The friction factors, however, are based on over-all core data, although in no case were there less than 13 tube rows in a core so that entrance and exit effects are probably quite small.

When the six staggered-tube-pattern test results are compared

Fig. 5 Basic Heat-Transfer and Flow-Friction Design Data, Transient Tests, $X_t = 1.50$, $X_l = 1.25$
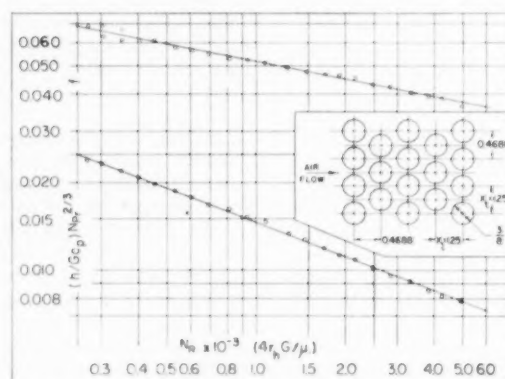
Fig. 7 Basic Heat-Transfer and Flow-Friction Design Data, Transient Tests, $X_t = 1.25$, $X_l = 1.25$
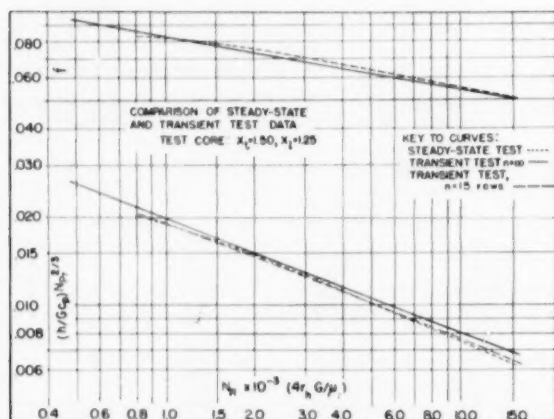
Fig. 6 Comparison of Steady-State and Transient-Technique Results, $X_l = 1.50$, $X_t = 1.25$, 15 Tube Rows
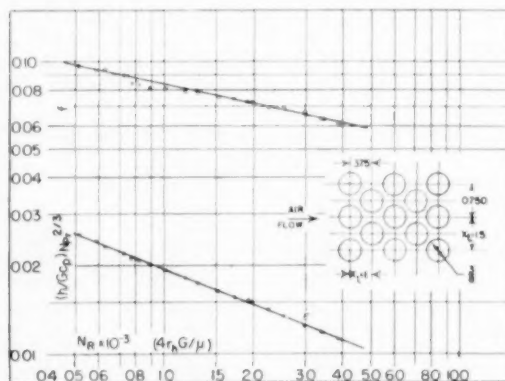
Fig. 8 Basic Heat-Transfer and Flow-Friction Design Data, Transient Tests, $X_t = 1.50$, $X_l = 1.00$
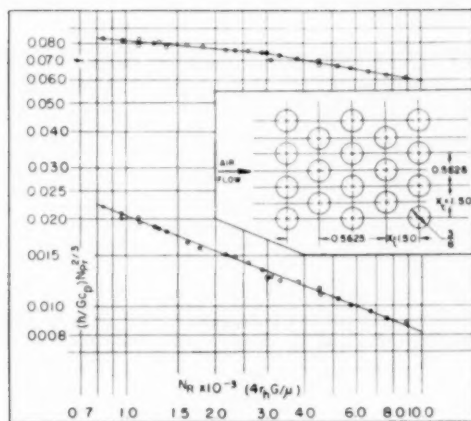
Fig. 9   BASIC HEAT-TRANSFER AND FLOW-FRICTION DESIGN DATA, TRANSIENT TESTS, $X_t = 1.50$, $X_l = 1.50$
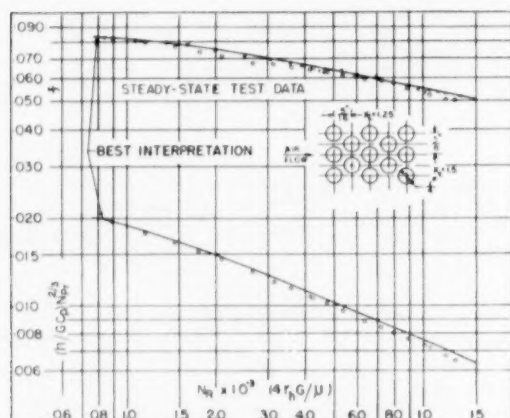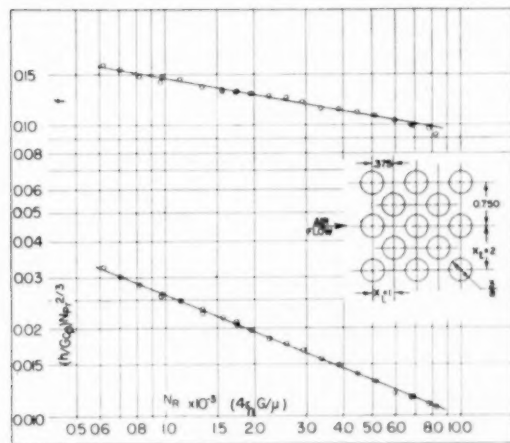

Fig. 10   BASIC HEAT-TRANSFER AND FLOW-FRICTION DESIGN DATA, TRANSIENT TESTS, $X_t = 2.00$, $X_l = 1.00$
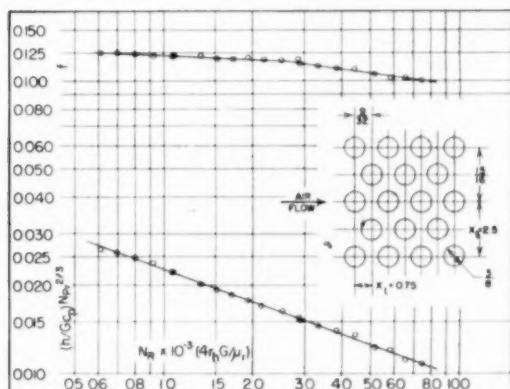
Fig. 11   BASIC HEAT-TRANSFER AND FLOW-FRICTION DESIGN DATA, TRANSIENT TESTS, $X_t = 2.50$, $X_l = 0.75$

TABLE 3   SUMMARY OF BASIC HEAT-TRANSFER AND FRICTION DATA, TRANSIENT TESTS; STAGGERED TUBES

N_R	$X_t=1.25, X_l=1.25$		$X_t=1.50, X_l=1.00$		$X_t=1.50, X_l=1.25$		$X_t=1.50, X_l=1.50$		$X_t=2.00, X_l=1.00$		$X_t=2.50, X_l=0.75$	
	$N_{St}N_{Pr}^{2/3}$	f	$N_{St}N_{Pr}^{2/3}$	f	$N_{St}N_{Pr}^{2/3}$	f	$N_{St}N_{Pr}^{2/3}$	f	$N_{St}N_{Pr}^{2/3}$	f	$N_{St}N_{Pr}^{2/3}$	f
300	.0233	.0658	—	—	—	—	—	—	—	—	—	—
400	.0208	.0620	—	—	—	—	—	—	—	—	—	—
500	.0191	.0593	.0257	.0972	.0258	.0940	—	—	—	—	.0373	.1250
600	.0178	.0572	.0239	.0932	.0241	.0907	—	—	.0323	.160	.0246	.1230
800	.0159	.0540	.0213	.0874	.0216	.0860	.0224	.0634	.0286	.152	—	—
1000	.0146	.0518	.0193	.0833	.0198	.0828	.0204	.0818	.0261	.146	.0287	.1220
1200	.0136	.0498	.0180	.0790	.0184	.0800	.0190	.0805	.0241	.141	.0212	.1213
1500	.0124	.0477	.0164	.0761	.0169	.0768	.0174	.0790	.0219	.135	.0195	.1200
2000	.0111	.0450	.0147	.0712	.0151	.0728	.0155	.0769	.0194	.128	.0178	.1180
2500	.0102	.0430	.0134	.0680	.0138	.0700	.0142	.0755	.0177	.122	.0162	.1175
3000	.00950	.0415	.0124	.0652	.0129	.0675	.0132	.0740	.0164	.118	.0158	.1145
4000	.00850	.0391	.0111	.0615	.0116	.0641	.0117	.0701	.0145	.112	.0136	.1100
5000	.00778	.0375	—	—	.0106	.0615	.0107	.0674	.0132	.104	.0126	.1065
6000	—	—	—	—	.00987	.0596	.00997	.0653	.0122	.0982	.01080	.1035
8000	—	—	—	—	.00883	.0566	.00868	.0619	.0108	—	—	—
10000	—	—	—	—	.00758	.0543	.00809	.0593	—	—	—	—
12000	—	—	—	—	.00755	.0525	—	—	—	—	—	—
15000	—	—	—	—	.00690	.0503	—	—	—	—	—	—

it is found that $N_{St}N_{Pr}^{2/3}$ varies in all cases very closely with the −0.4 power of N_R as suggested by Colburn. In all but two cases the friction factors plot as single straight lines on the log-log coordinates, and all vary closely as the −0.18 power of N_R. The two exceptions show a change of slope in the middle of the test range, but since this change is very small they too can be represented as a single power of N_R with little error. Taking advantage of these facts, Figs. 12 and 13 were prepared as a simple method of representing the heat-transfer and friction characteristics of all the staggered patterns. These plots provide a convenient, though somewhat speculative, method for interpolating to obtain the basic heat-transfer and flow-friction design data for intermediate tube layouts.

Fig. 14 reveals the results of the row-to-row heat-transfer traverses. It was found that the row-to-row behavior varied somewhat with Reynolds number, but nevertheless, a single curve
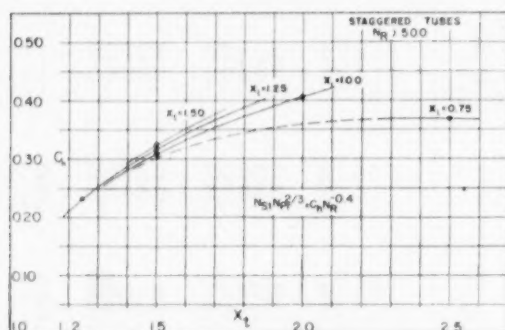
Fig. 12 INFLUENCE OF STAGGERED-TUBE-BUNDLE PITCH ON HEAT TRANSFER
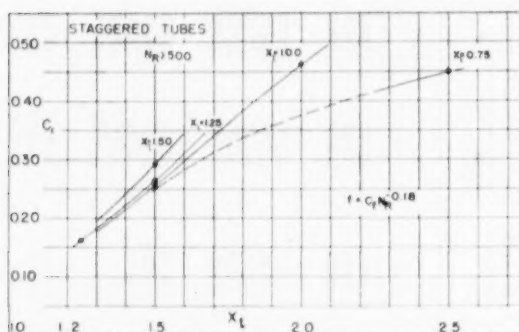
Fig. 13 INFLUENCE OF STAGGERED-TUBE-BUNDLE PITCH ON FRICTION

could be used over the Reynolds-number range considered with little error. The data shown in Fig. 14 were all obtained near the middle of the Reynolds-number test range. In order to present these data on a common basis they were reduced to the ratio of the conductance for a given tube to the conductance of any tube in the center of the core which is unaffected by the entrance and exit conditions.

As can be seen, the entrance and exit effects differ with pattern to a certain degree, although the behavior of all is qualitatively similar. Where high accuracy is required for a heat exchanger with a relatively few number of rows the particular curves drawn through the data points of Fig. 14 can be employed directly. However, to provide a more useful result for most heat-exchanger design work where the over-all correction is less than
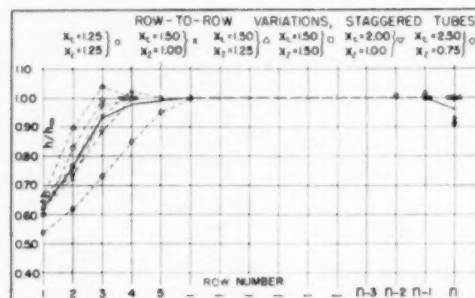
Fig. 14 ROW-TO-ROW VARIATION OF UNIT HEAT-TRANSFER CONDUCTANCE
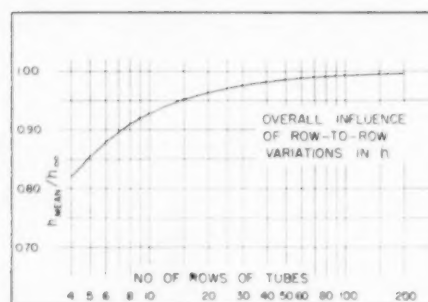
Fig. 15 INFLUENCE OF ROW-TO-ROW VARIATIONS ON OVER-ALL UNIT HEAT-TRANSFER CONDUCTANCE

10 per cent, the data of Fig. 14 are averaged by the full line, and the integrated results presented in Fig. 15. The curve in Fig. 15 then applies as a single direct correction to the infinite tube-bank conductances as determined from Figs. 5, 7 to 11.

The final test results presented are for the in-line pattern, X_l = 1.50, X_t = 1.25, obtained by the steady-state steam-to-air method, Fig. 16 and Table 2. A marked transition dip is evident for both heat transfer and friction, similar to that obtained for flow through tubes. Transient tests of the same pattern showed fair agreement in the turbulent-flow region ($N_R > 3000$), but differed substantially in the transition and laminar regions. Consequently the transient technique is not useful in these regions.

Note that in the transition region poor agreement was obtained for isothermal versus hot-core friction factors. This is a result of the row-to-row variations in heat-transfer conductance and their effect on the air-density variation through the test core.

DISCUSSION

It has been demonstrated in the preceding sections that the transient-test technique, which gives the heat-transfer behavior of a single tube in the bundle, can yield heat-transfer design data for flow over staggered tube banks in substantial agreement with that obtained by the steady-state methods. It should be emphasized strongly, however, that for in-line tube banks in viscous and transition flow, the row-to-row boundary-layer influence is substantial and flow-mixing between the rows is small. As a consequence the transient-technique single-tube results cannot be extended to predict tube-bundle behavior, except for turbulent main-stream flow.

The test results for only one core are compared with those of previous investigators, Fig. 4, but it should be added that a similar comparison is obtained for all four of the patterns for which there are earlier test data. In each case the Grimison data
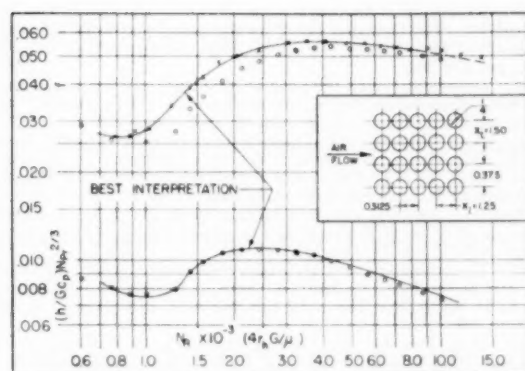
FIG. 16   BASIC HEAT-TRANSFER AND FLOW-FRICTION DESIGN DATA, STEADY-STATE TESTS, IN-LINE. $X_l = 1.50$, $X_t = 1.25$

Tube outside diameter, 0.25 in.
Hydraulic radius, r_h, 0.00415 ft
Minimum free-flow area, transverse spacings
No. of rows deep, 15
o, Hot-core test points.   Heat-transfer data evaluated on basis of zero steam-side resistance
x, Cold-core friction factors
Best interpretation of friction data based on cold-core tests
Best interpretation of heat-transfer data based on an allowance for steam-side resistance

(3) yield both friction and heat-transfer curves that lie 15 to 20 per cent above the data presented here.   In all cases the Colburn equation for $N_{St}N_{Pr}^{2/3}$ actually lies closer to the test data, although not always as close as shown in Fig. 4.

The fact that the heat-transfer characteristics, for the infinite tube bundle, for the staggered patterns, plot as a straight line on log-log co-ordinates, and that the slope is virtually the same in all cases, appears to indicate that there is no basic change in flow mechanism over the Reynolds-number and tube-pattern range considered.   There is apparently a partial laminar boundary layer on each tube with separation and a turbulent main stream. The tendency of the friction-factor curve slope to decrease at low Reynolds numbers for two of the test cores may indicate a beginning of transition to viscous flow.   The data of Bergelin (5) using oil indicates that transition in staggered-tube arrangements is not well defined, but should become noticeable at about the lowest Reynolds numbers of these tests.   It is thus not recommended that these data be extrapolated to lower Reynolds numbers.   Bergelin indicates a much more pronounced transition for in-line arrangements, and the present results, Fig. 16, bear this out very strikingly.

Transient tests of the in-line pattern, $X_t = 1.50$, $X_t = 1.25$ (not shown), indicate good heat-transfer agreement with the steady-state performance in the turbulent-flow region, but only a 15 to 20 per cent "dip" in the transition to viscous flow.   This is due to the unmixed character of viscous flow and the tendency for a temperature profile to extend completely across the flow stream in the steady-state core, rather than being confined to a relatively thin boundary layer.   In this situation the transient technique does not yield information useful for heat-exchanger design.

Because of the very pronounced dip in the transition region of the in-line arrangement, an in-line heat exchanger does not appear to be attractive where low Reynolds-number design becomes necessary (low-density fluids, small-diameter tubes).   The dip means a relatively large-size heat exchanger for a given heat-transfer performance and pressure drop (as compared to a staggered arrangement) and also probably involves a considerable degree of design uncertainty since this is a region of flow instability.

A further point of interest in the in-line tube-bank behavior is

that an objectionable howl developed and persisted for all tests at $N_R > 8000$.   This aerodynamically induced vibration has been noted before (8) and is discussed in (14) as a Strouhal number effect ($V/D \times$ sound frequency).   When the frequency of the alternate shedding vortexes from the tubes and the natural bending frequency of the tubes coincide, a resonant condition develops which may completely obviate the use of the in-line arrangement. Apparently, in a staggered arrangement the regular type of von Kármán vortex street does not develop and no resonant condition has been observed.   These phenomena should be considered by heat-exchanger designers.

The row-to-row heat-transfer behavior for the staggered-tube arrangements, shown in Fig. 14, indicates not only that the heat-transfer conductance of the rows near the tube-bank entrance is considerably lower than those rows in the bank interior, but that this low conductance occurs only to a marked extent in the first two or three rows, and sometimes in the last.   Over-all tube-bank tests (1) had appeared to indicate a gradual increase in conductance as the number of rows is increased to ten but obviously this is only the integrated effect of the first few rows.   The low conductance of the first tube is evidently due to the relatively low velocity to which the front side of this tube is exposed, together with the low intensity of turbulence in the oncoming stream.   A higher-velocity stream impinges on the second-row tubes raising the conductance but the turbulence intensity is still essentially that of the oncoming stream.   The third-row tubes in most cases come within a few per cent of full conductance.   In some cases the last tube conductance drops off owing to the fact that the flow is not forced around the rear side of the tube by succeeding tubes.

The integrated effect of these few rows is shown in Fig. 15 and indicates that even for 10 rows there is a 7 per cent effect.   It is interesting to compare the ratio of the mean conductance for a 10-row bank, with the corrections given by Pierson (1):

No. of rows	4	5	6	7	8	9	10
$h_{mean}/h_{10(mean)}$	0.88	0.92	0.94	0.97	0.98	0.99	1.00
Pierson	0.87	0.92	0.94	0.96	0.97	0.99	1.00

The results are practically identical, but of course the earlier data give no indication of the relationship of a 10-row bank to deeper banks.

The effect of core depth on friction was not obtained in these tests.   Since all the test cores had from 13 to 26 rows it is believed that the different friction behavior of the first and last tubes will have only a minor influence on the over-all friction factor. Pierson indicates higher friction factors for shallow tube banks, which is apparently a result of the free expansion at the core exit. However, elementary analysis indicates that for the core tested not more than 1 to 2 per cent of the total pressure drop possibly could be attributed to excess form drag on the last tube row.

CONCLUSIONS

The following conclusions result from this investigation:

1   The transient heat-transfer test technique is a simple, accurate method for determination of the basic heat-transfer characteristics of tube banks providing that the pattern and flow conditions are such that there is adequate mixing between the tube rows.   The method is not adequate for viscous flow.

2   The transient method has the advantages that essentially isothermal heat-transfer data are obtained, so that the effects of temperature-dependent fluid properties are eliminated; and the performance of individual tubes within the bank is obtained instead of merely the over-all bank.

3   The turbulent-flow heat-transfer characteristics of compact staggered-tube banks, $N_{St}N_{Pr}^{2/3}$, vary closely as the -0.4 power of the Reynolds number, while the friction factors vary closely as the -0.18 power of the Reynolds number.   These design data can

be correlated by functions of geometry alone. Figs. 12 and 13 present tentative correlations which need further experimental verification.

4   The effects on heat transfer of the entrance and exit of the tube bank are evident to a marked degree only in the first two rows, and to a lesser degree in the third and last rows, Fig. 14. However, the integrated effect of these rows is significant even for banks 10 rows deep, Fig. 15.

5   In-line tube banks show a very marked transition from turbulent to viscous flow in the approximate Reynolds-number range 1000–4000 with an appreciable decrease in heat-transfer conductance and friction factor. Staggered banks do not exhibit this marked transition and thus are better suited to low Reynolds-number heat-exchanger design. Additionally, in-line banks in turbulent flow will tend to vibrate under certain conditions which are not yet fully established.

ACKNOWLEDGMENTS

BIBLIOGRAPHY

1   "Experimental Investigation of the Influence of Tube Arrangement on Convection Heat Transfer and Flow Resistance in Cross Flow of Gases Over Tube Banks," by O. L. Pierson, Trans. ASME, vol. 59, 1937, pp. 563–572.

2   "Experimental Investigation of Effects of Equipment Size on Convection Heat Transfer and Flow Resistance in Cross Flow of Gases Over Tube Banks," by E. C. Huge, Trans. ASME, vol. 59, 1937, pp. 573–582.

3   "Correlation and Utilization of New Data on Flow Resistance and Heat Transfer for Cross Flow of Gases Over Tube Banks," by E. D. Grimison, Trans. ASME, vol. 59, 1937, pp. 583–594.

4   "Heat Transfer and Pressure Drop During Viscous Flow Across Unbaffled Tube Banks," by O. P. Bergelin, A. P. Colburn, and H. L. Hull, University of Delaware Engineering Experiment Station Bulletin No. 2, Newark, Del., June, 1950.

5   "Heat Transfer and Fluid Friction During Flow Across Banks of Tubes—IV," by O. P. Bergelin, G. A. Brown, and S. C. Doberstein, Trans. ASME, vol. 74, 1952, pp. 953–968.

6   "Determination of Unit Conductances For Heat and Mass Transfer by the Transient Method," by A. L. London, H. B. Nottage, and L. M. K. Boelter, Industrial and Engineering Chemistry, vol. 33, 1941, p. 467.

7   "Heat Transfer and Flow-Friction Characteristics of Some Compact Heat-Exchanger Surfaces, Part 1—Test System and Procedure," by W. M. Kays and A. L. London, Trans. ASME, vol. 72, 1950, pp. 1075–1086.

8   "Gas Turbine Plant Heat Exchangers," by W. M. Kays, A. L. London, and D. W. Johnson, ASME Monograph, 1951.

9   "Heat-Transfer and Flow-Friction Characteristics of Some Compact Heat-Exchanger Surfaces, Part 3—Design Data for Five Surfaces," by A. L. London, W. M. Kays, and D. W. Johnson, Trans. ASME, vol. 74, 1952, pp. 1167–1178.

10   "An Investigation of Aircraft Heaters—Part II, Properties of Gases," by Myron Tribus and L. M. K. Boelter, NACA W-9, October, 1942.

11   "A Summary of Viscosity and Heat-Conduction Data for He, A, H_2, O_2, N_2, CO, CO_2, H_2O, and Air," by F. G. Keyes, Trans. ASME, vol. 73, 1951, pp. 589–596.

12   Discussion, by M. Jakob, Trans. ASME, vol. 60, 1938, pp. 384–386.

13   "Heat Transmission," by W. H. McAdams, McGraw-Hill Book Company, Inc., New York, N. Y., 1942.

14   "Dynamics of Real Fluids," by E. G. Richardson, Edward Arnold and Company, London, England, 1950.

15   "Development of a Transient Technique for Determining the Convective Heat Transfer Characteristics for Flow of a Gas Normal to Circular Tube Banks," by R. K. Lo, thesis for the Degree of Engineer, Stanford University, Stanford, Calif., June, 1951.

Erosion by Melting and Evaporation[1]

By KURT BERMAN,[2] BALLSTON SPA, N. Y.

This work represents an investigation of the erosion of solid bodies placed in an air stream. The test specimens were formed into cylindrical and conical shapes. Ice, acetophenone, and para-dichloro-benzene were used as the materials for the solid models. It was possible to correlate the rate of erosion as a function of the Reynolds number.

NOMENCLATURE

The following nomenclature is used in the paper:

A = a pure number in Equation [5]

c_p = heat capacity at constant pressure

Δd = rate of change of diameter at a given distance x from tip of specimen

$\mathfrak{D}_{12}$ = normal diffusion coefficient

h = heat-transfer coefficient

k = thermal-conductivity coefficient

L_f = heat of fusion of solid

L_s = heat of sublimation

L_v = heat of vaporization of diffusing substance at temperature T_s

m = exponent in Equation [5]

n = exponent in Equation [5]

N_{Nu} = Nusselt number = hx/k

N_{Pr} = Prandtl number = $\dfrac{\nu \rho c_p}{k}$

N_{Re} = Reynolds number = ux/ν

N_{Sc} = Schmidt number = $\dfrac{\nu}{\mathfrak{D}_{12}}$

N_{St} = Stanton number = $\dfrac{h}{u_0\,\rho_0\,c_{p_0}}$

N_{Ta} = Taylor number = $\dfrac{\beta x}{\mathfrak{D}_{12}}$

p = partial pressure of diffusing substance in free stream

p_v = water vapor partial pressure in free-air stream

q = heat-transfer rate per unit area

R_1 = gas constant for the diffusing substance per unit mass

$r = \dfrac{\alpha}{\pi - \alpha}$

s = distance along surface from leading edge where local velocity equals free-stream velocity (Equation [9])

T = static temperature

u_1 = local velocity at edge of flow boundary layer

u_0 = free-stream fluid velocity

x = actual distance along solid surface, starting from tip

α = slope angle (Fig. 4) radians

β = mass-transfer coefficient

ϕ = indicates a function in Equation [5]

ρ = density

ν = kinematic viscosity

---

0 = subscript, refers to free-stream condition

s = subscript, refers to solid-surface condition

m = subscript, refers to average condition

INTRODUCTION

The problem of erosion is of sufficient technological importance to have warranted extended study. The word "erosion," as usually employed in the literature, is defined as the destruction of materials by physical effects, while corrosion is the result of chemical or electrochemical action. Since it is usually quite difficult to separate the chemical from the physical effects, in all subsequent discussions, the word erosion will be used to cover all mechanisms, including corrosion, which are active in wearing away solid surfaces placed in a flow field. Although the corrosive and abrasive destruction of metals and other materials has been investigated in great detail, comparatively little interest has been expressed in the erosion of solid surfaces by evaporation and melting. A few workers in the field of heat transfer have considered this type of erosion mechanism. However, their motive was not primarily to study the phenomenon but rather to use the process of erosion as a means for obtaining heat-transfer data.[3]

Since it is ordinarily quite difficult to obtain local heat-transfer coefficients without a great deal of equipment and consequent large financial expenditure, V. Klein[4] conceived the idea of simplifying the procedure by constructing cylindrical ice models and placing them in a transverse stream of warm air inside a duct. Studying the change in the specimens as the ice melted, he was able to calculate the local heat transfer at various points along the surface. His measuring technique consisted of molding the deformed cylinders in plasticine and making reproductions in plaster of paris. The changes in dimensions were then studied from these models.

More recently, C. C. Winding and A. J. Cheney, Jr.,[5] using naphthalene sticks instead of ice, obtained mass and heat-transfer data for various types of tube banks inside a duct. At the end of the experiment they measured the deformations of the tubes by placing them in the same molds in which they had been prepared originally, determining the change in dimensions by means of feeler gages.

It is the purpose of this paper to report the results of a study on the erosion deformation of solid materials placed in a free-air stream.

EXPERIMENTAL APPARATUS AND TECHNIQUE

Cylindrical and conical ice, acetophenone, and para-dichlorobenzene specimens were supported in a free-air stream whose temperature, velocity, and humidity could be controlled. A record of the erosion process was obtained by taking pictures of the test substance at selected time intervals. The analysis of the photographic plates consisted of measuring, by means of a comparator, the diameter of the specimens at various points along their surface.

---

[3] Recently Messinger has studied the phenomenon in reference to icing problems "Equilibrium Temperature of an Unheated Icing Surface as a Function of Air Speed," by B. L. Messinger, *Journal of the Aeronautical Sciences*, vol. 20, 1953, pp. 29-42.

[4] Thesis by V. Klein, Technische Hochschule, Hannover, Germany, 1933; summary in *Archiv Wärmewirt*, vol. 15, 1934, p. 150.

[5] "Mass and Heat Transfer in Tube Banks," by C. C. Winding and A. J. Cheney, Jr., *Industrial and Engineering Chemistry*, vol. 40, 1948, pp. 1087-1093.
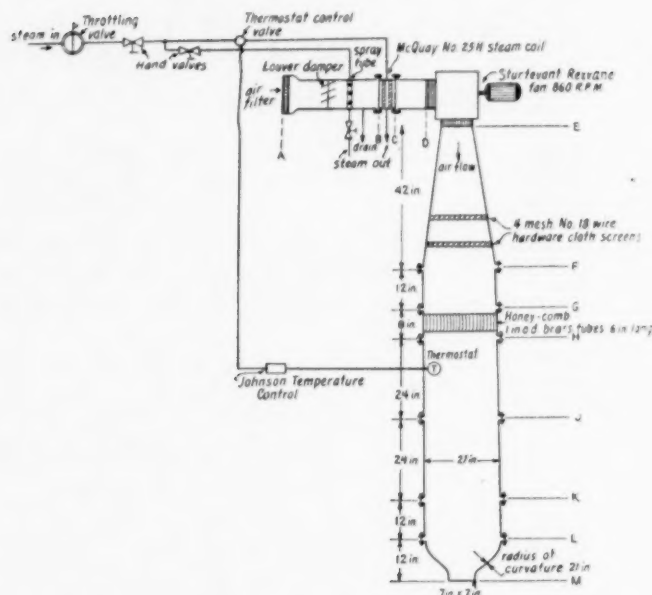
Fig. 1 Air-Supply System

The two main components of the apparatus were an air-supply system and the photographic equipment for recording the erosion progress. A brief description follows:

Air-Supply System. A fan was mounted in such a direction that the air flow was vertically downward. A square cross-section duct led from the blower outlet to the test area. The inside cross-sectional area of every section, except the diffuser and the nozzle, was 21 × 21 in. The nozzle dimensions changed smoothly from an initial 21 × 21 in. to an exit cross-sectional area of 7 × 7 in. A schematic diagram of the complete duct work is shown in Fig. 1.

The air entered the fan through a section containing a steam-heating coil, a louver damper, and a spray tube, which permitted an increase in the water-vapor content of the entering air. The air velocity could be varied from zero to 45 fps. A Johnson thermostat control permitted air-temperature control.

Photographic Equipment. A Kodak Recomar camera was mounted 24½ in. in front of the nozzle. The pictures were taken on Eastman Kodak 9 × 12 cm "super-ortho press" plates.

Selection and Preparation of Test Specimens. Ice was selected as the principal test material, although several tests were conducted with acetophenone and para-dichloro-benzene. The experimental work was restricted to cylindrical and conical shapes. The molds were constructed by sealing pieces of pyrex-glass tubing in a hemispherical nose. All but two of the cylindrical models were prepared in 2.45-cm-ID tubes. The two exceptions were frozen in a 4-cm-ID tube. The length of the individual test specimens varied from 30 to 35 cm. Conical molds were drawn out on a glass-blower's lathe from glass tubing. The models were frozen in the molds which had been immersed in a dry ice-alcohol bath. Wooden sticks were permitted to become imbedded in the specimens and served as the mounting support. A cylindrical ice test specimen is shown in Fig. 2. The test specimen was placed in the free-air stream about 4 in. below the nozzle edge.

Evaluation of Photographic Plates. The variable width of the specimen, as shown on the photographic plate, was measured by
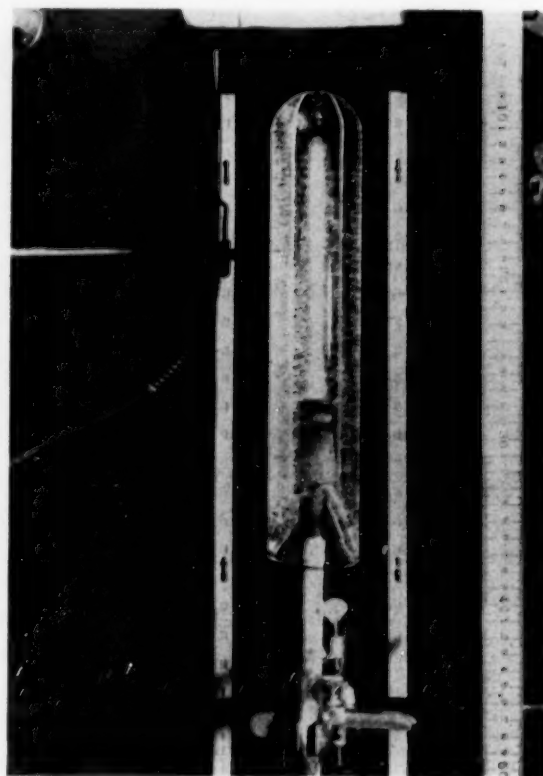
Fig. 2 Cylindrical Ice Specimen

TABLE 1 ORGANIZATION OF EXPERIMENTAL DATA

	Plate No. 443			Plate No. 444		Change from Plate 443 to 444	
Reference mark of meter stick	Diameter, cm	Distance from tip, cm. Tip at 17.95 cm	Diameter, cm		Distance from tip cm. Tip at 20.92 cm	Change in diameter per 3 min, cm	Average distance from tip, cm
19	0.5624	1.09					
20	0.8353	2.10					
						Column I	
22	1.3299	4.12	0.7375	1.14		0.5924	2.63
24	1.7257	6.13	1.3192	3.16		1.4065	4.65
26	2.1175	8.14	1.7800	5.17		0.3375	6.66
28	2.4710	10.15	2.1794	7.18		0.2916	8.66
30	2.8586	12.16	2.5848	9.19		0.2738	10.67
32	3.2749	14.17	3.0192	11.20		0.2557	12.69
34	3.6553	16.18	3.4173	13.21		0.2380	14.70
36	4.0575	18.19	3.8090	15.22		0.2485	16.71
38	4.3683	20.20	4.1544	17.23		0.2139	18.72
40	4.6463	22.20	4.4602	19.24		0.1861	20.72
42	5.0293	24.21	4.8061	21.25		0.2232	22.73

means of a microscope comparator, originally built by Wolz of Bonn.[6] The change in diameter of a specimen, as determined from successive plates, supplied the experimental data.

EXPERIMENTAL RESULTS

The rate of diameter change at identical fixed points of successive plates of the same specimen was calculated and plotted on log-log paper, using the rate of change of the diameter and the distance from the tip of the specimen as the co-ordinates. The diameter change was deemed a suitable correlating factor since it is proportional to the rate of mass removal per unit area of surface. The actual distance x along the surface, starting from the tip, was approximated by means of straight-line cords drawn between selected points of the surface. It was assumed that the specimen was symmetrical with respect to its axis of rotation, so that half of the measured diameter can be regarded as the true radius of the cross section. The method of calculation is illustrated in Fig. 3. The various operations can probably be best

$$\tan \alpha = \frac{\frac{d_{24} - d_{22}}{2}}{2}$$

$$x_{22 \rightarrow 24} = 2 \sec \alpha$$

d_{24} is the measured diameter at point 24
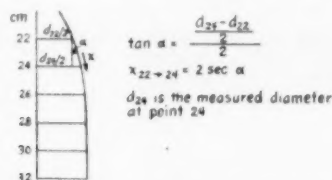
FIG. 3 ILLUSTRATION DEMONSTRATING APPROXIMATION OF A DISTANCE ALONG A CURVED SURFACE BY STRAIGHT LINES

explained by means of Table 1 in which are recorded the diameter measurements for a specimen at one time interval, i.e., the actual measurements on the photographic plates multiplied by the magnification factor. Column I contains the quantities which were plotted in the graphs.

Experiments With Cylindrical Specimens Placed Parallel to Air Stream. Eleven experiments were made with ice specimens, two with acetophenone and one with para-dichloro-benzene. Unless the hemispherical surface of the models has a smooth contour, a necklike erosion of the specimen will occur. This is illustrated in Fig. 4.

Pictures were taken at the beginning of the experiment and usually at successive 3-min intervals. The duration of the experiments varied from 9 min to 39 min, except for the case of the para-dichloro-benzene specimen where the test lasted 7 hr.

Data for one of the tests with ice are shown in Figs. 5 to 7, while photographs of the eroding specimen are shown in Fig. 8. The rate of erosion increases considerably, especially at points near the tip, as the specimen surface becomes more curved. The experimental data, therefore, were separated into components

[footnote] See *"The Astrophysical Journal,"* vol. 23, April, 1906, no. 3, p. 205, second paragraph.

No.286-beginning No.287-3 min No.288-6 min.

No.289-9 min. No.290-12 min No.291-15 min.

No.292-18 min. No.293-21 min. No.294-24 min.

Air velocity=29.5 ft/sec
Air temperature = 81 F
p_v = .14 psia

No.295-27 min. No.296-30 min.
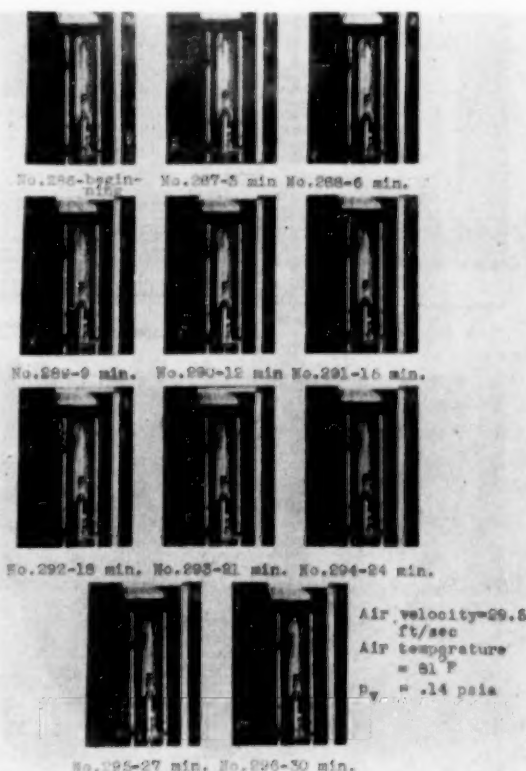
FIG. 4 NECK FORMATION ON AN ERODING ICE SPECIMEN

representing the initial and the later stages of the erosion process. The rate of diameter change for the first 9 to 12 min was plotted on one graph and the remaining data on a separate one. The experimental points could be correlated within 10 per cent by straight lines. The results are summarized in Table 2.

Experiments With Conical Ice Specimens. Ten experiments were performed with conical ice specimens, having apex angles of 12, 16, and 30 deg, respectively. Photographs of a specimen undergoing test are shown in Fig. 9. The results of the experiments are summarized in Table 3.

DISCUSSION OF RESULTS

At least three factors must be considered in evaluating the data:

Fig. 5

Fig. 6

FIG. 7 (*right*)

FIG. 8   EROSION OF A CYLINDRICAL ICE SPECIMEN
(Air velocity 29.5 fps; air temperature 84 F; p_c = 0.18 psi.)

FIG. 9   EROSION OF A CONICAL ICE SPECIMEN
(Air velocity 30.4 fps; air temperature $96^{1}/_{2}$ F; p_c = 0.32 psi.)

TABLE 2   SUMMARY OF EXPERIMENTAL DATA WITH CYLINDRICAL MODELS PLACED PARALLEL TO AIR STREAM

Test material	Air velocity, fps	Water vapor pressure in free-air stream, p_o, psia	Air-stream temperature, deg F	Duration of experiment, min	Change of diameter of specimen, cm/3 min In initial stage	In later stage
Ice..............	29.5	0.18	77	21	$0.268\,x^{-0.43}$	$0.330\,x^{-0.40}$
Ice..............	29.5	0.18	84	18	$0.305\,x^{-0.43}$	$0.395\,x^{-0.40}$
Ice..............	29.5	0.43	$92\frac{1}{2}$	30	$0.560\,x^{-0.46}$	$0.800\,x^{-0.43}$
Ice..............	29.5	0.25	$91\frac{1}{4}$	39	$0.410\,x^{-0.470}$	$0.570\,x^{-0.44}$
Ice..............	29.5	0.46	$93\frac{3}{4}$	15	$0.640\,x^{-0.48}$	$0.825\,x^{-0.43}$
Ice..............	29.5	0.09	94	9	$0.250\,x^{-0.46}$	
Ice..............	29.5	0.095	$61\frac{3}{4}$	12	$0.160\,x^{-0.44}$	
Ice..............	29.5	0.18	107	21	$0.430\,x^{-0.43}$	$0.635\,x^{-0.43}$
Ice..............	43.3	0.15	81	21	$0.310\,x^{-0.43}$	$0.395\,x^{-0.41}$
Ice..............	35.6	0.15	78	18	$0.255\,x^{-0.43}$	$0.310\,x^{-0.40}$
Ice..............	24.1	0.15	$75\frac{1}{2}$	15	$0.200\,x^{-0.43}$	
Acetophenone....	29.5		118	15	$0.650\,x^{-0.55}$	
Acetophenone....	29.5		$83\frac{3}{4}$	15	$0.260\,x^{-0.54}$	
p-dichloro-benzene........	29.5		93	7 hr	$0.172\,x^{-0.5}$ cm/hr	

TABLE 3   SUMMARY OF EXPERIMENTAL WORK ON CONICAL ICE SPECIMENS

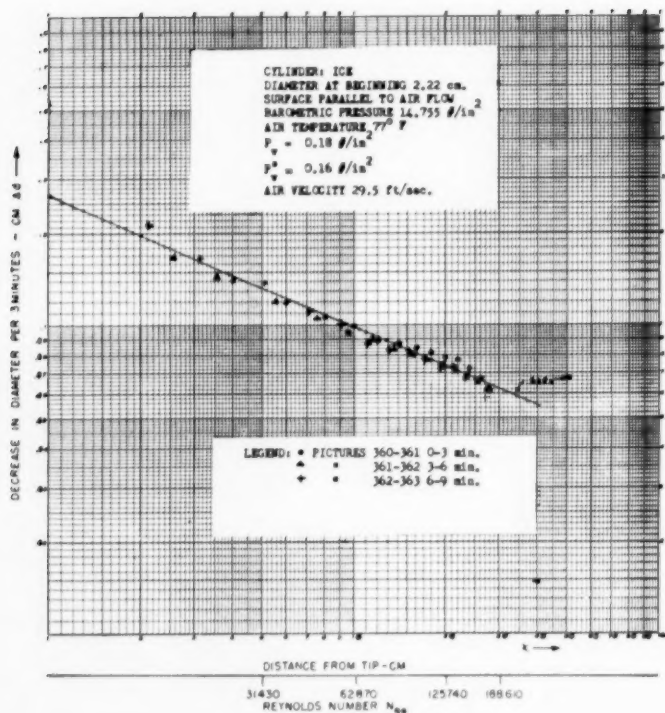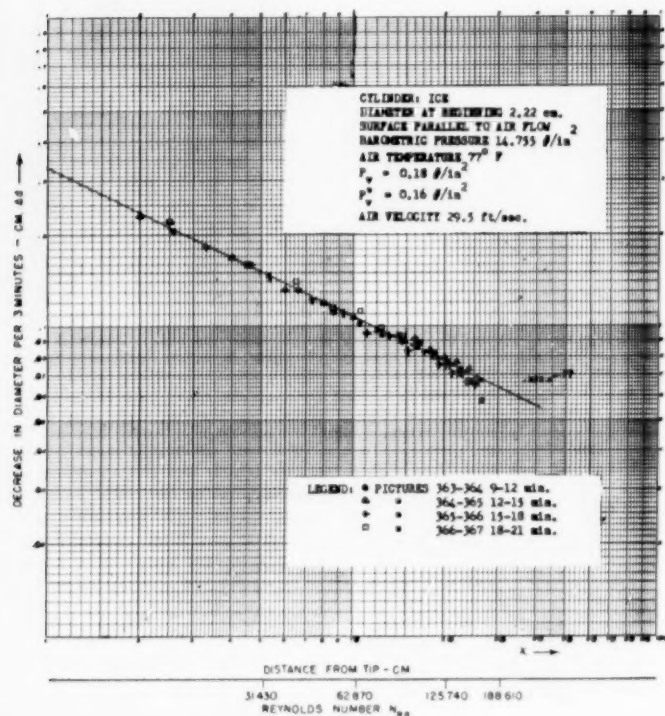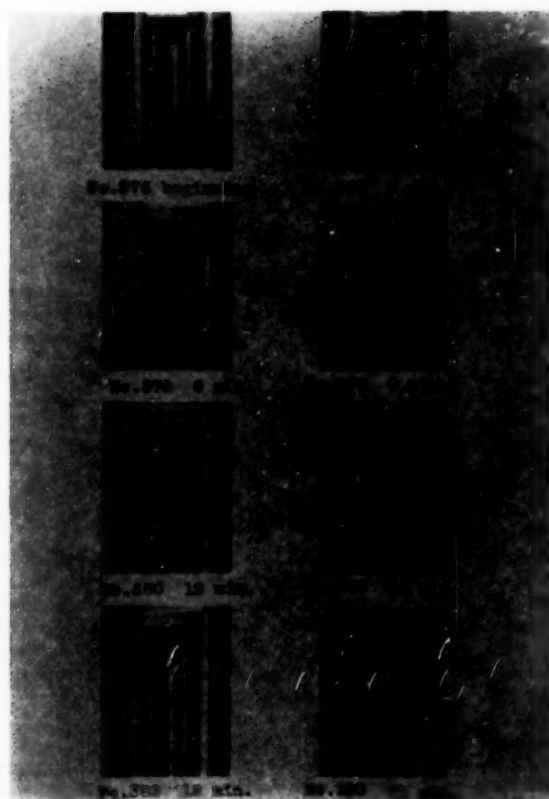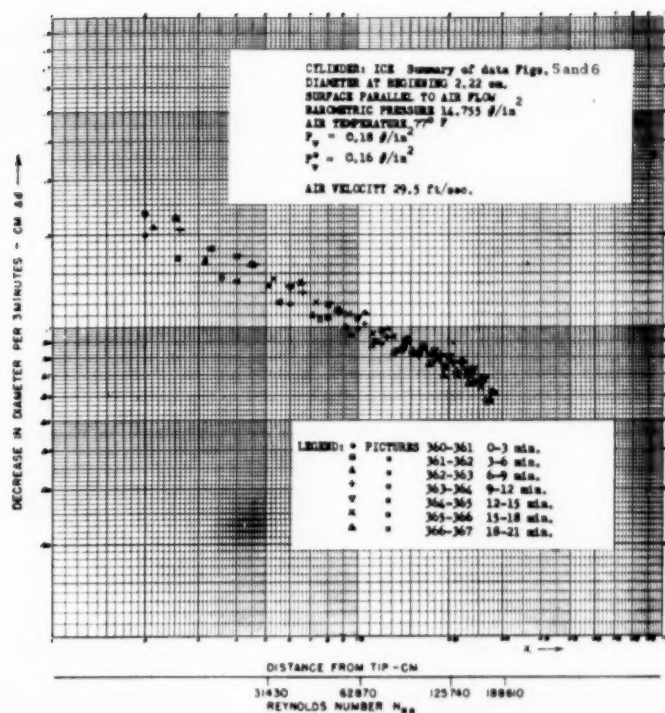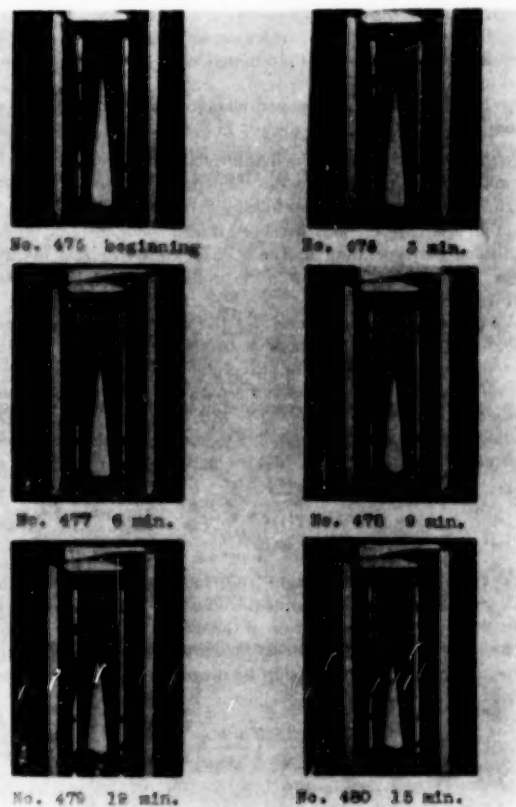| Test material	Air velocity, fps	Water-vapor pressure in free-air stream, psia	Air-stream temperature, deg F	Duration of experiment, min	Total apex angle of cone, deg	Rate of change of diameter of specimen, cm/3 min
Ice......	29.5	0.10	108	6	12	$0.485\,x^{-0.5}$
Ice......	30.4	0.29	94	18	12	$0.650\,x^{-0.49}$
Ice......	30.4	0.32	$96\frac{1}{2}$	15	12	$0.720\,x^{-0.49}$
Ice......	29.5	0.29	121	12	12	$0.860\,x^{-0.49}$
Ice......	29.5	0.46	$94\frac{3}{4}$	15	12	$0.900\,x^{-0.5}$
Ice......	29.5	0.28	$94\frac{1}{2}$	21	12	$0.630\,x^{-0.5}$
Ice......	29.5	0.09	$61\frac{1}{2}$	12	12	$0.245\,x^{-0.5}$
Ice......	29.5	0.09	86	9	12	$0.300\,x^{-0.49}$
Ice......	30.4	0.30	89	12	30	$0.700\,x^{-0.5}$
Ice......	30.4	0.32	$97\frac{1}{2}$	18	16	$0.770\,x^{-0.5}$

1   A liquid film forms on the surface of a solid which erodes with a phase transition from solid to liquid. Thus there is established a cocurrent gas-liquid flow on the solid surface.

2   Diffusion and heat transfer occur simultaneously in the same field and it must be determined what mutual effect they exert on each other.

3   The shape of the specimen changes during the process of erosion.

Without repeating here the details of the analysis made in the original work[7] to determine the influence of these factors, the conclusions are summarized as follows:

(a) In the case of both ice and acetophenone erosion, under conditions corresponding to those encountered in this investigation, the liquid layer is so thin that it exerts no influence on the heat transfer.

(b) The modification caused by the mass transfer is small enough so it appears that the heat transfer and diffusion can be treated as independent and additive phenomena.

(c) The data will be discussed separately for the initial and later stages of erosion.

In accordance with the foregoing assumption, the rate of heat transfer per unit area to the solid is equal to the sum[8]

$$q = h\,(T_0 - T_s) + \frac{\beta}{R_1 T}\,(p_0 - p_s)\,L_v \dots\dots\dots\,[1]$$

where the first term on the right is the heat-transfer contribution while the second one constitutes the effect on the solid surface of the condensation or evaporation of the diffusing mass.

The heat and mass-transfer coefficients can be written in the following functional relationship by means of analogy considerations[7]

$$\beta = h\,\frac{\mathfrak{D}_{12}}{k}\left(\frac{k}{\mathfrak{D}_{12}\rho c_p}\right)^n \dots\dots\dots\dots\,[2]$$

Substituting this expression in Equation [1] and noticing further that the total heat transfer is related to the measured rate of erosion by the relation

$$q = \rho_s\,\frac{\Delta d}{2}\,L_f \cos\alpha \dots\dots\dots\dots\,[3]$$

one obtains

$$h = \frac{\rho_s\,\dfrac{\Delta d}{2}\,L_f \cos\alpha}{\left[(T_0 - T_s) + \dfrac{\mathfrak{D}_{12}L_v}{k}\left(\dfrac{k}{\mathfrak{D}_{12}\rho c_p}\right)^n \dfrac{p_0 - p_s}{R_1 T_m}\right]} \dots\,[4]$$

Dividing both sides of the expression by the rate of energy transfer per unit temperature difference parallel to the flow direction in the free stream, $\rho_0 u_0 c_{p_0}$, the equation becomes dimensionless. The desired form of the correlating function therefore becomes

$$\frac{\rho_s\,\dfrac{\Delta d}{2}\,L_f \cos\alpha}{\rho_0 u_0 c_{p_0}\left[(T_0 - T_s) + \dfrac{\mathfrak{D}_{12}L_v}{k}\left(\dfrac{k}{\mathfrak{D}_{12}\rho c_p}\right)^n \dfrac{p_0 - p_s}{R_1 T_m}\right]}$$
$$= \frac{h}{\rho_0 u_0 c_{p_0}} = A\phi(N_{Re}^{-m}) \dots\dots\,[5]$$

The experimental data will be evaluated in terms of Equation [5].

The choice of a specific temperature at which to evaluate the various properties of matter is somewhat arbitrary. For the relatively small temperature differences encountered in these experiments, the question of selecting the right datum temperature is not a serious one. In the following calculations, all properties were evaluated at the free-stream temperature. Tables of pertinent values are given in the Appendix.

Initial Stages of Erosion of Cylindrical Specimens. Table 2 indicates that the exponent of z varies somewhat for the different experiments. Since -0.43 is the most prevalent value, it was used as the exponent m in Equation [5]. The following example illustrates the procedure:

[7] "Erosion by Heat Transfer and Diffusion," by Kurt Berman, PhD thesis, Harvard University, 1950.

[8] See Nomenclature for explanation of symbols.

TABLE 4 CORRELATION OF CYLINDRICAL SPECIMENS FOR INITIAL STAGE OF EROSION

Test material	Air velocity, fps	Water-vapor pressure in free-air stream, p_v, psia	Air-stream temperature, deg F	Measured rate of change in diameter, cm/3 min	Corrected rate of change in diameter, cm/3 min	$\dfrac{h}{\rho_0 u_0 c_{p_0}}$
Ice	29.5	0.18	77	$0.268\,x^{-0.45}$	$0.268\,x^{-0.43}$	$0.250\,N_{Re}{}^{-0.43}$
Ice	29.5	0.18	84	$0.305\,x^{-0.43}$	$0.305\,x^{-0.43}$	0.257
Ice	29.5	0.18	107	$0.430\,x^{-0.45}$	$0.410\,x^{-0.43}$	0.261
Ice	29.5	0.09	94	$0.250\,x^{-0.45}$	$0.240\,x^{-0.43}$	0.236
Ice	29.5	0.095	$61^{3}/_{4}$	$0.160\,x^{-0.44}$	$0.155\,x^{-0.43}$	0.228
Ice	29.5	0.46	$93^{3}/_{4}$	$0.640\,x^{-0.44}$	$0.595\,x^{-0.43}$	0.249
Ice	29.5	0.43	$91^{1}/_{2}$	$0.560\,x^{-0.45}$	$0.535\,x^{-0.43}$	0.242
Ice	29.5	0.25	$91^{1}/_{4}$	$0.410\,x^{-0.475}$	$0.365\,x^{-0.43}$	0.235
Ice	43.3	0.15	81	$0.310\,x^{-0.43}$	$0.310\,x^{-0.43}$	0.242
Ice	35.6	0.15	78	$0.255\,x^{-0.43}$	$0.255\,x^{-0.43}$	0.233
Ice	24.1	0.15	$75^{1}/_{2}$	$0.200\,x^{-0.43}$	$0.200\,x^{-0.43}$	0.239
Acetophenone	29.5		118	$0.650\,x^{-0.55}$	$0.480\,x^{-0.43}$	0.245
Acetophenone	29.5		$83^{3}/_{4}$	$0.260\,x^{-0.54}$	$0.195\,x^{-0.43}$	0.298
p-dichloro-benzene	29.5		93	$0.172\,x^{-0.5}$	$0.145\,x^{-0.43}$	$0.253\,N_{Re}{}^{-0.43}$

TABLE 5 CORRELATION OF CYLINDRICAL SPECIMENS FOR LATER STAGES OF EROSION

Specimen	Air temperature, deg F	Air velocity, fps	Water-vapor pressure in free-air stream, psia	Measured rate of change in diameter, cm/3 min	Corrected rate of change in diameter, cm/3 min	Correlation function, $\dfrac{h}{\rho_0 u_0 c_{p_0}}$
Ice	77	29.5	0.18	$0.330\,x^{-0.49}$	$0.337\,x^{-0.50}$	0.573
Ice	84	29.5	0.18	$0.395\,x^{-0.50}$	$0.395\,x^{-0.50}$	0.610
Ice	107	29.5	0.18	$0.635\,x^{-0.53}$	$0.590\,x^{-0.50}$	0.686
Ice	$93^{3}/_{4}$	29.5	0.46	$0.825\,x^{-0.53}$	$0.770\,x^{-0.50}$	0.588
Ice	$91^{1}/_{2}$	29.5	0.43	$0.800\,x^{-0.53}$	$0.745\,x^{-0.50}$	0.614
Ice	$91^{1}/_{4}$	29.5	0.25	$0.570\,x^{-0.54}$	$0.495\,x^{-0.50}$	0.579
Ice	81	43.3	0.15	$0.395\,x^{-0.51}$	$0.386\,x^{-0.50}$	0.566
Ice	78	35.6	0.15	$0.310\,x^{-0.49}$	$0.317\,x^{-0.50}$	$0.538\,N_{Re}{}^{-0.5}$

Assume $\Delta d = 0.430\,x^{-0.45}$ cm/3 min. This can be written as $0.430\,x^{-0.43}\,x^{-0.02}$ cm/3 min. Calculating the quantity $x^{-0.02}$ for representative values of x, and finding Δd in terms of $x^{-0.43}$, i.e.

at $x =$	$x^{-0.02} =$	$\Delta d = 0.43\,x^{-0.45}$ cm/3 min
5 cm	1.0325	$= 0.416\,x^{-0.43}$ cm/3 min
10 cm	1.0475	$= 0.411\,x^{-0.43}$ cm/3 min
15 cm	1.0555	$= 0.407\,x^{-0.43}$ cm/3 min
20 cm	1.0618	$= 0.405\,x^{-0.43}$ cm/3 min

it is seen that the original correlation can be represented by $0.410\,x^{-0.43}$ cm/3 min within the limits of the experimental error. This procedure was used in all cases requiring such correction. Since correlations of convective heat-transfer data indicate that the exponent n equals approximately $1/2$, this value was inserted in Equation [5].

The results of the correlation for the cylindrical specimens are summarized in Table 4. In the computation for the acetophenone specimens, diffusion was neglected. The average value of the correlation function is $0.243\,N_{Re}{}^{-0.43}$, with a maximum deviation of 8 per cent from the mean.

When the erosion occurs by the process of sublimation, the heat-transfer rate from the air stream to the solid body, after equilibrium conditions have been reached, is equal to the sublimation heat required to vaporize the material which is carried away through the air stream. This is equivalent to saying that

$$h\,(T_0 - T_s) = \frac{\beta}{R_t T}\,(p_s - p_0)\,L_s = \frac{\rho_s}{2}\,\Delta d\,(\cos\alpha)\,L_s \quad [6]$$

where L_s is the heat of sublimation. Using the analogy relation between h and β, it is possible to write a dimensionless relationship

$$\frac{h}{\rho_0 u_0 c_{p_0}} = A\phi(N_{Re}{}^{-n})$$

$$= \frac{\dfrac{\rho_s}{2}\,\Delta d\,\cos\alpha}{\rho_0 u_0 c_{p_0}\left[\dfrac{\mathfrak{D}_{12}}{R_1 T_m k}\left(\dfrac{k}{\mathfrak{D}_{12}\rho c_p}\right)^{1/s}(p_s - p_0)\right]} \quad [7]$$

Assuming $p_0 = 0$, the correlation for the p-dichloro-benzene specimen becomes

$$\frac{h}{\rho_0 u_0 c_{p_0}} = 0.253\,N_{Re}{}^{-0.43} \quad [8]$$

The results for all the cylindrical specimens are in substantial agreement. Therefore it may be concluded that the various assumptions underlying this correlating procedure are good approximations.

Later Stage of Deformations. It would be expected that greater discrepancies would occur in the correlation for the later stages of the erosion process, since the data are then a function of the instantaneous shape of the specimen.

In the following calculations all exponents of x were reduced to -0.5; otherwise the calculations were identical to those of the previous section. The results are presented in Table 5.

The average of the correlation functions is $0.594\,N_{Re}{}^{-0.5}$ with a maximum deviation of 15 per cent from the mean. The corresponding local Nusselt number hx/k is $0.416\,N_{Re}{}^{0.5}$.

Conical Ice Specimens. The problem of a conical specimen differs from the cylindrical case in that the velocity at the edge of the boundary layer no longer can be considered constant. If, as an approximation, the flow along a cone is considered analogous to that of a wedge,[a] then the local velocity would have the form

$$\frac{u_1}{u_0} = \left(\frac{x}{s}\right)^r \quad [9]$$

where

u_1 = local velocity at edge of flow boundary layer

u_0 = free-stream fluid velocity

x = distance along surface from leading edge

s = distance along surface from leading edge where local velocity equals free-stream velocity

$r = \dfrac{\alpha}{\pi - \alpha}$

2α = total cone angle (radians)

[a] "Die Berechnung des Wärmeüberganges in der laminaren Grenzschicht umströmter Körper," by Ernst Eckert, *VDI Forschungsheft* 416, September-October, 1942, 24 pp.

TABLE 6 CORRELATION OF CONICAL ICE SPECIMEN EROSION DATA

Specimen	Total apex angle, deg	Air temperature, deg F	Air velocity, fps	Water-vapor pressure, p_s, psia	Measured rate of change of diameter, cm/3 min	Corrected rate of change of diameter, cm/3 min	$\dfrac{h}{\rho_0 u_0 c_{p_0}}$
Ice	12	121	29.5	0.29	$0.860\,x^{-0.46}$	$0.880\,x^{-0.5}$	$0.731\,N_{Re}^{-0.5}$
Ice	12	$94^{3}/_{4}$	29.5	0.46	$0.900\,x^{-0.50}$	$0.900\,x^{-0.5}$	$0.693\,N_{Re}^{-0.5}$
Ice	12	$94^{1}/_{2}$	29.5	0.28	$0.630\,x^{-0.50}$	$0.630\,x^{-0.5}$	$0.671\,N_{Re}^{-0.5}$
Ice	12	$96^{1}/_{2}$	30.4	0.33	$0.720\,x^{-0.50}$	$0.735\,x^{-0.5}$	$0.678\,N_{Re}^{-0.5}$
Ice	12	94	30.4	0.29	$0.650\,x^{-0.49}$	$0.665\,x^{-0.5}$	$0.690\,N_{Re}^{-0.5}$
Ice	12	108	29.5	0.10	$0.485\,x^{-0.50}$	$0.485\,x^{-0.5}$	$0.679\,N_{Re}^{-0.5}$
Ice	12	86	29.5	0.09	$0.300\,x^{-0.44}$	$0.330\,x^{-0.5}$	$0.667\,N_{Re}^{-0.5}$
Ice	12	$61^{1}/_{2}$	29.5	0.09	$0.245\,x^{-0.50}$ (cm/4 min)	$0.245\,x^{-0.5}$ (cm/4 min)	$0.683\,N_{Re}^{-0.5}$
Ice	16	$97^{1}/_{2}$	30.4	0.32	$0.770\,x^{-0.50}$	$0.770\,x^{-0.5}$	$0.717\,N_{Re}^{-0.5}$
Ice	30	89	30.4	0.30	$0.700\,x^{-0.50}$	$0.700\,x^{-0.5}$	$0.720\,N_{Re}^{-0.5}$

One would expect a correlation of the form

$$\frac{\rho_s \dfrac{\Delta d}{2} L_f \cos \alpha}{\rho_0 u_0 c_{p_0}\left[(T_0 - T_s) + \dfrac{\mathfrak{D}_{12} L_v}{R_1 T_m k}\left(\dfrac{k}{\mathfrak{D}_{12} \rho c_p}\right)^{1/2} (p_0 - p_s) \right]} = \phi_1\left[N_{Re}^{-m}\left(\frac{x}{s}\right)^{r(m-1)}\right] \dots [10]$$

where $N_{Re} = u_1 x/\nu$.

For a 12-deg cone, $r = 0.034$ and it is clear that the value u_1/u_0, as a function of x/s, varies very slowly. Since the values of u_1 for a cone is unknown, the correlations will be carried through in the same manner as for the cylinders, with the free-stream velocity used as the characteristic velocity ($u_1/u_0 = 1$). The results are given in Table 6. All exponents of x have been corrected to -0.5.

The average of the correlation functions for the 12-deg cone is $0.686\,N_{Re}^{-0.5}$ with a maximum deviation of 6 per cent from the mean; the corresponding Nusselt number, $N_{Nu} = 0.48\,N_{Re}^{0.5}$.

All results, so far, have been stated in terms of the dimensionless groups which are conventional in heat-transfer work, i.e., the Nusselt number and the relationship $h/(u_0 \rho_0 c_{p_0})$ which is sometimes designated as the Stanton number. The correlation could just as well have been made in terms of the Taylor number $N_{Ta} = \beta x/\mathfrak{D}_{12}$. From the analogy relationship as expressed in Equation [2], it is apparent, however, that once the Nusselt or Stanton number is known, the other number can be written down at once. Since

$$\frac{h}{\beta} = \frac{k}{\mathfrak{D}_{12}}\left(\frac{\mathfrak{D}_{12} \rho c_p}{k}\right)^{1/2}$$

$$N_{Nu} = \frac{hx}{k} = \frac{\beta x}{\mathfrak{D}_{12}}\left(\frac{\mathfrak{D}_{12} \rho c_p}{k}\right)^{1/2} = N_{Ta}\left(\frac{N_{Pr}}{N_{Sc}}\right)^{1/2} \dots [10a]$$

$$N_{St} = \frac{h}{u_0 \rho_0 c_p} = \frac{\beta k}{\mathfrak{D}_{12} u_0 \rho_0 c_{p_0}}\left(\frac{\mathfrak{D}_{12} \rho c_p}{k}\right)^{1/2} = \frac{N_{Ta}}{N_{Pr}^{1/2} N_{Sc}^{1/2} N_{Re}}$$

where

$$N_{Pr} = \frac{\nu \rho c_p}{k} = \text{Prandtl number}$$

$$N_{Sc} = \frac{\nu}{\mathfrak{D}_{12}} = \text{Schmidt number}$$

Therefore it is unnecessary to make a separate set of calculations for the Taylor number.

CONCLUSIONS

Based on the discussion and data presented, it is now possible to formulate some definite conclusions about the erosion of solid surfaces in a laminar-flow field. The data are correlated by calculating the Stanton number $h/(\rho_0 u_0 c_{p_0})$ as a function of the Reynolds number. Stating the results in terms of more conventional Nusselt-number relationship, the erosion rate for the cylindrical specimens in the initial stage is $N_{Nu} = 0.17\,N_{Re}^{0.57}$. Within the Reynolds-number range from 50,000 to 100,000, this also can be approximated closely by the value $N_{Nu} = 0.37\,N_{Re}^{0.5}$. The corresponding Taylor number, $\beta d/\mathfrak{D}_{12}$, is $0.36\,N_{Re}^{0.5}$. For the latter stages of erosion the Nusselt-number correlation is $N_{Nu} = 0.42\,N_{Re}^{0.5}$.

For the 12-deg cones the Nusselt number is $N_{Nu} = 0.48\,N_{Re}^{0.5}$, or about 20 per cent greater than it is for the cylinders.

Although the primary purpose of this work was concerned with the erosion problem, nevertheless it might be noticed that the techniques used in this investigation could well be adapted to obtaining various heat-transfer and diffusion data for turbulent as well as laminar-flow conditions.

Appendix

COLLECTION OF "PROPERTIES OF MATTER" DATA

Diffusion coefficient of water vapor in air:

Temperature, deg C	$\mathfrak{D}_{12}$, cm²/sec	Source
0	0.209	"Verdunstung und Wärmeübergang
10	0.224	an senkrechten Platten in ruhender
20	0.240	Luft," by R. Hilpert, VDI Forschung-
30	0.252	sheft 355, vol. 3, July–August, 1932.

Diffusion coefficient of para-dichloro-benzene in air: $\mathfrak{D}_{12}$ for para-dichloro-benzene in air was calculated by means of an equation presented by Sherwood.[10]

At 33 deg C and $p_s = 1$ atm, $\mathfrak{D}_{12} = 0.069$ cm²/sec

Thermal-conductivity coefficient of air:

Temperature	$k \times 10^{-5}$ cal/cm sec deg C	Source
0° C	5.782	Recalculated from "Thermodynamic Properties
8° C	5.906	of Air," by J. H. Keenan and J. Kaye, John
32° C	6.443	Wiley & Sons, Inc., New
60° C	6.938	York, N. Y., 1945, p. 36.

[10] "Absorption and Extraction," by T. K. Sherwood, McGraw-Hill Co., 1937, p. 18, equation 31.

Density of air:

0° C	12.931	$\times$ 10^{-4} gm/cc	"Handbook of Chemis-
10° C	12.472		try," by N. A. Lange
20° C	12.046		and G. M. Forker,
30° C	11.647		Handbook Publishers,
40° C	11.247		Inc., New York, N. Y.,
			1946, p. 1439.

Kinematic viscosity of air:

0° C	0.132 cm²/sec	"Handbook of Chemistry"
10° C	0.141	
20° C	0.150	
30° C	0.159	
40° C	0.169	
50° C	0.179	

Heat capacity of air at constant pressure:

$C_p = 0.24$ cal/gm deg C

Universal gas constant:

$$R = 0.08479 \times 10^6 \frac{\text{gm cm}}{\text{gm mole}} \text{ deg K}$$

$$R_1 = \frac{R}{M_1} \qquad M_1 = \text{molecular weight}$$

Heat of fusion and density of ice: Dorsey[11] states an average value of 79.7 cal/gm for the heat of fusion of ice. We used 80 cal/gm throughout the calculation. For the density he recommends a value of 0.916 gm/cm³.

Density of para-dichloro-benzene:[12] The density is 1.458 gm/cm³ at 21 C.

Density of acetophenone (solid): No actual experimental data are available for solid acetophenone. It is slightly heavier than the liquid. We used a value of 1.04 gm/cm³ in the calculations.

Vapor pressure of para-dichloro-benzene: The vapor pressure was calculated from the equation[13]

$$\log_{10} p_{mm} = -\frac{0.05223 (72,218)}{T} + 12.480$$

Heat of fusion of acetophenone: The heat of fusion of acetophenone was taken as 30.1 cal/gm.

[11] "Properties of Ordinary Water Substance," by N. E. Dorsey, Reinhold Publishing Corporation, New York, N. Y., 1940, pp. 463 and 615–618.

[12] Loc. cit., "Handbook of Chemistry," p. 435 (No. 1954).

[13] "International Critical Tables," McGraw-Hill Book Company, Inc., New York, N. Y., vol. 3, 1928, p. 208.

Rapid Measurements of Thermal Diffusivity[1]

By G. E. McINTOSH,[2] D. C. HAMILTON,[3] and W. L. SIBBITT[4]

An apparatus and a technique were developed for determining the thermal diffusivity of metals by a periodic heat-flow method. Measurements with a probable error of ± 6.8 per cent were made on specimens of Armco iron, titanium, zirconium, and Haynes Stellite 25 at temperatures of 456, 564, and 672 R.

NOMENCLATURE

The following nomenclature is used in the paper:

A = cross-sectional area of specimen, sq ft
α = thermal diffusivity, sq ft/hr
C_p = specific heat at constant pressure, Btu/lb$_M$ deg F
h = surface heat-transfer coefficient, Btu/hr sq ft deg F
k = thermal conductivity, Btu/hr ft deg F
K = dimensional constant depending upon experimental units and period of temperature wave
ρ = density, lb$_M$/cu ft
T = temperature, deg F, deg R
τ = time, hr
$\Delta\phi$ = phase lag of temperature wave between two station points, radians
x, y, z = distance, ft
ΔX = distance between two thermocouple-station points, ft

INTRODUCTION

At present there is a great need for accurate data on thermal conductivity k, and thermal diffusivity $\alpha = k/(\rho C_p)$, of metals in the temperature range from 1000 to 2000 F. Since the structure of metal is not stable at these elevated temperatures the measurements should be made as rapidly as possible. Most of the present data were obtained on metals which had been maintained at elevated temperatures for periods of hours or even days.

For heat flow in homogeneous isotropic bodies in which there is no energy generation the following simplified equation approximates the conditions

$$\frac{\partial T}{\partial \tau} = \alpha \left[\frac{\partial^2 T}{\partial x^2} + \frac{\partial^2 T}{\partial y^2} + \frac{\partial^2 T}{\partial z^2} \right] \quad \text{[1]}$$

Although α is a thermal property it is defined without heat or temperature units (length^2/time). Thermal diffusivity is a function of state and is usually defined as a function of pressure, temperature, and load stresses for unit temperature gradient in a given material.

The direct measurement of thermal diffusivity has definite theoretical advantages. Since α contains no heat term, the need for time-consuming and frequently inaccurate heat measurements is eliminated. In addition, some methods of measuring α dispense with most of the direct temperature measurements so that the actual experimental technique becomes rather simple. Since α is a transient-state property, it lends itself to more rapid determination than properties requiring steady-state conditions. Unfortunately, the very rapidity of some of the methods for obtaining α causes them to be unsatisfactory because accurate measurements are difficult to make in the short time available.

METHODS OF MEASURING THERMAL CONDUCTIVITY

The two common indirect methods of determining thermal conductivities experimentally involve either heat flow or electrical measurements.

Electrical Flow Methods in Metals. The electrical conductivity is related to the thermal conductivity since both depend upon the presence of free electrons. This theory has been developed b,. Lorenz (1).[5] The Lorenz relationship accounts for electronic heat conduction but it neglects the conduction component resulting from thermal vibration of the lattice structure. Some attempts have been made to correct for the lattice component of heat conduction; however, the relationships for alloys are so complex that only qualitative results have been obtained. For metals of very high purity, such as special aluminum and copper, the results agree with the Lorenz relation within about 4 per cent.

The primary object of most of the research prior to 1935 was to correlate thermal and electrical conductivities. This work has been summarized by Hall (2). The data correlated by Hall and Austin (1) show that the Lorenz relations cannot be used to obtain precise values of thermal conductivities of alloys; however, the theory does allow relatively rapid and easy measurements.

Heat-Flow Methods. Steady-state heat-flow methods, if properly conducted, can be relied on to give accurate results. Usually the test specimen is controlled to allow only steady-state unidirectional heat flow. The main errors occur in the measurement of the rate of heat flow since the heat flows in three directions. Because of the lack of a perfect insulator and the difficulty of controlling guard heaters it is impossible actually to obtain steady-state unidirectional heat flow. The errors in the measurements increase rapidly as the temperature level is raised above room temperature.

When rods are used with axial heat flow the temperature gradients are small; thus it is not possible to study the thermal conductivity as a function of the energy gradient. If a radial-flow method is used, the difficulty of locating thermocouples in the specimen with sufficient precision introduces large errors.

TRANSIENT METHODS OF MEASURING DIFFUSIVITY

The Forbes (2) bar method has been used to obtain accurate values of thermal diffusivity rapidly at high temperatures. Forbes determined the thermal diffusivity by the technique of matching

---

[5] Numbers in parentheses refer to Bibliography at end of paper.

two cooling curves at points of equal temperatures (as described by Forbes in 1868). A modern method of the same type is the system of moving heat sources which was proposed by Rosenthal (3) and tried experimentally by Rosenthal and Ambrosio (4).

Periodic Heat-Flow Methods. All of the periodic heat-flow methods have been based upon the mathematical theory of heat conduction as developed by Fourier (5) in 1822. Angström (6) was the first investigator to report the use of the periodic heat-flow method. He used a long rod and assumed a semi-infinite rod with a uniform cross-sectional temperature distribution. He did not control the radial heat flow; consequently, he modified Fourier's equation to obtain

$$\frac{\partial T}{\partial \tau} = \alpha \left(\frac{\partial^2 T}{\partial x^2} \right) - HT \dots\dots\dots [2]$$

where

$$H = \frac{h\rho}{\rho C_p A}$$

Angström alternately heated the end of the test specimen with a current of steam and then cooled it with cold water, using a period of 24 min. The diffusivity was calculated from the decrease in temperature amplitude between two measuring stations.

Neumann suggested that the diffusivity could be determined from the decrease in the amplitude of the temperature wave as a function of position along a finite rod, and Weber (7) applied this idea. Weber alternately heated and cooled both ends of a finite rod.

King (8) used a slight modification of the Angström method. King calculated the diffusivity from the phase lag of the temperature wave between two measuring stations. The diffusivity was dependent only upon the wave shape as a function of time; thus it was not necessary to measure the absolute temperatures. King used an ingenious heater to give a temperature wave as a cosine function; consequently, he measured only the elapsed time while the maximum of the temperature wave passed from one measuring station to another.

Starr (9) used a slight modification of King's method. Starr's sinusoidal heat-input wave was more complicated than King's but the purpose was the same.

Of these various methods, only the Forbes bar technique has been applied to yield a significant quantity of acceptable data.

METHOD AND APPARATUS

The object of this investigation was to evaluate experimentally the periodic transient method of determining the thermal diffusivity of metals. This investigation was initiated in February, 1949, and continued over a period of more than three years.

In these experiments a long rod with controlled radial heat losses was used. Thus the equation for heat flow in one dimension was as follows

$$\frac{\partial T}{\partial \tau} = \alpha \left(\frac{\partial^2 T}{\partial x^2} \right) \dots\dots\dots\dots [3]$$

Fig. 1 illustrates an ideal situation in which the imposed temperature function is a sine wave. A marked change of temperature amplitude from θ_1 to θ_2 is indicated and a 180-deg phase difference in the temperature wave is also evident. By applying either of these experimental measurements to a solution of the partial differential equation for heat flow in one dimension, it is possible to calculate the thermal diffusivity (8, 9, 10, 11, 12). The phase angles at each of two measuring stations were determined by a 48-ordinate harmonic analysis of the recorded temperature wave. Equation [3] was manipulated to give the
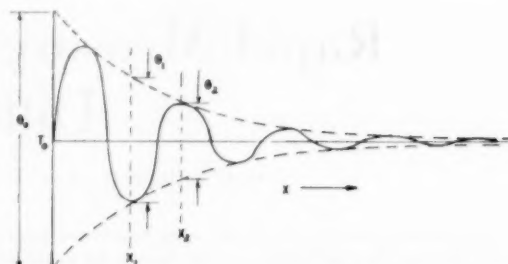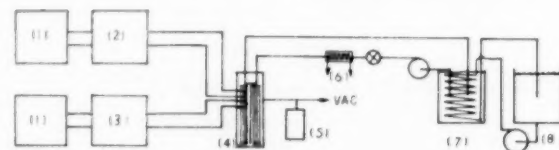

FIG. 1   TEMPERATURE DISTRIBUTION ALONG SEMI-INFINITE ROD AT TIME τ FOR SINUSOIDAL VARIATION AT $x = 0$

1. Recording milliammeters
2. First thermocouple amplifier
3. Second thermocouple amplifier
4. Glass test enclosure
5. Vacuum gage
6. Temperature-varying heater
7. Primary bath
8. Secondary bath

FIG. 2   THERMAL DIFFUSIVITY APPARATUS

following simple relation which was used in the actual calculations of the thermal diffusivities (8, 9, 10, 11)

$$\alpha = \left(\frac{\Delta x}{\Delta \phi} \right)^2 K \dots\dots\dots\dots [4]$$

The apparatus is shown schematically in Fig. 2. The rod-type specimen (from $1/16$ to $1/4$ in. diam and from 6 to 24 in. long) was surrounded by radiation shields and suspended in an evacuated glass chamber. The complete measuring circuit consisted of two No. 36 chromel-copnic thermocouples which were spark-welded to the test specimen; then each thermocouple was connected to an electronic amplifier the output of which was recorded on a recording milliammeter. Both amplifiers were of the a-c type, employing 60-cycle vibrators to alternate the input and rectifying tubes to reconvert to d-c output. Since the amplifiers gave full scale output with 0.0002 volts input, voltage-divider devices were used to buck all but the portion of the thermocouple voltage to be amplified. Temperature amplitudes as small as 0.25 deg F were recorded; although the average recorded cycles had an amplitude of approximately 2 deg F. The time-temperature wave shapes were recorded on Esterline-Angus (0–5 ma) milliammeters 1, Fig. 2. These wave-shape records provided the data for the harmonic analyses.

The glass vacuum chamber 4, Fig. 2, was provided with a 71/60 taper joint. The copper tubing for the heat-transfer fluid was held in place in the glass wall by Sauereisen cement No. 30 and sealed with high-temperature varnish. The thermocouple seals were made with DeKhotinsky cement. A Zimmerli vacuum gage was used for the pressure measurements.

During the first phase of the investigation, an induction heater was used as the energy source for heating the specimens. This technique was discontinued in order to eliminate some of the difficulties associated with "pickup" in the amplifiers. The primary constant-temperature bath 7, Fig. 2, which with the cyclic heater 6, Fig. 2, replaced the induction heater, was a standard type with a thermoregulator, electric heater, cooling coil, and a

circulating pump. The secondary constant-temperature bath served merely to provide coolant for the primary bath. The primary bath maintained a constant temperature within the limits of ±0.18 deg F.

The temperature wave at $x = 0$ was provided by intermittently heating the oil as it was pumped from the primary constant-temperature bath. The temperature of the oil was increased about 10 F by the cyclic heater 6, which was controlled by the timing switch.

OPERATION

The operating procedure was simple. After the vacuum pump had been in operation for a period of over 1 hr, the other components were turned on at approximately 15-min intervals as follows: Bath controls and circulating pumps, timer for cyclic heater, amplifiers, and then the recording milliammeters. Wave shapes were recorded for only six to twelve of the 105-sec cycles.

RESULTS

It was possible to make a complete thermal-diffusivity determination in a period of 1 hr. Repeated measurements could be made in a period of 45 min. The maximum probable error of these measurements was ±6.8 per cent. The principal source of error was involved in the harmonic analysis of the time-temperature data. The greatest experimental difficulty was associated with the maintenance of a steady flow of constant-temperature oil from the primary bath. Considerable time and labor were required to analyze the data.
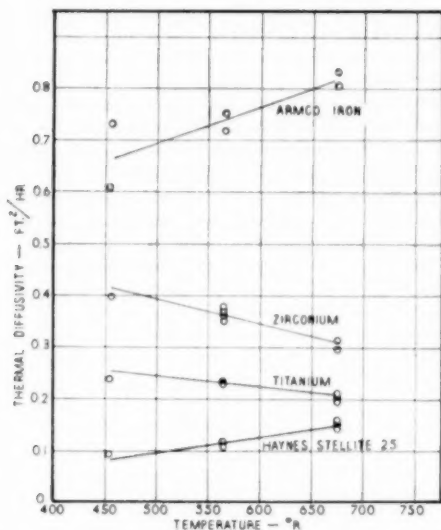

FIG. 3 THERMAL DIFFUSIVITY OF ARMCO IRON, ZIRCONIUM, TITANIUM, AND HAYNES STELLITE NO. 25

Specimens of Armco iron, titanium, zirconium, and Haynes Stellite No. 25 were tested at 456, 564, and 672 R. The calculated values of the thermal diffusivities are shown in Fig. 3.

CONCLUSIONS AND DISCUSSION

A periodic heat-flow method can be used to make determinations of the thermal diffusivities of metals with an accuracy of about 5 per cent. The experimental data can be obtained in a period of 1 hr after the specimen has attained the mean temperature level at which the experiments are to be made. The necessary apparatus is complex and expensive and the detailed analysis of the data is difficult. The method is not sufficiently accurate to study the influence of temperature gradient or mechanical strain on thermal conductivity.

The work recently reported by Sidles and Danielson (12) confirms these conclusions. Sidles developed a new modification of this method and he measured diffusivities at temperatures to above 1000 F. He estimated his measurements to be within ca 0.25 per cent at 32 F and within ca 10 per cent at 400 F.

Starr (9) claimed a very high accuracy of ±0.06 per cent. However, he tested only one brass rod the conductivity of which was known to within ca ± 5 per cent.

The Forbes bar method remains as the most promising technique for obtaining reliable values of thermal diffusivities at high temperatures in a short interval of time. The experimental determinations can be made in a period of 10 min after the specimen has attained the mean temperature level. Since an accuracy of better than 1 per cent can be obtained, the Forbes bar method can be used to study conductivity-temperature gradient or conductivity-strain relations.

BIBLIOGRAPHY

1 "Flow of Heat in Metals," by J. B. Austin, American Society for Metals, Cleveland, Ohio, 1942, 144 pp.
2 "Concerning Thermal Conductivity of Iron," by E. H. Hall, *Physical Review*, vol. 10, 1900, pp. 277–310.
3 "The Theory of Moving Sources of Heat and Its Application of Metal Treatments," by D. Rosenthal, Trans. ASME, vol. 68, 1946, pp. 849–866.
4 "A New Method of Determining Thermal Diffusivity of Solids at Various Temperatures," by D. Rosenthal and A. Ambrosio, Trans. ASME, vol. 73, 1951, pp. 971–974.
5 "Theorie Analytique de la Chaleur," by J. B. J. Fourier, reprinted in 1945 by G. E. Stechert and Company, New York, N. Y.
6 "Periodic Flow Methods," by A. J. Angström, *Annalen der Physik und Chemie*, vol. 123, 1864, p. 628.
7 "Über das Wärmeleitungsvermögen von den Eisen und Neusilber," by Heinrich Weber, *Annalen der Physik*, vol. 146, 1872, pp. 257–283.
8 "A Method of Measuring Heat Conductivities," by R. W. King, *Physical Review*, series 2, vol. 6, 1915, pp. 437–445.
9 "An Improved Method for the Determination of Thermal Diffusivities," by C. Starr, *Review of Scientific Instruments*, vol 8, 1937, pp. 61–64.
10 "Thermal Conductivity of Metals by a Periodic Heat Flow Method," by G. E. McIntosh, MS thesis, Purdue University, Lafayette, Ind., January, 1952.
11 "Thermal Diffusivity of Metals," by G. E. McIntosh, Ph.D. Thesis, Purdue University, Lafayette, Ind., June, 1952.
12 "Thermal Conductivity of Metals at High Temperatures," by P. H. Sidles and G. C. Danielson, ISC-198, Atomic Energy Commission, Ames Laboratory, Ames, Iowa, December, 1951.

Discussion

G. C. DANIELSON,[6] P. H. SIDLES,[6] AND G. J. PEARSON.[6] The purpose of the investigation reported in this paper was to evaluate experimentally the periodic heat-flow method of determining the thermal diffusivity of metals. The conclusions were that this method was inferior to the Forbes bar method from the standpoint of accuracy and the rapidity with which data could be obtained and that the Forbes method is to be preferred for studying thermal conductivity versus temperature gradient or thermal conductivity versus strain. We would like to discuss these conclusions.

Both the Forbes bar and the periodic heat-flow methods re-

[6] Institute for Atomic Research and Department of Physics, Iowa State College, Ames, Iowa.

quire an equilibrium condition before data can be taken. The time required to attain this equilibrium is long compared with that required to actually take the necessary data. Therefore the total time required for one thermal-conductivity determination is essentially the same for each of the two methods.

To the best of our knowledge, no Forbes bar technique has been used to measure thermal conductivity at high temperatures with an accuracy of better than 1 per cent as was stated by the authors. Hall[7] concludes his discussion of the Forbes method with a quote from a paper by Stewart to the effect that Angström's method (a periodic heat-flow method) should be adopted in preference to the Forbes method. Hogan and Sawyer[8] in a recent study using the Forbes bar technique fail to indicate any accuracy for their measurements, stating only that the assumptions made in deriving the theory would cause an error of less than 1 per cent for the samples they measured.

When one considers that periodic heat-flow methods permit the necessary data for a thermal-conductivity determination to be obtained simultaneously from a single sample while Forbes bar methods require either separate experiments on the same bar or simultaneous experiments on different bars, one concludes that the periodic heat-flow technique is inherently more accurate. It has been our experience that this conclusion is correct.

As was pointed out in a recent report by Sidles and Danielson,[9] experiments of the periodic heat-flow type which required two separate experiments for one determination of thermal diffusivity were definitely inferior to the technique developed by the writers and described in that report[9] in which all necessary data were obtained simultaneously on a single sample. It should be pointed out that the large errors reported at 400 C were not caused by inherent difficulty with the method but by the decreased stability of the sample at that temperature.

In view of the results of previous studies of thermal conductivity versus strain it is quite evident that accuracies of considerably better than 1 per cent are required for studies of this type. Bridgman,[10] in a study of seven different metals, found effects of tension on thermal conductivity ranging from about 0.39 per

cent for a 2050 kg/cm^2 load in Fe to 0.015 per cent for a 770 kg/cm^2 load in Pd.

We would like to point out that neither the periodic heat flow nor the Forbes bar method seems to be well adapted for studying relations of thermal conductivity versus strain. The difficulty inherent in both methods is that each requires an equilibrium condition which would be altered by straining the sample. Measurements of the afterstrain conductivity can be made only after waiting for this equilibrium condition to prevail. During this period of time, annealing will take place, thus partially erasing the effect on conductivity caused by the strain. A suitable method for measurements of this type should be free from this difficulty.

We would like to propose that a technique similar to the moving heat-source method of Rosenthal and Ambrosio[11] might be useful for measurements of this type. A sensitive amplifier-recorder system and very small heat pulses would be used. A determination of the before-strain conductivity would be made and the sample allowed to return to equilibrium with the ambient temperature. The sample would then be strained and the heat source immediately moved along the sample to measure the afterstrain conductivity. The distinction between this proposed technique and both the Forbes bar and the periodic heat-flow technique is that here only a temperature equilibrium is required and that this equilibrium would not be altered by straining the sample as would a temperature-gradient equilibrium or a periodic heat-pulse equilibrium.

AUTHORS' CLOSURE

The authors thank Messrs. Danielson, Sidles, and Pearson for their logical and unusually well-informed discussion. In view of the broader experience of this group, the authors wish only to clarify their stand on the Forbes method of determining thermal diffusivity.

If experimental error is the criterion, a method requiring one experiment, such as the authors used, is superior to the Forbes method, which requires two experiments, only when the total error of the two experiments is greater than the error from the single experiment. It was the authors' experience that the maximum theoretical error in their experiments (6.8 per cent) was considerably greater than could be expected for similar Forbes method experiments. This finding, plus the simpler apparatus required for the Forbes method, provides the basis for the authors' recommendation.

[7] Authors' Bibliography (2), p. 284.

[8] "Thermal Conductivity of Metals at High Temperature," by C. L. Hogan and R. B. Sawyer, *Journal of Applied Physics*, vol. 23, 1952, pp. 177–180.

[9] Authors' Bibliography (12), p. 9.

[10] "Effect of Tension on the Thermal and Electrical Conductivity of Metals," by P. W. Bridgman, Proceedings of the American Academy of Arts and Sciences, vol. 59, 1923, p. 127.

[11] Authors' Bibliography (4).

Thermal Lags in Flowing Systems Containing Heat Capacitors

By J. W. RIZIKA,[1] CAMBRIDGE, MASS.

The method of procedure to find the thermal lag in systems, such as heat exchangers and pipes, is shown and the case of the parallel flow heat exchanger is partially treated. The Laplace transformed solutions are presented. An equivalent treatment of the counterflow heat exchanger is given in the Appendix.

NOMENCLATURE

The following nomenclature is used in the paper:

$A = \dfrac{r_o h_o}{r_i h_i}$, dimensionless

$B = \dfrac{\pi(r_o^2 - r_i^2)\rho_m c_m}{2\pi r_i h_i}$, hr

c = specific heat, Btu/(lb)(deg F)

$C = \dfrac{\pi(r_o^2 - r_i^2)\kappa_m}{2\pi r_i h_i}$, sq ft

$D = \dfrac{w_f c_{pf}}{2\pi r_i h_i}$, ft

$E = \dfrac{w_a c_{pa}}{2\pi r_i h_o}$, hr

F = inverse time constant in fluid exponential temperature input function, 1/hr

G = amplification constant in fluid exponential temperature input function, dimensionless

h = film coefficient of heat transfer between fluid and tube material, Btu/(hr)(sq ft)(deg F)

φ_i = Bessel function of first kind

k = integer $(0, 1, 2, 3, \ldots \infty)$, dimensionless

l = length of tube or pipe, ft

p = Laplace transform variable, 1/ft

P = pressure, lb/sq ft

q = variable upper limit of integration in a function, dimensionless

r = radius of tube or pipe, ft

R = gas constant, ft/deg F

Re = Reynolds number, dimensionless

s = variable in a function, dimensionless

T = temperature, deg F

u = temperature of inner fluid at any distance and time, $u(x, \theta)$, deg F

U = transformed temperature of inner fluid,

$\int_0^\infty e^{-px} u\, dx$, (ft)(deg F)

v = temperature of outer fluid at any distance and time, $v(x, \theta)$, deg F

V = transformed temperature of outer fluid,

$\int_0^\infty e^{-px} v\, dx$, (ft)(deg F)

w = mass flow rate of fluid, lb/hr

x = axial distance from fluid inlet station to any section along tube or pipe, ft

y = temperature of tube or pipe material at any distance and time, $y(x, \theta)$, deg F

Y = transformed temperature of tube or pipe material,

$\int_0^\infty e^{-px} y\, dx$, (ft)(deg F)

z = variable of integration, dimensionless

μ = absolute viscosity, lb/(sec)(ft)

ρ = density, lb/cu ft

θ = time, hr

κ = thermal conductivity, Btu/(hr)(ft)(deg F)

ω = variable of integration, ft

Subscripts:

a = refers to fluid outside tube or pipe

f = refers to fluid inside tube or pipe

i = refers to inside surface of tube or pipe; also refers to fluid inlet condition at tube entrance $(x = 0)$

m = refers to tube or pipe material

p = refers to constant pressure

o = refers to outside surface of tube or pipe

INTRODUCTION

Problems involving the thermal lag in gaseous-fluid[2] systems containing heat capacitors, such as heat exchangers and pipes, are continually arising in aeronautical, chemical, and mechanical applications where "temperature control" is necessary. The controllability of the fluid discharge temperature from a system is a direct function of the thermal lag of the system; viz., if a length of pipe connects a fluid source to a sink, the controllability of the fluid temperature at the pipe exit is a function of the thermal lag of the pipe.

This paper presents a method for finding the thermal lag in any parallel flow system[3] which may be approximated by the simple system shown in Fig. 1, i.e., a fluid flowing on each side of a
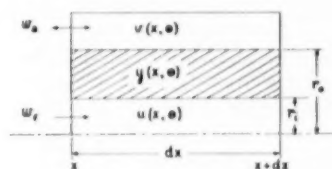
FIG. 1

cylindrical heat capacitor, the entire system being insulated. The particular system of Fig. 1 can be considered as an element of a tube or pipe, in which and over which fluids are flowing. Thus

---

[2] This analysis is applied to systems which employ only gaseous fluids (fluids in the vapor phase) and wherever the word "fluid" appears it is understood to be a fluid in the vapor phase.

[3] A counterflow system, approximating a counterflow heat exchanger, is considered in the Appendix.

this figure could represent an element of a single tube, with its proportion of total fluid flow, in a heat exchanger. Similarly, if there were no heat transfer to the fluid outside the tube, the system would represent a fluid flowing through an element of an insulated pipe. This latter case is examined in detail since it is easily manageable and is frequently encountered in engineering systems.

Basic Analysis and Assumptions

Consider the elemental section of tube, dx in length, and corresponding fluid, at any time θ, as shown in Fig. 1.

The following assumptions are made:

1 The heat flow and temperature distribution are functions of both time and axial distance from the tube inlet.

2 Both the inner radius and the outer radius of the tube are assumed constant.

3 The tube material is homogeneous and isotropic; the density and the specific heat are constant.

4 The thermal conductivity of the tube material is constant in the axial direction; the thermal conductivity of the tube material is considered infinite in the radial direction.

5 There is no energy source within the tube material itself.

6 The film coefficients of heat transfer between the fluid and tube material h are uniform and constant over the inner and outer tube surfaces for constant fluid mass flow rates.

7 The specific heats at constant pressure of both the inner and outer fluids are assumed to be constant.

8 The fluid pressure at any section is independent of time for both the inner and outer fluids.

9 The heat transferred at any section due to the fluid thermal conductivity in the axial direction, within the fluid, is negligible compared to other heat transfers from the fluid at the same section.

The inner fluid will be considered to be moving in the direction of positive x with a mass flow rate w_f. If the outer fluid is flowing in the same direction as the inner fluid, the system is referred to as "parallel flow;" if the outer fluid is flowing in the opposite direction with respect to the inner fluid motion, the system is referred to as "counterflow."

The characteristics of the fluid inside the tube will be designated by a subscript f, while the characteristics of the fluid outside of the tube will be designated by a subscript a; subscript m will signify the characteristics of the tube material; u, v, and y are the temperatures of the inside fluid, outside fluid, and tube material, respectively, at any distance x and any time θ. The inner and outer radii of the tube are r_i and r_o, and the heat-transfer film coefficients between the fluids and the tube material are h_i and h_o, respectively. Density, specific heat, and thermal conductivity are ρ, c, and κ, respectively.

An application of the first law of thermodynamics, the Fourier law of conduction, and Newton's law of cooling to the element of tube material at any instant gives

$$u - y - \frac{r_o h_o}{r_i h_i}(y - v) = \frac{\pi(r_o{}^2 - r_i{}^2)\rho_m c_m}{2\pi r_i h_i} \frac{\partial y}{\partial \theta}$$
$$- \frac{\pi(r_o{}^2 - r_i{}^2)\kappa_m}{2\pi r_i h_i} \frac{\partial^2 y}{\partial x^2} \quad \cdots \cdots [1]$$

The first law of thermodynamics and Newton's law of cooling applied to both the inner and outer elements of fluid at any instant give (see footnote 4, right-hand column)

$$u - y = -\frac{w_f c_{pf}}{2\pi r_i h_i} \frac{\partial u}{\partial x} \quad \cdots \cdots \cdots [2]$$

$$y - v = \pm \frac{w_a c_{pa}}{2\pi r_o h_o} \frac{\partial v}{\partial x} \left\{ \begin{array}{l} + \text{ parallel flow} \\ - \text{ counterflow} \end{array} \right\} \cdots \cdots [3]$$

If the outer fluid flow rate w_a is zero and there is a reservoir of outer fluid which provides for a heat loss from the tube through free convection, Equation [3] is no longer valid and is replaced by

$$v = T_a \cdots \cdots \cdots \cdots \cdots [3']$$

where T_a is the temperature of outer fluid and is assumed to be a constant. Hereinafter, all primed equations will represent this case of free convection to the outer fluid and will be shown for convenience only.

Now, defining the following Laplace transforms

$$Y(p, \theta) \equiv \int_0^\infty e^{-px} y(x, \theta)\, dx$$

$$U(p, \theta) \equiv \int_0^\infty e^{-px} u(x, \theta)\, dx$$

$$V(p, \theta) \equiv \int_0^\infty e^{-px} v(x, \theta)\, dx$$

It is easily seen that

$$\int_0^\infty e^{-px} \frac{\partial y}{\partial \theta}\, dx = \frac{\partial Y}{\partial \theta}$$

$$\int_0^\infty e^{-px} \frac{\partial^2 y}{\partial x^2}\, dx = -\frac{\partial y(0, \theta)}{\partial x} - py(0, \theta) + p^2 Y$$

$$\int_0^\infty e^{-px} \frac{\partial u}{\partial x}\, dx = -u(0, \theta) + pU$$

$$\int_0^\infty e^{-px} \frac{\partial v}{\partial x}\, dx = -v(0, \theta) + pV$$

Multiplying Equations [1], [2], and [3] by $e^{-px}dx$ and integrating between the limits of zero and infinity

$$U - Y - A(Y - V) = B\frac{\partial Y}{\partial \theta} + C\frac{\partial y(0, \theta)}{\partial x}$$
$$+ Cpy(0, \theta) - Cp^2 Y \cdots \cdots [1a]$$

$$U - Y = Du(0, \theta) - DpU \cdots \cdots \cdots \cdots [2a]$$

$$Y - V = \mp Ev(0, \theta) \pm EpV \left\{ \begin{array}{l} \text{parallel flow} \\ \text{counterflow} \end{array} \right\} \cdots \cdots [3a]$$

---

4 The first law of thermodynamics and Newton's law of cooling applied to the inner element of fluid at any instant give

$$-2\pi r_i h_i(u - y) - w_f c_{pf}\frac{\partial u}{\partial x} = \pi r_i{}^2 c_{vf} \frac{\partial(\rho_f u)}{\partial \theta} - \pi r_i{}^2 \kappa_f \frac{\partial^2 u}{\partial x^2} \quad [a]$$

But if the inner fluid is in the vapor phase

$$\rho_f \simeq \frac{P_f}{R} \cdots \cdots \cdots \cdots \cdots \cdots \cdots [b]$$

Then

$$\frac{\partial(\rho_f u)}{\partial \theta} = \frac{\partial(P_f/R)}{\partial \theta} \cdots \cdots \cdots \cdots [c]$$

From this relation and assumption (8)

$$\frac{\partial(\rho_f u)}{\partial \theta} = 0 \cdots \cdots \cdots \cdots \cdots [d]$$

Also, from assumption (9)

$$\pi r_i{}^2 \kappa_f \frac{\partial^2 u}{\partial x^2} \simeq 0 \cdots \cdots \cdots \cdots \cdots [e]$$

Therefore

$$2\pi r_i h_i(u - y) = -w_f c_{pf}\frac{\partial u}{\partial x} \cdots \cdots \cdots \cdots [f]$$

which is equivalent to Equation [2].

Similar reasoning may be applied to obtain Equation [3].

or, in the case of free convection to the outer fluid ($w_a = 0$)

$$V = -\frac{T_a}{p} \dots\dots\dots\dots [3'a]$$

where

$$A \equiv \frac{r_o h_o}{r_i h_i}$$

$$B \equiv \frac{\pi(r_o{}^2 - r_i{}^2)\rho_m c_m}{2\pi r_i h_i}$$

$$C \equiv \frac{\pi(r_o{}^2 - r_i{}^2)\kappa_m}{2\pi r_i h_i}$$

$$D \equiv \frac{w_f c_{pf}}{2\pi r_i h_i}$$

$$E \equiv \frac{w_a c_{pa}}{2\pi r_o h_o}$$

TRANSFORMED SOLUTIONS TO PARALLEL FLOW SYSTEM WITH A STEP-FUNCTION TEMPERATURE INPUT

Now, consider the solution to Equations [1a], [2a], and [3a] for a parallel flow system with a step-function temperature input. Physically this would correspond to the solution of the parallel flow heat-exchanger lag (neglecting the outer shell of the exchanger) or the thermal lag of a fluid issuing from a pipe, the pipe entrance temperature of the fluid being a constant, T_{fi}.

TABLE 1 BOUNDARY CONDITIONS

Mathematical	Physical
(1) $y(x, 0) = T_o$	T_o is initial tube material temperature (constant) at zero time and at any distance
(2) $u(0, \theta) = T_{fi}$	T_{fi} is inside fluid temperature (constant) at entrance or zero distance and at any time
(3) $v(0, \theta) = T_{ai}$	T_{ai} is outside fluid temperature (constant) at entrance or zero distance and at any time
(4) $\dfrac{\partial y(0, \theta)}{\partial x} = 0$	Heat transferred from end of tube at entrance to system is zero at any time

NOTE: These boundary conditions are shown graphically in Fig. 2.

$$u(0,\theta) = T_{fi}$$
$$v(0,\theta) = T_{ai}$$
$$\frac{\partial y(0,\theta)}{\partial x} = 0$$
$$y(x,0) = T_o$$
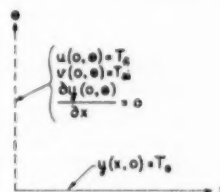
FIG. 2

The boundary conditions for this system are given in Table 1. Combining Equations [1a], [2a], and [3a] with these boundary conditions and solving the resulting differential equation for Y

$$Y = \left\{ \frac{T_o}{p} + \left[\frac{\dfrac{DT_{fi}}{1 + Dp} + \dfrac{AET_{ai}}{1 + Ep} - \dfrac{(CT_{fi} + ACT_{ai})p}{1 + A}}{\dfrac{1}{1 + Dp} + \dfrac{A}{1 + Ep} + Cp^2 - A - 1} \right] - \left[\frac{CT_o p - \dfrac{(CT_{fi} + ACT_{ai})p}{1 + A}}{\dfrac{1}{1 + Dp} + \dfrac{A}{1 + Ep} + Cp^2} \right] \right\} e^{\left[\frac{1}{1 + Dp} + \frac{A}{1 + Ep} + Cp^2 - A - 1 \right] \frac{\theta}{B}}$$

$$+ \left\{ \frac{CT_o p - \dfrac{(CT_{fi} + ACT_{ai})p}{1 + A}}{\dfrac{1}{1 + Dp} + \dfrac{A}{1 + Ep} + Cp^2} \right\} e^{-[1 + A] \frac{\theta}{B}} - \left\{ \frac{\dfrac{DT_{fi}}{1 + Dp} + \dfrac{AET_{ai}}{1 + Ep} - \dfrac{(CT_{fi} + ACT_{ai})p}{1 + A}}{\dfrac{1}{1 + Dp} + \dfrac{A}{1 + Ep} + Cp^2 - A - 1} \right\} \dots\dots [4]$$

or, in the case of free convection to the outer fluid ($w_a = 0$), from Equations [1a], [2a], and [3'a] with the boundary conditions

$$Y = \left\{ \frac{T_o}{p} + \left[\frac{\dfrac{DT_{fi}}{1 + Dp} - \dfrac{AT_a}{p} - \dfrac{(CT_{fi} + ACT_a)p}{1 + A}}{\dfrac{1}{1 + Dp} + Cp^2 - A - 1} \right] - \left[\frac{CT_o p - \dfrac{(CT_{fi} + ACT_a)p}{1 + A}}{\dfrac{1}{1 + Dp} + Cp^2} \right] \right\} e^{\left[\frac{1}{1 + Dp} + Cp^2 - A - 1 \right] \frac{\theta}{B}}$$

$$+ \left\{ \frac{CT_o p - \dfrac{(CT_{fi} + ACT_a)p}{1 + A}}{\dfrac{1}{1 + Dp} + Cp^2} \right\} e^{-[1 + A] \frac{\theta}{B}} - \left\{ \frac{\dfrac{DT_{fi}}{1 + Dp} - \dfrac{AT_a}{p} - \dfrac{(CT_{fi} + ACT_a)p}{1 + A}}{\dfrac{1}{1 + Dp} + Cp^2 - A - 1} \right\} \dots\dots [4']$$

If the tube thermal conductivity κ_m in the axial direction is assumed zero, Equation [4] reduces to the following

$$Y = \left\{ \frac{T_o}{p} + \left[\frac{\dfrac{DT_{fi}}{1 + Dp} + \dfrac{AET_{ai}}{1 + Ep}}{\dfrac{1}{1 + Dp} + \dfrac{A}{1 + Ep} - A - 1} \right] \right\} e^{\left[\frac{1}{1 + Dp} + \frac{A}{1 + Ep} - A - 1 \right] \frac{\theta}{B}} - \left\{ \frac{\dfrac{DT_{fi}}{1 + Dp} + \dfrac{AET_{ai}}{1 + Ep}}{\dfrac{1}{1 + Dp} + \dfrac{A}{1 + Ep} - A - 1} \right\} \dots\dots [5]$$

or, in the case of free convection to the outer fluid ($w_a = 0$)

$$Y = \left\{ \frac{T_o}{p} - \left[\frac{(DT_{fi} - ADT_a)p - AT_a}{(1 + A)Dp^2 + Ap} \right] \right\} e^{-\left[A + 1 - \frac{1}{1 + Dp} \right] \frac{\theta}{B}} + \left\{ \frac{(DT_{fi} - ADT_a)p - AT_a}{(1 + A)Dp^2 + Ap} \right\} \dots\dots [5']$$

If the heat-transfer coefficient between the outer fluid and the tube, h_o, is also zero, the case of a fluid flowing through an *insulated* tube or pipe, both Equations [5] and [5'] reduce to

$$Y = \left(\frac{T_o - T_{fi}}{p}\right) e^{-\left[1 - \frac{1}{1 + Dp}\right]\frac{\theta}{B}} + \frac{T_{fi}}{p} \dots \dots [6]$$

In all the foregoing solutions, A, B, C, D, and E are positive and are given constants of the system. The inverse Laplace transforms of these solutions are the actual solutions for $y(x, \theta)$, the tube material temperature. The solution for $y(x, \theta)$, the initial basic equations, and the boundary conditions allow one to find $u(x, \theta)$ and $v(x, \theta)$, the fluid temperatures at any time and at any distance.

SOLUTION FOR CASE OF A FLUID FLOWING, WITH A STEP-FUNCTION TEMPERATURE INPUT, IN AN INSULATED PIPE

Now consider the case of a fluid flowing, with a step-function temperature input, in an insulated pipe. Equation [6] was shown to be the transformed solution for this case. The inverse transform of this solution[6] can be found

$$y = (T_o - T_{fi}) e^{-\frac{\theta}{B}}\left[1 + \sqrt{\frac{\theta}{DB}} \int_0^x \frac{e^{-\frac{\omega}{D}}}{\sqrt{\omega}}\right.$$
$$\left. \varphi_1\left(2\sqrt{\frac{\theta\omega}{DB}}\right) d\omega\right] + T_{fi} \dots \dots [7]$$

where φ_1 is the Bessel function of the first kind, defined as

$$\varphi_1\left(2\sqrt{\frac{\theta\omega}{DB}}\right) \equiv \sum_{k=0}^{\infty} \frac{\left(\frac{\theta\omega}{DB}\right)^{k+\frac{1}{2}}}{(k!)^2(k+1)}$$

Rearranging this expression, it can be seen that

$$\frac{y - T_o}{T_{fi} - T_o} = 1 - e^{-\frac{\theta}{B}}\left[1 + \sum_{k=0}^{\infty}\left(\frac{\theta}{B}\right)^{k+1} \frac{1}{(k!)^2(k+1)}\right.$$
$$\left. \int_0^{\frac{x}{D}} e^{-z} z^k dz\right]$$
$$= e^{-\frac{x}{D}} \sum_{k=0}^{\infty}\left(\frac{x}{D}\right)^k \frac{1}{(k!)^2} \int_0^{\frac{\theta}{B}} e^{-z} z^k dz \dots \dots [7a]$$

This is the solution for the pipe material temperature as a function of both time and distance, where T_o is the initial temperature of the pipe (for any x and $\theta = 0$) and T_{fi} is the inlet temperature of the fluid (for $x = 0$ and any θ).

Equation [1], for the case in which κ_m and h_o are both zero, can be stated in the form

$$\frac{T_{fi} - u}{T_{fi} - T_o} = \left(1 - \frac{y - T_o}{T_{fi} - T_o}\right) + B\frac{\partial}{\partial\theta}\left(1 - \frac{y - T_o}{T_{fi} - T_o}\right) \dots [1b]$$

Thus, by taking the partial derivative of Equation [7a] with respect to θ, substituting this and Equation [7a] into Equation

[1b] and rearranging, a relation for the fluid temperature can be found as a function of both time and distance from the pipe inlet

$$\frac{T_{fi} - u}{T_{fi} - T_o} = e^{-\frac{\theta}{B}} \sum_{k=0}^{\infty}\left(\frac{\theta}{B}\right)^k \frac{1}{(k!)^2} \int_0^{\frac{x}{D}} e^{-z} z^k dz \dots \dots [7b]$$

An examination of Equations [7a] and [7b] reveals the symmetry of these solutions and shows the eight first-order boundary conditions to be as follows:

For the metal

$$\frac{y(x, 0) - T_o}{T_{fi} - T_o} = 0$$

$$\frac{y(x, \infty) - T_o}{T_{fi} - T_o} = 1$$

$$\frac{y(0, \theta) - T_o}{T_{fi} - T_o} = 1 - e^{-\frac{\theta}{B}}$$

$$\frac{y(\infty, \theta) - T_o}{T_{fi} - T_o} = 0$$

For the fluid

$$\frac{T_{fi} - u(x, 0)}{T_{fi} - T_o} = 1 - e^{-\frac{x}{D}}$$

$$\frac{T_{fi} - u(x, \infty)}{T_{fi} - T_o} = 0$$

$$\frac{T_{fi} - u(0, \theta)}{T_{fi} - T_o} = 0$$

$$\frac{T_{fi} - u(\infty, \theta)}{T_{fi} - T_o} = 1$$

It is interesting to note that the percentage temperature change is independent of the initial temperature potential, for both the fluid and the pipe material. This follows immediately from the linearity of the differential equations. Both Equations [7a] and [7b] represent surfaces in a three-dimensional "temperature-time-distance" space. Therefore the solutions for the fluid and pipe transient temperatures can be given in two simple dimensionless plots for all systems in which a fluid is flowing, with a step-function inlet temperature, in an insulated pipe. Such plots are presented[6] in Figs. 3 and 4.

SOLUTION FOR CASE OF FLUID FLOWING, WITH AN EXPONENTIAL TEMPERATURE INPUT, IN AN INSULATED PIPE

In a similar manner to the development of Equation [6] (the transformed solution for the case of a fluid flowing, with a step-function temperature input, in an insulated pipe), the transformed solution for the case of a fluid flowing, with any temperature input function, in an insulated pipe may be developed. This solution is

$$Y = \left[\frac{T_o}{p} + \frac{D}{B(1 + Dp)} \int_0^{\theta} e^{\left[\frac{Dp}{1+Dp}\right]\frac{\theta}{B}} u(0, \theta) d\theta\right] e^{-\left[\frac{Dp}{1+Dp}\right]\frac{\theta}{B}} \dots [8]$$

If an exponential temperature input function of the form

$$\frac{T_{fi} - u(0, \theta)}{T_{fi} - T_o} = Ge^{-F\theta} \dots \dots \dots \dots \dots [9]$$

is assumed to exist in the fluid at the pipe inlet, the resultant solutions for the fluid and pipe temperatures, as functions of time and distance, can be shown to be

[6] "Fourier Integrals for Practical Applications," by G. A. Campbell and R. M. Foster, D. Van Nostrand Company, Inc., New York, N. Y., 1948, p. 79, No. 654.2.

[6] Tabulations of functions $(y - T_o/T_{fi} - T_o)$ and $(T_{fi} - u/T_{fi} - T_o)$ versus (θ/B) and (x/D) for Figs. 3 and 4 were taken from the basic tabulations necessary for Figs. 5 and 6.
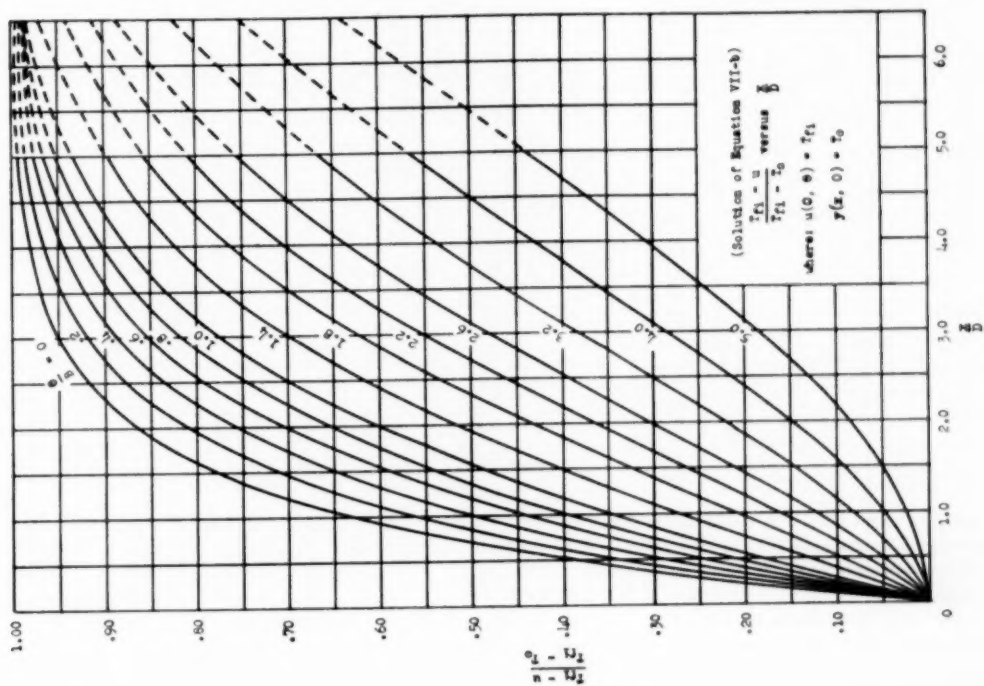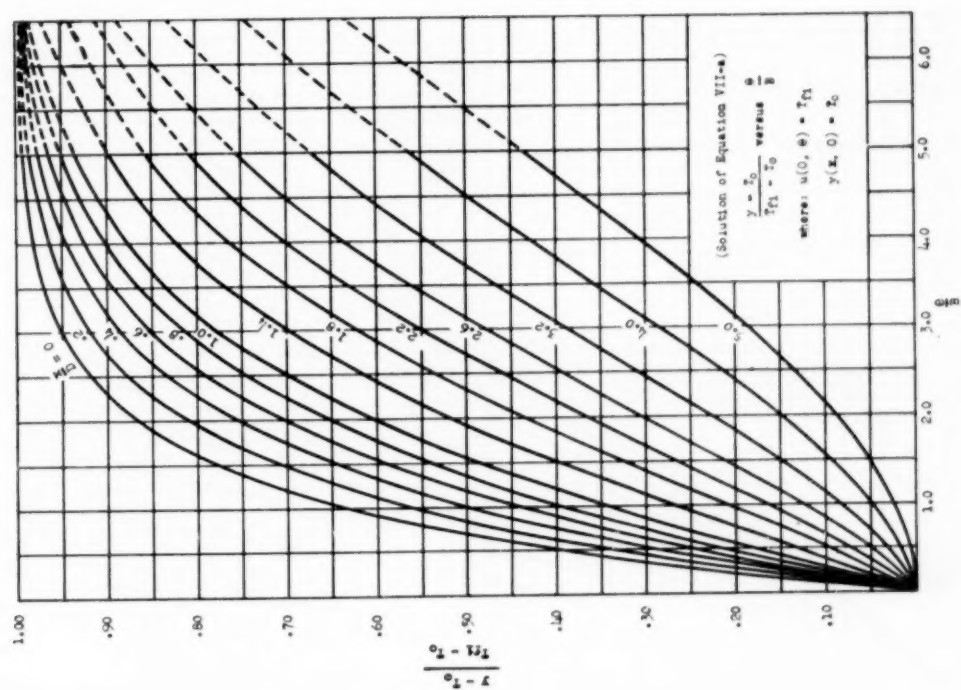
Fig. 4

Fig. 3

$$\frac{y - T_o}{T_{fi} - T_o} = 1 - e^{-\frac{\theta}{B}} \left[1 + \sum_{k=0}^{\infty} \left(\frac{\theta}{B}\right)^{k+1} \frac{1}{(k!)^2(k+1)} \int_0^{\frac{z}{D}} e^{-z} z^k dz \right]$$

$$- \frac{Ge^{\left(\frac{FB}{1-FB}\right)\frac{z}{D}}}{(1-FB)} \left\{ e^{-F\theta} - e^{-\frac{\theta}{B}} \left[1 + \sum_{k=0}^{\infty} \left(\frac{\theta}{B}\right)^{k+1} \frac{(1-FB)^{k+1}}{(k!)^2(k+1)} \int_0^{\left[\frac{1}{1-FB}\right]\frac{z}{D}} e^{-z} z^k dz \right] \right\}$$

$$= e^{-\frac{z}{D}} \sum_{k=0}^{\infty} \left(\frac{x}{D}\right)^k \frac{1}{(k!)^2} \int_0^{\frac{\theta}{B}} e^{-z} z^k dz$$

$$- \frac{Ge^{-\left(\frac{z}{D}+F\theta\right)}}{(1-FB)} \sum_{k=0}^{\infty} \left(\frac{y}{(1-FB)D}\right)^k \frac{1}{(k!)^2} \int_0^{(1-FB)\frac{\theta}{B}} e^{-z} z^k dz \dots \dots [10]$$

$$\frac{T_{fi} - u}{T_{fi} - T_o} = e^{-\frac{\theta}{B}} \sum_{k=0}^{\infty} \left(\frac{\theta}{B}\right)^k \frac{1}{(k!)^2} \int_0^{\frac{z}{D}} e^{-z} z^k dz$$

$$+ Ge^{\left(\frac{FB}{1-FB}\right)\frac{z}{D}} \left[e^{-F\theta} - e^{-\frac{\theta}{B}} \sum_{k=0}^{\infty} \left(\frac{\theta}{B}\right)^k \frac{(1-FB)^k}{(k!)^2} \int_0^{\left[\frac{1}{1-FB}\right]\frac{z}{D}} e^{-z} z^k dz \right] \dots \dots [10a]$$

It can readily be seen that if $G = 0$, Equations [10] and [10a] become equivalent to Equations [7a] and [7b]. In most engineering applications $G = 0$ or $G = 1$. It can again be noted that the percentage temperature change is independent of the maximum temperature potential, for both the fluid and pipe.

Although a simple graphical representation cannot give the complete result of Equations [10] and [10a] for all systems, a dimensionless plot of either

or

$$\left[1 + \sum_{k=0}^{\infty} \frac{s^{k+1}}{(k!)^2(k+1)} \int_0^q e^{-z} z^k dz \right]$$

$$\left[\sum_{k=0}^{\infty} \frac{s^k}{(k!)^2} \int_0^q e^{-z} z^k dz \right]$$

versus s, with q as a parameter, will reduce appreciably the arith-

Fig. 5

$$\sum_{k=0}^{\infty} \frac{s^k}{(k!)^2} \int_0^q e^{-z} z^k dz \quad \text{versus} \quad s$$

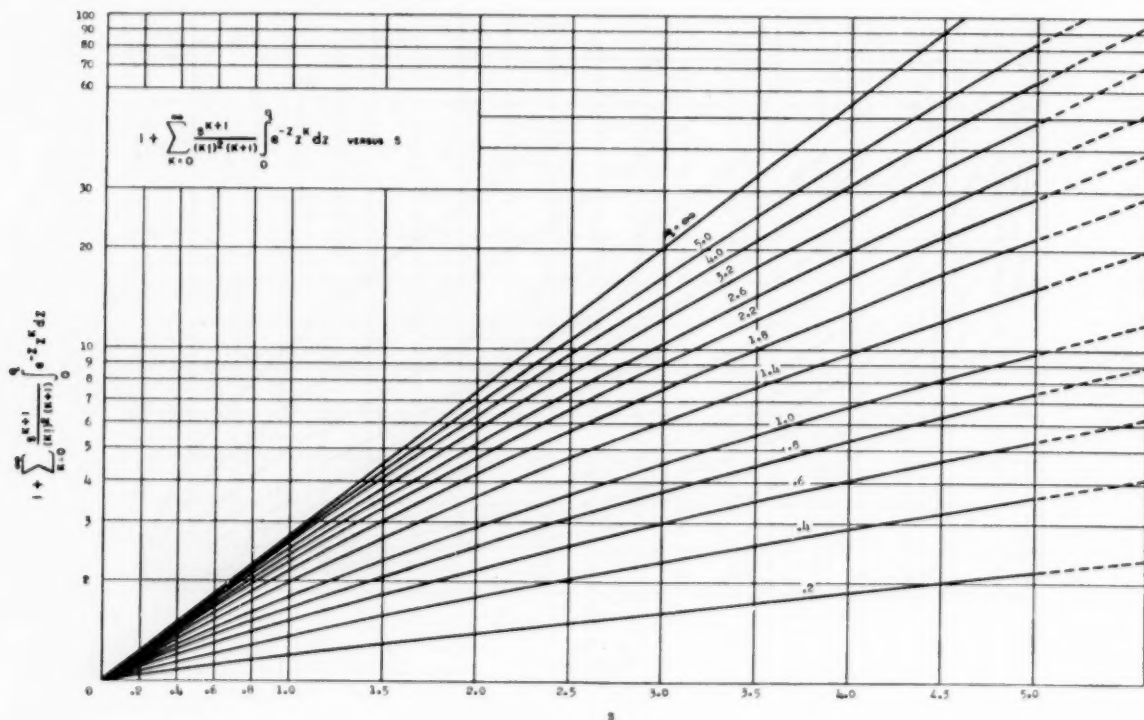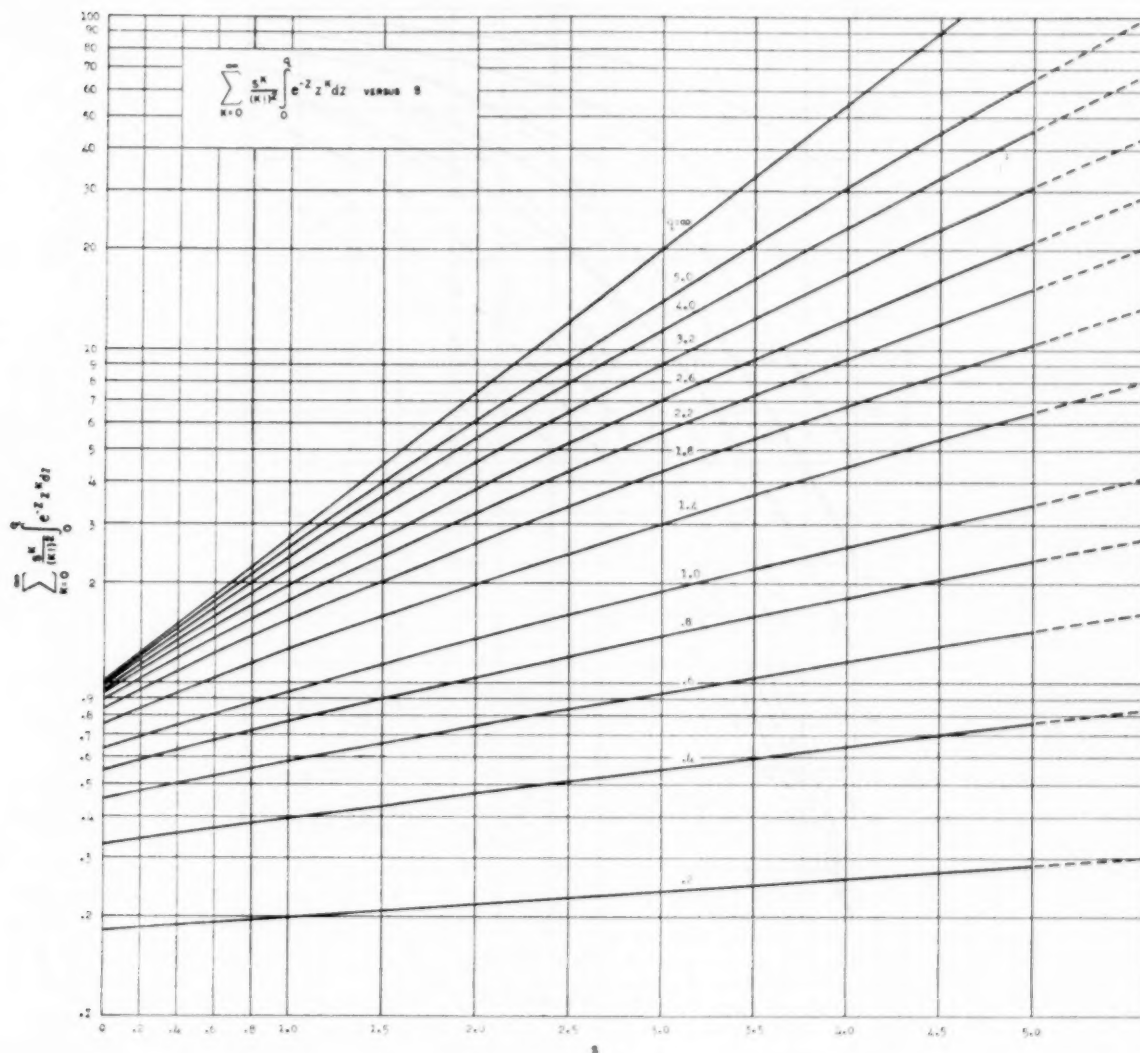$$\sum_{k=0}^{\infty} \frac{s^k}{(k!)^2} \int_0^q e^{-z} z^k dz$$

Fig. 6

metic solution time. These plots are presented[7] in Figs. 5 and 6.

Numerical Examples

Example 1. Consider the case in which 10 lb per sec of air at a temperature of −100 F is introduced into an insulated 20-in., Schedule 30 XS pipe, originally at a constant temperature of 80 F.

---

[7] The tabulations of the functions

$$\left[1 + \sum_{k=0}^{\infty} \frac{s^{k+1}}{(k!)^2(k+1)} \int_0^q e^{-z} z^k dz \right]$$

and

$$\left[\sum_{k=0}^{\infty} \frac{s^k}{(k!)^2} \int_0^q e^{-z} z^k dz \right]$$

versus s, for Figs. 5 and 6, were carried out in the differential analyzer and IBM machines at the Massachusetts Institute of Technology, in connection with a fluid temperature-control problem analyzed by Jackson and Moreland Company, Consulting Engineers, of Boston, Mass., for the General Electric Company.

It is desired to examine the transient conditions for both the fluid and pipe metal temperatures at various sections down the pipe.

Conditions of the problem are as follows:

$T_o = 80$ F
$T_{fi} = -100$ F
$w_f = 10$ lb/sec = 36,000 lb/hr
$r_i = 9.5$ in = 0.792 ft
$r_o = 10.0$ in = 0.833 ft
$\pi(r_o^2 - r_i^2)\rho_m = 104$ lb/ft
$c_m = 0.107$ Btu/(lb) (deg F)

From the text, "Gas Tables,"[8] for air

$c_{pf} \simeq 0.24$ Btu/(lb) (deg F)
$\mu_f \simeq 100 \times 10^{-7}$ lb/(sec) (ft)
$\kappa_f \simeq 0.012$ Btu/(hr) (ft) (deg F)

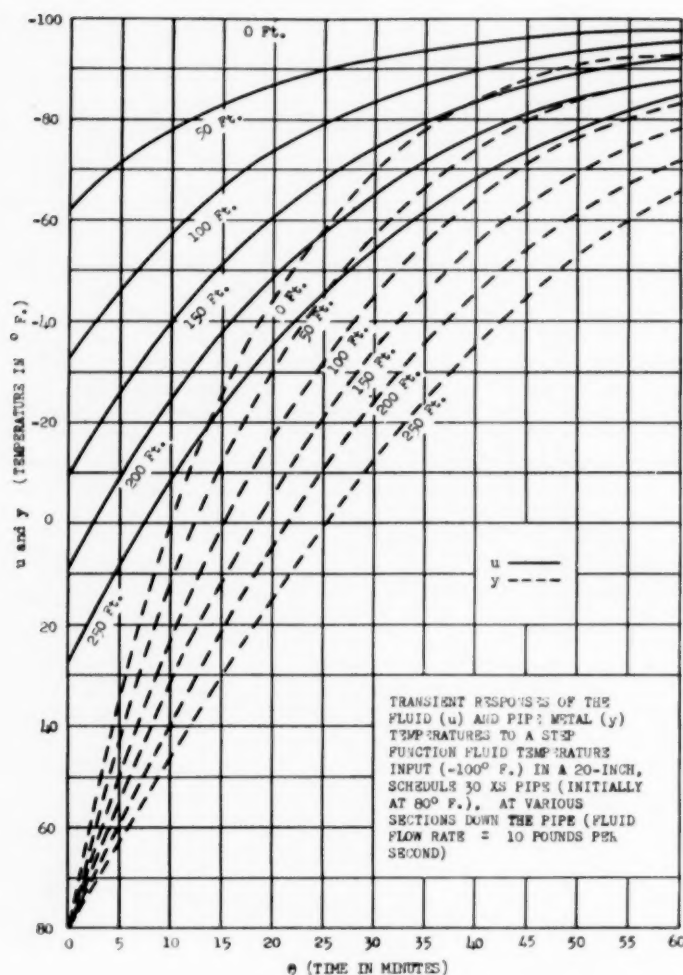[8] "Gas Tables," by J. H. Keenan and J. Kaye, John Wiley & Sons, Inc., New York, N. Y., 1950, p. 34.

FIG. 7   EXAMPLE 1

Thus

$$\text{Re} = \left(\frac{2w_f}{\pi r_i \mu_f}\right) \simeq 8.05 \times 10^5$$

From "Heat Transmission"[9]

$$h_i = \frac{0.02\kappa_f}{2r_i} (\text{Re})^{0.8} \simeq 8.03 \text{ Btu}/(\text{hr}) \text{ (sq ft) (deg F)}$$

Thus

$$B = \frac{\pi(r_o{}^2 - r_i{}^2)\rho_m c_m}{2\pi r_i h_i} = 0.279 \text{ hr}$$

$$D = \frac{w_f c_{pf}}{2\pi r_i h_i} = 216.5 \text{ ft}$$

From Figs. 3 and 4, values of $(T_{fi} - u)/(T_{fi} - T_o)$ and $(y - T_o)/(T_{fi} - T_o)$ may be obtained for various values of (θ/B) and (x/D). Thus the resulting transient temperatures of both the

fluid and pipe may be plotted in graphical form. These are presented in Fig. 7.

Example. 2.   Consider the case in which 5 lb per sec of air with an exponential temperature input of

$$\left[\frac{T_{fi} - u(0, \theta)}{T_{fi} - T_o} = e^{-4.93\theta}\right]$$

is introduced into an insulated 20-in., Schedule 30 XS pipe, originally at a constant temperature T_o. Compare this transient fluid temperature response at a section 60 ft from the pipe entrance to the transient fluid temperature response for a step-function fluid temperature input of $[u(0, \theta) = T_{fi}]$

Therefore

$$F = 4.93 \text{ 1/hr}$$

As in Example 1, it can be seen that

$$w_f = 5 \text{ lb/sec} = 18,000 \text{ lb/hr}$$
$$r_i = 0.792 \text{ ft}$$
$$r_o = 0.833 \text{ ft}$$
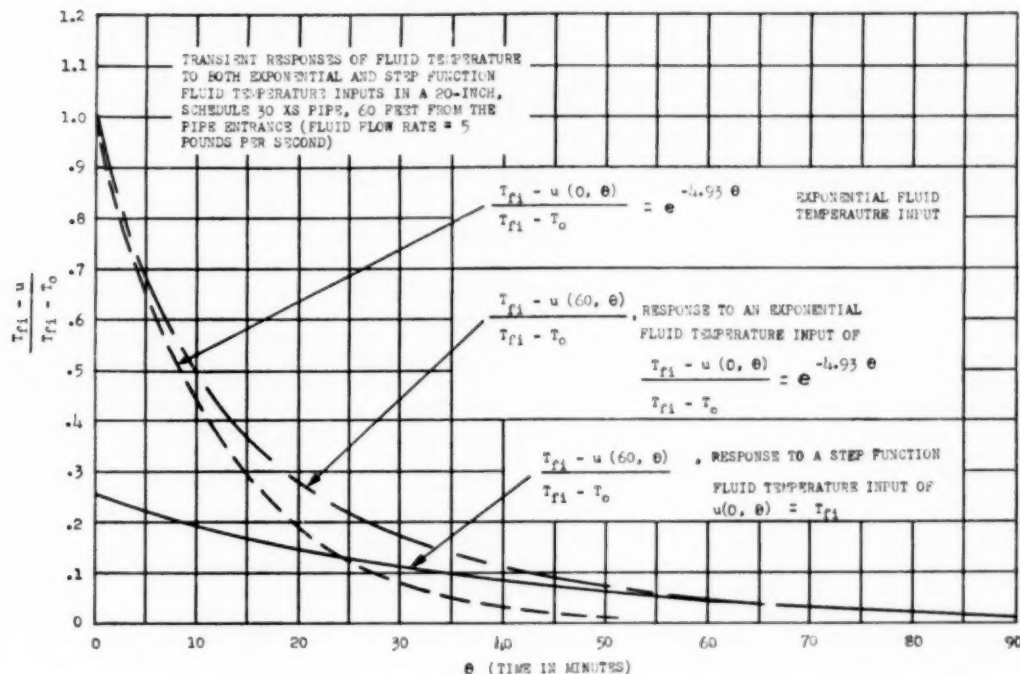$$\pi(r_o{}^2 - r_i{}^2)\rho_m = 104 \text{ lb/ft}$$

[9] "Heat Transmission," by W. H. McAdams, McGraw-Hill Book Company, Inc., New York. N. Y., 1942, p. 170, equation [4f].

TRANSIENT RESPONSES OF FLUID TEMPERATURE
TO BOTH EXPONENTIAL AND STEP FUNCTION
FLUID TEMPERATURE INPUTS IN A 20-INCH,
SCHEDULE 30 XS PIPE, 60 FEET FROM THE
PIPE ENTRANCE (FLUID FLOW RATE = 5
POUNDS PER SECOND)

$$\frac{T_{fi} - u(0, \theta)}{T_{fi} - T_o} = e^{-4.93\theta}$$ EXPONENTIAL FLUID TEMPERAUTRE INPUT

$$\frac{T_{fi} - u(60, \theta)}{T_{fi} - T_o}$$, RESPONSE TO AN EXPONENTIAL FLUID TEMPERATURE INPUT OF

$$\frac{T_{fi} - u(0, \theta)}{T_{fi} - T_o} = e^{-4.93\theta}$$

$$\frac{T_{fi} - u(60, \theta)}{T_{fi} - T_o}$$, RESPONSE TO A STEP FUNCTION FLUID TEMPERATURE INPUT OF $u(0, \theta) = T_{fi}$

θ (TIME IN MINUTES)

Fig. 8   Example 2

$c_m = 0.107$ Btu/(lb) (deg F)
$c_{pf} \simeq 0.24$ Btu/(lb) (deg F)
$\mu_f \simeq 180 \times 10^{-7}$ lb/(sec) (ft)
$\kappa_f \simeq 0.018$ Btu/(hr) (ft) (deg F)
Re $\simeq 2.22 \times 10^6$
$h_i \simeq 4.26$ Btu/(hr) (sq ft) (deg F)

Thus

$B = 0.525$ hr
$D = 205$ ft

Figs. 5 and 6 enable a plot to be made showing the transient responses of fluid temperature to both exponential and step-function fluid temperature inputs. This plot, for a section 60 ft from the pipe inlet, is shown in Fig. 8. It should be noted that the percentage fluid temperature response to the exponential temperature input becomes asymptotic to the percentage fluid temperature response to the step-function temperature input and they are essentially equal at

$$\left[\frac{T_{fi} - u(60, \theta)}{T_{fi} - T_o} = 0.05\right]$$

DISCUSSION AND CONCLUSIONS

The method of procedure to find the thermal lag in systems, such as heat exchangers and pipes, has been shown and the case of the parallel flow heat exchanger was partially treated. The Laplace transformed solutions were presented in Equations [4] and [5]. An equivalent treatment of the counterflow heat exchanger is given in the Appendix.

A convenient method for finding the thermal lag of a fluid flowing, with a step-function temperature input, in an insulated tube or pipe was presented in the form of two plots, Figs. 3 and 4. If the temperature input of the fluid is an exponential function, the thermal lag of the fluid or pipe may be found from Equations [10]

and [10a] with arithmetic simplifications being provided by Figs. 5 and 6.

It has been shown that for the case of a fluid flowing, with a step-function temperature input, in an insulated pipe, the percentage temperature change is independent of the initial temperature potential, for both the fluid and the pipe at any time and at any distance from the pipe inlet. It also has been shown for the case of a fluid flowing, with an exponential temperature input, in an insulated pipe, that the percentage temperature change is independent of the maximum temperature potential, for both the fluid and the pipe.

Two numerical examples have been given. It seems, from the result of the latter example, that if the time constant of an exponential temperature input to the pipe is appreciably less than the time constant of the temperature response of the fluid at the pipe exit to a step-function input to the pipe, 95 per cent of the maximum temperature potential would be attained by the fluid at the pipe exit for the total system in the same length of time, with either an exponential or step-function fluid temperature input.

Analogously, for a heat exchanger followed by a long length of pipe, if the time constant of the temperature response of the fluid at the discharge of the heat exchanger is less than the time constant of the temperature response of the fluid, at the pipe exit, to a step-function input to the pipe, 95 per cent of the maximum potential, for the combined system, will be attained by the fluid at the pipe exit in the same length of time that the fluid at the pipe exit, considered separately with a step-function input, would take to attain 95 per cent of its steady-state value. Thus the temperature response of the fluid at the pipe exit to a step-function input to the pipe can be assumed to represent the temperature response of the entire system, a relatively long pipe preceded by a heat exchanger, when the heat-exchanger thermal capacity is comparatively low.

Appendix

Basic Analysis for a Counterflow System

Since a counterflow system contains boundary conditions both at the inlet ($x = 0$) and at the exit ($x = l$), the Laplace transformation should be taken with respect to time θ, which physically extends to infinity, rather than distance x, which is finite. Therefore the transformations for this case are defined as

$$Y(x, p) \equiv \int_0^\infty e^{-p\theta} y(x, \theta) d\theta$$

$$U(x, p) \equiv \int_0^\infty e^{-p\theta} u(x, \theta) d\theta$$

$$V(x, p) \equiv \int_0^\infty e^{-p\theta} v(x, \theta) d\theta$$

Multiplying Equations [1], [2], and [3] by $e^{-p\theta} d\theta$ and integrating between the limits of zero and infinity

$$U - Y - A(Y - V) = -By(x, 0) + BpY - C \frac{\partial^2 Y}{\partial x^2} \quad [1c]$$

$$U - Y = -D \frac{\partial U}{\partial x} \quad\dots\dots\dots\dots\dots [2c]$$

$$Y - V = -E \frac{\partial V}{\partial x} \quad\dots\dots\dots\dots\dots [3c]$$

Considering the counterflow system with step-function temperature inputs, the boundary conditions are given in Table 2.

Combining Equations [1c], [2c], and [3c] with these boundary conditions, neglecting the thermal conductivity down the tube material ($\kappa_m = 0 = C$), and solving the resulting differential Equation for Y

$$Y = \left[\eta - \gamma + (\gamma - \delta) e^{-\frac{\alpha - \sqrt{\alpha^2 + 4\beta}}{2} l} \right] e^{-\frac{\alpha}{2}(x-l)}$$

$$\times \frac{\sinh\left(\frac{\sqrt{\alpha^2 + 4\beta}}{2} x \right)}{\sinh\left(\frac{\sqrt{\alpha^2 + 4\beta}}{2} l \right)} + (\delta - \gamma) e^{-\frac{\alpha - \sqrt{\alpha^2 + 4\beta}}{2} x} + \gamma \quad [5a]$$

where

$$\alpha = \frac{(EA - D) + (E - D)Bp}{ED(1 + A) + EDBp}$$

$$\beta = \frac{Bp}{ED(1 + A) + EDBp}$$

$$\gamma = \frac{BT_a}{ED(1 + A) + EDBp}$$

$$\delta = \frac{\frac{T_{fi}}{p}\left(1 + \frac{E}{D}\right) + BT_a}{\left(1 + \frac{E}{D}\right) + Bp}$$

$$\eta = \frac{\frac{AT_{ai}}{p}\left(1 + \frac{D}{E}\right) + BT_a}{A\left(1 + \frac{D}{E}\right) + Bp}$$

TABLE 2   BOUNDARY CONDITIONS

Mathematical	Physical
(1) $y(x, 0) = T_o$	T_o is initial tube material temperature (constant) at zero time and at any distance
(2) $u(0, \theta) = T_{fi}$	T_{fi} is inside fluid temperature (constant) at entrance or zero distance and at any time
(3) $v(l, \theta) = T_{ai}$	T_{ai} is the outside fluid temperature (constant) at entrance or distance equal to l and at any time
(4) $\frac{\partial y(0, \theta)}{\partial x} = 0$ $\frac{\partial y(l, \theta)}{\partial x} = 0$	Heat transferred from ends of tube equals zero at distances equal to zero and l and at any time

NOTE: These boundary conditions are shown graphically in Fig. 9.
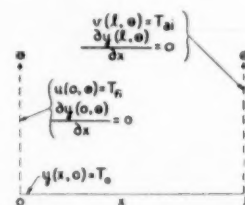
Fig. 9

The inverse Laplace transform of this solution is again the actual solution for $y(x, \theta)$, the tube material temperature. The solution for $y(x, \theta)$, the initial basic equations, and the boundary conditions allow one to find $u(x, \theta)$ and $v(x, \theta)$, the fluid temperatures at any time and at any distance. When considering a specific system, one is often interested in the temperatures only at the sections $x = 0$ and $x = l$. In such cases it is usually advantageous to make the substitution for x in Equation [5a] before taking the inverse transformation.

Calculation of Transient Temperatures in Pipes and Heat Exchangers by Numerical Methods

By G. M. DUSINBERRE,[1] STATE COLLEGE, PA.

An interest has been shown in the prediction of transient phenomena in pipes and heat exchangers. The numerical methods for the solution of such problems exist in a general form in the literature, but it may be of service to research workers and designers to have these methods developed into explicit iteration formulas and computation guides. This is done for a number of cases.

NOMENCLATURE

The following nomenclature is used in the paper:

C, c = heat capacity of fluid within an element or subdivision of apparatus, Btu/F
H, h, k = surface coefficient of heat transfer within an element of apparatus, Btu/hr F
F = temperature change or temperature difference, deg F
t = temperature (or transformed temperature)
V, v = heat capacity of a stream, Btu/hr F
W, w = heat capacity of a wall within an element of the apparatus, Btu/F
Δ = a finite interval
τ = time
a, b = subscripts designating elements of a wall
$1, 2$ = subscripts designating points in fluid stream at boundaries of elements
$'$ = superscript designating a condition at end of a particular time interval

INTRODUCTION

This paper will be divided, like Gaul, into three parts. The reader will want to know, as soon as possible, whether the paper is likely to do him any good. Therefore, in the first part we shall state in general form a number of typical problems. If these are to one's taste, then the proposed methods of solution, the results, and an estimate of accuracy may be of interest. These will appear in the second part. Finally, one may wish to check the assumptions and derivations, and these are given in the Appendix.

PROBLEMS

1 A metal tube, substantially insulated externally, has a specified initial temperature distribution along its length. A stream of fluid is introduced, at a specified mass flow rate, with the entering temperature specified in respect to time. The

temperature history of the fluid and of the tube metal is to be calculated.

In the example which follows, the initial temperature of the tube metal is taken as uniform and the entering temperature of the gas is taken as constant. This is merely for comparison with another method of solution, and neither condition is a necessary restriction on the numerical method.

2 After the system of problem 1 has been in operation for some time, the direction of flow is reversed. The entering fluid temperature is again arbitrarily specified with respect to time. The mass rate of flow may be the same as before, or it may be different. (We do not here take up cases in which the mass rate of flow varies continuously with time.) Again the temperature history is to be calculated.

The methods of this example may be useful for predicting the performance of valved or rotary regenerators.

3 A heat exchanger is operating under a specified set of conditions. A change is imposed on the entering temperature of one or both of the fluid streams. The temperature history is to be calculated.

This analysis may be useful for predicting starting conditions, or lag effects in control problems. (Prof. W. A. Hadley of Columbia University has worked along this line.)

SOLUTIONS

1 For purposes of comparison we choose a problem offered by Rizika[2] in a companion paper. We have a 20-in. schedule 30XS steel pipe of indefinite length. This is initially at a temperature of 80 F throughout. At time zero there is introduced a stream of air at −100 F, at a mass flow rate of 10 lb per sec. External heat transfer from the pipe is negligible. Other data are given as follows:

Outside radius	0.833 ft
Inside radius	0.792 ft
Weight per foot	104 lb/ft
Specific heat of steel	0.107 Btu/lb F
Surface coefficient of heat transfer	8.03 Btu/hr sq ft F

We have to choose a convenient length of pipe as the element for analysis. We select 50 ft, subject to a criterion noted later. Then we calculate certain quantities which are defined in the Appendix as follows:

V = 10 lb/sec × 3600 sec/hr × 0.24 Btu/lb F
= 8650 Btu/hr F
W = 104 lb/ft × 0.107 Btu/lb F × 50 ft = 556 Btu/F
H = 8.03 Btu/hr sq ft F × 2π × 0.792 ft × 50 ft
= 2000 Btu/hr F

We note that $H = 2000 < 17300 = 2V$, so the choice of 50 ft as the unit element is satisfactory.

A finite time interval is to be chosen to satisfy the criterion: $\Delta\tau < W/H = 556/2000 = 0.278$ hr. For convenience we choose $\Delta\tau = 5$ min $= \frac{1}{12}$ hr.

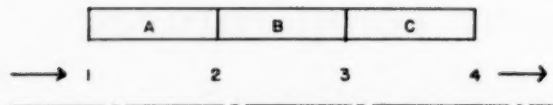[2] "Thermal Lags in Flowing Systems Containing Heat Capacitors" by J. W. Rizika, published in this issue, pp. 411–420.

FIG. 1 SUBDIVISION OF A PIPE

We now write two working equations which are derived in the Appendix

$$t_2 = \frac{2H}{2V + H} t_a + \frac{2V - H}{2V + H} t_1$$

$$= \frac{4000}{19,300} t_a + \frac{15,300}{19,300} t_1$$

$$= 0.207\, t_a + 0.793\, t_1$$

$$t'_a = \left(1 - \frac{H\Delta\tau}{W}\right) t_a + \frac{H\Delta\tau}{2W} t_1 + \frac{H\Delta\tau}{2W} t_2$$

$$= 0.700\, t_a + 0.150 t_1 + 0.150\, t_2$$

For purposes of illustration we shall calculate only three elements of the pipe, or 150 ft. It will be apparent how the calculation can be extended to any greater length that may be desired. Fig. 1 represents schematically the pipe divided into 50-ft elements. At the beginning of a finite time interval $\Delta\tau$, the entering temperature of the air is t_1; at the end of an interval it is t'_1. The average temperature of the wall, taken as existing at the midpoint of the element, is t_a at the beginning and t'_a at the end of an

interval. The same scheme of notation applies to the other elements of the pipe.

According to the first equation, given t_1 and t_a at any instant, we can calculate t_2 at that instant. This presupposes that changes in the air temperature take place in a very short time as compared with the interval $\Delta\tau$. (For explanation see Appendix.)

According to the second equation, given t_a, t_1, and t_2 at the beginning of an interval, we can calculate t'_a at the end of that interval.

With subscripts changed, these equations can be applied at any element of the pipe, over any particular time interval. Thus, by a succession of arithmetical operations, the entire temperature history can be calculated for as long a period as desired. We must not expect the results to be too accurate near the origin of a disturbance, in time or space, because this would be like using too few terms in evaluating a series. If accurate results are required in such a region, we must use a closer subdivision in space and time.

The actual calculation is best done in a tabular form. First we set up a table of coefficients from the formulas. This is shown at the top of Table 1. For convenience, a transformation is used, so that the quantities actually calculated are 80 F — t. Then the initial temperature of the pipe is shown as 0 F and the entering temperature as 180 F. But at time zero, the entering-air temperature is assumed to change instantly over a range of 180 deg F. In the numerical analysis we use the mean value at this instant, and the constant value thereafter. Then the appropriate equations are applied successively, as shown in the table.

TABLE 1 COEFFICIENTS

	1	a	2	b	3	c	4
1		0.150	0.793				
a	—	0.700	0.207				
2		0.150		0.150	0.793		
b				0.700	0.207		
3				0.150	—	0.150	0.793
c						0.700	0.207
4						0.150	—

TEMPERATURES

$\tau/\Delta\tau$	1	a	2	b	3	c	4
			71(3)		56(10)		44
			0(6)		0(12)		0
			—		—		—
0	90(1)	0(2)	71(7)	0(2)	56(13)	0(2)	44
		14(4)		11(9)		8	
		0(5)	143	0(11)	117	0	96
		11(8)	5	8	4	7	3
1	180(14)	25(15)	148	19	121	15	99
		27		22		18	
		18	143	13	124	10	107
		22	14	18	11	15	9
2	180	67	157	53	135	43	116
		27		24		20	
		47	143	37	129	30	116
		24	20	20	17	17	14
3	180	98	163	81	146	67	130
4	180	120	168	103	154	89	140
5	180	136	171	120	161	106	149
6	180	148	174	134	166	120	157
7	180	156	175	145	169	133	162
8	180	162	177	153	172	142	166
9	180	167	178	160	174	150	169

Notes:

(1) This is the mean value for step change
(2) These are the initial values for wall
(3) This is 90 times coefficient above, 0.793
(4) This is 90 times coefficient above, 0.150
(5) This is t_a (= 0) times coefficient above, 0.700
(6) This is t_a times coefficient above, 0.207
(7) This is sum of (3) and (6), which gives t_1
(8) This is t_2 times coefficient above; same for (9) and (10)
(11) This is t_b times coefficient above; same for (12)
(13) The sum of (10) and (12) gives t_1
(14) From here on we use actual value of t_1
(15) The sum of (4), (5), and (8) gives t'_a which becomes a new t_a, and the calculation is continued

TABLE 2 COMPARATIVE RESULTS OF PROBLEM

Time, min	Air temperature at 150 ft		Wall temperature at 100 ft	
	Rizika	Dusinberre	Rizika	Dusinberre
0	−10	36	80	80
5	−26	−19	50	63
10	−40	−36	22	32
15	−52	−50	0	6
20	−61	−60	−18	−16
25	−68	−69	−33	−33
30	−74	−77	−45	−47
35	−79	−82	−56	−59
40	−83	−86	−64	−68
45	−87	−91	−72	−75

TABLE 3 COEFFICIENTS FOR REVERSED FLOW

	1	a	2	b	3	c	4
4					0.793	0.150	——
c					0.207	0.700	
3			0.793	0.150		0.150	
b			0.207	0.700	——		
2	0.793	0.150		0.150			
a	0.207	0.700	——				
1	——	0.150					

TEMPERATURES FOR REVERSED FLOW

z/Δτ							
	88		78		67		
	35		33		31		
9	123	167	111	160	98	150	84
		17		17		13	
	41	117	22	112	0	105	
	31	18	30	15	28	15	
10	72	152	52	144	28	133	0
		8		4		0	
	31	106	16	101	0	93	
	26	11	23	8	20	4	
11	57	125	39	113	20	97	0
		6		3		0	
	24	88	12	79	0	68	
	21	9	18	6	15	3	
12	45	103	30	88	15	71	0

Rizika[2] uses this same problem as an example. His results are obtained by picking off values from a family of curves obtained by an analytical solution. Some of these, with the corresponding results from Table 1, are shown in Table 2. It will be noted that the discrepancy between the two solutions is on the order of 2 per cent of the range, after the first few points.

2 After the system has been in operation for some time, let us suppose that the direction of flow is reversed, air being introduced at the 150-ft point, at the same mass-flow rate and at a temperature of 80 F. The heat-transfer coefficient is assumed unchanged. It is required to calculate the temperature history following this reversal.

It should be noted that an analytical solution of this problem would be extremely difficult, and it would hardly be possible to precalculate curves for all the situations that might arise. The following steps would be required:

(a) Find an analytical expression for the existing temperature distribution at the moment of reversal.

(b) Introduce this equation as a boundary condition for solution of the differential equation.

(c) Solve the differential equation.

(d) Evaluate the solution at a sufficient number of points to plot the results.

(e) Repeat this entire process for each new set of boundary conditions.

However, with the numerical setup, only the following steps are required:

(a) Write a new table of coefficients for the reversed flow, as shown at the top of Table 3. If the rate of flow is also changed, the coefficients must be recalculated, but this is easy.
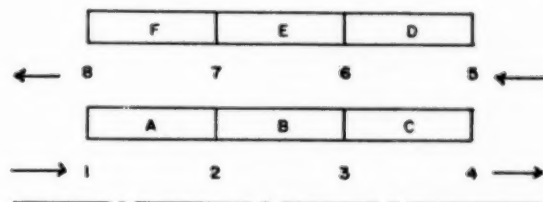

FIG. 2 SUBDIVISION OF A DOUBLE-PIPE EXCHANGER

(b) Write in the temperature distribution in the wall at the instant of reversal.

(c) Write in the new entering-air temperatures and proceed with the arithmetical work.

(d) Repeat steps (b) and (c) for each necessary value of the time of reversal. All quite easy and simple.

In Table 3 we assume that the reversal occurs 45 min after the start, or 9 intervals of Δτ, and the temperatures are calculated for the succeeding 15 min.

3 As a more complex problem, let us calculate the temperature history in a counterflow double-pipe exchanger where both inner and outer pipes have an appreciable heat capacity. Not to introduce too many effects at once, let it be assumed that the outer pipe is externally adiabatic. Initially, both streams are at the same temperature, say zero. At time zero, the entering temperature of one stream is suddenly raised to 100 F and maintained at that value. (But, as before, any arbitrary temperature distribution and any arbitrary temperature change at entrance can be written in with equal facility.)

We assume that the exchanger is made of $1\frac{1}{4}$-in. and 2-in. schedule 40 pipe, 30 ft long, and we decide to use a 10-ft length as the element for analysis. The system is indicated in Fig. 2. Omitting here the detailed calculations, we arrive at the following quantities:

For the (hot) stream inside the inner pipe

$$V = 12{,}000 \text{ Btu/hr F}$$

For the part of this stream within an element

$$C = 6.5 \text{ Btu/F}$$

For the outer stream

$$v = 9000 \text{ Btu/hr F}$$
$$c = 5.15 \text{ Btu/F}$$

For the inner and outer pipe walls within an element

$$W = 2.5 \text{ Btu/F}$$
$$w = 4.0 \text{ Btu/F}$$

For convection from inner stream to inner pipe, within an element

$$H = 3500 \text{ Btu/hr F}$$

For convection from outer stream to inner pipe, within an element

$$h = 4500 \text{ Btu/hr F}$$

For convection from outer stream to outer pipe, within an element

$$k = 5500 \text{ Btu/hr F}$$

We write the convergence criteria

$$H = 3500 < 2V = 24{,}000$$
$$h + k = 10{,}000 < 2v = 18{,}000$$
$$\Delta\tau < \frac{2C}{2V + H} = \frac{13}{24{,}000 + 3500} \text{ hr} = 1.7 \text{ sec}$$
$$\Delta\tau < \frac{2c}{2v + h + k} = \frac{10.3}{18{,}000 + 10{,}000} \text{ hr} = 1.33 \text{ sec}$$

$$\Delta\tau < \frac{W}{H+h} = \frac{2.5}{8000}\ \text{hr} = 1.125\ \text{sec}$$

$$\Delta\tau < \frac{w}{k} = \frac{4}{5500}\ \text{hr} = 2.62\ \text{sec}$$

We choose $\Delta\tau = 1$ sec $= 1/3600$ hr. In the Appendix, heat-
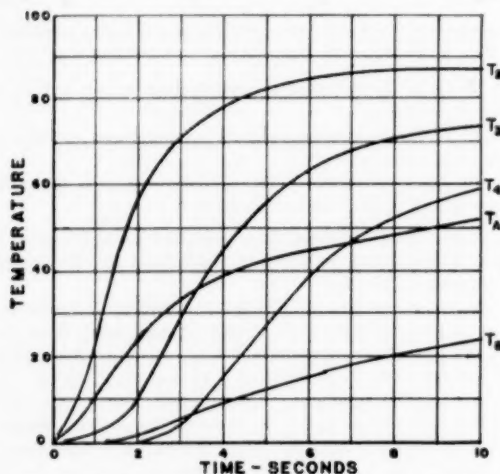
FIG. 3   CALCULATED TEMPERATURES IN AN EXCHANGER

balance equations are developed, analogous to those already used. Substituting in these, we get

$$t'_2 = 0.438\, t_1 + 0.150\, t_a + 0.412\, t_2$$
$$t'_a = 0.216\, t_7 + 0.243\, t_a + 0.297\, t_f + 0.244\, t_8$$
$$t'_a = 0.250\, t_7 + 0.250\, t_8 + 0.194\, t_1 + 0.194\, t_2 + 0.112\, t_a$$
$$t'_f = 0.191\, t_7 + 0.191\, t_8 + 0.618\, t_f$$

Equations for other elements follow by change of subscripts. There are no "current" temperatures in this calculation. The coefficients are written into the operations guide, and temperatures are calculated as shown in Table 4. Some of the results are plotted in Fig. 3.

This system is tending toward a steady state in which, approximately, $t_4 = 68$ and $t_5 = 43$.

It might be felt that rounding-off errors would tend to become serious in a calculation of this sort, but actually they tend to compensate one another. To demonstrate this, the entire calculation was done over using one decimal place, and the results are shown on the last line of the table.

Appendix

We shall first analyze the left-hand element of Fig. 1. The mass-flow rate times the specific heat of the fluid is V Btu/hr F. The heat capacity of the fluid momentarily in the element is C Btu/F. The heat capacity of the wall within the element is W Btu/F. The conductance between the fluid and wall is the area times the surface coefficient, H Btu/hr F.

TABLE 4 COEFFICIENTS

	1	8	a	2	f	7	b	3	e	6	c	4	d	5
1	—		0.194	0.438										
8		0.244	0.250		0.191									
a		0.243	0.112	0.150										
2			0.194	0.412			0.194	0.438						
f		0.297			0.618									
7		0.216	0.250		0.191	0.244	0.250		0.191					
b						0.243	0.112	0.150						
3							0.194	0.412			0.194	0.438		
e						0.297			0.618					
6						0.216	0.250		0.191	0.244	0.250		0.191	
c										0.243	0.112	0.150		
4											0.194	0.412		
d										0.297			0.618	
5										0.216	0.250		0.191	

TEMPERATURES

τ	1	8	a	2	f	7	b	3	e	6	c	4	d	5
0	50	0	0	0	0	0	0	0	0	0	0	0	0	0
			10	22										
1	100	0	10	22	0		4	10						0
2	100	2	24	55	0	0	4	10	0		2	4		0
3	100	6	33	71	0	1	13	29	0	0	2	4	0	0
4	100	9	39	78	1	3	21	45	0	0	7	15	0	0
5	100	12	41	82	4	6	27	56	1	2	13	27	0	0
6	100	15	45	84	5	8	32	63	2	3	17	38	0	0
7	100	18	46	86	8	12	35	68	4	5	22	47	1	0
8	100	20	48	86	10	14	38	71	5	6	25	52	2	0
9	100	23	50	86	13	16	41	73	7	8	29	56	2	0
10	100	24	52	87	15	17	42	74	9	10	30	59	3	0
10	100.0	24.9	51.3	86.9	15.4	17.2	41.4	73.5	8.8	9.5	30.1	58.8	3.0	0

If small changes can be taken as linear, the mean temperature difference between fluid and wall is

$$\frac{t_1 + t_2 + t'_1 + t'_2}{4} - \frac{t_a + t'_a}{2}$$

As an approximation we can use the initial difference

$$\frac{t_1 + t_2}{2} - t_a$$

The effect of this approximation will not be serious because the primed quantities will be used in the succeeding time interval. Then the heat flow by convection is taken as

$$Q_h = \left(\frac{t_1 + t_2}{2} - t_a\right) H\Delta\tau \dots\dots\dots\dots [1]$$

On the linear assumption, the change of temperature of the fluid passing through the element is $(t_1 + t'_1 - t_2 - t'_2)/2$, and approximately, it is $t_1 - t_2$. Then the heat given up is

$$Q_v = (t_1 - t_2)V\Delta\tau \dots\dots\dots\dots\dots [2]$$

The change of temperature of the fluid within the element is $(t_1 + t_2 - t'_1 - t'_2)/2$ and, approximately, it is $t_2 - t'_2$. Then the heat given up in this way is

$$Q = (t_2 - t'_2)C \dots\dots\dots\dots\dots [3]$$

By heat balance, $Q_h = Q_v + Q_c$, so

$$\left(\frac{t_1 + t_2}{2} - t_a\right) H\Delta\tau = (t_1 - t_2)V\Delta\tau + (t_2 - t'_2)C \dots [4]$$

From this we get the explicit equation

$$t'_2 = \left[1 - \left(\frac{2V + H}{2C}\right)\Delta\tau\right] t_2 + \left[\left(\frac{2V - H}{2C}\right)\Delta\tau\right] t_1 + \left[\frac{H}{C}\Delta\tau\right] t_a \dots\dots [5]$$

In this equation, for convergence, all the coefficients should be positive. So we should choose the system size and the time interval to satisfy the following criteria

$$H \leqq 2V \dots\dots\dots\dots\dots [6]$$

$$\Delta\tau \leqq \frac{2C}{2V + H} \dots\dots\dots\dots\dots [7]$$

If C is small in comparison with V, it may be inconvenient to observe the condition of Equation [7]. But if C is very small, it may be ignored. Then from Equations [1] and [2] we get

$$\left(\frac{t_1 + t_2}{2} - t_a\right) H\Delta\tau = (t_1 - t_2)V\Delta\tau \dots\dots\dots [8]$$

$$t_2 = \left(\frac{2V - H}{2V + H}\right) t_1 + \left(\frac{2H}{2V + H}\right) t_a \dots\dots [9]$$

This equation was used in the first problem. The time interval and the primed symbols do not appear. The assumption is that the fluid temperature changes in a very short time relative to $\Delta\tau$. The only criterion is Equation [6].

It will be noted that t'_1, although it is assumed to be a known quantity, does not appear in the working equations. If only the assumption of linearity is made, some rather complicated equations result, in which t'_1 appears with a negative coefficient. The author believes, with Southwell, that in numerical calculations it is better to use the simplest working equations and reach the de-

sired degree of precision by a close subdivision, than to adopt complex equations for the sake of obtaining high precision with a crude network.

The heat flow by surface convection can be equated to the heat stored in the wall, thus

$$\left(\frac{t_1 + t_2}{2} - t_a\right) H\Delta\tau = (t'_a - t_a)W \dots\dots\dots [10]$$

$$t'_a = \left(1 - \frac{H\Delta\tau}{W}\right) t_a + \frac{H\Delta\tau}{2W} t_1 + \frac{H\Delta\tau}{2W} t_2 \dots\dots [11]$$

This gives the criterion

$$\Delta\tau < \frac{W}{H} \dots\dots\dots\dots\dots [12]$$

which was observed in the first problem.

When a step change of temperature is imposed on a system, the rule in numerical calculation is to use the mean value at the instant of the change. This was done at point 1 in the first problem, at point 4 in the second problem, and at point 1 in the third problem.

Referring to Fig. 2, in the third problem the equation for the outer stream, corresponding to Equation [5], is

$$t'_s = \left[1 - \left(\frac{2v + h + k}{2c}\right)\Delta\tau\right] t_s + \left[\left(\frac{2v - h - k}{2c}\right)\Delta\tau\right] t_t + \frac{h\Delta\tau}{c} t_a + \frac{k\Delta\tau}{c} t_f \dots\dots [13]$$

with the criteria

$$h + k \leqq 2v \dots\dots\dots\dots\dots [14]$$

$$\Delta\tau \leqq \frac{2c}{2v + h + k} \dots\dots\dots\dots\dots [15]$$

The equations for the walls are

$$t'_a = \left[1 - \left(\frac{h + H}{W}\right)\Delta\tau\right] t_a + \frac{h\Delta\tau}{2W} t_t + \frac{h\Delta\tau}{2W} t_s + \frac{H\Delta\tau}{2W} t_1 + \frac{H\Delta\tau}{2W} t_2 \dots\dots [16]$$

$$t'_f = \left(1 - \frac{k\Delta\tau}{w}\right) t_f + \frac{k\Delta\tau}{2w} t_2 + \frac{k\Delta\tau}{2w} t_s \dots\dots [17]$$

The criteria are

$$\Delta\tau \leqq \frac{W}{h + H} \dots\dots\dots\dots\dots [18]$$

$$\Delta\tau \leqq \frac{w}{k} \dots\dots\dots\dots\dots [19]$$

This completes the equations used in the example problems. In conclusion, a few additional situations will be mentioned without writing the equations at length.

If a single heat capacity will represent the wall adequately, but if the latter has an appreciable thermal resistance, then half this resistance may be added to the surface resistance on each side.

If the thermal resistance of the wall is appreciable and if in addition it has a relatively large heat capacity, then it may be necessary to subdivide the wall into layers, assigning a proper conductance and heat capacity to each layer.

We have seen that with a gas flowing in a heavy tube, it may be possible to neglect terms such as C in comparison with terms

such as W. With a liquid flowing in large thin-walled tubes, exactly the opposite may occur; the heat capacity of the walls may be negligible in comparison with that of the contained fluid. This would give a corresponding simplification and a greater permissible time interval. In this case the two terms such as H should be combined into an over-all coefficient. The equations are readily written out.

If the apparatus is arranged for parallel or crossflow instead of counterflow, the same formulas are used, solving always for the downstream point of an element and applying the iteration in the appropriate sequence.

Discussion

M. B. COYLE.[2] Professor Dusinberre is to be congratulated on placing yet another tool for the solution of complex heat-flow problems into the hands of the engineer. The latest one is the more valuable in that it deals with problems that are particularly difficult to solve by other methods. He has packed a remarkable amount of information into this short paper, though the important Appendix suffers some loss of clarity in the process. It is, for example, rather alarming at first sight to read that if the value of C is so small that Equation [7] is difficult to satisfy, it may be disregarded, even though further thought shows the advice to be perfectly sound.

The physical interpretation of the formulas (taking the first

[2] Metropolitan-Vickers Electrical Co Limited, Manchester, England.

problem as an example) is presumably that Equations [5] and [11] define two different types of transient, the first taking place as temperature changes in the fluid travel with the fluid down the pipe, and the second arising from thermal lag in the walls. The values of $\Delta\tau$ derived from Equations [7] and [12] give the maximum values of the time interval which permit a detailed study of the corresponding type. The fact that one of these values may be small compared with the other means not that the effect of the corresponding transients will necessarily be small too, but that their duration will be relatively short. Should one type be so rapid that its detailed study is without interest, a "present value" equation like Equation [9] can be used which, while not ignoring the effect of the transients, implies that they occur instantaneously. The use of the small value of $\Delta\tau$ is then unnecessary. This is well shown in the first problem, Table 1, where the air temperatures at $\tau/\Delta\tau = 0$ derived from Equation [9] represent conditions after the sudden change in air temperature has passed down the pipe (which only takes about half a minute) and before the more gradual fall in wall temperature has properly begun.

AUTHOR'S CLOSURE

This author's failure to use words enough is an old and regrettable habit, so Mr. Coyle's clarification is most welcome However, to say that Equations [5] and [11] define transients different in type, is less precise than to say that they describe events in different regions of the system under study, these regions being different in physical structure and behavior.

A Wall-Thickness Formula for High-Pressure, High-Temperature Piping

By WINSTON R. BURROWS,[1] R. MICHEL,[2] AND A. W. RANKIN[3]

Early in 1951 the Executive Committee[4] of the ASA B31 Sectional Committee, Code for Pressure Piping, authorized the formation of a Task Force[5] to try to resolve the differences in points of view on the criteria to be used in calculating the wall thickness required for high-pressure steam piping. After considerable study and discussion, this Task Force recommended to the Executive Committee the formula given in the following paragraph. Inasmuch as this formula has now been adopted[6] by the Power Boiler Section of the ASME Boiler Code, and has been approved by the Power Piping Committee of the ASA B31 Code for Pressure Piping, it was believed that the detailed work of this Task Force and, in particular, the development of this particular formula, should be published; that is the purpose of this paper.

Wall-Thickness Formula [30]

The formula developed by the ASA B31 Task Force is as follows:

$$t = \frac{pD}{2S + 2y\,p}$$

t = minimum thickness[a]
p = internal pressure
D = outside diameter
S = Code allowable S-value

In this formula, y is a temperature-dependent parameter with the following values:

Temp F	900 and below	950	1000	1050	1100	1150 and above
y, ferritic steels	0.4	0.5	0.7	0.7	0.7	0.7
y, austenitic steels	0.4	0.4	0.4	0.4	0.5	0.7

For values of y of 0.4, the foregoing formula reduces to the former ASME and ASA B31 Code formulas for calculating the thickness of high-pressure steam piping.

[a] To this thickness are to be added the current allowances for corrosion, threading, mill tolerance, etc.

NOMENCLATURE

The following nomenclature is used in the paper:

A_1, A_2 = constants
C_1, C_2, C_3 = constants
d = inside diameter, in.
D = outside diameter, in.
e = principal strain in torsion test specimen, in. per in.
F, F_1 = symbols denoting functions

[1] Assistant Chief Engineer, Whiting Refinery, Standard Oil Company (Indiana), Whiting, Ind.
[2] Head Engineer, Scientific and Performance Section, Bureau of Ships, Navy Department, Washington, D. C. Mem. ASME.
[3] Assistant Division Engineer, Large Steam Turbine Engineering Division, General Electric Co., Schenectady, N. Y. Mem. ASME.
[4] F. S. G. Williams, Chairman, Taylor Forge and Pipe Works, Inc., New York 7, N. Y.; L. W. Benoit, Secretary, Manufacturers Standardization Society of the Valve and Fittings Industry, New York 17, N. Y.
[5] D. G. Reid, Chairman, Sargent and Lundy; J. E. Lattan, Secretary, Taylor Forge and Pipe Works; Dr. H. C. Boardman, Chicago Bridge and Iron Company; W. R. Burrows,[7] Standard Oil Company (Indiana); Sabin Crocker, Ebasco Services, Inc.; A. R. Gatewood, American Bureau of Shipping; M. L. Ireland, Jr., Newport News Shipbuilding and Dry Dock Company; H. C. E. Meyer, Gibbs and Cox, Inc.; R. Michel,[7] Bureau of Ships, Navy Department; J. J. Murphy, The M. W. Kellogg Company; Dr. A. Nadai, Pittsburgh, Pa.; A. W. Rankin,[7] General Electric Company; Capt. R. A. Smyth, U. S. Coast Guard; Prof. C. R. Soderberg, Massachusetts Institute of Technology; H. A. Wagner, The Detroit Edison Company.
[6] To the extent of offering it as a proposed revision of the Code; MECHANICAL ENGINEERING, vol. 74, September, 1952, p. 763.
[7] Subcommittee on Selection of Formulas.
Contributed by the Power Division and presented at the Annual Meeting, New York, N. Y., November 30–December 5, 1952, of THE AMERICAN SOCIETY OF MECHANICAL ENGINEERS.
NOTE: Statements and opinions advanced in papers are to be understood as individual expressions of their authors and not those of the Society. Manuscript received at ASME Headquarters, December 2, 1952. Paper No. 52—A-151.

K = adjustable constant used as divisor of criterion stress in cylinder, dimensionless; in Formula [28], K is a temperature-dependent factor varying between 1.00 and 1.15.
m = constant in Bailey's estimate of strain ratio, dimensionless
n = exponent in power function expressing stress-strain diagram, dimensionless
p = internal pressure, psi
r = any radius of cylinder, in.
s = principal stress in torsion test specimen, psi
t = minimum wall thickness = $\frac{1}{2}(D - d)$, in.
y = temperature-dependent parameter varying between 0.4 and 0.7; used in Formula [30]
α = angle of slope of straight-line stress-strain diagram, deg
β = $2/n$
δ = $2r$, any diameter of cylinder, in.
ϵ = principal strain in tensile test specimen, in. per in.
ϵ_r = radial strain in cylinder, in. per in.
ϵ_t = tangential strain in cylinder, in. per in.
ϵ_δ = strain in tensile test specimen corresponding to maximum shear strain in cylinder at any diameter δ, when maximum shear strain in cylinder at outside surface corresponds to yield strain ϵ_0, in tensile test specimen, in. per in.
ϵ_0 = yield strain in tensile test specimen, in. per in.
η = exponent in numerical expression for K, dimensionless
ν = Poisson's ratio, dimensionless
ρ = outward radial deformation of cylinder at any point r, in.
σ = principal stress in tensile test specimen, psi
σ_{eq} = equivalent stress, based on some theory of creep or failure

σ_r = radial stress in cylinder, psi

σ_t = tangential stress in cylinder, psi

$\sigma_{t,\,avg}$ = average tangential stress, psi

σ_z = axial stress in cylinder, psi

INTRODUCTION

The calculation of the stresses in pipe walls has been the subject of a great many papers during the last one-hundred years. In particular, piping has been a fertile field for the application of various theories of failure, and also for the application of theories of high-temperature creep. The vast majority of these papers, however, have been of a mathematical nature only, and there are relatively few which have presented experimental test data on failure pressures, particularly at elevated steam temperatures. Unfortunately, it is at the higher temperature levels, where only few test data are available, that there is the greatest need for careful choice of pipe-wall thickness. It is self-evident that here the wall thickness must be adequate to protect against wall bursting, but to obtain this protection by overconservatism can itself lead to serious consequences. At modern steam pressures, temperatures, and mass flows, such overconservatism can impose a severe economic burden, and, in addition, a wall that is too heavy can adversely affect reliable operation due to the thermal stresses set up by temperature differences between the inner and outer wall surfaces during temperature transients. In naval and marine work, overconservatism imposes a heavy penalty in the additional weight of piping which must be carried, while for all installations the heavier piping results in difficult problems in expansion stresses which can themselves result in operational troubles if not solved correctly (1, 2).[3] It is accordingly evident that this Task Force faced a problem requiring the exercise of considerable engineering judgment.

EXPERIMENTAL DATA

The test data obtained by several investigators on the room-temperature yielding and bursting of tubes were summarized in the recent paper by Blair (3). The results of the bursting tests have been replotted in Fig. 1, and from this it can be seen that a

---

[3] Numbers in parentheses refer to the Bibliography at the end of the paper.
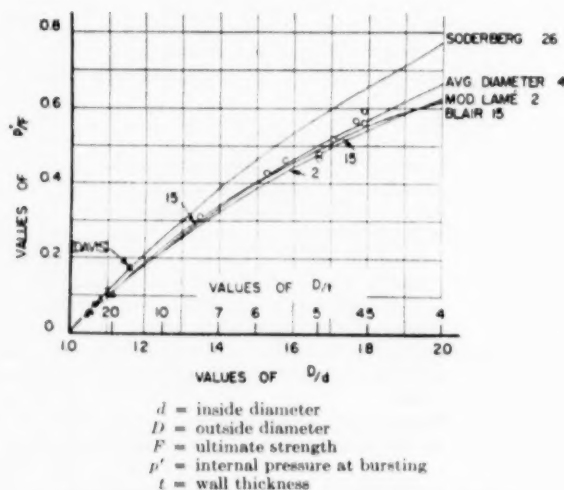
FIG. 1 ROOM-TEMPERATURE TUBULAR BURSTING TESTS

(Comparison of calculated stresses by Formulas [2, 4, 15, and 26] with test data of Blair, Reference 3, and Davis, Reference 4.)

d = inside diameter

D = outside diameter

F = ultimate strength

p' = internal pressure at bursting

t = wall thickness

relatively wide range of D/t (outside pipe diameter/wall thickness) was covered by these tests. The D/t ratio varies from approximately 50 down to 4.5, and this covers the range of values encountered normally in steam piping. A series of combined-stress experiments on tubes was conducted by Davis (4), and the point from the Davis paper corresponding to the usual (approximate) piping-stress configuration in which the axial stress is one half the average tangential stress has also been replotted in Fig. 1.

Other test data on room-temperature tests on tubes and pipes are available in the literature, but the results presented in Fig. 1 are sufficiently complete to furnish a reasonably sound basis for the selection of a wall-thickness formula at room and slightly elevated temperatures. At the higher operating temperatures of modern boilers and turbines, however, the only test data available are in the recent publication by Kooistra, Blaser, and Tucker (5) which presented experimental results on pipe bursting at 850 F and 950 F; these data are reproduced in Figs. 2 and 3.
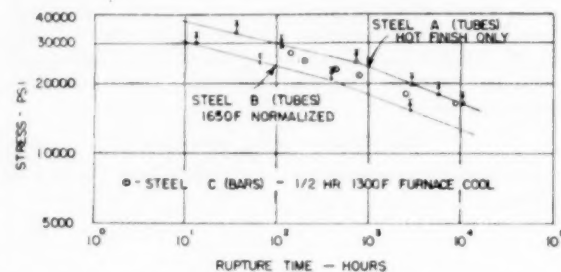
FIG. 2 HIGH-TEMPERATURE, 850 F, TUBULAR STRESS-RUPTURE TESTS ON SA 210 TUBES

(Comparison of calculated stresses by Formula [3]—bases of arrows—and Formula [30]—tips of arrows—with test data of Kooistra, Blaser, and Tucker, Reference 5.)
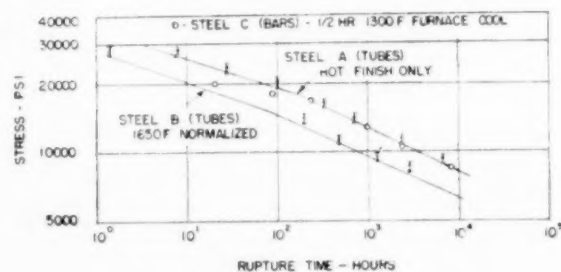
FIG. 3 SAME AS FIG. 2, BUT AT 950 F

While the latter paper is a valuable contribution to the technical literature on high-temperature pipe bursting, the wall thicknesses used, at least in the published results, were too small relative to the diameter to be of unquestioned value in differentiating between various wall-stress formulas. In Figs. 2 and 3 the bases of the arrows show the wall stress as calculated by the Common Formula [3], which is simply the average tangential stress based on the internal pressure and inside pipe diameter, while the tips of the arrows show the wall stress as calculated by the proposed wall-thickness Formula [30]. At 850 F, this latter formula duplicates the modified-Lamé [2], which is the tangential stress at the inside surface based on elastic-stress analysis, while at 950 F the proposed Formula [30] differs from the modified-Lamé [2] by only a small amount. The differences in calculated stress between the tips and bases of the arrows are too small to furnish an unequivocal justification for either of the two Formulas [3] and

[30], and accordingly these particular tests would also fail to differentiate unequivocally between most of the other wall-thickness formulas considered in this study.

WALL-STRESS FORMULAS

During the course of this investigation, a total of thirty-one formulas were considered. Most of these formulas were taken from the technical literature,[9] but several were developed empirically during the investigation. These thirty-one formulas are detailed in Table 1 where the first column gives the identification as used in this paper, the second column gives a brief description of the formula and its analytical or empirical basis, while the third column gives the formula itself. Some apologies are in order with respect to the proper names used in the identification column; these are simply the means employed by this Task Force to identify concisely the various expressions, and it is not intended to credit unduly those to whom reference is made nor to disparage those not mentioned who also may have been instrumental in the development of a particular theory or formula. This Task Force is deeply grateful to the many persons who assisted in this study by suggesting formulas based on both theoretical grounds or empirical relations, and regrets that space does not permit a more detailed acknowledgment.

NUMERICAL STUDIES OF WALL-STRESS FORMULAS

A numerical evaluation was made of all thirty-one formulas by calculating the wall stresses given by each expression at 1000 psi internal pressure for D/t values ranging from 4 to 200. These calculated stresses are given in Table 2. The degree to which the required wall thickness varies between the different formulas can be evaluated from Table 2, while the allowable pressures for specific Code S-values and D/t ratios are directly determinable. It should be noted that the results presented in Table 2 are the specific calculated stresses obtained directly from the various expressions; no modifications have been made to compensate for the fact that some formulas give average stresses, some give point stresses determined from elastic or plastic theory, and others are equivalent stresses based on some particular theory of failure.

The relatively wide range in calculated stresses that is obtained with these thirty-one formulas is clearly shown in Table 2. At the lowest selected value of $D/t = 4$, the calculated stresses range from 1000 psi for the Common Formula [3] up to 2667 psi as obtained by the Guest Formula [7]. On the other end of the selected field, $D/t = 200$, the calculated stresses range from 107,298 psi for the Meyer II Formula [31] down to 76,538 psi for the Average Shear Expression [14]. It will be recalled that these are all calculated wall stresses at 1000 psi internal pressure; in all expressions, the wall stress varies directly with the internal pressure.

One of the major purposes of this numerical investigation was to determine the range in values given by the various formulas and to place in separate groups those expressions which gave approximately the same results. If several formulas, irrespective of the basis of their development, gave the same wall thickness (or calculated wall stress at 1000 psi internal pressure) within engineering accuracy, for D/t values within the range of 4 to 200, that formula which was the simplest to use was considered equivalent to all others giving the same approximate wall thickness and was used generally in place of the others in further discussions. This procedure was not intended as a rejection or criticism of the theories upon which the more complex expressions are based and should not be so construed; instead it simply recognizes the need for simplicity in Code calculations of wall thickness. Since the primary aim of the Task Force

[9] In particular, reference was made to (6) and (7) of the Bibliography.

was to recommend a pipe-wall-thickness formula for engineering design, simplicity of expression was an important goal, and the rejection of complex expressions in favor of simpler equivalent ones is understandable.

Table 3 gives the equivalent groups into which the calculated results of Table 2 have been rearranged; the close equivalence between a number of the formulas of Table 1 is evident from the groups of Table 3. In the latter Table 3, the first formula of each group is the simplest expression in that group. It should be noted in Table 3 that equivalence between formulas at low values of D/t was deemed of more importance than equivalence at large values of D/t; this point will be discussed more fully in the following section.

DEVELOPMENT OF WALL-THICKNESS FORMULA [30]

The experimental data given in Fig. 1 are adequate to provide a reasonably firm foundation for the use of the modified-Lamé Formula [2] for room and slightly elevated-temperature operation. Although the Average-Diameter Formula [4] and the Blair Formula [15] both furnish closer agreement with the test data than the modified-Lamé [2], neither differs from the latter by any significant degree, even for relatively heavy-walled pipe. In particular, the slightly better correlation with the test data as obtained with the Average-Diameter [4] and the Blair [15] formulas is not sufficient to warrant discarding the modified-Lamé Formula [2] which has been used in engineering design for so many years.

A particular point should be noted regarding the acceptance of the modified-Lamé Expression [2] for design at room and slightly elevated temperatures. The modified-Lamé Formula [2] gives essentially the same results as the Lamé Tangential Formula [1], and the former was introduced originally as an alternate for the latter because of its greater simplicity. The Lamé Tangential Formula [1] is based directly on elastic-stress analysis, but the recommendation of this Task Force to use the modified-Lamé Formula [2] for room and slightly elevated temperature does not imply an acceptance of elastic-stress analysis in the problem of pipe bursting. The modified-Lamé Formula [2] has been recommended solely because it agrees reasonably well with the available data on actual pipe bursting at the lower temperatures.

In the elevated-temperature regions, the paucity of adequate test data made more difficult the selection of a satisfactory criterion of pipe-wall thickness. The problems of creep and rupture here assume dominant roles, while the intercrystalline breaks which occur at high temperature render questionable the results of room-temperature bursting tests. In addition, with the Code allowable S-values determined by applying a factor of safety to the long-time high-temperature rupture stress (with which procedure the authors of this paper are in complete agreement), there is a reserve of strength in high-temperature piping which is not present in lower-temperature designs. With the current factors of safety on the 100,000-hr life, the true time to rupture is usually many times the planned equipment life, and moderate errors in design, fabrication, or operation will not reduce the true life below the planned equipment life. In addition, for short periods of inadvertent misoperation, the ultimate strength is several times the long-time rupture strength. These reserves of strength, however, must be balanced against the more difficult problems which exist in piping designed for high-temperature operation, as, for instance, the lower ductility at failure as well as the greater difficulty in holding the expansion stresses to acceptable values.

Considering first the allowable creep strains, or creep rates, in high-temperature piping, it is a moot question whether such creep should be limited at the outer or inner pipe surface. If one

TABLE 1   FORMULAS FOR PIPE-WALL STRESSES

Identification	Description	Formula
1. Lamé tangential (so-called Lamé)	maximum principal elastic stress due to Lamé, the tangential stress at the inner surface. Equivalent stress, at inner surface, based on maximum stress criterion of failure and elastic stress distribution.	$\sigma_t = \sigma_{eq} = p\left[\dfrac{\frac{1}{2}\left(\frac{D}{t}\right)^2 - \frac{D}{t} + 1}{\left(\frac{D}{t} - 1\right)}\right]$
2. Modified Lamé (Reference 8)	Boardman's approximation to formula I.	$\sigma_t = p\left[\frac{1}{2}\left(\frac{D}{t}\right) - 0.4\right]$
3. Common (sometimes called the average-stress expression) (Reference 9)	average tangential stress, based on inner diameter.	$\sigma_{t,\,avg} = p\left[\frac{1}{2}\left(\frac{D}{t}\right) - 1\right]$
4. Average—diameter (Reference 10)	pseudo-average tangential stress, based on average of inner and outer diameters.	$\sigma_{t,\,avg} = p\left[\frac{1}{2}\left(\frac{D}{t}\right) - 0.5\right]$
5. Barlow (Reference 9)	psuedo-average tangential stress, based on outer diameter.	$\sigma_{t,\,avg} = p\frac{1}{2}\left(\frac{D}{t}\right)$
6. Clavarino (References 6, 9, 11)	equivalent stress, at inner surface, based on maximum strain criterion of failure, elastic stress distribution, and a value of 0.3 for Poisson's ratio.	$\sigma_{eq} = p\left[\dfrac{0.425\left(\frac{D}{t}\right)^2 - 0.4\left(\frac{D}{t}\right) + 0.4}{\left(\frac{D}{t} - 1\right)}\right]$
7. Guest (References 6, 11)	equivalent stress, at inner surface, based on maximum shear criterion of failure and elastic stress distribution.	$\sigma_{eq} = p\left[\dfrac{\frac{1}{2}\left(\frac{D}{t}\right)^2}{\left(\frac{D}{t} - 1\right)}\right]$
8. Beltrami (References 6, 11)	equivalent stress, at inner surface, based on energy criterion of failure, elastic stress distribution, and a value of 0.3 for Poisson's ratio.	$\sigma_{eq} = p\dfrac{\sqrt{\begin{array}{l}0.2375\left(\frac{D}{t}\right)^4 - 0.6\left(\frac{D}{t}\right)^3 + \\ 1.8\left(\frac{D}{t}\right)^2 - 2.4\left(\frac{D}{t}\right) + 1.2\end{array}}}{\left(\frac{D}{t} - 1\right)}$
9. von Mises (References 6, 11)	equivalent stress, at inner surface, based on modified energy criterion of failure and elastic stress distribution.	$\sigma_{eq} = p\left[\dfrac{0.433\left(\frac{D}{t}\right)^2}{\left(\frac{D}{t} - 1\right)}\right]$
10. Bailey–Nadai, (inner surface) (References 6, 12, 13)	equivalent stress, at inner surface, based on maximum shear criterion of failure, plastic stress distribution, and a power-function stress-strain diagram.	$\sigma_{eq} = p\left[\dfrac{\beta}{1 - \left(\frac{d}{D}\right)^{\delta}}\right]$
11. Bailey–Nadai, (outer surface) (References 6, 12, 13)	Same as formula 10, except evaluated at outer surface.	$\sigma_{eq} = p\left[\dfrac{\beta}{\left(\frac{D}{d}\right)^{\delta} - 1}\right]$

TABLE 1 (*Continued*)

Identification	Description	Formula
12. Bailey–Nadai, (outer surface) (References 6, 12, 13)	tangential stress, at outer surface, based on plastic stress distribution and a power function stress-strain diagram. Note that this formula is identical with formula 11 since radial stress is zero at outer surface.	$\sigma_t = p \left[\dfrac{\beta}{\left(\dfrac{D}{d}\right)^{\beta} - 1} \right]$
13. Creep–common–I (Reference 14)	approximation of formulas 11 or 12 for representative values of β.	$\sigma_{eq} = p \left[\tfrac{1}{2}\left(\dfrac{D}{t}\right) - 0.8 \right]$
14. Average—shear (References 7, 14)	an expression for average shear which utilizes an empirical relation that shear rupture strength is 65% of tensile rupture strength.	$\sigma_{eq} = p \dfrac{0.50}{0.65} \left[\tfrac{1}{2}\left(\dfrac{D}{t}\right) - 0.5 \right]$
15. Blair (Reference 3)	equivalent stress, at inner surface, based on energy criterion of failure, a value of 0.25 for Poisson's ratio, elastic stress distribution (Lamé) for σ_r and σ_a, and average stress distribution (formula 3) for σ_t ("Extended" strain energy).	$\sigma_{eq} = p \dfrac{\sqrt{\left(\dfrac{D}{d}\right) + \dfrac{\left(\dfrac{D}{d}\right)^3 + 3}{2} + \left(\dfrac{D}{d}\right)^4}}{\left(\dfrac{D}{d}\right)^2 - 1}$
16. Beliaev–Sinitski (References 7, 15)	equivalent stress, uniform from inner to outer surface, based on modified energy criterion of failure, plastic stress distribution, and idealized stress-strain diagrams.	$\sigma_{eq} = p \dfrac{\dfrac{\sqrt{3}}{2}}{\ln\left(\dfrac{D}{d}\right)}$
17. Bailey, (inner surface) (References 7, 16)	equivalent strain, at inner surface, based on maximum shear criterion of failure, plastic stress distribution, a power function stress-strain diagram for second-stage creep, and a ratio of diametral to tensile creep of $\left(\dfrac{1}{2}\right)\left(\dfrac{3}{4}\right)^m \left[1 + \left(\dfrac{1}{2}\right)^{n-2m}\right]$	$\sigma_{eq} = p \left(\dfrac{2}{n}\right)\left(\dfrac{3}{4}\right)^{\frac{m}{n}} \left[\dfrac{1 + \left(\dfrac{1}{2}\right)^{n-2m}}{2} \right]^{\frac{1}{n}} \times$ $\times \left[\dfrac{1}{1 - \left(\dfrac{d}{D}\right)^{2/n}} \right]$
18. Nadai, (inner surface) (Reference 13)	equivalent stress, at inner surface, based on modified energy criterion of failure, plastic stress distribution, and a power function stress-strain diagram.	$\sigma_{eq} = p \left[\dfrac{\dfrac{\sqrt{3}}{2} \cdot \dfrac{2}{n}}{1 - \left(\dfrac{d}{D}\right)^{2/n}} \right]$
19. Nadai, (outer surface) (Reference 13)	Same as formula 18, except evaluated at outer surface.	$\sigma_{eq} = p \left[\dfrac{\dfrac{\sqrt{3}}{2} \cdot \dfrac{2}{n}}{\left(\dfrac{D}{d}\right)^{2/n} - 1} \right]$
20. Same as (19, but evaluated for $n = 5$ whereas (19) was evaluated for $n = 6$		
21. Bailey–Nadai, (inner surface) (References 12, 13)	equivalent strain, at inner surface, based on maximum shear criterion of failure, plastic stress distribution, a power function stress-strain diagram for second-stage creep, and a ratio of diametral to tensile creep of 0.5.	$\sigma_{eq} = p \left[\dfrac{\dfrac{1}{n} \cdot 2^{\frac{n-1}{n}}}{1 - \left(\dfrac{d}{D}\right)^{2/n}} \right]$

TABLE 1 (*Continued*)

Identification	Description	Formula
22. Same as (21), but evaluated for n=5 whereas (21) was evaluated for n=6		
23. Same as (10), but evaluated for n=6 whereas (10) was evaluated for n=5		
24. Boiler Code (tubes, 1951)	as published in Mechanical Engineering, August 1951, page 673, with e taken as zero: note that this formula is equivalent to calculating the wall thickness by the common formula and then increasing this thickness by 0.0135D, accordingly the calculated *stress* increases to infinity for thin-walled tubes of $\frac{D}{t} = 74$	$\sigma = p\left[\dfrac{\left(\dfrac{D}{t}\right)}{\left(2 - 0.027\,\dfrac{D}{t}\right)} - 1\right]$
25. Creep–Common–II	approximation of formulas 17 and 18 for representative values of m and n.	$\sigma_{eq} = p\left[\frac{1}{2}\left(\dfrac{D}{t}\right) - 0.6\right]$
26. Soderberg (References 17, 18, 19, 20)	equivalent stress, uniform from inner to outer surface, based on modified energy criterion of failure, average, uniform stress distribution for both σ_t and σ_r, and $\sigma_z = 0.5\,(\sigma_t + \sigma_r)$. Approximation of the average of formulas 18 and 19 for representative values of n.	$\sigma_{eq} = p\,\frac{\sqrt{3}}{2}\left[\frac{1}{2}\left(\dfrac{D}{t}\right) - 0.5\right]$
27. Meyer I (Reference 21)	approximation similar to formula 25.	$\sigma = p\left[\dfrac{1}{1.95}\left(\dfrac{D}{t}\right) - 0.667\right]$
28. Burrows (Reference 22)	proposed by W. R. Burrows for use through entire temperature range with K = 1.00 for 850 F and below, K = 1.03 for 900 F, and K = 1.15 for 950 F and higher. For K = 1.00, this expression is the same as Boardman's formula 2 and approximates the result obtained assuming plastic stress distribution and the maximum shear criterion of failure; for K = 1.15, this expression is the same as formula 2 divided by 1.15, and as such approximates the result obtained assuming plastic stress distribution and the modified energy criterion of failure.	$\sigma = \dfrac{1}{K}\,p\left[\frac{1}{2}\left(\dfrac{D}{t}\right) - 0.4\right]$
29. Creep–Common III	an empirical formula designed to be intermediate between formulas 13, 21, 25, 26, 27 and 28 (K = 1.15).	$\sigma = p\left[\frac{1}{2}\left(\dfrac{D}{t}\right) - 0.7\right]$
30. General–I (Reference 23)	An expression for the entire temperature range with y so chosen that at low temperatures the expression reduces to formula 2 while at high temperatures the expression reduces to formula 29	$\sigma = p\left[\frac{1}{2}\left(\dfrac{D}{t}\right) - y\right]$

Temp.	900	950	1000	1050	1100	1150
y (ferritic)	.4	.5	.7	.7	.7	.7
y (austenitic)	.4	.4	.4	.4	.5	.7

Identification	Description	Formula
31. Meyer II (Reference 21)	approximation similar to formulas 13, 25, 27, and 29.	$\sigma = p\left[\dfrac{1}{1.85}\left(\dfrac{D}{t}\right) - 0.81\right]$

TABLE 2   FORMULAS FOR PIPE-WALL STRESSES; CALCULATED STRESSES PER 1000 PSI INTERNAL PRESSURE

Values of D/t	4	5	6	7	10	20	50	100	200
1. Lamé Tangential	1667	2125	2600	3083	4556	9,526	24,510	49,505	99,503
2. Modified Lamé	1600	2100	2600	3100	4600	9,600	24,600	49,600	99,600
3. Common	1000	1500	2000	2500	4000	9,000	24,000	49,000	99,000
4. Average Diameter	1500	2000	2500	3000	4500	9,500	24,500	49,500	99,500
5. Barlow	2000	2500	3000	3500	5000	10,000	25,000	50,000	100,000
6. Clavarino	1867	2256	2660	3071	4322	8,547	21,284	42,529	85,027
7. Guest	2667	3125	3600	4083	5556	10,526	25,510	50,505	100,503
8. Beltrami	2181	2594	3032	3484	4884	9,687	24,266	48,619	97,346
9. von Mises	2309	2706	3118	3536	4811	9,116	22,092	43,737	87,035
10. Bailey-Nadai (n = 5, inner surface)	1652	2164	2672	3176	4684	9,693	24,697	49,696	99,701
11. Bailey-Nadai (n = 5, outer surface)	1252	1764	2272	2776	4284	9,294	24,301	49,322	99,256
12. Bailey-Nadai (n = 5, outer surface)	1252	1764	2272	2776	4284	9,294	24,301	49,322	99,256
13. Creep-Common I	1200	1700	2200	2700	4200	9,200	24,200	49,200	99,200
14. Average Shear	1154	1538	1923	2308	3462	7,308	18,846	38,077	76,538
15. Blair	1616	2043	2498	2967	4415	9,361	24,331	49,323	99,317
16. Beliaev-Sinitski	1249	1695	2136	2574	3881	8,220	21,198	42,884	86,178
17. Bailey (m = 2, n = 6, inner surface)	1357	1789	2215	2639	3907	8,115	20,713	41,734	83,843
18. Nadai (n = 6, inner surface)	1399	1844	2283	2721	4027	8,365	21,360	43,009	86,326
19. Nadai (n = 6, outer surface)	1111	1555	1995	2432	3738	8,077	21,071	42,703	85,915
20. Nadai (n = 5, outer surface)	1084	1528	1967	2404	3710	8,049	21,046	42,714	85,958
21. Bailey-Nadai (n = 6, inner surface)	1439	1897	2349	2799	4143	8,605	21,973	44,244	88,806
22. Bailey-Nadai (n = 5, inner surface)	1438	1884	2326	2765	4078	8,439	21,500	43,263	86,795
23. Bailey-Nadai (n = 6, inner surface)	1616	2129	2637	3142	4650	9,659	24,664	49,662	99,681
24. Boiler Code (tubes, 1951 e = 0)	1114	1681	2264	2865	4780	12,698	75,923	. . . . . .	. . . . . .
25. Creep-Common II	1400	1900	2400	2900	4400	9,400	24,400	49,400	99,400
26. Soderberg	1299	1732	2165	2598	3897	8,227	21,218	42,868	86,170
27. Meyer I	1384	1897	2410	2923	4461	9,589	24,974	50,615	101,897
28. Burrows									
K = 1.00	1600	2100	2600	3100	4600	9,600	24,600	49,600	99,600
K = 1.03	1553	2039	2524	3010	4466	9,330	23,884	48,157	96,695
K = 1.15	1391	1826	2261	2696	4000	8,348	21,392	43,132	86,610
29. Creep-Common III	1300	1800	2300	2800	4300	9,300	24,300	49,300	99,300
30. General I									
y = 0.4	1600	2100	2600	3100	4600	9,600	24,600	49,600	99,600
y = 0.5	1500	2000	2500	3000	4500	9,500	24,500	49,500	99,500
y = 0.7	1300	1800	2300	2800	4300	9,300	24,300	49,300	99,300
31. Meyer II	1352	1893	2433	2974	4595	10,001	26,217	53,244	107,298

TABLE 3 FORMULAS FOR PIPE-WALL STRESSES; GROUPING OF APPROXIMATELY EQUIVALENT FORMULAS

Values of D/t	4	5	6	7	10	20	50	100	200
Group I									
2. Modified Lamé	1600	2100	2600	3100	4600	9,600	24,600	49,600	99,600
1. Lamé Tangential	1667	2125	2600	3083	4556	9,526	24,510	49,505	99,503
4 Average Diameter	1500	2000	2500	3000	4500	9,500	24,500	49,500	99,500
6. Clavarino	1867	2256	2660	3071	4322	8,547	21,284	42,529	85,027
10. Bailey-Nadai									
(n = 5, inner surface)	1652	2164	2672	3176	4684	9,693	24,697	49,696	99,701
15. Blair	1616	2043	2498	2967	4415	9,361	24,331	49,323	99,317
23. Bailey-Nadai									
(n = 6, inner surface)	1616	2129	2637	3142	4650	9,659	24,664	49,662	99,681
28. Burrows K = 1.00	1600	2100	2600	3100	4600	9,600	24,600	49,600	99,600
Burrows K = 1.03	1553	2039	2524	3010	4466	9,330	23,884	48,157	96,695
30. General I y = 0.4	1600	2100	2600	3100	4600	9,600	24,600	49,600	99,600
General I y = 0 5	1500	2000	2500	3000	4500	9,500	24,500	49,500	99,500
Group II									
5. Barlow	2000	2500	3000	3500	5000	10,000	25,000	50,000	100,000
7. Guest	2667	3125	3600	4083	5556	10,526	25,510	50,505	100,503
8. Beltrami	2181	2594	3032	3484	4884	9,687	24,266	48,619	97,346
9. von Mises	2309	2706	3118	3536	4811	9,116	22,092	43,737	87,035
Group III									
13. Creep-Common I	1200	1700	2200	2700	4200	9,200	24,200	49,200	99,200
11. Bailey-Nadai									
(n = 5, outer surface)	1252	1764	2272	2776	4284	9,294	24,301	49,322	99,256
12. Bailey-Nadai									
(n = 5, outer surface)	1252	1764	2272	2776	4284	9,294	24,301	49,322	99,256
16. Beliaev-Sinitski	1249	1695	2136	2574	3881	8,220	21,198	42,884	86,178
17. Bailey (m = 2, n = 6, inner surface)	1357	1789	2215	2639	3907	8,115	20,713	41,734	83,843
18. Nadai									
(n = 6, inner surface)	1399	1844	2283	2721	4027	8,365	21,360	43,009	86,326
21. Bailey-Nadai									
(n = 6, inner surface)	1439	1897	2349	2799	4143	8,605	21,973	44,244	88,806
22. Bailey-Nadai									
(n = 5, inner surface)	1438	1884	2326	2765	4078	8,439	21,500	43,263	86,795
25 Creep-Common II	1400	1900	2400	2900	4400	9,400	24,400	49,400	99,400
26. Soderberg	1299	1732	2165	2598	3897	8,227	21,218	42,868	86,170
27 Meyer I	1384	1897	2410	2923	4461	9,589	24,974	50,615	101,897
28. Burrows K = 1.15	1391	1826	2261	2696	4000	8,348	21,392	43,132	86,610
29. Creep-Common III	1300	1800	2300	2800	4300	9,300	24,300	49,300	99,300
30. General I y = 0.7	1300	1800	2300	2800	4300	9,300	24,300	49,300	99,300
31. Meyer II	1352	1893	2433	2974	4595	10,001	26,217	53,244	107,298
Group IV									
3. Common	1000	1500	2000	2500	4000	9,000	24,000	49,000	99,000
19. Nadai									
(n = 6, outer surface)	1111	1555	1995	2432	3738	8,077	21,071	42,703	85,915
20. Nadai									
(n = 5, outer surface)	1084	1528	1967	2404	3710	8,049	21,046	42,714	85,958
Group V									
14. Average Shear	1154	1538	1923	2308	3462	7,308	18,846	38,077	76,538
Group VI									
24. Boiler Code (tubes, 1951, e = 0)	1114	1681	2264	2865	4780	12,698	75,923		

is concerned about the actual diametral growth, the more important consideration should be at the outer surface, but if the maximum creep is deemed of greater importance, then it is the creep at the inner surface (at which point it is a maximum) which should be considered. The creep at the inner surface could be considered of fundamental importance as the initial indication of long-time rupture, but in this respect it is of questionable value because the elongation at rupture varies considerably between different alloys. It is here deemed more important to evaluate the creep at the outer pipe-wall surface (where it can be measured if desired and at which point it could interfere with dimensional tolerances) and to obtain protection against rupture by utilizing a factor of safety on the extrapolated test-rupture strength.

Many expressions have been published in the technical literature giving the equivalent creep stress at the inner and outer pipe-wall surfaces, and a number of these have been evaluated in Tables 2 and 3 [10, 11, 12, 17, 18, 19, 20, 21, 22, and 23]. In general, these are rather complex expressions which could become difficult to evaluate numerically because of the exponents involved. The calculated stresses given in the accompanying Tables 2 and 3 utilize representative values for these exponents as obtained from published creep data, and since the calculated results do not vary by any major degree with reasonable changes in these exponents, these calculated results can be accepted as representative of, at least, the more common alloys. In order to utilize these studies of high-temperature creep without introducing the complexity involved in the corresponding formulas, the various equivalent expressions [13, 25, 27, 29, and 31] were developed empirically to give the same numerical results as the more complex creep expressions, but in a form more easy to evaluate. That this could be done is due to the relative insensitivity of the complex expressions to moderate variations in the numerical values of the exponents.

With the equivalent-creep stresses effectively bracketed by the foregoing numerical evaluations, the problem of high-temperature tubular rupture was considered. This problem was approached in several ways and, with the relatively little actual test data available, it was fortunate that the results of these several approaches could be satisfactorily approximated by a single compromise formula. Considering first the case of brittle fracture, there is considerable opinion that the average tensile stress across the pipe section is the dominating variable, although the evidence to support this is not conclusive. The average tensile stress is given by the Common Formula [3], and to some degree this establishes a lower limit for heavy-walled pipe since this formula gives the lowest stresses of all those considered. If, however, rupture in piping steels is dependent upon the radial and axial stresses as well as the dominating tangential stress (as is the case for the incidence of yielding), then the Soderberg Formula [26] offers a reasonably firm and logical basis. The Soderberg Formula [26] (which was developed to predict the incidence of yielding) is based on the utilization of the average elastic tangential, radial, and axial stresses in the von Mises theory of failure, and although conclusive experimental evidence is lacking to prove the applicability of the von Mises theory of failure to long-time high-temperature rupture, it is generally acceptable as a conservative approach. If, instead of using the average elastic stresses, the average creep stresses as evaluated by Bailey and Nadai are used, the Soderberg Formula [26] is approximately 6 and 1 per cent conservative for D/t values of 4 and 10, respectively. If the inner-bore stresses for steady-state creep are used instead of the average values, the Soderberg Formula [26] underestimates the equivalent stress by approximately 8 and 3 per cent for D/t values of 4 and 10, respectively. Accordingly, the Soderberg Formula [26] is acceptable for heavy-

walled pipe whether the average creep stresses or the inner-bore creep stresses are considered. In addition, the Soderberg Formula [26] approximates the calculated stresses obtained by the various equivalent-creep expressions, as is shown by the tabulations of Tables 2 and 3, and also shows satisfactory correlation with published tubular creep tests. A more detailed analysis of theoretical and experimental data as presented in the Appendix also gives numerical results closely duplicating those of the Soderberg Formula [26].

The major objection to the Soderberg Formula [26], however, is that, while at $D/t = 4$ it is approximately 30 per cent conservative with respect to the Common Formula [3], it gives lower calculated stresses than the Common Formula [3] for D/t values greater than approximately 10. Because of the paucity of high-temperature tubular bursting tests, it was not deemed advisable to recommend any formula which would give thinner pipe walls than the Common Formula [3]. In addition, of course, it was desired to continue with the use of the modified-Lamé Formula [2] at room and slightly elevated temperatures on the basis of the available data on room-temperature tubular bursting tests. Accordingly, consideration was given to modifications of the Soderberg Formula [26] by which acceptable results for high-temperature thin-walled piping would be obtained, and the modified-Lamé Formula [2] would result for room and slightly elevated temperatures. Obviously, this requires a double formula with a temperature-dependent transition range.

The Creep-Common Formula III [29] was developed empirically to eliminate the objections to the Soderberg Formula [26] for high-temperature thin-walled tubing. The Creep-Common Formula III [29], as well as a number of the equivalent creep-stress expressions, duplicate the Soderberg Formula [26] for heavy-walled pipe, but will not give thinner walls than the Common Formula [3] for the lighter schedules. In duplicating the Common Formula [3] for the lighter piping, the Creep-Common Formula III [29] also duplicates the modified-Lamé [2] since there is little difference between the Common [3] and modified-Lamé [2] formulas for the lighter schedules. It should be noted also that the Creep-Common Formula III [29] is midway between the Common Formula [3] and the modified-Lamé Formula [2] for the entire D/t range from 4 to 200.

To combine the Creep-Common III [29] and modified-Lamé [2] formulas into a single expression applicable to all temperatures over the entire practical D/t range, the General Formula [30] with the temperature-dependent parameter y was developed. At room and slightly elevated temperatures, the General Formula [30] reduces to the modified-Lamé Formula [2], while at high temperatures it reduces to the Creep Common Formula III [29]; the temperature-dependent parameter y performs the transition between these two end formulas. The General Formula [30] accordingly approximates satisfactorily the available room-temperature tubular bursting data; agrees reasonably well with the various creep-stress expressions for high-temperature operation; duplicates for high-temperature heavy-walled pipe the Soderberg Formula [26] and its theoretical considerations of yielding, creep, and high-temperature rupture as well as the alternative theoretical approach given in the Appendix; and reduces to both the Common [3] and modified-Lamé [2] formulas for thin-walled piping.

TEMPERATURE-DEPENDENT PARAMETER y

Inasmuch as the expression, to which the General Formula [30] reduces at high temperature, will give lower calculated stresses for any given D/t ratio than the corresponding formula obtained at low temperatures, the transition zone in which the temperature-dependent parameter y varies must be selected with careful consideration of the Code allowable S-values. If the

transition zone were placed in a temperature region in which the Code S-values did not decrease sufficiently rapidly, an anomalous situation would result in which the permissible pressure at a given temperature, for a particular wall thickness, would be greater than the permissible pressure, for the same wall thickness, at some lower temperature. It is for this reason that the temperature-dependent parameter y differs between the ferritic and austenitic steels. The temperature ranges in which the transition is effected between the low-temperature formula and the high-temperature formula have been selected by consideration of the Code S-values for the ferritic and austenitic steels. In particular, these transition ranges have been so selected that, with the current Code S-values, the anomalous situation described previously regarding permissible pressures will not occur.

TYPICAL PRESSURE-TEMPERATURE CURVES

Figs. 4, 5, 6, and 7 have been prepared to illustrate the relation of the proposed General Formula [30] to the current Code formula and other expressions for calculating pipe-wall thickness. These curves show the allowable pressure versus temperature,
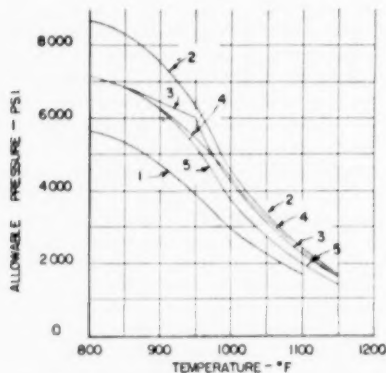
1 = Code formula and allowable S-values both as published in Code for Pressure Piping, ASA B31.1–1951 (this formula is the same as the modified-Lamé [2])
2 = Soderberg Formula [26] and revised allowable S-values (as published in *Mechanical Engineering*, August, 1951, p. 676)
3 = Burrows Formula [28] and revised allowable S-values of 2 above
4 = General Formula [30] and revised allowable S-values of 2 above
5 = Code formula of 1 above and revised allowable S-values of 2 above

FIG. 4 CALCULATED ALLOWABLE INTERNAL PRESSURES VERSUS TEMPERATURES, FOR $D/t = 5$, BY VARIOUS FORMULAS AND ALLOWABLE S-VALUES
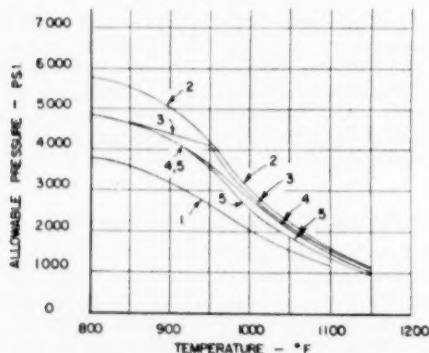
FIG. 5 SAME AS FIG. 4, BUT AT $D/t = 7$
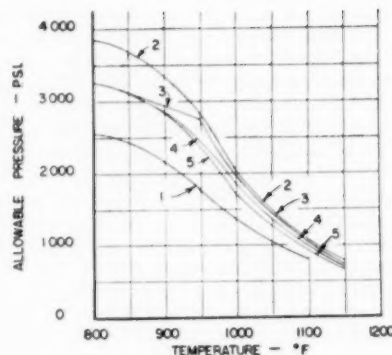
FIG. 6 SAME AS FIG. 4, BUT AT $D/t = 10$
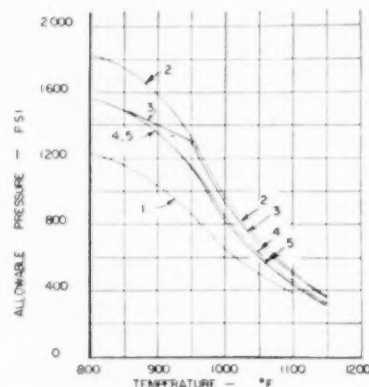
FIG. 7 SAME AS FIG. 4, BUT AT $D/t = 20$

for D/t values of 5, 7, 10, and 20, as evaluated in terms of both the former and the current Code S-values for $2^1/_4$ per cent chromium, 1 per cent molybdenum piping, ASTM-213-T22. The formulas selected for comparison, together with the allowable S-values for each expression, are as follows:

1 Code formula and allowable S-values as published in the Code for Pressure Piping, ASA B31.1–1951. (This formula is the same as the modified-Lamé [2].)

2 Soderberg Formula [26] and revised allowable S-values as published in *Mechanical Engineering*, vol. 73, August, 1951, page 676.

3 Burrows Formula [28] and revised allowable S-values of 2 above.

4 General Formula [30] and revised allowable S-values of 2 above.

5 Code formula of 1 above and revised allowable S-values of 2 above.

BIBLIOGRAPHY

1 "Thickness of Steam Piping for High-Pressure, High-Temperature Service," by H. C. E. Meyer, Trans. SNAME, vol. 57, 1949, p. 379.

2 "Thermal Shock and Other Comparison Tests of Austenitic and Ferritic Steels for Main Steam Piping," by W. C. Stewart, Trans. ASME, vol. 72, 1950, p. 1043.

3 "Stresses in Tubes Due to Internal Pressure," by J. S. Blair, *Engineering*, London, England, vol. 172, September 15, 1950, p. 218.

4 "Yielding and Fracture of Medium-Carbon Steel Under Combined Stress," by E. A. Davis, *Journal of Applied Mechanics*, Trans. ASME, vol. 67, 1945, p. A-13.

5   "High-Temperature Stress-Rupture Testing of Tubular Specimens," by L. F. Kooistra, R. V. Blaser, and J. T. Tucker, Trans. ASME, vol. 74, 1952, pp. 783–792.

6   "Formula for Pipe Thickness," by W. J. Buxton and W. R. Burrows, Trans. ASME, vol. 73, 1951, pp. 575–587.

7   "Higher Steam Conditions for Ships' Machinery," by M. L. Ireland, Jr., H. W. Semar, and N. L. Mochel, presented at the International Conference of Naval Architects and Marine Engineers, London, England, 1951, Paper No. 3.

8   "Formulas for the Design of Cylindrical and Spherical Shells to Withstand Uniform Internal Pressure," by H. C. Boardman, *The Water Tower*, vol. 30, September, 1943, pp. 14–15.

9   "National Pipe Standards," by the National Tube Company, Pittsburgh, Pa., 1924, p. 291.

10   "API-ASME Code for Unfired Pressure Vessels," American Petroleum Institute and THE AMERICAN SOCIETY OF MECHANICAL ENGINEERS, New York, N. Y., 1943, p. 13.

11   "Strength of Materials," by R. V. Southwell, *Encyclopedia Britannica*, vol. 15, fourteenth edition, pp. 58–59.

12   "Thick-Walled Tubes and Cylinders Under High Pressure and Temperature," by R. W. Bailey, *Engineering*, London, vol. 152, June 13, 1930, pp. 772–773, June 20, 1930, pp. 785–786, and June 27, 1930, pp. 818–819; "Creep of Steel Under Simple and Compound Stresses," by R. W. Bailey, *Engineering*, London, vol. 152, February 21, 1930, pp. 265–266, and March 7, 1930, pp. 327–329; "Testing of Materials for Service in High-Temperature Steam Plant," by R. W. Bailey and A. M. Roberts, *Engineering*, London, vol. 154, February 26, 1932, pp. 261–265, and March 4, 1932, pp. 295–298; and "The Utilization of Creep-Test Data in Engineering Design," by R. W. Bailey, Proceedings of The Institution of Mechanical Engineers, London, England, vol. 131, 1935, pp. 131–349.

13   "Plasticity," by A. Nadai, McGraw-Hill Book Company, Inc., New York, N. Y., 1931.

14   "Design and Fabrication of Steam Piping," by A. W. Rankin and R. W. Clark, *The Welding Journal*, June, 1951, pp. 508–522; (also see Discussion of Reference 6).

15   "The Inelastic Behavior of Engineering Materials and Structures," by A. M. Freudenthal, John Wiley & Sons, Inc., New York, N. Y., 1950, p. 430.

16   "The Utilization of Creep-Test Data in Engineering Design," by R. W. Bailey, Proceedings of The Institution of Mechanical Engineers, London, England, vol. 131, 1935, pp. 131–349.

17   "Interpretation of Creep Tests on Tubes," by C. R. Soderberg, Trans. ASME, vol. 63, 1941, pp. 737–748.

18   "Report on Tubular Creep Tests," by F. H. Norton and C. R. Soderberg, Trans. ASME, vol. 64, 1942, pp. 769–777.

19   "Task Force Correspondence" from M. L. Ireland, Jr., September 6, 1951, and September 27, 1951.

20   "Task Force Correspondence" from C. R. Soderberg, October 16, 1951, and October 25, 1951.

21   "Task Force Correspondence" from H. C. E. Meyer, November 6, 1951, and November 15, 1951.

22   "Task Force Correspondence" from W. R. Burrows, August 15, 1951.

23   "Task Force Correspondence" from A. W. Rankin, November 13, 1951.

24   "Theory of Flow and Fracture of Solids," by A. Nadai, McGraw-Hill Book Company, Inc., New York, N. Y., vol. 1, 1950.

25   "Mitteilungen der mechanisch technischen Versuchsanstalt," by H. Wehage, Berlin, Germany, 1888.

26   "Thick-Walled Tubes and Cylinders Under High Pressure and Temperature," by R. W. Bailey, *Engineering*, London, England, vol. 130, June 13, 1930, pp. 772–773; June 20, 1930, pp. 785–786, and June 27, 1930, pp. 818–819.

27   "Steam Piping for High Pressures and High Temperatures," by R. W. Bailey, Proceedings of The Institution of Mechanical Engineers, London, England, vol. 164, 1951, pp. 324–350.

28   "The Mathematical Theory of Plasticity," by R. Hill, Oxford University Press, London, England, 1950 (page references in text).

Appendix

The main text of this paper has presented the development of the General Formula [30] in essentially its chronological form. The general interchange of information among the Task Force members and other interested persons has clarified considerably various basic concepts, and the purpose of this Appendix is to attempt to integrate these ideas into a possible generalized solution.

FAILURE THEORIES

Formulas [1, 6, 7, 8, and 9] (Lamé, Clavarino, Guest, Beltrami, von Mises), Table 1, result when the Lamé expressions for inner-surface elastic stresses, Table 4, are introduced into the five alternative criteria of elastic failure shown in Table 5. The failure criteria of Table 5 have been specifically particularized for pipe structures through the introduction of the simplifying relationship

$$\sigma_a = 0.5(\sigma_t + \sigma_r) \dots \dots \dots \dots \dots [A1]$$

This relation holds not only in the elastic range, but also in the plastic range (13, p. 201). The Lamé [1] and Clavarino [6] formulas have been widely used for pipes operating in the elastic range, while the Guest [7], Beltrami [8], and von Mises [9] formulas have enjoyed little favor even though they are based on more acceptable criteria of elastic failure.

All five of these formulas are developed by introducing into the failure criteria of Table 5 the Lamé expressions for the inner-surface elastic stresses. As such, complete elastic failure of the tensile specimen is related to elastic failure at the inner surface of the pipe, even though the entire wall section is otherwise free of elastic failure. An alternative concept would be to compare complete elastic failure of the test specimen with complete elastic failure of the pipe wall. This alternative concept requires the adjustment of the failure criteria to plastic conditions, and the use of pipe formulas based on plastic-stress conditions. It is to be recognized that such an analysis would be practically identical to a study of plastic conditions (creep) for pipes operating at elevated temperatures (24, pp. 409–415).

The failure criteria are adjusted to plastic conditions by introducing a Poisson's ratio of 0.5 into the failure criteria of Table 5. The results are presented in Table 6, with the more important criteria summarized in Table 7. From Table 6 it is seen that the four most important failure criteria can be consolidated into the single condensed formula

$$\sigma = \frac{\sigma_t - \sigma_r}{K} \dots \dots \dots \dots \dots [A2]$$

This synthesis is shown clearly by Table 7 in which K assumes the values of 1.00, 1.15, and 1.33. The validity of the maximum strain criterion is open to considerable question (25), and opinions expressed in the literature favor the assumption that K varies only from 1.00, for the maximum shear criterion of Tresca, to 1.15 for the modified energy criterion of von Mises. This single compact formula, within the indicated range of K, thus supplants Formulas [1, 6, 7, 8, and 9] Table 1, while its concise form considerably simplifies the problem by reducing dissimilarities among the most acceptable failure criteria to a degree that the only differences whatsoever consist of variations in the value of the parameter K. The use of this formula requires the evaluation of the criterion stress, $\sigma_t - \sigma_r$, in terms of plastic stress distribution obtained either by analysis or by estimate.

STRAIN RELATIONSHIPS

The analytical determination of the pipe criterion stress, $\sigma_t - \sigma_r$, rests on a knowledge of the plastic stress-strain diagram in pure shear (13, p. 202; 26, p. 785). The correlation between plastic-stress distribution and the pure shear stress-strain diagram is indicated more clearly by Table 8 which shows, in the left and center columns, the parallelism which exists between a pipe under internal pressure and a test specimen under torsion. Stresses causing plastic strains, and the strains themselves, are in one-to-one correspondence. With a state of pure shear in the test specimen

$$s = F_1(2e) \dots \dots \dots \dots \dots [A3]$$

TABLE 4

Formulas of Lamé for principal elastic stresses $(\sigma_t > \sigma_z > \sigma_r)$ in uniformly thick, infinite, hollow, closed-end cylinder, under internal pressure

FORMULA	VALUE OF σ_t	VALUE OF σ_r
Lamé, General Any Diameter δ $D \geq \delta \geq d$	$p\dfrac{(dD/\delta)^2 + d^2}{D^2 - d^2}$	$-p\dfrac{(dD/\delta)^2 - d^2}{D^2 - d^2}$
Lamé Inner Surface $\delta = d$	$^*p\dfrac{D^2 + d^2}{D^2 - d^2}$	$-p$
$\sigma_z = 0.5(\sigma_t + \sigma_r) = 2\dfrac{p\,d^2}{D^2 - d^2}$		
*Same as so-called Lamé formula 1		
Lecons, G. Lamé, Paris, 1852, pp. 188-191.		

TABLE 6

Alternative failure criteria of Table 5 when plasticity is assumed with consequent adoption of constant volume (infinite bulk modulus) so that Poisson's ratio is 0.5

CRITERION	FORMULA
Maximum Stress	$\sigma = \sigma_t$
Maximum Strain	$\sigma = (3/4)(\sigma_t - \sigma_r)$
Maximum Shear	$\sigma = \sigma_t - \sigma_r$
Energy	$\sigma = (3/4)^{0.5}(\sigma_t - \sigma_r)$
Modified Energy	$\sigma = (3/4)^{0.5}(\sigma_t - \sigma_r)$

TABLE 5

Alternative criteria of elastic failure relating principal elastic stresses $[\sigma_t > \sigma_z = 0.5(\sigma_t + \sigma_r) > \sigma_r]$ in uniformly thick, infinite, hollow, closed-end cylinder, under internal pressure, to major principal stress σ in tensile test specimen

CRITERION	FORMULA
Maximum Stress* Lamé (1831) Rankine (1888)	$\sigma = \sigma_t$
Maximum Strain* Poncelet (1840) Saint-Venant (1870)	$\sigma = (3/4)(\sigma_t - \sigma_r) + (1/4)(1 - 2\nu)(\sigma_t + 3\sigma_r)$
Maximum Shear Coulomb (1773) Tresca (1864) Guest (1900)	$\sigma = \sigma_t - \sigma_r$
Energy Beltrami (1885) Haigh (1919)	$\sigma = (3/4)^{0.5}(\sigma_t - \sigma_r)\{[(5 - 4\nu)/3] + 4(1 - 2\nu)\sigma_t\sigma_r(\sigma_t - \sigma_r)^{-2}\}^{0.5}$
Modified Energy Hüber (1904) Hencky (1924) von Mises (1913-1926)	$\sigma = (3/4)^{0.5}(\sigma_t - \sigma_r)$
*Least Acceptable at Present	

and with one-to-one correspondence, the corresponding expression for the pipe is

$$0.5(\sigma_t - \sigma_r) = F_1(2\epsilon_t) \ldots\ldots\ldots\ldots [A4]$$

The plastic stress-strain diagram in tension is

$$\sigma = F(\epsilon) \ldots\ldots\ldots\ldots\ldots\ldots [A5]$$

and the problem is to establish a relation between the plastic stress-strain diagrams in pure shear and pure tension. For simplifying purposes, the following two assumptions are made:

1 It is possible to represent adequately the plastic stress-strain diagram in pure tension by means of an analytical expression.

2 It is possible to construct from 1 above the plastic stress-strain diagram in pure shear.

Let the following power function represent, for both room and elevated temperatures, the plastic stress-strain diagram in tension

$$\sigma = A_1\epsilon^{0.4\beta} \ldots\ldots\ldots\ldots\ldots [A6]$$

To relate this expression to that for the plastic stress-strain rela-

TABLE 7

Important failure criteria of Table 6 summarized

σ	$= \dfrac{\sigma_t - \sigma_r}{K}$	$= \dfrac{\sigma_t - \sigma_r}{(4/3)^\eta}$	
CRITERION	η	$K = (4/3)^\eta$	$K = (3/4)^\eta$
Maximum Shear	0.0	1.00	1.00
Energy	0.5	1.15	0.87
Modified Energy	0.5	1.15	0.87
Maximum Strain*	1.0	1.33	0.75

*Least Acceptable

TABLE 8

Stresses and strains in uniformly thick, infinite, hollow, closed-end cylinder, under internal pressure; in torsion test specimen; and in tensile test specimen

CYLINDER	PURE SHEAR	PURE TENSION
TENSILE STRESSES		
$0.5(\sigma_t - \sigma_r)^*$	s	σ
0	0	0
$-0.5(\sigma_t - \sigma_r)$	$-s$	0
TENSILE STRAINS		
ϵ_t	e	ϵ
0	0	-0.5ϵ
$-\epsilon_t$	$-e$	-0.5ϵ
SHEAR STRESSES		
$0.5(\sigma_t - \sigma_r)$	s	0.5σ
$-0.25(\sigma_t - \sigma_r)$	$-0.5s$	0
$-0.25(\sigma_t - \sigma_r)$	$-0.5s$	-0.5σ
SHEAR STRAINS		
$2\epsilon_t$	$2e$	1.5ϵ
$-\epsilon_t$	$-e$	0
$-\epsilon_t$	$-e$	-1.5ϵ

*Obtained by Adding Hydrostatic compression in the amount

$$-\sigma_z = -0.5(\sigma_t + \sigma_r) \text{ , thus:}$$

$$\sigma_t \qquad - 0.5(\sigma_t + \sigma_r) = 0.5(\sigma_t - \sigma_r)$$
$$0.5(\sigma_t + \sigma_r) - 0.5(\sigma_t + \sigma_r) = 0$$
$$\sigma_r \qquad - 0.5(\sigma_t + \sigma_r) = -0.5(\sigma_t - \sigma_r)$$

TABLE 9

Samples of assumed and adjusted relationships between strain, ϵ, in tensile test specimen, and circumferential (diametral) strain, ϵ_t, in cylinder under internal pressure. Adjustments are based specifically on use of a power-function-type stress-strain diagram

tionship in pure shear for the pipe, it has been customary to assume that when ϵ/ϵ_t has a certain constant value then $(\sigma_t - \sigma_r)/\sigma$ has some constant value. In Table 9 are listed a number of the better-known values for these ratios. Lately, it appears that the von Mises criterion has been taken as the most generally acceptable procedure for establishing these ratios, and, based on the values given in Table 9, this criterion will give

$$\epsilon = (4/3)^{0.5} \epsilon_t$$

when

$$\frac{\sigma_t - \sigma_r}{\sigma} = (4/3)^{0.5} \dots \dots [A7]$$

The various assumptions of Table 9 can be summarized for a given temperature by the following expression: When

$$\sigma = \frac{\sigma_t - \sigma_r}{C_1}$$

then

$$\epsilon/\epsilon_t = C_2 \dots \dots \dots [A8]$$

This relation, in turn, gives the following expression when using the selected power-function stress-strain diagram

$$\frac{\sigma_t - \sigma_r}{\sigma} = A_2(\epsilon/\epsilon_t)^{-0.6\beta} \dots \dots [A9]$$

in which A_2 is a constant. The estimates of the ϵ/ϵ_t ratio given in Table 9 can be transformed to values between 2 and 3, when σ equals $\sigma_t - \sigma_r$, so that there has actually been little change with the years in the assumed magnitude of this ratio. Moreover, it is thus also shown that the pipe stress $[(\sigma_t - \sigma_r)/K]$ will equal the stress σ in the tensile specimen when the strain ϵ_t in a pipe

equals the strain ϵ in the tensile test specimen for appropriate values of K. It is thus seen that when a power-function stress-strain diagram is specifically assumed, the relationship needed to determine creep in a pipe from creep in the tensile test specimen takes the form

$$\sigma = \frac{\sigma_t - \sigma_r}{K} \qquad \qquad [A10]$$

which is the same concise expression as that developed for failure. For equal strains in a pipe and in a tensile test specimen, it appears from Table 9 that the most acceptable values of K lie between 1.15 and 1.20, while for simultaneous failure in a pipe and in a tensile test specimen, the most acceptable values of K lie between 1.00 and 1.15.

The foregoing discussion is believed sufficient to establish that it has been customary for a given temperature to assume, as previously stated, that when

$$\sigma = \frac{\sigma_t - \sigma_r}{C_1}$$

then

$$\epsilon/\epsilon_t = C_2 \qquad \qquad [A11]$$

in relating the plastic stress-strain diagram in pure shear with the plastic stress-strain diagram in pure tension.

PLASTIC-STRESS DISTRIBUTION

The stress distribution in pipes under plastic conditions has been published previously by Bailey (26, pp. 785–786), by Nadai (13, pp. 201–206), by Buxton and Burrows (6), and by others, but a very brief repetition of this work appears to be warranted here.

The assumption of constant volume together with no change in the pipe length (26, p. 773; 18, p. 771) gives the relation

$$\epsilon_t = -\epsilon_r \qquad \qquad [A12]$$

which, when incorporated with the strain-deformation relations

$$\epsilon_r = \frac{d\rho}{dr} \qquad \qquad [A13]$$

and

$$\epsilon_t = \rho/r \qquad \qquad [A14]$$

produces the differential equation for radial displacement

$$\frac{d\rho}{dr} + (\rho/r) = 0 \qquad \qquad [A15]$$

The differential equation for equilibrium of stress is

$$\frac{d\sigma_r}{dr} = \frac{\sigma_t - \sigma_r}{r} \qquad \qquad [A16]$$

Utilizing the plastic stress-strain diagram in tension and the relationships between it and the plastic stress-strain diagram in pure shear, both as previously stated, together with the known boundary conditions, the following solutions are obtained

$$\rho = C_2/r \qquad \qquad [A17]$$

and

$$\sigma_r = \int_{0.5D}^{0.5\delta} \frac{\sigma_t - \sigma_r}{r} \, dr \qquad \qquad [A18]$$

Other relationships are

$$\rho = C_2/r = r\epsilon_t \qquad \qquad [A19]$$

$$\epsilon_t = C_2/r^2 = \epsilon/C_2 \qquad \qquad [A20]$$

$$\epsilon = C_2C_2/r^2 \qquad \qquad [A21]$$

$$\frac{dr}{r} = -0.5 \frac{d\epsilon}{\epsilon} \qquad \qquad [A22]$$

$$\sigma_t - \sigma_r = C_1\sigma = C_1F(\epsilon) \qquad \qquad [A23]$$

It follows that

$$\sigma_r = 0.5C_1 \int_{\epsilon_\delta}^{\epsilon_\delta(\delta/D)^2 = \epsilon_d} \frac{F(\epsilon)}{\epsilon} \, d\epsilon \qquad \qquad [A24]$$

and, based on conditions at the inner surface

$$p = 0.5C_1 \int_{\epsilon_\delta(\delta/D)^2 = \epsilon_\delta}^{\epsilon_\delta(\delta/d)^2} \frac{F(\epsilon)}{\epsilon} \, d\epsilon \qquad \qquad [A25]$$

If the plastic stress-strain diagram in tension is taken as a power function (as previously stated) so that work hardening is considered (13, p. 203; 26, p. 785), the following expression is obtained

$$\sigma = \frac{\sigma_t - \sigma_r}{K} \frac{pA_1 \, \epsilon_\delta^{0.5\delta}}{0.5 \, KA_1 \int_{\epsilon_\delta(\delta/D)^2 = \epsilon_0}^{\epsilon_\delta(\delta/d)^2} \epsilon^{0.5\delta} \frac{d\epsilon}{\epsilon}} \qquad \qquad [A26]$$

This in turn reduces to Formula A detailed in Table 10.

If the plastic stress-strain diagram in tension is taken in the form of a sloped line (13, p. 173)

$$\sigma = F(\epsilon) = \sigma_0 + (\epsilon - \epsilon_0) \tan \alpha \qquad \qquad [A27]$$

the following expression is obtained

$$\sigma = \frac{\sigma_t - \sigma_r}{K} = \frac{p[\sigma_0 + (\epsilon_\delta - \epsilon_0) \tan \alpha]}{0.5K \int_{\epsilon_\delta(\delta/D)^2 = \epsilon_0}^{\epsilon_\delta(\delta/d)^2} \left[\sigma_0 + (\epsilon - \epsilon_0) \tan \alpha \right] \frac{d\epsilon}{\epsilon}} \qquad \qquad [A28]$$

and this in turn reduces to Formula B of Table 10.

Assuming an idealized plastic stress-strain diagram in tension with zero slope ($\alpha = 0$), the preceding expression reduces immediately to Formula C of Table 10.

Formula D of Table 10 is that given by Soderberg (17, p. 738). This expression is obtained by substituting into the criterion stress, $\sigma_t - \sigma_r$, the average tangential stress (Formula [3], Table 1) as obtained from statical considerations, and the average radial stress of $\sigma_r = -0.5p$, while concurrently retaining the relation

$$\sigma_s = 0.5 (\sigma_t + \sigma_r) \qquad \qquad [A29]$$

It is believed that the mode of derivation indicates that this formula is itself an approximation of Formulas A, B, and C, Table 10.

DERIVED FORMULAS

Four formulas for plastic-stress distribution have now been obtained in the form
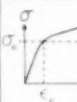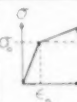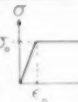
$$\sigma = \frac{\sigma_t - \sigma_r}{K} \qquad \qquad [A30]$$

Formulas A and B are for any diameter δ, while C and D are independent of δ. The bearing of these four formulas on those of Table 1, and on other published formulas, will now be given.

Formula A, with K related to equivalent failure, is the basis of Formulas [10, 11, 12, 18, 19, 20, and 23], Table 1; and with K related to equivalent strain (Table 9), is the basis of Formulas

TABLE 10

Tabulation of formulas for $\sigma_t - \sigma_r$, based on plastic stress distribution, and their derivations by means of either analysis or estimation

[17, 21, and 22] Table 1. Formula C is the same as Formula [16], Table 1, when $K = 1.15$. When $K = 1.00$, C is usually called the van Iterson Formula, although it was probably known earlier to Turner (28, p. 110). Formula B, which is believed to be new, introduces the effect of strain hardening into Formula C. Formula D, with $K = 1.0$ consistent with the maximum shear criterion of failure, is the same as Formula [4], Table 1; and is the same as Formula [26], Table 1, when $K = 1.15$ consistent with the modified energy criterion of failure.

Formula A is also the basis of three formulas given by Bailey (27, Equations [4, 5, 6]) for the design of pipes at elevated temperatures. One of these is the same as Formula [18], Table 1, for the inner pipe surface; in this K is related to equivalent failure and equals 1.15 in accordance with the modified energy criterion of failure. The other two are related to equivalent strain, and both employ the value of K shown in Table 9

$$K = (4/3)^{0.25}(2+\beta) \quad\quad\quad [A31]$$

These two formulas are given below as E and F; E is for the inner pipe surface, and F is for the outer pipe surface

$$(E) \quad \sigma = \frac{p\beta}{\left(\frac{4}{3}\right)^{0.25(2+\beta)}\left[1-\left(\frac{d}{D}\right)^{\beta}\right]} \quad\quad [A32]$$

$$(F) \quad \sigma = \frac{p\beta}{\left(\frac{4}{3}\right)^{0.25(2+\beta)}\left[\left(\frac{D}{d}\right)^{\beta}-1\right]} \quad\quad [A33]$$

BOARDMAN APPROXIMATION

With $K = 1.00$, Formula D reduces to the following

$$\sigma = p\left[0.5\left(\frac{D}{t}\right)-0.5\right] \quad\quad\quad [A34]$$

which is the Average-Diameter Formula [4], Table 1. The factor 0.5 was reduced to 0.4 by Boardman (8) thereby giving

$$\sigma = p\left[0.5\left(\frac{D}{t}\right)-0.4\right] \quad\quad\quad [A35]$$

which is Formula [2], Table 1, and this is in use in many national codes for pipe design. It is an approximation to the Lamé Tangential Formula [1], Table 1, and has been shown by Buxton and Burrows (6) to be a good approximation of the plastic-stress criterion.

TABLE 11

Comparison of numerical values of plastic stress criterion $\sigma_t - \sigma_r$

$K = 1.00$	$\delta = d$		n AS SHOWN			$p = 1000$		
FORMULA	VALUES OF (D/t)							
	5	6	7	10	20	50	100	200
C	1958	2466	2972	4481	9491	24497	49499	99499
4 (SODERBERG) *	2000	2500	3000	4500	9500	24500	49500	99500
B, INSIDE	2056	2551	3050	4548	9549	24547	49551	99546
2 (BOARDMAN) *	2100	2600	3100	4600	9600	24600	49600	99600
A, INSIDE, $n = 6$	2129	2637	3142	4650	9659	24664	49652	99681
A, INSIDE, $n = 5$	2164	2672	3176	4684	9693	24697	49696	99711
A, INSIDE, $n = 4$	2219	2725	3229	4736	9743	24748	49746	99758
A, INSIDE, $n = 3$	2310	2815	3318	4823	9829	24831	49833	99833
AVERAGE OF ALL FORMULAS IN TABLE	2117	2621	3123	4628	9636	24640	49637	99637

*EXCERPTED FROM TABLE II

NUMERICAL COMPARISONS

Stress values given by the derived formulas are shown in Table 11, with $K = 1.00$ in all cases so that only the plastic-stress criterion is compared. Formulas A and B are computed for the inside surface at which point these formulas exhibit maximum stresses. Formulas B and C apply only to the elastic design range, according to the concept of failure adopted in this Appendix; Formula A also applies to the elastic-design range, but, in addition, it alone applies in the elevated-temperature, plastic-design range.

For small values of D/t, the stresses of Formula C, which neglects strain hardening, are lower than those of Formula A. Formula B, which is Formula C with strain hardening introduced, gives stresses in close agreement with those of Formula A when $(\epsilon_0/\sigma_0)\tan\alpha = 0.05$ is used in Formula B and $n = 5$ or 6 is used in Formula A. These calculated stresses indicate that, with $n = 5$, Formula A is a suitable approximation for both Formulas B and C for the entire design range.

Although Formulas A, B, and C all take the form

$$\sigma = \frac{\sigma_t - \sigma_r}{K} \quad\quad\quad [A36]$$

for equivalent failure in both the elastic and elevated-temperature range, only Formula A takes this simplified form for the case of equivalent strain (creep) which is important in the elevated-temperature range. It is the replacement of Formulas A, B, and C by Formula A alone which makes possible the use of the simplified form with values of K consistent with both equivalent failure and equivalent strain.

The maximum stresses of Formula A, for a given value of K, are at the inner surface. Since the development of a single standard design formula is desirable, then Formula A should

be used at this point at which maximum stresses are obtained. Table 11 then shows that Formula A, evaluated at the inner surface with $n = 5$, is itself well approximated by the Boardman Expression [2], Table 1, with K added

$$\sigma = \frac{\sigma_t - \sigma_r}{K} = \frac{p\beta}{K\left[1 - \left(\frac{d}{D}\right)^\beta\right]} \cong \frac{p}{K}\left[0.5\left(\frac{D}{t}\right) - 0.4\right]$$

$$\dots\dots[A37]$$

This approximation appears to be superior numerically to the other formulas cited and has the considerable advantage of retaining present code practice.

The establishment of a single design formula has now progressed to the point at which only values of K need further consideration. In the elastic range, K rests on equivalent failure, but in the elevated-temperature, plastic range, K is based on either equivalent failure or equivalent strain (creep). But values of K for equivalent failure lie between 1.00 and 1.15, while a suitable value of K for equivalent strain exceeds 1.15, and probably is of the order of 1.19. Hence, to obtain a single design formula, considerations of equivalent strain could be excluded in favor of exclusive consideration of equivalent failure.

EXPERIMENTAL VERIFICATION

As shown in Fig. 1, experimental data on failure in the elastic design range indicate that K should be about 1.00. In the elevated-temperature, plastic range, the steady-state rupture data of Table 12, based on Figs. 2 and 3, favor the use of $K = 1.15$. If the experimental evidence just cited is accepted, then Formula [28], Table 1, is reasonably representative of a proper standard design formula.

TABLE 12

Comparison of $[(\sigma_t - \sigma_r)/K]$ stresses with stress-rupture data from Figs. 2 and 3, limited to steady-state creep condition

°F TEMPERATURE	(D/t) AS FABRICATED	FAILURE TIME , HOURS TUBE OR TENSILE TEST SPECIMEN	STRESS , PSI , TENSILE TEST SPECIMEN INTERPOLATED FROM FIG. 2 AND FIG. 3	STRESS , PSI , FORMULA A $n=5$ $\dfrac{(\sigma_t - \sigma_r)}{(4/3)^{0.5}}$ INSIDE
850	11.796	5682	17030	17690
950	12.048	328	15800	15580
950	11.765	712	13800	13260
950	12.422	2404	10460	10750
950	12.422	8661	8760	8700

FINAL SECTION OF A WORKING FORMULA

Although Formula [28], Table 1, can be deduced logically as a single standard design formula for the determination of pipe-wall thickness, it is by no means the only possible answer. A number of other formulas were considered, but final approval was given to a combination of Formulas [2] and [29], Table 1. This arrangement yields the desired simplicity; represents the least change from the forms in current use; and has the added advantage of thinning the present walls of heavy pipe, the same as Formula [28], Table 1, without affecting the present wall thicknesses of lighter schedules. According to Hill (28, p. 124), this latter procedure coincides with British practice.

In conclusion, it appears that the theoretical discussions of this Appendix suggest a specific method for examining and comparing experimental data to determine Code S-values. If such data rest on strain (creep), they should be increased by the approximate ratio of 1.19/1.15. This should be done before comparing them with stress-rupture data, or, if critical, using them as Code S-values

Discussion

H. C. E. MEYER.[10] It has been a pleasure and an education to have been associated with the authors of this excellent paper on the Task Force which was appointed to develop an acceptable formula for pipe thicknesses.

The authors deserve the plaudits and thanks not only of this Society but of the entire engineering community for the excellent work they have performed for the Task Force, and also for their excellent presentation of the thorough study and preparation that preceded the selection of the final formula recommended by the Task Force.

In 1948 the writer was asked to prepare a paper on high-pressure, high-temperature steam piping. At about the same time, both the American Bureau of Shipping and the U. S. Coast Guard were considering revision of their rules for pipe thicknesses and were contemplating reducing the permissible S-values, as published by the Boiler Code, by one third which would result in piping materially heavier than needed.

Owing to the trend toward higher pressures and temperatures, the wall thicknesses of piping for power stations had increased tremendously and the writer became seriously concerned with the danger of internal cracking for such heavy-walled piping as the result of sudden temperature changes such as when carryover occurs. Some throttle valves were then being manufactured which had nozzles with an outside diameter of 15 in. and a bore of only 8 in.; i.e., the wall thickness was $3\frac{1}{2}$ in. which appeared so startling that the subject of the paper became confined to a discussion of the question of pipe thicknesses. This proved to be a subject of sufficient importance to justify the paper.

To the everlasting credit of both the American Bureau of Shipping and the U. S. Coast Guard, when during discussions with reference to the proposed paper they were alerted to this phase of the situation, they produced an "Interim Guide" which for the higher temperatures has provided a satisfactory bridge to span the gap for the time being, thus avoiding the requirement of excessive thicknesses. This action was taken even before the paper was presented and in itself constituted an amazing example of the ability of our regulatory bodies to meet an emergency.

This Society also was concerned about this subject at the time, as evident from the fact that for the higher temperatures, particularly for the alloys, permissible stresses were being increased. This action was followed by the formation of the Task Force for the selection of the most satisfactory formula.

While it was of the utmost importance that any formula finally selected should be justifiable from theoretical considerations (backed up, wherever possible by tests) certain important practical aspects had to be considered. Some of these were:

(a) For carbon-steel piping at temperatures below 650 F the present thicknesses as determined by the then prescribed formula had generally proved satisfactory in service.

(b) The formula to be adopted, therefore, should be such that, especially for the better materials at higher temperatures, the increase in permissible S-values would be reflected in reduction in thicknesses and yet should not upset the practice in the low-temperature range for ordinary steels except as the result of any minor modification in the permissible stress.

[10] Chief Engineer, Gibbs & Cox, Inc., New York, N. Y. Mem. ASME.

(c) For higher temperatures and pressures, considerations of creep should be given due weight for the special alloys and this was one justification for the factor Y which was introduced into the proposed formula.

The formula finally agreed upon meets these requirements; it is simple in form, and the authors' excellent paper clearly shows that it has had an excellent background of scientific consideration.

Prior to the advent of high temperatures, the simplest way to meet a strength problem was to say "we'll thicken up the pipe or tube." In watertube boilers this actually was done with disastrous results, and it was soon found that thinning the tubes resulted in almost complete elimination of failure.

For steam piping at high temperatures, we are now also headed in the right direction by reducing rather than increasing pipe thicknesses in order to obtain greater reliability. The proposed formula should result in less trouble, considerable saving in weight, and last, but by no means least, a simpler problem in dealing with expansion stresses.

In the final formula in the Code it is expected there will be included a factor C which is additive to the computed thickness and is for corrosion, thread cutting, and so on.

It would seem that this factor should be considered most carefully.

For instance, for superheated steam piping properly insulated, there does not seem to be any need for a corrosion factor and the writer, therefore, feels that the values of C should be defined carefully so that we do not add anything to the thickness of a pipe in cases where this addition fills no justifiable need and where its introduction can be detrimental rather than helpful.

The work of the Task Force is one step toward accomplishing a result that has been needed for many many years, namely, the setting up of a set of requirements that can be used alike by the U. S. Navy, the U. S. Coast Guard, the American Bureau of Shipping, and by industry in general.

A steam pipe does not know whether it has been figured by the U. S. Navy, U. S. Coast Guard, American Bureau of Shipping, or The American Society of Mechanical Engineers' rules, nor does it care. If it is adequate it gives good service, if inadequate it fails, and the writer personally is delighted at the progress made.

The authors are to be congratulated on their presentation and the writer expresses his pleasure for being associated with them on the Task Force.

MARSHALL HOLT.[11] The authors have undoubtedly done a lot of work in compiling the information presented in this paper which presents a recommendation for a working formula. It is indeed unfortunate that such an important recommendation is based on such a small amount of substantiating test data. Many of the formulas considered were developed in studies of theories of elastic failure and have no strong supporting evidence. The fact that the values of y were selected "with careful consideration of the Code allowable S-values" should not be confused with empirical verification.

In the sense that Formulas [2], [3], [4], and [5] are different formulas, the various values of y recommended by the Task Force lead to different formulas for various temperatures. This follows from the fact that Formula [2], the thin-cylinder formula, is obtained when y is set equal to unity. The mean-diameter Formula [4] corresponds to a value of 0.5 for y and Barlow's

adaptation is obtained when y is set equal to zero. Since the proposed values of y range from 0.4 to 0.7, the proposed design rule is equivalent to saying "use one formula if the temperature is X and another formula if the temperature is Y."

The problem of predicting the bursting pressure of a seamless tube is complicated by several unknowns: (a) the diameter at burst, hence total force on the tube wall, (b) the thickness of the tube wall, and (c) the strength of the material under the multiaxial state of stress. As a working tool, the formula should express the working pressure in terms of the initial diameter and wall thickness of the tube and the tensile strength of the material as determined by test on a longitudinal specimen loaded in uniaxial tension.

Data from bursting tests on tubes of various aluminum alloys covering a rather wide range of ductility as measured by elongation in the tension test indicate that a formula of the type of [28] is satisfactory. The value of K seems to depend on the ductility and can be expressed in terms of the ratio of yield strength (0.2 per cent offset) to the tensile strength.

The adoption of a formula as important as this proposal should be made only after a reasonable substantiation by test results.

AUTHORS' CLOSURE

The authors are most grateful for the kind remarks of Mr. H. C. E. Meyer, whose counsel was ever helpful in the resolution of this problem by the Task Force; and for his amplification of the historical background of this work. In addition, the authors wish to take this opportunity to express publicly their appreciation of the technical counsel furnished not only by the members of this Task Force but also by other engineers who participated in this work.

The technical comments of Mr. Marshall Holt are also most welcome. The authors agree with Mr. Holt that it is indeed unfortunate that more specific experimental data are not available in the high-temperature range. As pointed out by Mr. Meyer, however, the rapid advances in pressures and temperatures are resulting in wall thicknesses so heavy that there was concern about the possibility of internal cracking as a result of temperature transients, and this Task Force was formed because of the possibility that simply making the wall heavier would not necessarily result in a safer installation.

It is both difficult and expensive to conduct pipe-bursting tests at the higher temperatures and with adequately long test durations, and only Messrs. Kooistra, Blaser, and Tucker seem to have obtained any recent results along these lines. Their published data seem to verify the proposals of this paper, although, as previously mentioned, their D/t ratios were too large to furnish the needed unequivocal justification. At ordinary temperatures there exists a considerable amount of experimental evidence, and at high temperatures a considerable amount of secondary experimental evidence. The important experimental work of G. Cook and A. Robertson, W. Lode, R. W. Bailey, Norton and Soderberg, and many others, surely cannot be discounted. These probably show, if anything, that the value of $y = 0.4$ is on the conservative side, and that 0.7 could have been used throughout the entire temperature range. Nevertheless, no change was made in the 0.4 value by the Task Force for the present time. Thus no advantage was momentarily taken of the work of Professor Van den Broek at the University of Michigan. Perhaps in the paper a broader application has been made of the theories of failure than originally contemplated for them, but it seems more and more that a failure theory, such as, for example, that of von Mises, is interpreted in the manner proposed by Dr. Nadai: All structures with the same octahedral shear behave similarly under load even to the point of ultimate failure. The paper attempts to clarify existing important formulas, and to accentuate clearly the true

---

[11] Assistant Chief, Engineering Design Division, Aluminum Research Laboratories, Aluminum Company of America, New Kensington, Pa. Mem. ASME.

relationship among existing theoretical approaches. On the assumption that the best advances in science are the result of hand-in-hand efforts of theory and experiment, it is hoped that the paper will promote the accelerated attainment of an answer more satisfactory than that presented.

In particular, however, the authors hope that publication of the work of this Task Force will more strongly emphasize the need for extensive testing of long-time high-temperature bursting pressures in pipes, and that our industrial and collegiate laboratories will initiate testing to answer this need. It is believed that the paper itself has been written so that when more test data become available any new wall-thickness formula, or modifications in the one proposed in this paper, can be developed both quickly and logically.

Effect of Exhaust Pressure on the Economy of Condensing Turbines

By A. KELLER[1] AND J. E. DOWNS[2]

The purpose of this paper is to provide quick and accurate methods of determining the change in heat rate, nonextraction steam rate, or turbine capability, resulting from changes in the exhaust pressure of condensing turbines. The methods are applicable for turbines from 25,000 kw to the maximum size built by the authors' company. It is believed tha these data will be useful to the power-station designer in selecting between alternative turbine designs with different last-stage-bucket annulus areas available in the larger ratings, and also helpful in the selection of condenser size. It also will be useful to the operating engineer in determining when condenser maintenance is advisable, for correcting test data to base exhaust pressure for comparison with guarantee or expected information, and showing the desirability of operation with less than maximum condenser circulating-water pump capacity in cold weather.

NOMENCLATURE

The following nomenclature is used in the paper:

A_a = last-stage-bucket annulus area, sq ft
A_b = last-stage-bucket exit area, sq ft
E_s = stage isentropic-expansion energy, Btu/lb
T_1 = tangential component of steam velocity relative to bucket, at bucket entrance, fps
T_2 = tangential component of steam velocity relative to bucket, at bucket exit, fps
V_n = steam theoretical spouting velocity based on nozzle energy, fps
V_s = steam theoretical spouting velocity based on stage energy, fps
W = wheel speed, i.e., linear speed of moving bucket at pitch line, fps
η_s = stage efficiency based on stage energy E_s
$(\eta_s E_s)$ = stage output, Btu/lb

INTRODUCTION

Data are readily available on vacuum corrections for a theoretical regenerative steam cycle,[3] and theoretical nonextraction vacuum corrections can be derived from the theoretical steam-rate tables. In most practical situations, however, correction factors for the specific turbine under consideration are required since these are considerably different from the theoretical corrections due primarily to changes in exhaust loss as exhaust pressure is changed. These changes in exhaust loss must be accounted for properly if accurate exhaust-pressure corrections are obtained and specific last-stage-bucket design used in the turbine under consideration must form a part of any accurate exhaust-pressure-correction method. In the past, expansion lines and exhaust-loss curves for the specific turbine were used to calculate successive heat balances or nonextraction steam rates at different exhaust pressures to obtain exhaust-pressure corrections. Elston and Knowlton[4] give data which may be used in this manner. The purpose of this paper is to provide data so that the corrections may be derived quickly and easily. The effect of changes in exhaust loss is treated by consideration of the major parameters affecting slope of the exhaust-loss curves for different last stages.

In this study, the authors have related extraction heat rates, nonextraction steam rates, and turbine capability at constant flow to throttle and initial steam conditions (constant valve position) to the values obtained at "optimum exhaust pressure." This approach facilitates the derivation of a general exhaust-pressure-correction method as shown later under "Theory" and "Test Data." For a turbine operating straight-condensing, i.e., no extraction for feedwater heating or other purposes, "optimum exhaust pressure" is defined as the maximum pressure at the turbine-exhaust flange that will give the minimum steam rate obtainable at constant flow to throttle and initial steam conditions. The existence of sonic velocity in the exhaust hood will prevent any further increase in used energy as the exhaust pressure is lowered below "optimum." In this region, the increase in exhaust loss is equal to the increase in available energy. Thus the kilowatts generated and the steam rate will remain constant for lower exhaust pressures. A higher than optimum exhaust pressure will result in a loss in used energy, a reduction in kilowatt generation, and therefore an increase in steam rate.

For a turbine operating with extraction to its feedwater-heating cycle, "optimum exhaust pressure" is defined as that pressure at the exhaust flange which will give minimum heat rate when operating at constant throttle flow and initial (and reheat) steam conditions. At higher or lower exhaust pressures the kilowatt generation is less and the heat rate is higher because of the relation between the two effects described as follows:

1 As exhaust pressure is lowered toward the point described in the foregoing as "optimum" for nonextraction operation, the increase in available energy per pound of steam flow to the condenser results in a varying increase in used energy per pound as determined by change in exhaust loss with a resulting increase in kilowatt generation.

2 Meanwhile, the lower exhaust pressure and corresponding lower saturation temperature in the condenser result in lower condensate temperature entering the lowest-pressure feedwater heater. Accordingly, additional steam is extracted from the turbine to this heater causing a reduction in the steam flow through the later stages of the turbine with a resulting loss in kilowatt generation.

Optimum exhaust pressure occurs at the point where these two effects are equal. At exhaust pressures lower than optimum, the

increase in kilowatt generation due to item (1) is less than the decrease due to (2) so a net reduction in kilowatt generation and increase in heat rate result as exhaust pressure is lowered further. At exhaust pressures higher than optimum, a reduction in exhaust pressure will cause a greater increase in (1) than decrease in (2) with a net increase in kilowatt generation and decrease in heat rate.

It should be realized that the word "optimum" signifies the exhaust pressure which gives the lowest heat rate for a turbine of given design operating at a given flow to throttle. It should not be interpreted as the "optimum" from an over-all economic standpoint when selecting between alternative condensers or between alternative last-stage-bucket lengths offered on the larger steam turbines. The method outlined herein is limited to the prediction of comparative heat rates, steam rates, and kilowatt capabilities for different exhaust pressures. The economics in a given situation must be dealt with separately.

WORKING METHOD

Reheat Turbines. For a reheat unit operating with feedwater-heating extraction, the optimum exhaust pressure in inches Hg abs has been determined by calculations and tests to be equal to

$$\frac{\text{Flow to condenser, lb per hr}}{7900 \times \text{Total last-stage-bucket annulus area, sq ft}}$$

where flow to condenser equals total flow through last-stage buckets at optimum exhaust pressure; total last-stage-bucket annulus area equals [(bucket pitch diameter, in.) (bucket length, in.) (number of exhaust ends)] $\pi/144$.

The flow to condenser, if not known, may be estimated by decreasing the flow to throttle by 1 per cent per 10 deg rise in feedwater temperature in the feedwater-heating cycle. If the condenser flow is known at some other exhaust pressure than optimum, changes in condenser flow (at constant flow to throttle) as exhaust pressure is changed can be estimated using a 2 per cent decrease in condenser flow for halving the absolute exhaust pressure. If neither the condenser flow nor throttle flow is known, an estimate of the throttle flow can be obtained using Fig. 1. The increase in heat rate from that existing at optimum exhaust pressure for higher or lower pressures (in per cent of the heat rate at optimum) is shown in Fig. 2 for a reheat turbine with steam

Fig. 2   REHEAT TURBINES OPERATING WITH FEEDWATER-HEATING EXTRACTION

conditions of 1800 psig, 1000 F, reheat to 1000 F, and with 52.4 sq ft total (double flow) last-stage-bucket annulus area. For different last-stage buckets, this per cent increase in heat rate has been found to vary directly with the change in the function

$$W\left(0.185 + \frac{A_b}{A_a}\right)$$

This function equals 612 for the turbine represented in Fig. 2. The value of this function for any specific turbine can be obtained from the manufacturer. For turbines built by the authors' company in recent years, if the last-stage-bucket annulus area is known, the "bucket factor" from Table 1 can be used directly. For other steam conditions, the per cent increase in heat rate has been found to vary inversely with the total available energy of the steam in Btu per lb from throttle conditions to the cold reheat line plus that from the reheat-section inlet to $1\frac{1}{2}$ in. Hg abs exhaust pressure. This total available energy for the turbine represented in Fig. 2 is 730 Btu per lb. The total available energy for the specific turbine can be read from the steam chart and the curve in Fig. 3, used to obtain a direct multiplying factor to apply to Fig. 2. For convenience, the tabulation in Fig. 3 gives this factor for several steam conditions, assuming typical reheat pressures. Thus, the per cent increase in heat rate for any turbine equals the value read from Fig. 2 (factor for last-stage buckets from Table 1) (steam-conditions factor from Fig. 3). The decrease in turbine kilowatt output from that existing at optimum

Fig. 1   ESTIMATING THROTTLE STEAM RATES FOR EXTRACTION OPERATION OF NONREHEAT TURBINES WITH FINAL FEEDWATER TEMPERATURES AS SHOWN

(Throttle steam rate with reheat initial temperature is approximately 17 per cent less than nonreheat for same throttle conditions.)
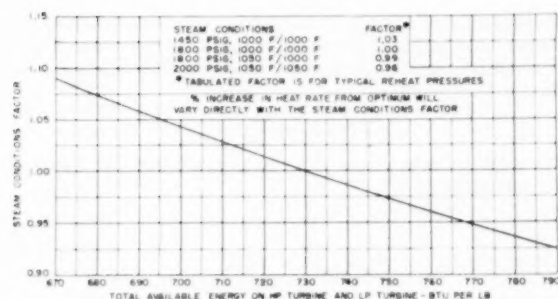
FIG. 3   REHEAT TURBINES—MULTIPLYING FACTOR TO CORRECT FOR
DIFFERENT INITIAL AND REHEAT STEAM CONDITIONS
(Per cent increase in heat rate from optimum will vary directly with steam-
conditions, factor.)

exhaust pressure for higher or lower pressures (in per cent of the
kilowatt output at optimum) equals

$$\frac{\text{Per cent increase in heat rate}}{1 + \dfrac{\text{Per cent increase in heat rate}}{100}}$$

Thus a 10 per cent increase in heat rate means a 9.1 per cent de-
crease in kilowatt output at the same flow to throttle.

*Nonreheat Turbines Operating With Feedwater-Heating Extrac-
tion.* Optimum exhaust pressure in inches of Hg abs for these
units equals

$$\frac{\text{Flow to condenser, lb per hr}}{8200 \times \text{Total last-stage-bucket annulus area, sq ft}}$$

The flow to condenser, if not known, may be estimated as already
described for reheat turbines except for a 1 per cent decrease per
11-deg rise in feedwater temperature.

The per cent increase in heat rate is shown in Fig. 4, for a 75,000-
kw-capability 3600-rpm turbine with initial steam conditions
of 850 psig, 900 F, and with 52.4 sq ft total last-stage-bucket
annulus area.   For different last-stage buckets, the per cent in-
crease in heat rate varies directly with last-stage function de-
scribed previously and the multiplying factors from Table 1 may
be used.   The per cent increase in heat rate for nonreheat tur-
bines has been found to vary directly with the nonextraction
steam rate at capability and $1\frac{1}{2}$ in. Hg abs exhaust pressure.
The nonextraction steam rate for the turbine for which Fig. 4 is
plotted is 7.55 lb per kwhr.   If the nonextraction steam rate is
not readily available for the specific turbine, the theoretical non-
extraction steam rate may be used to enter Fig. 5, to obtain
directly the "steam conditions and rating factor."   Fig. 5 is a
plot of the ratio of nonextraction steam rates for various steam
conditions and ratings to that for the base turbine.   The formula
for per cent change in turbine kilowatt output is the same as just
given for reheat units.

Nonreheat Turbines Operating Without Extraction. Optimum ex-
haust pressure in inches of Hg abs for these units equals

$$\frac{\text{Flow to condenser, lb per hr}}{8600 \times \text{Total last-stage-bucket annulus area, sq ft}}$$

The per cent increase in steam rate resulting from having higher
than this "optimum exhaust pressure" is shown in Fig. 6, for the
same turbine for which Fig. 4 is plotted.   Fig. 5 and Table 1 may
be used to correct for different last stages, ratings, and steam
conditions as described for nonreheat turbines operating with feed-
water-heating extraction.   The decrease in turbine kilowatt out-
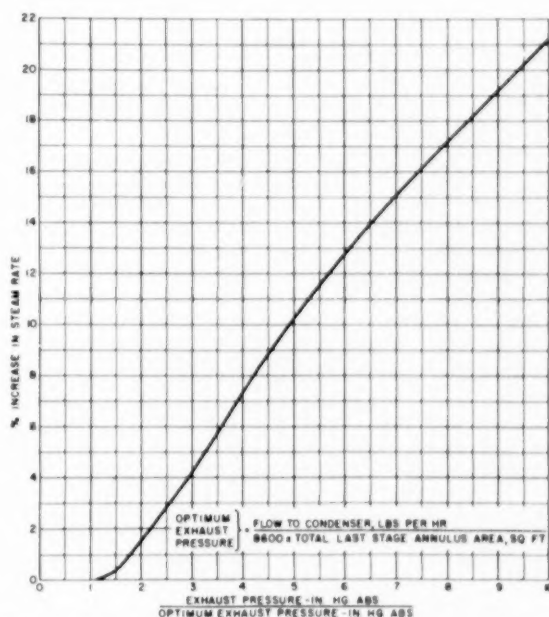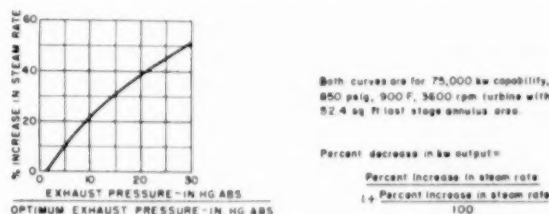
FIG. 4   NONREHEAT TURBINES OPERATING WITH FEEDWATER-
HEATING EXTRACTION
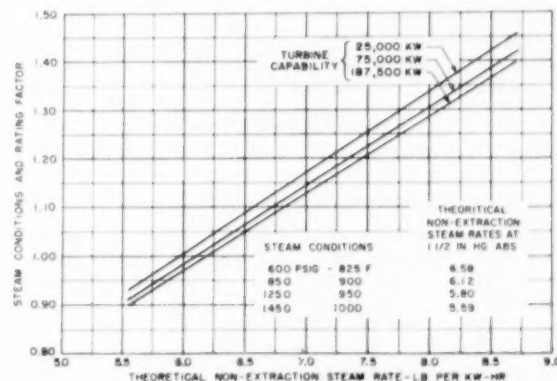
FIG. 5   NONREHEAT TURBINES—MULTIPLYING FACTOR TO CORRECT
FOR DIFFERENT RATINGS AND INITIAL STEAM CONDITIONS

put for higher exhaust pressures (in per cent of the kilowatt output
at optimum) equals

$$\frac{\text{Per cent increase in steam rate}}{1 + \dfrac{\text{Per cent increase in heat rate}}{100}}$$

TABLE 1   MULTIPLYING FACTOR TO CORRECT FOR
DIFFERENT LAST-STAGE BUCKETS

(Per cent increase in heat rate or nonextraction steam rate from optimum
will vary directly with bucket factor)

—3600 rpm—		Bucket factor	—1800 rpm—		Bucket factor
—Area, sq ft—			—Area, sq ft—		
17.7,	35.4	1.00	24.4		0.72
19.3,	38.6	0.91	31.4		0.77
20.9,	41.8	0.98	45.6		0.86
24.9,	49.7	1.12	58.4		0.92
26.2,	52.4	1.00(base)	67.9,	135.8	0.93
32.9,	65.7, 98.6	1.13	84.0,	168.0	1.16
41.1,	82.2, 123.3	1.20	95.4,	190.8	1.01
			123,	246	1.13
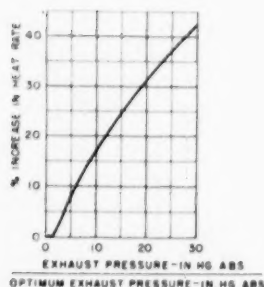
Both curves are for 75,000 kw capability,
850 psig, 900 F, 3600 rpm turbine with
52.4 sq ft last stage annulus area

Percent decrease in kw output =

Percent increase in heat rate
────────────────────────────────
1 + Percent increase in heat rate
    ────────────────────────────
              100
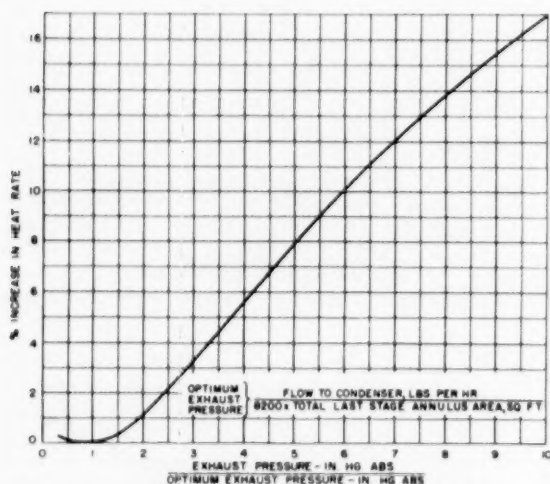
FIG. 6   NONREHEAT TURBINES OPERATING WITHOUT EXTRACTION

THEORY UNDERLYING THE METHOD

The theory herein presented is qualitative only. Quantitative answers are then obtained by analyzing back-pressure test data in the light of the qualitative theory. A logical deduction of the qualitative theory is as follows:

Consider an axial-flow turbine stage. Fig. 7 shows a cross section through the steam path of such a stage and a typical velocity diagram for the stage.

Next consider a filament of flow passing through the stage. It can be shown that the used-energy output per pound of flow is given by the formula

$$(\eta_s E_s) = \frac{W(T_1 + T_2)}{778.26 \times 32.1740} \quad \ldots\ldots\ldots\ldots [1]$$

This formula is 100 per cent accurate; however, a problem still exists to evaluate T_1 and T_2.

Assume that the turbine stage has 0-deg nozzle and bucket exit

angles and that the nozzle and bucket velocity coefficients are unity; i.e., the stage hydraulic efficiency is 100 per cent. This is equivalent to saying that the only loss in the stage is leaving loss. Under these conditions

$$T_1 = T_2 = V_n - W \quad \ldots\ldots\ldots\ldots [2]$$

For a pure-impulse stage, all of the pressure drop takes place in the nozzle, hence

$$V_n = V_s \quad \ldots\ldots\ldots\ldots [3]$$

Combining Equations [1], [2], and [3]

$$(\eta_s E_s) = \frac{2}{778.26 \times 32.1740} W(V_s - W) \quad \ldots\ldots [4]$$

or

$$(\eta_s E_s) = \frac{2}{778.26 \times 32.1740} WV_s - \frac{2}{778.26 \times 32.1740} W^2 \ldots [5]$$

If the stage now be operated at constant speed but variable energy, the second term of Equation [5] is constant and the change of output with change of steam velocity is given by the formula

$$\Delta(\eta_s E_s) = \frac{2}{778.26 \times 32.1740} W\Delta V_s \ldots\ldots\ldots [6]$$

The energy of isentropic expansion of steam may be expressed quite closely as a function of the enthalpy of the steam and the pressure ratio of the expansion. All conventional condensing turbines within a given group (reheat turbines, for instance) have approximately the same enthalpy at the condenser. Therefore, for such stages, the isentropic energy can be calculated quite closely as a constant times a function of the stage-pressure ratio. Then, since velocity varies as the square root of kinetic energy, the theoretical steam-spouting velocity can be evaluated as another constant times another function of the stage-pressure ratio. The latter relationship can be transformed to the following equation useful for the present purpose

V_s at optimum $\quad — \quad V_s$ at any other
   exhaust   exhaust
   pressure   pressure

$$\approx \text{Constant } f_1 \left(\frac{\text{Exhaust pressure}}{\text{Optimum exhaust pressure}} \right) \ldots [7]$$
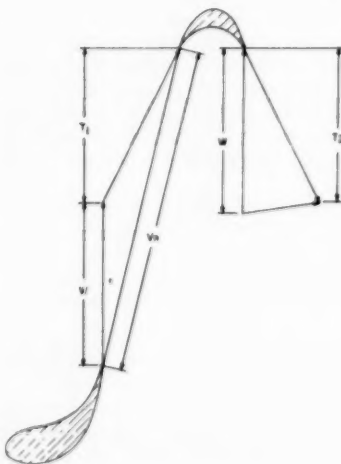
FIG. 7   VELOCITY DIAGRAM FOR TURBINE STAGE

Substituting Equation [7] in [6] and changing the function of exhaust pressure over optimum exhaust pressure to include the coefficients of Equation [6] and the constant of [7] gives

$(\eta_e E_s)$ at optimum — $(\eta_e E_s)$ at any other
    exhaust   exhaust pressure
    pressure

$$= W f_2 \left(\frac{\text{Exhaust pressure}}{\text{Optimum exhaust pressure}} \right) \dots [8]$$

All of the reasoning thus far has been for a stage having 0-deg exit angles and 100 per cent hydraulic efficiency. A closer approximation to the back-pressure characteristics of an actual stage can be obtained by introducing a function of A_b/A_a to allow for the bucket-exit angle and changing f_2 to f_3 to allow for the actual hydraulic efficiency. Making these changes gives

$(\eta_e E_s)$ at optimum — $(\eta_e E_s)$ at any other
    exhaust   exhaust pressure
    pressure

$$= f\left(\frac{A_b}{A_a} \right) \, W f_3 \left(\frac{\text{Exhaust pressure}}{\text{Optimum exhaust pressure}} \right) \dots [9]$$

An analysis of vacuum tests on many turbines with different last-stage nozzle and bucket angles indicates that good agreement between test and theory is obtained when

$$f\left(\frac{A_b}{A_a} \right) = 0.185 + \frac{A_b}{A_a} \dots \dots [10]$$

Substituting Equation [10] in [9] and letting the f-function take any form required to get good agreement between test and theory gives

$(\eta_e E_s)$ at optimum — $(\eta_e E_s)$ at any other
    exhaust   exhaust pressure
    pressure

$$= \left(0.185 + \frac{A_b}{A_a} \right) W f \left(\frac{\text{Exhaust pressure}}{\text{Optimum exhaust pressure}} \right) \dots [11]$$

The foregoing method of reasoning on a successive-approximation basis and the various concepts introduced are not new. The concepts introduced and further interpretations of them have been used in turbine-design work in the authors' company for about 20 years. The authors do not consider it happenstance that the last section of this paper shows good agreement between Equation [11] and test data on many turbines.

CONVERSION OF THEORETICAL EQUATION TO WORKING FORM

Equation [11] has been reduced to the working form of the first six figures of this paper by the following substitutions:

1   Figs. 2, 4, and 6 give the values of

$$f\left(\frac{\text{Exhaust pressure}}{\text{Optimum exhaust pressure}} \right)$$

for

(a) Reheat turbines operating with feedwater-heating extraction.

(b) Nonreheat turbines operating with feedwater-heating extraction.

(c) Nonreheat turbines operating without extraction.

2   Table 1 gives values of

$$\frac{\left(0.185 + \frac{A_b}{A_a} \right) W}{612}$$

for the various standard last stages used by the authors' company.

3 (a) Fig. 3 gives

$$\frac{730}{\text{Total isentropic energy}}$$

for reheat turbines.

(b) Fig. 5 gives

$$\frac{7.55}{\text{Approx nonextr steam rate at } 1\frac{1}{2} \text{ in. Hg abs}}$$

for nonreheat turbines. These have been introduced into the working method so that percentage change in turbine over-all output is calculated rather than changed output in Btu/lb of steam flowing to the condenser.

The constants used in the formulas for establishing the optimum exhaust pressures were obtained empirically. They are the values which the test data available indicate to be proper.

SUBSTANTIATING TEST DATA

The curves in Figs. 8, 9, and 10 are the same as those in Figs. 2, 4, and 6. The plotted points represent test results of exhaust-pressure runs on 28 turbines during the past several years.

The turbines tested had a wide range of kilowatts capability, steam conditions, and last-stage-bucket annulus areas. A typical exhaust-pressure run for many of these turbines consisted of
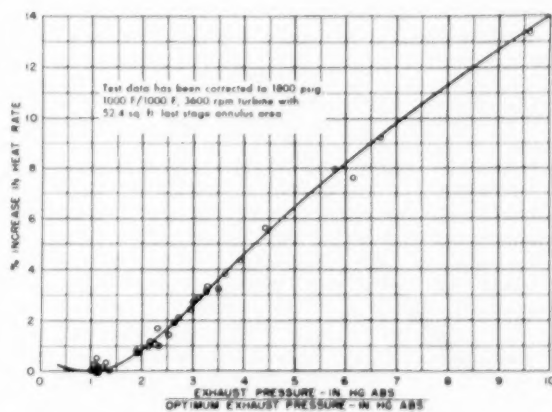
FIG. 8   TEST RESULTS FOR REHEAT TURBINES OPERATING WITH FEEDWATER-HEATING EXTRACTION

(Test data have been corrected to 1800-psig, 1000-F/1000-F, 3600-rpm turbine with 52.4 sq ft last-stage annulus area using Fig. 3 and Table 1.)

measuring the generator output with 1, $1\frac{1}{2}$, 2, and $2\frac{1}{2}$ in. Hg abs exhaust pressure with the throttle flow and initial steam conditions held constant. For many of the turbines, vacuum runs were made at more than one throttle flow. The load range covered by the plotted points is from maximum capability down to as low as 25 per cent of maximum capability in some cases.
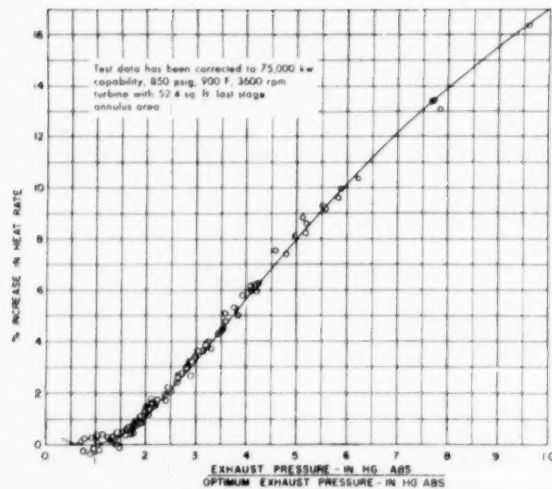
FIG. 9   TEST RESULTS FOR NONREHEAT TURBINES OPERATING WITH FEEDWATER-HEATING EXTRACTION

(Test data have been corrected to 75,000-kw capability, 850-psig. 900-F. 3600-rpm turbine with 52.4 sq ft last-stage annulus area using Fig. 5 and Table 1.)
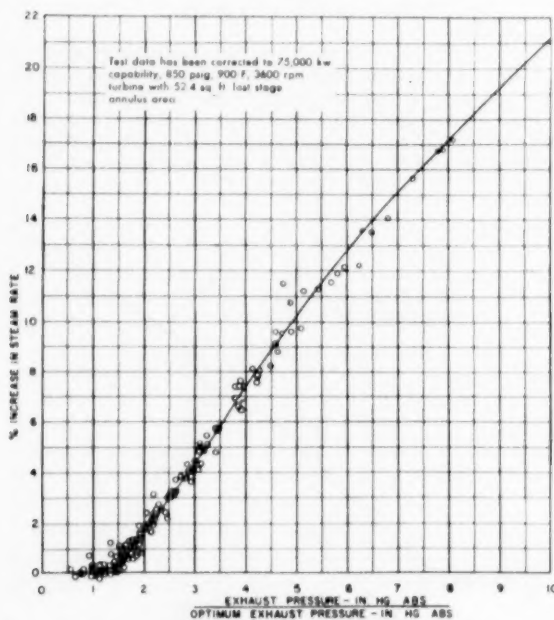

FIG. 10   TEST RESULTS FOR NONREHEAT TURBINE OPERATING WITHOUT EXTRACTION

(Test data have been corrected to 75,000-kw capability, 850-psig. 900-F. 3600-rpm turbine with 52.4 sq ft last-stage annulus area using Fig. 5 and Table 1.)

CONCLUSIONS

The authors believe that the method for obtaining exhaust-pressure corrections outlined in this paper will prove useful to users of steam turbines. The method, which is confirmed by test data, can be applied easily when only a few parameters for the specific turbine for which corrections are desired are known.

Appendix

Problem. A 100,000-kw-capability reheat turbine with initial steam conditions of 1450 psig, 1000 F, reheat to 1000 F has a heat rate of 8182 Btu/kwh when operating at 80,000 kw output, 1.5 in. Hg abs exhaust pressure. The throttle flow and condenser flow are 520,000 and 382,000 lb per hr, respectively. The turbine has a double-flow exhaust with 23-in-long, last-stage buckets on $65^{1}/_{2}$ in. pitch diameter. What are the heat rates and kilowatt outputs at other exhaust pressures, keeping constant initial and reheat steam conditions and constant throttle flow?

Solution. (1) Determine optimum exhaust pressure for this throttle flow

$$\text{Total last-stage annulus area} = \frac{65.5\,(23)\,2\pi}{144} = 65.7 \text{ sq ft}$$

$$\text{Optimum exhaust pressure} = \frac{382,000}{7900 \times 65.7} = 0.74 \text{ in. Hg abs}$$

which is a 50 per cent reduction in exhaust pressure from 1.5 in. Hg. Therefore, the flow to condenser at optimum exhaust pressure will be 2 per cent less than 382,000 or 374,000 lb per hr

$$\text{Optimum exhaust pressure} = \frac{374,000}{7900 \times 65.7} = 0.72 \text{ in. Hg abs}$$

(2) Determine heat rate and kilowatt output at optimum exhaust pressure:

From Table 1, at 65.7 sq ft, bucket factor = 1.13.

From Fig. 3, at 1450 psig, 1000 F/1000 F, steam conditions factor = 1.03.

With 1.5 in. Hg abs exhaust pressure

$$\frac{\text{Exh press}}{\text{Opt exh press}} = \frac{1.5}{0.72} = 2.1$$

From Fig. 2, uncorrected increase in heat rate = 0.9 per cent.

Corrected increase = 0.9 × 1.13 × 1.03 = 1.0 per cent of the heat rate at optimum.

Heat rate at optimum = 8182/1.010 = 8101 Btu per kwhr.

(NOTE: denominator = 1 + per cent increase/100.)

Decrease in kilowatt output equals

$$\frac{1.0}{1 + \dfrac{1.0}{100}} = 1.0 \text{ per cent of the kilowatt at optimum}$$

Kw at optimum = 80,000/0.990 = 80,810.

(NOTE: denominator = 1 − per cent decrease/100.)

(3) Determine heat rate and kilowatt output at other exhaust pressures:

Select operating exhaust pressure, say, 2.0 in. Hg abs

$$\frac{\text{Exh press}}{\text{Opt exh press}} = \frac{2.0}{0.72} = 2.8$$

From Fig. 2, uncorrected increase in heat rate = 2.2 per cent.

Corrected increase = 2.2 × 1.13 × 1.03 = 2.6 per cent of heat rate at optimum.

Increase in heat rate = 2.6 × 8101 = 211 Btu per kwhr.

Heat rate at 2.0 in. Hg abs = 8101 + 211 = 8312 Btu per kwhr.

TABLE 2   EXHAUST-PRESSURE DATA

Exh press, in. Hg abs	Exh press divided by opt exh press	Uncorrected increase in heat rate, per cent	Corrected increase in heat rate, per cent	Corrected increase in heat rate Btu/kwhr	Heat rate, Btu/kwhr	Decrease in kw output, per cent	Decrease in output, kw	Kw output
0.72	1.0	Base	Base	Base	8101	Base	Base	80810
1.0	1.4	0.2	0.2	16	8117	0.2	160	80650
1.5	2.1	0.9	1.0	81	8182	1.0	810	80000
2.0	2.8	2.2	2.6	211	8312	2.5	2020	78790
2.5	3.5	3.6	4.2	340	8441	4.0	3230	77580
3.0	4.2	5.0	5.8	471	8572	5.5	4450	76360
3.5	4.9	6.3	7.3	592	8693	6.8	5490	75320

Decrease in kilowatt output equals

$$\frac{2.6}{1 + \frac{2.6}{100}} = 2.5 \text{ per cent}$$

of the kilowatt output at optimum.

Decrease in kilowatt output = 2.5 per cent 80,810 = 2020 kw
Kilowatt output at 2.0 in. Hg abs = 80,810 − 2020 = 78,790 kw

(4) A tabulation, Table 2, may be easily calculated following the procedure outlined in item (3) from which an exhaust-pressure correction curve may be drawn.

Discussion

H. R. REESE.[5]   The authors are to be commended for a paper that should be very useful in power-plant economic studies for variable exhaust pressures and turbine-casing arrangements.

The paper is excellent for determining the correction to "heat rate and change in load" for a given number of exhaust ends and turbine-casing arrangements.   However, unless other factors are included, errors may be introduced when correcting a given design to a design with a different number of exhaust ends and casing arrangement.

The number of exhaust ends and casing arrangements affects the blade leakage, blade aspect ratio, and packing leakage of the elements, which may have a total effect on the heat rate and kilowatt output, ranging to approximately 1 per cent.   The speed of the elements also affects the element efficiency when considering 3600 or 1800-rpm intermediate or low-pressure elements.

It is suggested that a construction factor for turbine-casing arrangement be included with the other correction factors in determining the final heat rate and kilowatt output.   Construction factors can be determined for the single, tandem, and cross-compound units with varying number of exhaust ends, and the difference in these factors can be used to correct the heat rate and kilowatt output.

In defining the optimum exhaust pressure for the feedwater-heating cycle, it is well to emphasize "part 2" where it points out the additional steam extracted for lower exhaust pressure and corresponding lower saturation temperature, results in a loss in kilowatt generation which results in a poorer heat rate.   This factor often is overlooked when evaluating extra kilowatts for improved vacua when using leaving-loss curves for the correction.

H. J. RUBINSTEIN.[6]   This paper will be of much value to the purchasers and users of large steam turbines.   Heretofore, it behooved the steam-plant designer to rely heavily upon the turbine manufacturer for this kind of information for studies made previous to the actual purchase of a new machine.

This paper will prove useful in the evaluation of the whole

[5] Assistant Manager, Central Station Section, Steam Division, Westinghouse Electric Corporation, Lester, Pa.   Mem. ASME.

[6] Mechanical Engineering Associate, Steam Design Section, Department of Water and Power of the City of Los Angeles, Los Angeles, Calif.

TABLE 3   COMPARISON OF RESULTS

Per cent increase in heat rate in going from 2 in. Hg to 3.5 in. Hg exhaust pressure

Per cent maximum capability	100%	60%	40%
Valley Steam Plant No. 3 machine...	3.92	7.2	11.7
Authors' values...................	3.51	5.5	6.7

Per cent decrease in heat rate in going from 2 in. Hg to 1.5 in. Hg exhaust pressure

Valley Steam Plant No. 3 machine...	1.25	2.11	3.38
Authors' values...................	0.79	2.03	2.76

interdependent problem of condenser size, cooling-tower size, plant location (with reference to the temperature of cooling water available) and turbine exhaust-annulus area.   These matters can now be investigated in the light of value received in the form of changes in turbine economy.

A check has been made to compare the information presented with the information available to us after the purchase of a large turbine.   To perform this check we used the heat-rate correction curves given to us by the manufacturer of our Valley Steam Plant unit No. 3, which is a General Electric 156,250-kw maximum capability, 1800 psig, 1000 F throttle, 1000 F reheat machine. We calculated the change in heat rate in going from 2 in. Hg exhaust pressure to 3.5 in. Hg, and also in going from 2 in. Hg exhaust pressure to 1.5 in. Hg.   We did this for 40 per cent, 60 per cent, and 100 per cent of maximum capability.   Table 3 gives the results of our calculations.

Assuming that our calculations are correct we would appreciate knowing which method is considered more accurate.

We as purchasers and users of large steam turbines are grateful to the authors for making this kind of information available.

AUTHORS' CLOSURE

Mr. Reese properly points out that additional data is required if the user of this paper wishes to determine differences in heat rate between turbines with different exhaust-end arrangements. Such data may be obtained from the paper by C. W. Elston and P. H. Knowlton, published in 1952.[7]   Data on comparative performance of turbines with different casings and exhaust-end arrangements may be obtained from this reference at one exhaust pressure.   This paper will then readily furnish comparative heat rates at other exhaust pressures.   The authors agree with Mr. Reese's caution that additional steam extracted at the lower exhaust pressures must be properly accounted for.

Mr. Rubinstein points out differences between exhaust-pressure corrections furnished by the authors' company some time ago for a turbine being built for the Valley Steam Plant and exhaust-pressure corrections calculated from this paper.   Only recently has test data been obtained on modern reheat turbines and the organization of these data for this paper revealed that changes in heat rate were less as exhaust pressure was changed than had been previously expected.   The exhaust-pressure corrections furnished for the Valley Steam Plant were based on tests on nonreheat turbines before these reheat test data were available.   As can be seen in Fig. 8, the method contained in this paper agrees quite well with the test data.

[7] "Comparative Efficiencies of Central-Station Reheat and Nonreheat Steam-Turbine-Generator Units," by C. W. Elston and P. H. Knowlton, Trans. ASME, vol. 74, 1952, pp. 1389–1399.
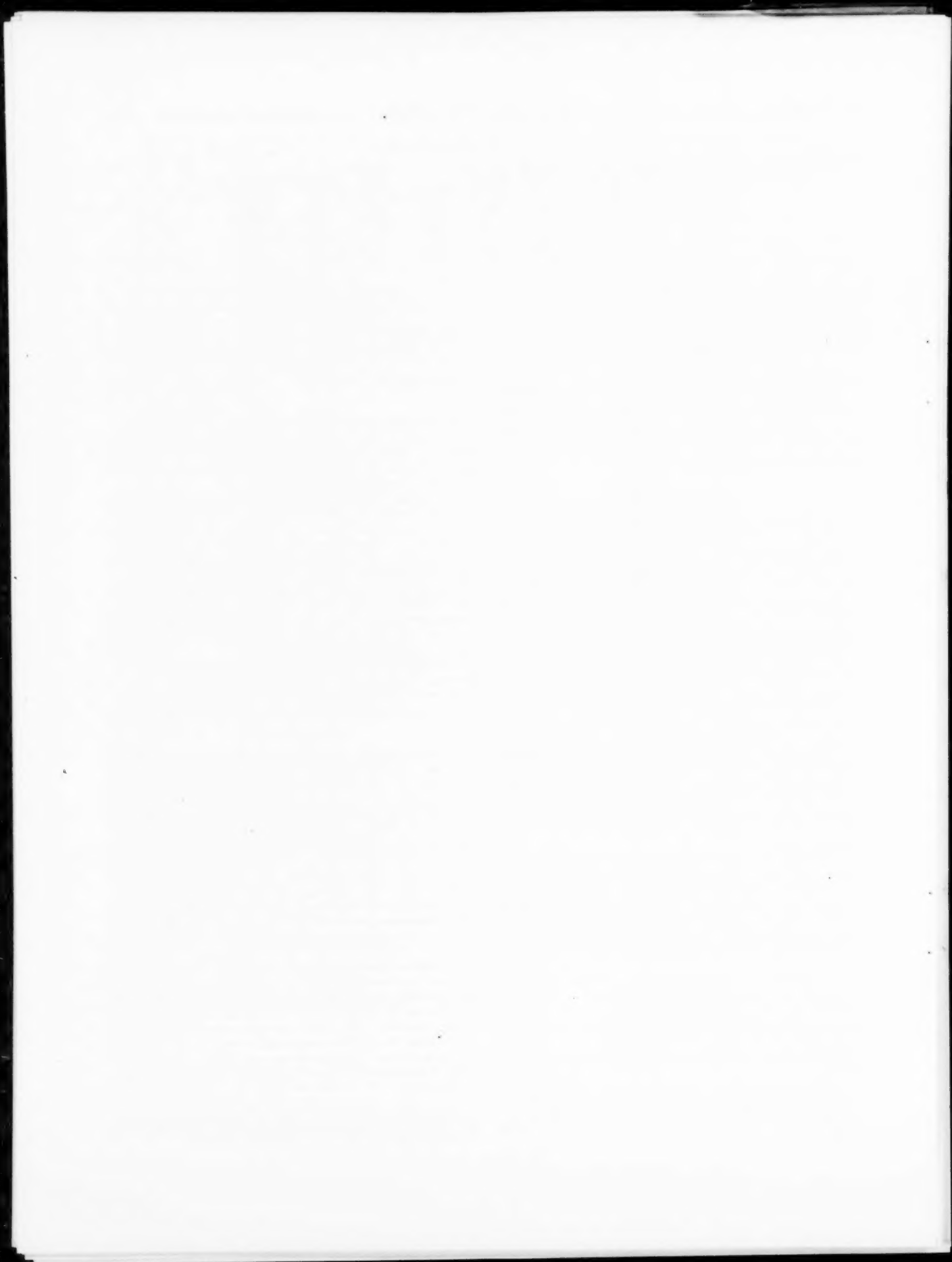
The Development of High-Output Free-Piston Gas Generators

By R. A. LASLEY[1] AND F. M. LEWIS[2]

The development of free-piston gas generators suitable for naval-propulsion purposes was started in 1943 at the Baldwin-Lima-Hamilton Corporation, then the General Machinery Corporation, under a contract with the U. S. Navy Department. At that time little was known in this country regarding the free-piston developments of Pescara in France or Sulzer in Switzerland, which had already been under way for some years. This paper traces the progress made in this project and describes the construction and operating characteristics of various models which have been made during the course of the program.

INTRODUCTION

FOR certain naval-propulsion purposes the free-piston gas-generator gas-turbine or "gasifier-turbine" power plant, as it will be called hereafter, has potential advantages.

As compared with steam there is a reduced fuel consumption and a reduced hazard. As compared with diesels there are a reduced size and weight and the advantages entailed in coupling a single turbine to the propulsion shaft, rather than a multiplicity of reciprocating units. As with any gas-turbine arrangement, it is necessary, for reversal, to utilize either a reversing gear with clutches or a reversible propeller. Developments in other types of gas turbines, as well as in atomic power, may influence the use of the gasifier-turbine plant to an extent as yet unknown.

The developments at Baldwin-Lima-Hamilton have been concerned exclusively with gasifiers of high specific output, suitable for naval propulsion or other applications which require light-weight machines.

The weight and volume of a gasifier-turbine plant of a given total output power are largely fixed by the weight and volume of the gasifier part of the plant. This is influenced by the following factors:

(a) The size and number of the gasifier units used for a given total power.

(b) Arrangement of the parts of the gasifier.

(c) Pressure and temperature of the cycle.

(d) Piston speed of the gasifier.

(e) Design as regards material used, thickness of stressed parts, and other similar factors.

SIZE AND NUMBER OF UNITS

Considering item (a) it is noted that the gasifier is subject to the same law of comparison as other prime movers. This states that for geometrically similar machines of the same piston speed,

pressures, and pressure drops, the weight and volume per horse-power are proportional to the linear dimension of the units.

In theory the total weight of the plant can therefore be reduced to any desired limit by using a sufficient number of units of small dimension and high cyclic speed. In practice this theoretical possibility is limited by difficulties of fuel injection and other practical considerations and by the natural desire to keep the number of parts in an installation to a minimum. Also, as the number of units is increased, the total volume required for service passages becomes progressively larger. These factors are so many and complex that the optimum size of the units, in the last analysis, becomes largely a matter of opinion.

Of the gasifiers constructed by Baldwin-Lima-Hamilton, the Model A is of 7-in. bore power cylinder, 21-in. bore compressor cylinder by 10-in. full power stroke, and the Model B of $8^1/_4$-in. bore power cylinder by 23-in. bore compressor cylinder by 11-in. full power stroke.

ARRANGEMENT OF PARTS

A considerable number of arrangements of gasifiers, some quite impracticable in design, have been proposed by patentees. Of these a few have been constructed and operated.

All arrangements utilize a pair of opposed pistons connected by some type of synchronizing mechanism to insure their operation in exactly opposite phase. This opposed-piston arrangement gives a balance of inertia forces, so that any vibratory reactions between the gasifier and its foundations are limited to forces produced by the pulsating flow of the discharge and scavenge gases.

In describing these various opposed-piston gasifiers, the following terms will be used:

Combend—the piston position when the pistons are closest together at the center of the machine; that is, "distance combend" is the distance a piston can be moved from this inner position toward the center of the machine until it touches its mate.

Scavend—the piston position when the pistons are farthest apart at the outer end of the stroke, and as a distance the inward travel of a piston until it touches its mate.

The stroke equals scavend minus combend.

Combend, scavend, and stroke are all functions of the operating conditions and vary with the load.

The gasifiers which have been constructed are all of two types—outward compression and inward compression. "Compression" here refers to the inital compression of the scavenge air.

Considering outward-compression gasifiers, the simplest arrangement, although it is not a practicable machine, is shown in Fig. 1. Starting from combend, the pistons move out under the combustion pressure, compressing air in the compressor spaces AA' and discharging it to the scavenge trunk B. The expansion of the residual compressed air in the compressor spaces AA' must provide sufficient energy to compress the trapped air in the combustion chamber C and return the pistons to combend.

The use of the compressor spaces to supply the return energy results in a low volumetric efficiency for the compressor, and therefore a large size of machine. It is also difficult to start this arrangement. There is a further difficulty in that proper combend can be obtained only at a single load condition. Suppose

that fuel is reduced from this first condition, then scavend will shorten and the increased compressor energy will shorten combend and give too high a compression pressure in the combustion cylinder.
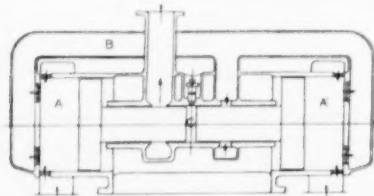

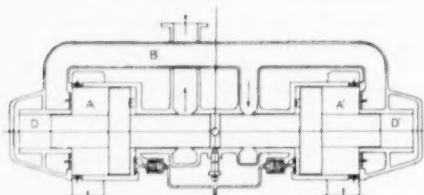FIG. 1 GASIFIER WITH OUTWARD COMPRESSION, NO SEPARATE BOUNCE

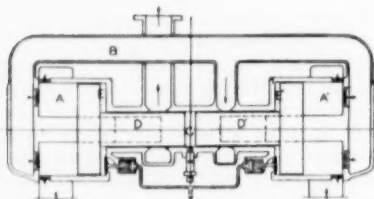FIG. 2 GASIFIER WITH OUTWARD COMPRESSION, OUTER BOUNCE CYLINDER

FIG. 3 GASIFIER WITH OUTWARD COMPRESSION, INVERTED BOUNCE CYLINDER

These various difficulties can be overcome by the use of an additional piston and cylinder which will be called the direct-bounce cylinder. Two arrangements for this are shown in Figs. 2 and 3. The direct-bounce cylinders are DD'. The principle of these two arrangements is the same, but in Fig. 3 the bounce cylinder is placed inside the compression and power cylinder, resulting in a shorter machine. With the use of the direct-bounce cylinder to supply the return energy, the compressor clearances can be reduced to the minimum required for safety, and combend at any load can be adjusted to any value which is desired.

Models A and B, which have been constructed by Baldwin-Lima-Hamilton, follow Fig. 2, and Model D follows Fig. 3. The machines which were constructed by Sulzer Brothers are as shown in Fig. 2. The spaces EE' are called reverse-bounce spaces. They are used for starting, in a manner to be described later, and may or may not be used for a measure of speed control.

OPERATING CHARACTERISTICS

The following operating characteristics of gasifiers of this type should be noted. A start is made at atmospheric pressure, and the direct-bounce pressure is adjusted so that the compression pressure in the combustion cylinder will be of the order of 500 psi, sufficient for combustion. With increased fuel and load the pressure rises. If combend position was held, the compression

pressure would rise in proportion to the scavenge pressure, and at 6 atm would reach 3000 psi with a still higher combustion pressure. These pressures are not permissible from the viewpoint either of liner or ring strength. As the scavenge pressure rises it is therefore necessary to increase combend so as to hold the pressure in the combustion cylinder to a safe limit.

Another important operating characteristic is the relation of load to stroke. Assuming the gasifier discharges to a fixed-orifice turbine, a reduction of fuel results in a reduction of the energy available for compression. The pistons then shorten their stroke, with a consequent decrease in volumetric efficiency, until the energy absorbed by the compressor, with an addition for friction, equals the energy output of the power cylinder. These changes are entirely automatic with a change in fuel setting. The direct-bounce pressure must be adjusted for correct combend.

In Fig. 4 is shown the simplest type of inward-compression gasifier. This is the arrangement of Pescara as constructed by SIGMA (Société Industrielle Générale de Mécanique Appliquée).

Here the outer side of the pistons serve as the direct-bounce space, while the inner side is the compressor space. Starting is effected by moving the piston to scavend and then suddenly injecting a fixed quantity of compressed air into the bounce space. This type of gasifier is subject to the following limitations:

It is necessary to place the compressor cylinder heads so that starting with minimum combend there is still a slight clearance. As the scavenge pressure rises it is necessary to increase combend just as with the outward-compression machine. But this increases the compressor clearance and thus reduces its volumetric efficiency. This effect increases the size of the gasifier necessary for a given output. Up to a pressure ratio of 3 to 4 atm these difficulties can be compromised to a certain extent, but above this limit the loss is too great. These limitations can be overcome but with some additional complications.

Among the several possibilities the most attractive is to move the compressor head through a short distance so that at starting there is a large compressor clearance and at full load, a small one.
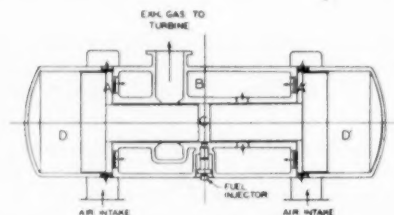
FIG. 4 GASIFIER WITH INWARD COMPRESSION, PESCARA TYPE
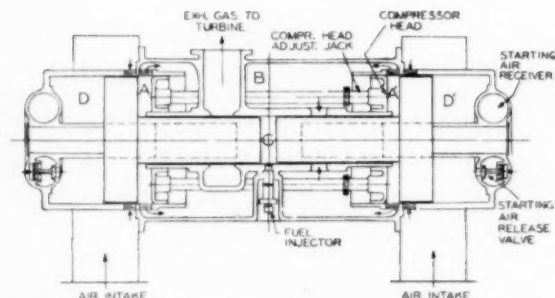
FIG. 5 GASIFIER WITH INWARD COMPRESSION, MOVABLE COMPRESSOR HEAD

The movement can be effected either by mechanical or hydraulic means, Fig. 5.

Many other gasifier arrangements can be imagined, but the foregoing appear to have the most desirable features of any so far proposed. In this connection we note two proposals often made. Referring to Fig. 2, these are as follows:

1   Use the direct-bounce spaces as combustion spaces.
2   Use the reverse-bounce spaces as compressor spaces, giving a double-acting compressor.

With both of these changes, the output of a given gasifier should be doubled. As regards (1), it is noted that any misfiring, and this is not unknown in starting, will throw a very heavy load on the synchronizing mechanism and would require this to be of very heavy construction. This slows the gasifier and leads to such an increase of weight that the change becomes useless. There is the further disadvantage of loop scavenging.

A double-acting arrangement for the compressor would be highly desirable. By reducing the piston size it would reduce the internal ring losses and an increase of valve area would be possible, further increasing the efficiency. The machine would be lighter on account of the smaller compressor piston bore. The attainment of these desirable objectives, however, is hampered by the annoying circumstance that if the power-cylinder bore is larger than 37 per cent of the compressor-cylinder bore, approximately, the synchronizing mechanism cannot be attached to the inner side of the compressor piston. No attractive method of circumventing this difficulty which will produce a double-acting machine as light and compact as the single-acting has as yet been proposed.

MAXIMUM OUTPUT AND EFFICIENCY

Highest output and efficiency will be attained by operating the gasifier at the highest possible pressure and temperature levels.

Considering only single-stage compression, the scavenging pressure level and therefore the pressure at the turbine are limited by the temperature rise in the compressor to about 100 psig, with a temperature of approximately 450 F. Higher pressures will lead to carbon deposits on the valves. With water-injection cooling in the compressor, this pressure could be raised somewhat, but this is not an attractive proposal for marine use. Also with pressures above 100 psi there is a steady decrease in the compressor volumetric efficiency so that the gain is not large. The pressure in the power cylinder is limited by the strength of the cylinder walls and also the possible effect on piston rings. In Model B, this pressure is of the order of 2200 psi at 90-psig turbine pressure.

The temperature to the turbine is limited first by the piston rings, and next by the turbine itself. The turbine limits depend on its design and the materials used, but 1300 F is entirely practicable.

The piston speed of the gasifier is limited by the permissible pressure drop in the valves and ports, and the cyclic speed is limited by difficulties of fuel injection and combustion. These limits can be higher than is usual in conventional diesel-engine practice.

The speed of a gasifier is fixed by the pressure relations in the various cylinder spaces and the weight of the pistons and synchronizing mechanism.

By fortuitous circumstance these pressure relations are such that with a piston of a minimum practicable weight the piston speeds are suitable.

BALDWIN-LIMA-HAMILTON GASIFIERS

The first of the four gasifier models constructed by Baldwin-Lima-Hamilton was of the outward-compression type with direct and reverse-bounce cylinders. The objective in constructing this machine was to obtain the maximum experimental versatility. It was desired to obtain experimental operating characteristics, and in particular to investigate the question of the maximum speed and pressure at which such a machine could be operated successfully.

Model A was operated for 1900 intermittent hours over the 20 to 100-psig pressure range, including one continuous run of 100 hr duration at 70 psi and higher. The principal defects were of a structural nature involving welding of water jackets where they were attached to heavy members, possibly at a different temperature level.

We will not discuss this model in detail, since it was followed by the slightly larger Model B of closely similar design. In this model, the welding defects of Model A were corrected, and it also differed from Model A in that the synchronization consisted of a single pair of racks on one side of the machine rather than the double pairs of Model A.

Three cylinders of the Model B design have been constructed and they have been tested both singly and in tandem operation feeding a gas turbine. Two of these units are now at the Naval Engineering Experimental Station at Annapolis, Md. While both Models A and B were intended to serve as prototypes for lightweight gasifiers, they were this only in so far as sizes, pressures, and speeds were concerned. No attempt was made to reduce the weight to a minimum by the reduction of the thickness of parts or the use of lightweight metals, except in the pistons, for it was believed that in the early development it was unwise to add the possibility of structural failures to the many other unknowns.

A longitudinal and cross section of Model B is shown in Figs. 6 and 7. Both Models A and B were designed so that they could be operated at any pressure up to 103 psig and, if reverse-bounce stimulation could be used, for speeds up to 1400 cpm.

STARTING OF OUTWARD-COMPRESSION GASIFIERS

In the heads of the reverse-bounce spaces are located four inside-opening dump valves which connect these spaces to the atmosphere. They are opened by air pressure and are closed by a spring. The starting sequence is as follows: Air pressure at approximately 20 psi is supplied to the reverse-bounce space. This moves the pistons to scavend. A pressure of approximately 150 psi is then supplied to the direct-bounce space. A valve is then rapidly opened which feeds to the dump valves and gives them a rapid opening, and at the same time the air supplied to the reverse bounce and direct bounce is cut off. The pistons are now moved inward to combend where fuel is injected, driving them outward. At the proper position in the stroke the dump-valve air is released and they close. The gasifier is now operating under atmospheric conditions.

For Model A a purely automatic starter with pneumatic elements was constructed. With this the operator had merely to push a single button and the starting cycle was carried out automatically.

For Model B a simpler type of mechanical starter was used in which the operator carried out the operation by rotating a hand wheel which opened the appropriate valves in successive positions. An important factor in proper starting is that the dump valves are closed in such a position that the proper amount of air is trapped in the reverse-bounce space. Four methods have been used to time this dump-valve closure. In the automatic Model A starter the closure was effected when the pressure in the direct-bounce space had dropped to a fixed level. In Model B the closure was based on time. The air suddenly supplied to open the dump valves acted on a small weighted piston and set it in motion. After traveling a fixed distance, ports were uncovered which released the air thus closing the dump valves, Fig. 9.
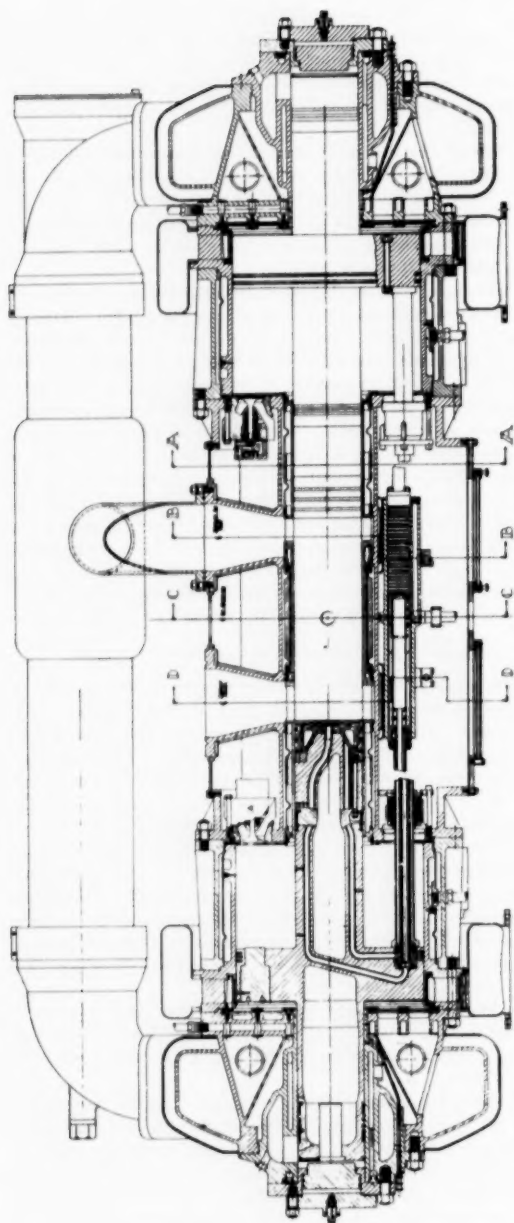
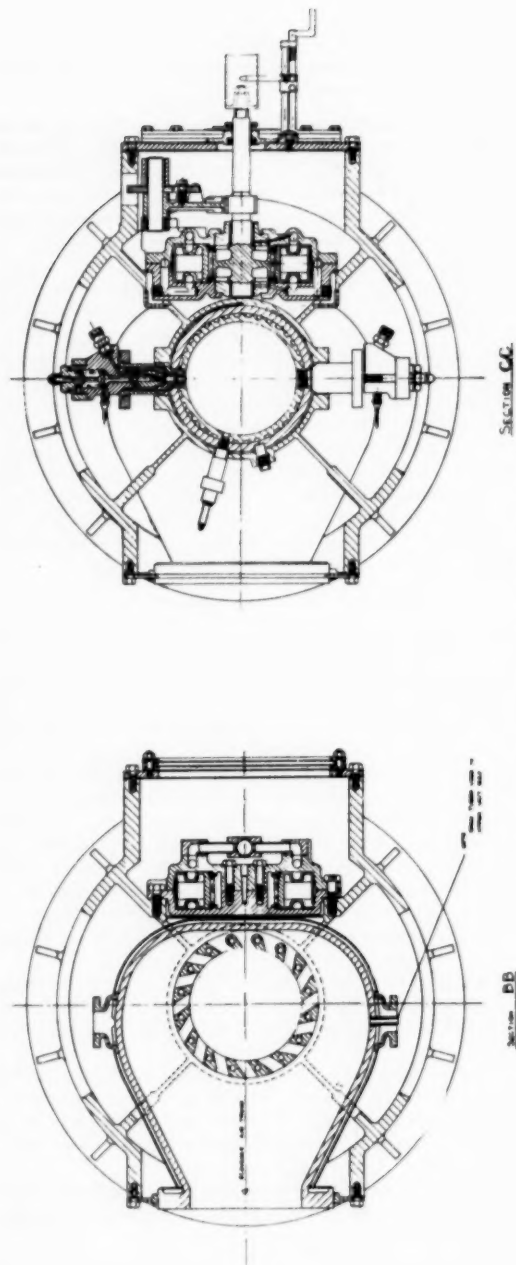Fig. 6 Longitudinal Section of B-L-H Model B Gasifier

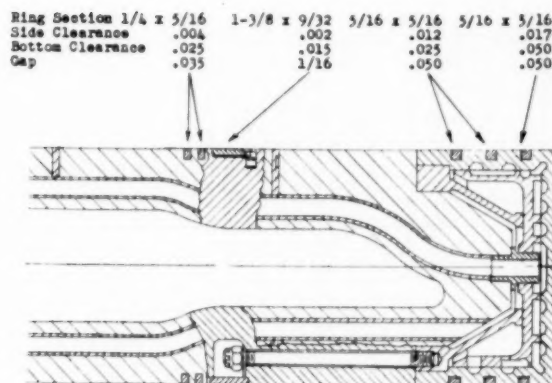Fig. 7 Cross Section of B-L-H Model B Gasifier

Section CC

Section BB

Ring Section	1/4 x 5/16	1-3/8 x 9/32	5/16 x 5/16	5/16 x 5/16
Side Clearance	.004	.002	.012	.017
Bottom Clearance	.025	.015	.025	.050
Gap	.035	1/16	.050	.050

FIG. 8 PISTON CROWN DETAIL OF B-L-H MODEL B GASIFIER

FIG. 9 BALLISTIC STARTER

In Model D the closure is based on piston position. A cam on the synchronizing pinion shaft opens a valve which releases the air in the dump-valve control lines, Fig. 10.

In all of these arrangements the rapidity of dump-valve closure is increased by the use of quick-release valves adopted from railway-brake practice, placed adjacent to the dump valves. More recently with Model D it has been found that starting can be effected by a slow closure of the dump valves, the air being released with a slow bleed, Fig. 11.

Another method of starting, but which was not used with these models, effects a start by releasing suddenly a fixed quantity of compressed air into the direct-bounce spaces.

COMPRESSOR VALVES

It is necessary that the compressor valves be of such strength that failures are unknown and shall be of the highest possible efficiency, since the valve efficiency is an important factor in fixing the over-all efficiency of the gasifier. An extensive test program to fix the design of the compressor inlet and outlet valves was started early in the gasifier-development program and has continued up to the present. Tests have been carried out on a single-cylinder, crank-driven test compressor which permitted measurements of all pertinent quantities, at pressures up to 130 psi and speeds up to 2000 cpm.

The reed-valve design adopted is shown in Fig. 12. In Model B the 213 intake reeds per cylinder end are located around the circumference of the cylinder and the 262 discharge reeds per end are located in the head. The discharge-reed plates are mounted on members with cooled passages in order to reduce carbon deposits.

The test compressor, fitted with reeds in such numbers so as to have closely the characteristics of Models A and B, has the characteristics shown in Fig. 13. At 100 psig pressure and 1100 cpm, adiabatic efficiency is of the order of 80 per cent. This figure has a very important influence on the over-all performance of the gasifier, and it would be very desirable to improve it.

Considerable research has been carried out in this direction, but as yet the diagram, Fig. 13, represents the best which it has been possible to attain. While valve systems with streamlined passages in which the individual valves have better characteristics can be devised, it is not possible to place as many units of such type valves in a given area, or the valves require large clearance volume, with a consequent reduction of volumetric efficiency, and so no gain can be made.

It is possible that with mechanically operated valves some improvement could be made, but these would add such undesirable
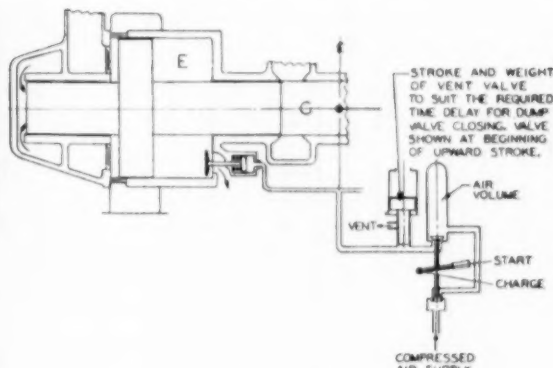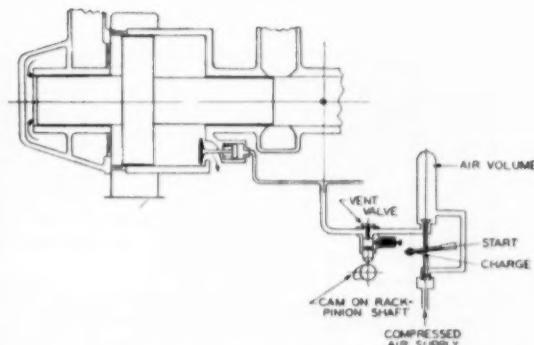
FIG. 10 CAM-RELEASE STARTER
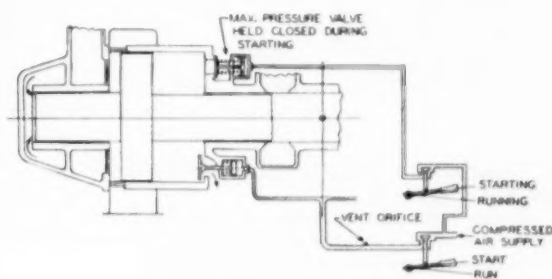
FIG. 11 BLEED-RELEASE STARTER

complications to the gasifier that they have not been considered seriously.

FUEL-INJECTION SYSTEM FOR FREE-PISTON GAS GENERATORS

In deciding upon the type of injection equipment best suited for use on a free-piston gas generator, several factors were considered. The first of these factors was concerned with the fact that the piston velocity decreases rather rapidly at the time fuel injection occurs. This results in a decreasing angular velocity of any cam attached to the unit, making it very difficult to design a cam with either a constant or an increasing rate of plunger rise during the injection period.

The second factor considered was the desirability of being able

SUCTION VALVE REED

DISCHARGE VALVE REED

SECTION THROUGH
SUCTION VALVE

SECTION THROUGH
DISCHARGE VALVE
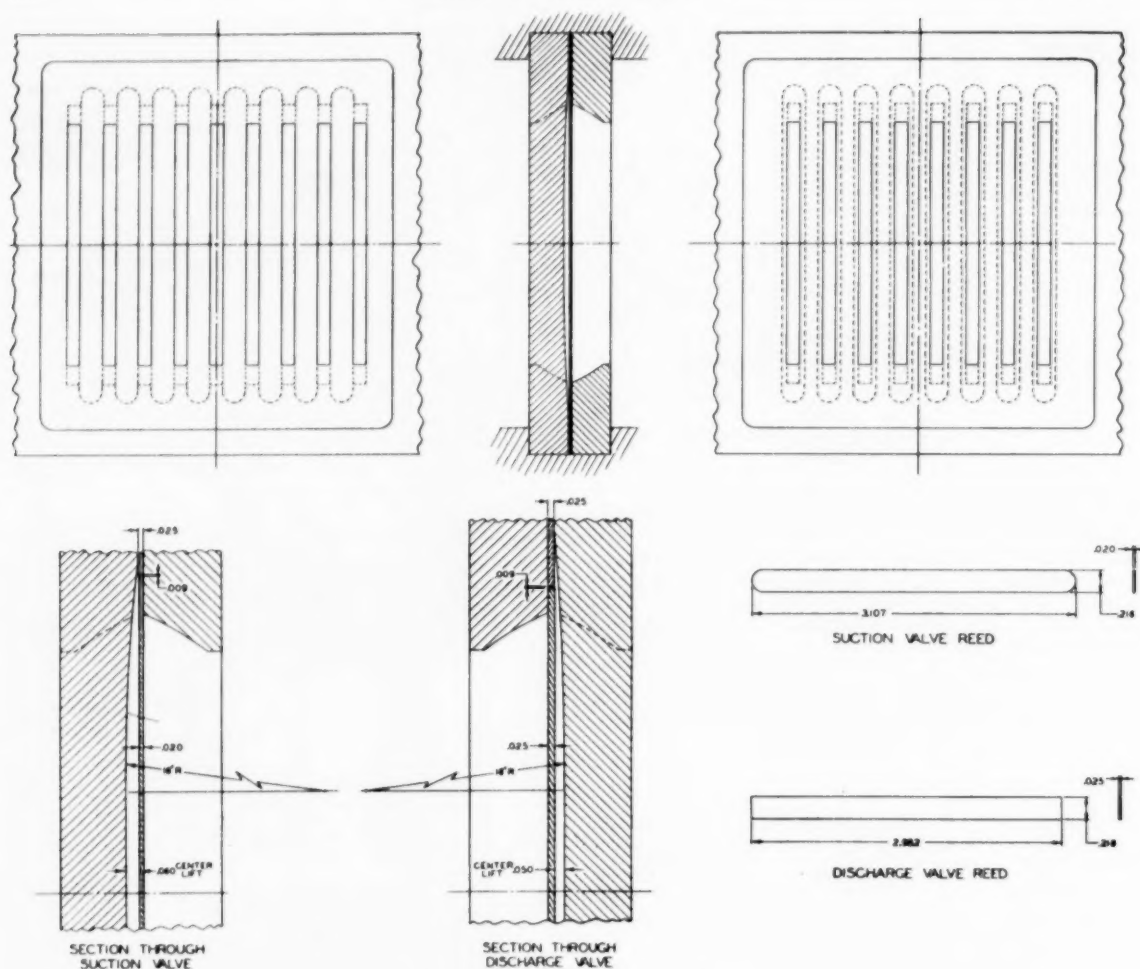
Fig. 12   Compressor Reed-Valve Design

to change injection timing in relation to piston stroke while the unit was in operation.

Another point considered was the accurate metering of the quantity of oil to be injected each stroke, co-ordinated with cyclic speed of the proposed unit.

An examination of the foregoing points leads to the serious consideration of the common rail-injection system. The advantages of this system consisted of injection characteristics that were not in any way tied to the velocity characteristics of the power pistons. It also was felt that, as only the timing function need be actuated mechanically, the loads imposed on synchronizing racks and pinions would be so small that no mechanical difficulty would be encountered.

The one drawback to using a conventional common rail-injection system seemed to be the lack of a positive control of the quantity injected each stroke. The common rail system therefore was modified to give a definite mechanical control of the quantity of fuel injected for each stroke.

Fig. 14 represents a schematic arrangement of the basic system finally used. This system incorporated a motor-driven high-pressure rail pump that supplied fuel at the desired pressures of 6000 to 10,000 psi. The assembly mounted on the free-piston gas

generator was known as a metering unit and had as its function only the timing and the metering of the fuel oil.

In the metering unit, timing plunger 1 was reciprocated by means of a cam attached to the synchronizing pinion shaft. Its angular position in the bore was controlled by rack 2 in the same manner as a conventional pump plunger. As the power pistons moved to scavend, plunger 1 was moved to the left until the annulus 3 of the plunger connected port 4 and port 5, thus permitting the high-pressure oil supplied by the rail pump to passage 6 to flow from port 4 through annulus 3 and out through port 5. This flow of high-pressure oil immediately applies hydraulic pressure to the larger end of differential valve 7, forcing it against its seat and blocking off passage 8. Thus, the oil is permitted to flow through check valve 9 to metering piston 10, equalizing the pressure on the two sides of the piston. As the pressure on the two sides of piston 10 is equal, spring 11 is free to move piston 10 until restrained by adjustable stop 12. At the end of the spring-actuated charging stroke of piston 10, check valve 9 returns to its seat, trapping a fixed quantity of oil. As the power pistons return on their compression stroke, timing plunger 1 is moved to the right until port 5 is closed and no flow of oil can take place until timing-control edge 13 connects port 5 with drain port 14. This
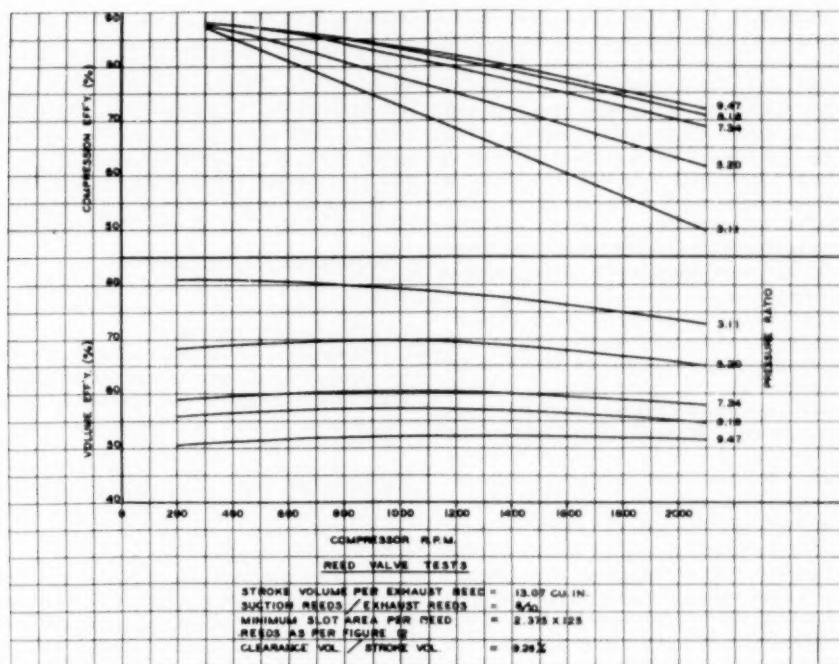
FIG. 13 COMPRESSOR CHARACTERISTICS

results in unloading the hydraulic pressure on differential valve 7, permitting it to open and connect cavity 15 with injection passage 8. The high-pressure oil acting on piston 10 displaces oil through passage 8 and injection tube 16 to injector 17. The movement of piston 10 is limited by the projecting stop contacting the end of the bore, ending the injection stroke. Upon the return stroke of timing plunger 1, the process of recharging pump cavity 15 takes place as described previously.

The quantity of oil injected each stroke is varied by means of adjustable stop 12 controlled by rack 18. For example, in the no-fuel position, stop 12 is moved toward piston 10 until the projecting stop on piston 10 is against the end of the bore, reducing piston travel to zero and thus preventing piston 10 from displacing any oil. For maximum fuel, stop 12 would be adjusted in the opposite direction, permitting piston 10 the maximum stroke and therefore the maximum quantity of fuel to be displaced.

As will be noted, the timing of injection can be controlled readily by changing the angular position of plunger 1 while the unit is in operation and is entirely independent of quantity of fuel being injected. This system also has the advantage of being relatively free from variations in individual injection quantities due to air or gas entrapped in the oil as the actual metering takes place under the full rail pressure, thus greatly compressing any entrapped gas or air and lessening the effect of any given quantity of gas on volumetric displacement.

This type of injection equipment functioned very satisfactorily on the first four units built. Its chief disadvantages were found in the complicated construction which made it very expensive to manufacture, and the necessity of using a large motor-driven rail pump to supply the high-pressure fuel oil. Therefore it was decided to develop another system that would eliminate many of the parts and also the high-pressure rail pump. This second system, as shown in Fig. 15, consists of a pump plunger 1 actuated by means of an eccentric geared to the piston-synchronizing
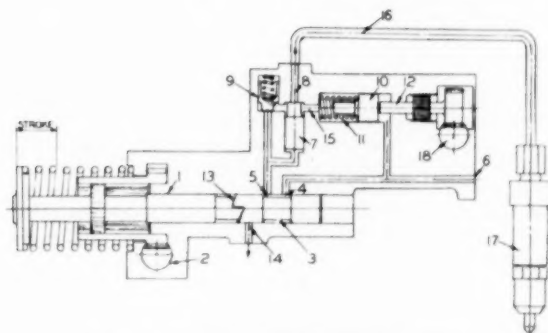
FIG. 14 FUEL-INJECTION SYSTEM, RAIL TYPE
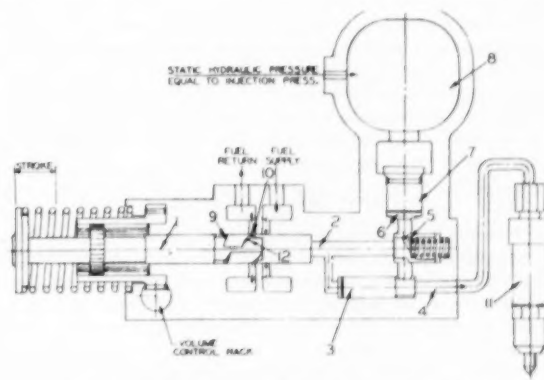
FIG. 15 FUEL-INJECTION SYSTEM, ACCUMULATOR TYPE

pinion. During the early part of the power-piston compression stroke, plunger 1 displaces oil through passage 2, thus applying oil pressure to the large diameter of differential valve 3, forcing it tightly against its seat, and closing off passage 4. Continued movement of plunger 1 displaces oil through passage 2 and through check valve 5 into cavity 6 under plunger 7. The opposite end of plunger 7 is exposed to the hydraulic pressure in accumulator 8. The hydraulic pressure in this accumulator is maintained at a constant level by use of a small rail pump. This rail pump is very small and inexpensive as it has no other function than to maintain pressure in the accumulator at the desired level. The accumulator pressure determines the actual injection pressure during the injection period.

Continued displacement of oil by plunger 1 causes displacement plunger 7 to move against the accumulator pressure, thus enlarging cavity 6 to accommodate the fuel displaced by plunger 1.

As plunger 1 reaches the end of its displacement stroke, helix edge 9 uncovers spill port 10. The uncovering of spill port 10 ends the pumping stroke of the plunger and determines the beginning of actual injection. Injection begins at this point as the uncovering of spill port 10 immediately drops the pressure in passage 2, permitting check valve 5 to seat, and also removes the hydraulic pressure holding differential valve 3 against its seat. Upon the removal of the hydraulic pressure on the large diameter of differential valve 3, it immediately connects passage 4 with cavity 6. The hydraulic pressure in accumulator 8 forces displacement plunger 7 downward, displacing oil through injection passage 4, thence to injector 11. Injection continues until the valve seat on displacement plunger 7 resumes its seat thus ending its stroke and, consequently, the delivery of fuel oil.

It will be readily apparent that this system is much simpler to manufacture and maintain than the earlier type. It has, however, certain limitations as the timing is not adjustable regardless of fuel quantity, as is the case on the previous model. The timing is controlled by helix 9 which is an integral part of the pump plunger as is the metering helix 12. This arrangement permits a fixed timing for each quantity of fuel, but once this time is established by the helix angle it cannot be changed except by designing a new plunger. The entire timing range can be shifted somewhat by changing the tappet adjustment that actuates plunger 1.

This injection unit can be designed to deliver fuel to two or more injectors and maintain equal delivery between each injector. This is accomplished by using a multiplicity of displacement plungers mechanically co-ordinated to maintain equal stroke. This again results in a considerable saving as only one pump plunger and actuating means need be used even when several injectors are required per cylinder.

This injection system as described has given results comparable to that obtained with the system originally used and gives every evidence of developing into a reliable mechanism. It does, however, impose added loading on the power piston-synchronizing mechanism, necessitating the use of larger, more durable parts.

A conventional differential-type fuel injector was used with both types of injection equipment.

PISTON RINGS AND LINERS

Above all other factors the success of the gasifier-turbine system is dependent upon the life of the piston rings and liners of the combustion cylinder. The rings must operate without breakage, and the wear of the rings and liners must be sufficiently small so as to give a reasonable life to these parts before replacement. It is evident that as the pressure and temperature in the combustion cylinder of a gasifier are increased, these problems become of greater and greater difficulty and there must exist a limit above which it is not worth while to operate. In constructing Model A, it was intended to determine this limit and, if possible, establish relations between the cycle pressure and temperature and the ring and liner life. In the test program of Models A and B many types of rings of varying dimensions and materials have been tested, but it has not been possible as yet to fix such an upper limit or to establish curves of ring and liner wear versus pressure.

Considering first the causes of ring breakage, many hypotheses can be advanced. We list some of the possibilities:

1 Maximum pressure excessive.
2 Maximum rate of pressure rise excessive.
3 Insufficient gas pressure behind rings.
4 Port-bridging stresses.
5 Irregularities of cylinder walls.
6 Carbon formations on combustion cylinder walls at combend and carbon deposits on ring grooves.
7 Weakening from excessive temperature.
8 Deficiencies of lubrication.

It cannot be stated with certainty to what degree any one of the foregoing factors is responsible for ring breakage, and breakages may be caused by several of these factors operating together or by other causes unlisted and unknown.

We attach particular importance to hypotheses (3) and (8). Considering (3), which is related to (2), it is observed that as the pressure in the combustion space rises, gas flows into the space behind the rings. If the rings fit their grooves too closely, the pressure behind the rings will be appreciably lower than that in the combustion space. The rings may then be driven back from the cylinder wall with an escape of gas around them, and the erratic bending thus caused will break them. To avoid this there should be an adequate side clearance of the fire rings in their grooves, and the space behind them should be reduced to a minimum.

Considering (8) it is observed that on the inward stroke of the pistons, gas pressure, friction, and inertia all combine to hold the rings against the bottoms of their grooves. On the reverse outward stroke, gas pressure tries to hold them against the bottom of the groove while friction gives an opposing force. With well-lubricated walls, the gas-pressure effect is the larger and the rings remain seated on the bottoms of the grooves. But if there is a failure of lubrication, a ring may freeze momentarily to the wall so that it now bears against the top of the groove. If there is good lubrication around part of the circumference and a failure in the other parts, part of the ring will try to bear on one face and part on the other. Heavy bending stresses will then be thrown into the ring.

In order to retain lubrication on the cylinder walls, it is desirable to keep both the cylinder walls and the piston rings at the lowest possible temperature.

The liner and piston construction have been designed with this in mind. The liner is of steel porous chrome-plated and of double-wall construction, so arranged that the water passages lie close to the inner surface. The steel piston crown, Fig. 8, likewise consists of two parts, a heavy inner member for strength, and a thin outer member, copper-brazed to this, in which cooling passages are machined close to the outer surface. The cooling oil to the pistons is led in and out through the hollow rack rods. These arrangements for holding the cylinder walls and rings at a minimum temperature minimize ring and liner wear. The piston body is of aluminum and is one piece with the direct-bounce and compressor pistons.

The lubrication of the combustion cylinder is by independently driven lubricators with outlet below; i.e., remote from the combustion space and in line with the port bridges.

Control of the Bounce Spaces

Controls are needed to maintain the proper pressure level of both the direct and reverse-bounce spaces. With a fixed reverse-bounce pressure, combend is controlled by the direct-bounce pressure. As the pressure level of both spaces increases, the cyclic speed and therefore the output of the gasifier are increased. It was originally intended to utilize this feature to obtain maximum output, although it was anticipated that this increased power would be obtained at the expense of a slightly decreased efficiency.

Test results from Model A showing the effect of stimulation are given in Fig. 16. It will be noted that there is very little change in thermal efficiency with stimulation, but this is because stimulation is accompanied by a rise of temperature. This increased temperature can be ascribed to the following causes:

With the increased speed the combustion efficiency is reduced.

The higher bounce pressures result in higher thermal losses, principally from piston-ring friction.

With the higher speeds the compressor efficiency is reduced.

In spite of these losses a moderate degree of stimulation appears to offer an advantage at a temperature of 1200 F or higher. The maximum horsepower output is reached, not with the maximum pressure, but with a somewhat lower pressure and a stimulated speed. This lower pressure-stimulated operation entails only a negligible loss of efficiency compared to the nonstimulated, higher pressure operation.

From these curves it may be inferred that for every specified exhaust temperature to the turbine, there exists a pressure and speed which will give a maximum output, and it is evident that this optimum relationship occurs at higher speeds and lower pressures than those at which the gasifier has been operated. To obtain this advantage further lightening of the piston would be desirable but is very difficult.

MODEL "A" PERFORMANCE
HP AND EFFICIENCIES NOT CORRECTED
FOR AUXILIARIES. ROOM TEMP. = 85°F
BAROMETER = 29.5" HG.

ALL PRESSURES IN LBS/IN² GAUGE
ALL TEMPERATURES IN °F
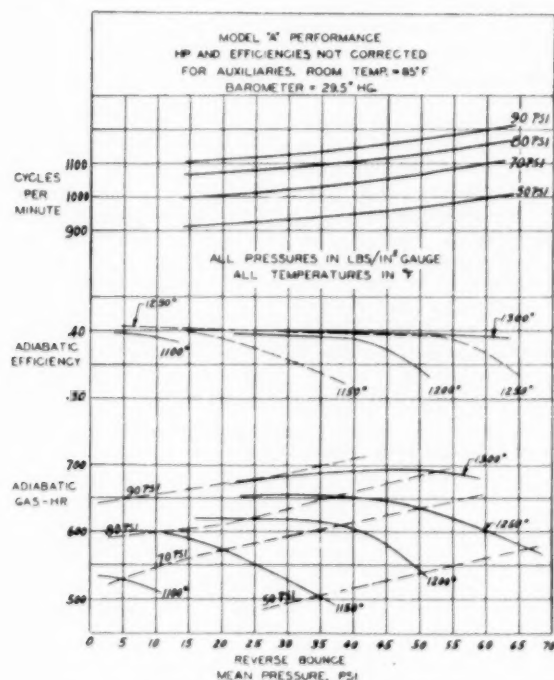
FIG. 16 TEST RESULTS, B-L-H MODEL A GASIFIER

As presently operated, the Model B reverse-bounce spaces are connected to atmosphere through a set of discharge-reed valves. This space then operates at a pressure below atmospheric, as the leakage into the reverse-bounce space which is discharged to atmosphere is very small. With the reverse-bounce pressure fixed, a feed valve holds the direct-bounce pressure to the proper level. This valve can be hand-controlled or operated on a balance so that the direct bounce bears a definite relationship to the scavenge pressure. In Models A and B, the bounce air is supplied by an independent source. The consumption at 90 lb full load is of the order of 18 cfm of free air, approximately 1 per cent of the output of the gasifier.

The gasifier can be made self-feeding by linking a small compressor piston to the synchronizer rack, or by so fixing the ratio of the bounce-cylinder diameter to the compressor-cylinder diameter and the pressure ratio in the bounce cylinder itself, that the minimum bounce-cylinder pressure is lower than the scavenge pressure under all conditions. It will still be necessary, however, to have an independent air supply for starting.

Operation With Multiple Units

Two of the Model B gasifiers have been operated feeding a turbine. These tests were made largely to gain experience with the operation of gasifiers connected to a turbine. The small size of the turbine used made it an inefficient unit.

Gasifiers can be connected to a turbine either by a single main gas line or by independent gas lines, each of which supplies its own nozzle bank in the turbine. The latter method was used. Each turbine was connected to a nozzle bank in the turbine by a pipe 8 in. diam and approximately 7 ft long. Bellows-expansion joints were placed in these pipes as well as a shutoff valve and a by-pass to atmosphere.

With this arrangement it was found that the output and efficiency of the gasifiers are unchanged whether they are connected to a turbine or an orifice.

No difficulty of any kind was experienced from the presence of pressure waves in the piping. With one unit operating, the other could be started if the delivery pressure of the first unit did not exceed 30 psi. Above this pressure it was necessary to open the by-pass of the second unit in order to start it, but it was not necessary to close the main line valve. Also, it was possible to make simultaneous starts.

With a synchronizing mechanism it is possible to make two or more gasifiers operate in step. There are several methods of accomplishing this. The mechanism used consisted of a piston of 2-in. bore by 2-in. stroke driving a crank and connecting rod, a small flywheel, and a rotary valve. This was open for one-half revolution and was closed for the other half. The space above the piston was connected by pipe to the reverse-bounce space of one unit, and the rotary valve was placed in the feed line to the direct-bounce space of the other unit. If this reciprocating pulse motor, which contains no valves of any kind, is set in rotation with a frequency equal to or higher than that of the gasifier operating it, it will continue to run at the speed of this gasifier. If the loads on the two gasifiers are not too far from equality, the second gasifier will then operate in synchronism with the first. While the synchronized gasifiers give a better sounding plant, the synchronization has no effect on either its output or efficiency.

In addition to Models A and B, two other gasifiers, one of outward-compression type with inverted direct bounce and another of inward-compression type have been constructed. Both of these units are of the approximate dimensions of Model B but are much lighter in construction. They have received only preliminary tests and no details are available.

Discussion

A. K. ANTONSEN[3] AND T. L. SHERMAN.[4] This paper is an excellent contribution to the understanding of this little used type of prime mover.

The authors state a machine built in accordance with Fig. 1 is not attractive because of its large size. This is controversial because in comparing Fig. 1 with Fig. 6, a late model, it would seem that if one type tends to give machines of large diameter then the other is handicapped by greater over-all length.

It has been stated frequently that multiple gasifiers have an advantage over conventional reciprocating engines in that each can operate at full-load efficiency throughout the combined load range. For example, a group of four units would have all operating at from 75 per cent to full load. Three units would be in operation at 50 to 75 per cent, two units at 25 to 50 per cent, with only one operating at lighter loads. At load changes of any magnitude, gasifiers should stop and start as required, thereby demanding considerable excellence and reliability in what is admitted to be a quite involved problem.

For such an arrangement, it would seem that starting from combend offers best possibilities because cylinder-charge conditions are more favorable for the first combustion. How are starting conditions in a Baldwin-Lima-Hamilton gasifier taken care of when units in multiple arrangement are started and stopped during load changes?

The problems involved in the exhaust system of a multiple-unit installation are also considerable. A unit cannot be left open for long intervals because of the liability of being seriously fouled, particularly when the outlet is vertically upward. Has any work been done in this direction?

One of the real weaknesses in the free-piston gasifier is the liability of damage to rings and pistons because of high rates of pressure rise and magnitude of peak pressures. The modern diesel finds this a distinct problem, but it is much accentuated in the gasifier.

PAUL SHIRLEY.[5] The writer is honored in being invited to discuss this well-organized and presented paper upon a subject that is very complex and comparatively new. Having had a part in this program at its start in 1943, and for several years thereafter, he would like to make the following comments.

As the authors state, the highest output and efficiencies will be obtained by operating the gasifiers at the highest possible pressure and temperature levels. The optimum for these conditions will be realized by designing for streamlining for mass flow and holding shock losses in the system to a minimum. For any one operating pressure the lowest operating temperature will produce the lowest fuel consumption and highest efficiency for the power plant.

[3] Supervisor, Research and Development Department, Fairbanks, Morse & Company, Beloit, Wis. Mem. ASME.
[4] Consulting Engineer, Research and Development Department, Fairbanks, Morse & Company.
[5] Nordberg Manufacturing Company, Milwaukee, Wis.

The size and number of gasifiers for a certain power output can be reduced by the use of supercharging or boosting the air pressure and mass flow of air to the gasifier-suction inlet and, with the use of moderate intercooling, a slight increase of efficiency may be attained with the system operating at a higher pressure level and with no increase in operating temperatures. Comparatively low boosting pressures will permit a considerable gain in power output.

Synchronization of a multiplicity of gasifiers to one or more turbines simplifies the suction ducting to the gasifiers and the piping between the gasifiers and the turbine and reduces interferences between gasifiers to a minimum in regard to scavenging, air mass flow and gas flow to the turbine. The arrangement amounts to much the same as is encountered in high-pressure charging of turbocharged engines of the two-cycle type.

The future of this type of power plant depends upon its ultimate dependability, availability, and how it will fit into our economic picture.

C. F. TAYLOR.[6] In supercharged diesel-engine practice to date, it apparently has not been found possible to secure satisfactory reliability and durability with inlet pressures greater than about 2 atm abs, with the fuel-air ratios required to yield exhaust temperatures in the range indicated in the paper. Apparently, these limitations are set by cylinder, piston, and piston-ring characteristics rather than by the crankshaft-connecting-rod system. In view of this experience, it seems optimistic to hope that the free-piston diesel cylinder can be made durable and reliable at inlet pressures up to 6 or 7 atm, as indicated in Fig. 16. Would the authors care to comment on this question?

AUTHORS' CLOSURE

The use of a direct-bounce cylinder does not necessarily involve greater over-all length. This is indicated by Fig. 3 which depicts an even later model than Fig. 6.

Messrs. Antonsen and Sherman, and Professor Taylor, note that the load limits of a gasifier depend largely upon the performance of piston rings and cylinder liners. We have ourselves emphasized this fact in the text and note that a load of, say, 70 psi or more is required for performance which is competitive with that of present diesel engines. We disagree with the two atmosphere absolute limit noted by Professor Taylor. The most recent model has already had a ring life in excess of 500 hours at six atmospheres absolute, and is expected to demonstrate further improvement. Supercharging pressures for diesels are continually rising and may ultimately reach values now being used in gasifiers. It is hardly safe to say what the limits are for either free piston machinery or diesels.

In the case of the gasifier, as in the case of any worthwhile development, certain problems must be met and overcome. Many have already been brought to satisfactory conclusions, and experience indicates that others also can be solved.

[6] Professor of Automotive Engineering, Massachusetts Institute of Technology, Cambridge, Mass.

Experimental Investigations of Propagating Stall in Axial-Flow Compressors

By T. IURA[1] AND W. D. RANNIE,[2] PASADENA, CALIF.

Measurements of velocity fluctuations in stalled operation of an axial-flow compressor have demonstrated that stalling occurs for the most part in well-defined regions over the compressor annulus. These stalled regions rotate without changing shape in the direction of the blade rotation with a speed proportional to, but of smaller magnitude than, the rotor speed. Two principal types of propagating stall were observed, one with the stalled region or regions extending over part of the blade height, the other with a single stalled region over the full blade height.

Nomenclature

The following nomenclature is used in the paper:

A = compressor annulus area
C_a = axial velocity component
$\bar{C}_a$ = axial velocity component averaged over the annulus
L = cycle length of velocity fluctuation
N_p = number of propagating stall regions
V = instantaneous velocity normal to radius of compressor
$\bar{V}$ = mean velocity normal to radius of compressor
c = airfoil chord length
p = static pressure
r, R = radius of a particular stream tube
r_0, R_0 = tip radius
s = cascade pitch
u_0 = velocity of rotor-blade tip
Δ = change of a quantity
ρ = fluid density
$\bar{\phi}$ = average flow coefficient, $\bar{C}_a/u_0$
ω = rotor angular velocity
$\bar{\psi}$ = average power coefficient, shaft power/$1/2 \rho A\, \bar{C}_a u_0^2$

Introduction

Observations of stalling in axial-flow compressors have demonstrated that the regions of separated or reversed flow are not axially symmetric but occur in more or less well-defined patches around the circumference of the compressor annulus. The regions of retarded flow remain approximately the same shape and are propagated circumferentially with a velocity proportional to the rotor speed. This phenomenon, where the total flow rate through the annulus does not vary with time, will be called propagating stall. Surging will be defined as a phenomenon where the net flow through the entire annulus fluctuates with time. It is possible that surging involves an oscillation from one propagating-stall pattern to another, the violence of the surge being determined by the natural frequency of the ducting or reservoirs in the compressor circuit. The propagating-stall phenomena

have been mentioned by other investigators although, to the authors' knowledge, the only paper reporting measurements is one given recently by Huppert and Benser.[3]

The investigations described here are concerned primarily with stall propagation; no distinct surge was observed. Probably more or less well-defined stall-propagation phenomena occur in all axial-flow compressors as they are throttled beyond the peak pressure. Similar phenomena have been observed in centrifugal impellers and even in straight cascades by H. Emmons. Pressure or velocity measurements with instruments of low response time give no indication of the propagating stall. Hot-wire anemometers or high-frequency pressure pickups are required for detection of the phenomena.

The propagating stall has been explained qualitatively as a successive unstalling and stalling of blades in a cascade. The stalled-blade channels offer a high resistance to flow through the cascade and the approaching flow tends to be diverted to each side of the stalled region as shown in Fig. 1. The incidence
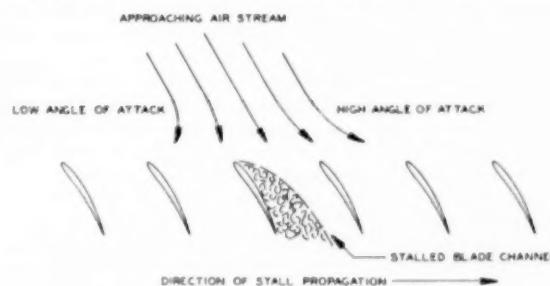
FIG. 1 STALL PROPAGATION IN A CASCADE
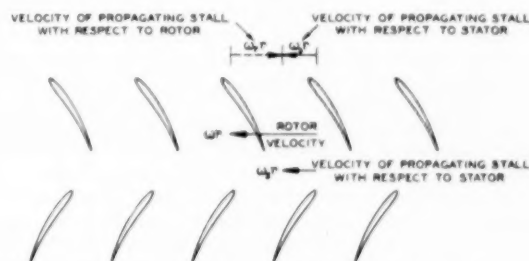
FIG. 2 STALL PROPAGATION IN COMPRESSOR-BLADE ROWS

angle is reduced to the left of the stalled blades and increased to the right. This tends to stall the next blade on the right and unstall the last stalled blade on the left. The stalled region hence moves to the right. Apparently, as the average flow angle of a cascade approaches stalling incidence, the preferred flow pattern is one with groups of blades severely stalled alternating with

[3] "Some Stall and Surge Phenomena in Axial-Flow Compressors," by M. C. Huppert and W. A. Benser, preprint of paper presented at Institute of Aeronautical Sciences' 21st Annual Meeting, New York, N. Y., January, 1953.

groups of unstalled blades rather than a uniform stalling of all blades. The velocity of propagation of the stalled regions is determined by some characteristic time, the origin of which is not understood definitely at present. For a moving cascade, the stall-propagation speed relative to a fixed system is the difference between the cascade speed and the propagation speed in the moving cascade. All propagating-stall patterns observed moved relative to the compressor casing in the direction of the rotor with a speed less than the rotor speed, Fig. 2.

Test Equipment

The compressor used in the stall-propagation measurements was one designed to simulate the internal-flow patterns commonly employed in modern high-performance turbomachines. The blade-tip diameter was 36 in. and the hub ratio 0.6. Two types of blades were available, three stages of "free-vortex" blading and one stage of "solid-body" blading. Both sets were designed for a power coefficient $\bar{\psi} = 0.40$ at a flow coefficient $\bar{\phi} = 0.45$. The design power coefficient actually was attained at $\bar{\phi} = 0.43$ because of the influence of wall boundary layers. The blade solidity ranged from a maximum of 1.15 at the rotor roots to a minimum of 0.69 for the free-vortex rotor tip. The blading is described in detail in another paper.[4] There were 30 rotor blades and 32 stator blades in respective rows. The axial spacing between center lines of adjacent blade rows was 2.875 in. Most of the measurements were made at 750 rpm ($u_9 = 118$ fps); hence compressibility effects were negligible, and the blades could be considered rigid in so far as aerodynamic forces were concerned.

The entrance duct had a volume of 51 cu ft and the exit duct (between the compressor and the throttle) a volume of about 46 cu ft. The calculated natural frequencies of the system considered as a Helmholtz resonator are above 22 cycles per sec (cps), except possibly one mode involving torsion of the drive shaft, estimated as 18 cps. All propagating-stall patterns, with one exception, had frequencies lower than the foregoing.

For velocity-fluctuation measurements, radial hot-wire anemometers utilizing platinum wires of 0.00024 in. diam and $^3/_{16}$ in. length were employed. In the majority of the tests, a constant current of 50 milliamp from a 90-volt B battery was used. The hot wires were calibrated in an air stream of known velocity before and after each run in which the velocity-fluctuation magnitudes were measured.[5] A schematic diagram of the apparatus is shown in Fig. 3. The hot-wire amplifier had a flat frequency response up to about 1000 cps. For phase measurements, two identical circuits were used so that simultaneous readings with two separate hot-wire probes could be made. The two circuits were checked for identity in response time so that phase measurements for the determination of the number of stalled regions could be made with two probes in different circumferential positions.

For the preliminary study of the stall propagation, it was found convenient to use a direct-inking-type oscillograph so chart records were immediately available. Although the frequency response of the oscillograph unit was flat only in the range from 0.5 to 100 cps, this was felt adequate for the investigations of the observed pulsation frequencies ranging from 1.5 to 15 cps. The over-all calibration of the amplifier system was found by introducing known resistance changes (by means of a vibrating contactor) in the hot-wire line and correlating this with the square-wave signals produced on the oscillograph. This, together with the hot-wire velocity response, provided the necessary informa-

[4] "Investigations of Axial-Flow Compressors," by J. T. Bowen, R. H. Sabersky, and W. D. Rannie, Trans. ASME, vol. 73, 1951, pp. 1–15.

[5] "Review of Hot-Wire Anemometry," by J. B. Willis, Australian Council for Aeronautics Report ACA-19, October, 1945.
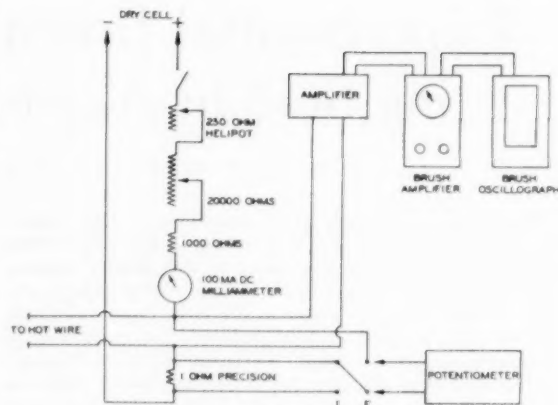
Fig. 3   Schematic Diagram of Hot-Wire Apparatus

tion to interpret the oscillograph signals in terms of velocity fluctuations. Because of the low-frequency response of the oscillograph system, it was not possible to record individual rotor wakes.

Compressor Stall With Three-Stage Free-Vortex Blading

The experimental results obtained from the compressor with three stages of free-vortex blading will be discussed first, because this configuration produced the most clear-cut examples of the various types of stall propagation observed. The regions of stall for this configuration are shown in Fig. 4 which is a plot of torque and exit-duct wall pressure as functions of flow coefficient at a compressor rotative speed of 750 rpm. It will be noted that the first signs of stall on closing the throttle occur in the form designated as "partial stall" at a flow coefficient slightly lower than the maximum torque and exit-duct pressure points. The region of partial stall extended to a flow coefficient slightly above $\bar{\phi} = 0.30$, where the exit-duct wall pressure dropped off suddenly, and the compressor went into a regime designated as "full stall." The exit-duct wall pressure did not change appreciably in the full stall region. On closing the throttle, the compressor went into both partial and full stall at lower flow coefficients than when the flow rate was being increased at constant rotor speed. There was a definite hysteresis loop in the transitions between partial and full stalls. In terms of audible noise, partial stall was detectable by a rumbling noise that was slightly louder than the normal operating noise, and full stall was perceptible by a rumbling sound of very distinct periodicity.

Partial Stall

When the term partial stall is used, it is in the sense that only a part of the radial extent of the blade is experiencing stall. Hot-wire-anemometer measurements showed periodic velocity fluctuations only in the region of the blades extending from the hub to about mid-radius. (Partial stall in the tip region was observed with other compressor-blade configurations, as will be discussed later.) Initially, as the flow was throttled (at 750 rpm or 12.5 revolutions per sec), the hub-region disturbance had an average frequency of about 4.7 cps. This disturbance extended to about mid-radius, and further throttling did not cause any appreciable change in the magnitudes of the velocity fluctuations. However, with throttling, the observed frequency increased to about 9.4 cps and, on further throttling, became 14.1 cps.

Figs. 5 (a and b) show examples of the chart data obtained with the oscillograph. The magnitudes of the instantaneous velocities, as measured, show strongly retarded flow regions that
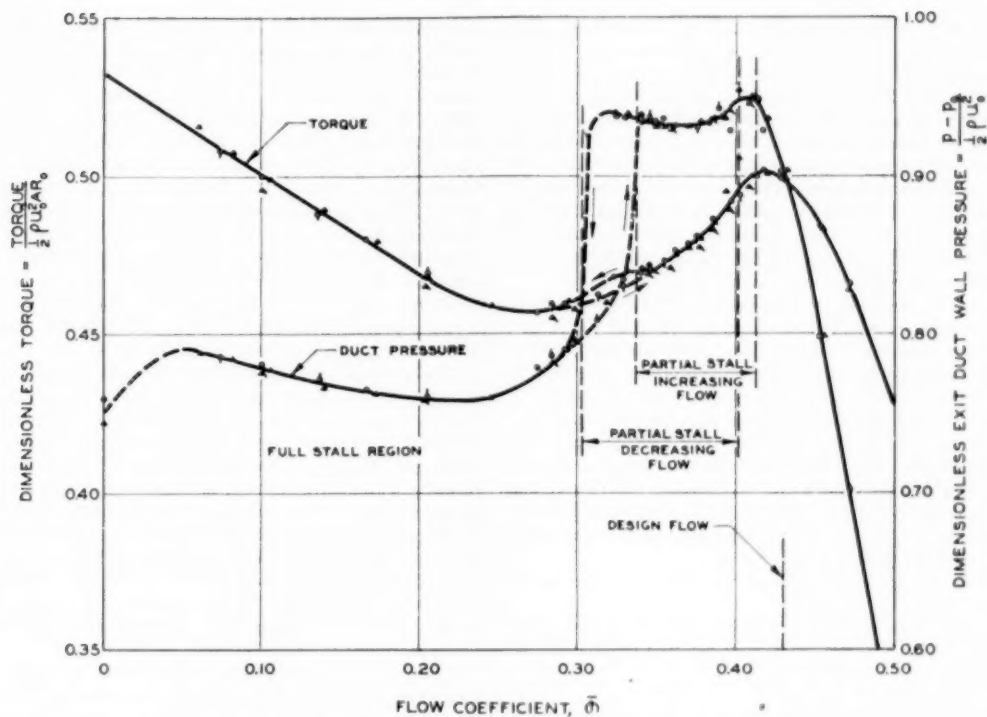
FIG. 4 VARIATION OF TORQUE AND EXIT-DUCT WALL PRESSURE WITH FLOW COEFFICIENT
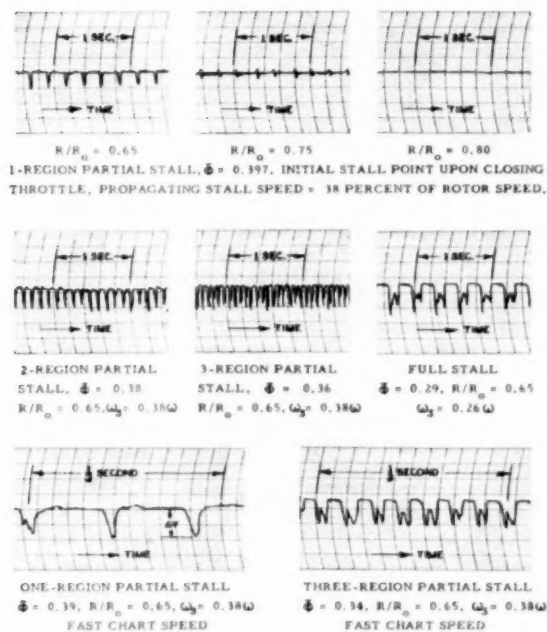(Three-stage free-vortex blading; 750 rpm.)

R/R₀ = 0.65   R/R₀ = 0.75   R/R₀ = 0.80

1-REGION PARTIAL STALL, ϕ = 0.397. INITIAL STALL POINT UPON CLOSING
THROTTLE, PROPAGATING STALL SPEED = 38 PERCENT OF ROTOR SPEED.

2-REGION PARTIAL   3-REGION PARTIAL   FULL STALL
STALL, ϕ = 0.30   STALL, ϕ = 0.36 ϕ = 0.29, R/R₀ = 0.65
R/R₀ = 0.65, ω_s = 0.38ω R/R₀ = 0.65, ω_s = 0.38ω ω_s = 0.26ω

ONE-REGION PARTIAL STALL   THREE-REGION PARTIAL STALL
ϕ = 0.39, R/R₀ = 0.65, ω_s = 0.38ω ϕ = 0.34, R/R₀ = 0.65, ω_s = 0.38ω
FAST CHART SPEED   FAST CHART SPEED

FIG. 5(a) OSCILLOGRAPH RECORDS OF PROPAGATING STALL
(Three-stage free-vortex blading; 750 rpm; data behind third rotor row.)

R/R₀ = 0.61   R/R₀ = 0.70   R/R₀ = 0.80

R/R₀ = 0.90   R/R₀ = 0.95   R/R₀ = 0.98

VELOCITY FLUCTUATIONS AT VARIOUS RADII. ϕ = 0.241, BEHIND 3rd ROTOR
PROPAGATING STALL SPEED = 28 PERCENT OF ROTOR SPEED

BEHIND SECOND ROTOR ROW AT MID-BLADE HEIGHT
ϕ = 0.29, ω_s = 0.26ω, CHART SPEED = 125 MM/SEC.

FIG. 5(b) OSCILLOGRAPH RECORDS OF PROPAGATING STALL
(Full stall; three-stage free-vortex blading; 750 rpm.)

can result only from flow separation (stalling) on the blades. The mean velocity $\bar{V}$ is the average of the instantaneous velocities with respect to time over a complete cycle as determined by the mean resistance of the hot wire. For velocity fluctuations large compared with the mean velocity, this procedure introduces some error. The portions of the velocity traces above the chart center line, in general, correspond to unretarded flow while those below correspond to retarded flow. The amplitude of the velocity fluctuation ΔV was taken as the difference of the minimum velocities in the unretarded and retarded flow regions. The radial distribution of the peak velocity fluctuation amplitude ratios, $\Delta V/\bar{V}$, is shown in Fig. 6.

Two hot-wire anemometers were inserted to the same radii in a plane normal to the compressor axis as shown in Fig. 7 and their angular separation varied. The phase difference of the velocity patterns as measured with the two probes was equal to their angular separation for the fluctuations with frequency 4.7 cps, equal to twice the angular separation for the fluctuations with frequency 9.4 cps and three times the angular separation at 14.1 cps, Fig. 8. The probe displaced in the direction of rotation lagged behind the other probe in all cases. It is clear from these observations that the three frequencies represent, respectively, one, two, and three propagating-stall regions uniformly spaced around the circumference, Fig. 9.

Since the rotor speed was 12.5 rps in these tests, the partial
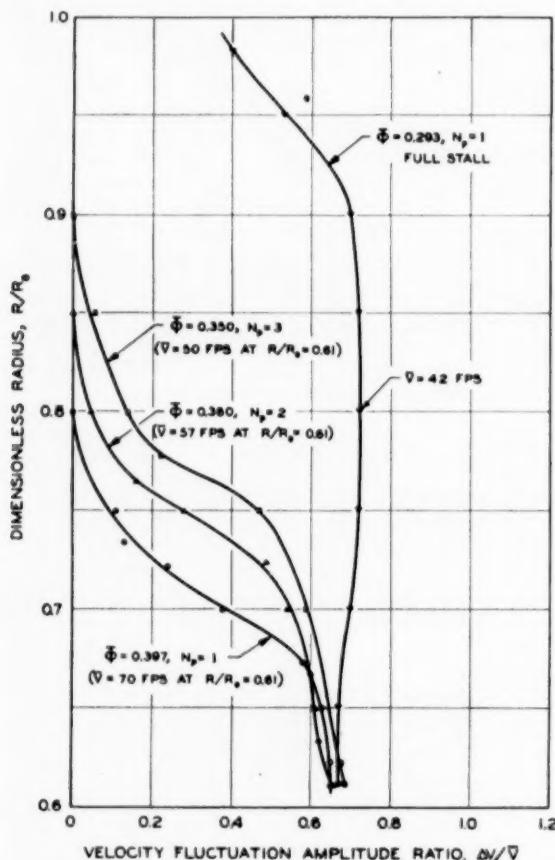
stall regions rotated with 38 per cent of the rotor speed in the direction of the rotor motion. Each of the three stalled patterns mentioned was stable in a narrow throttle range. The single pattern occurred in a very narrow flow-coefficient range of about $0.40 > \bar{\phi} > 0.39$ for closing throttle. The maximum width of the single region of retarded flow was about 17 per cent of the circumference, which corresponds to approximately 5 rotor-blade-channel widths. At a flow coefficient $\bar{\phi} \cong 0.39$ the single stalled region became unstable and split into two regions which oscillated in their relative positions, but with further slight throttling, the two regions separated and finally took up stable positions 180 deg apart. In this condition, the two regions were of nearly equal size and had the same maximum width, about 5 rotor-blade-channel widths. They did not differ significantly from the single region at the higher flow rate.

The two-region partial stall was the stable pattern for a range of approximately $0.39 > \bar{\phi} > 0.37$. At $\bar{\phi} \cong 0.37$ the two-region pattern became unstable, a further splitting and rearrangement occurred, and on very slight throttling, a three-region pattern of retarded flow became the stable pattern. The maximum width of each of the three regions, which were 120 deg apart, corresponded to about 4 rotor-blade-channel widths, Fig. 9. The radial extent of each of the regions increased slightly with closing throttle; however, the maximum velocity-fluctuation ratio at the hub remained the same ($\Delta V/V \cong 0.7$) for all three types. On closing the throttle to a flow coefficient $\bar{\phi} \cong 0.30$ the three-region pattern became unstable and full stall (described later) appeared.

When the throttle was opened from the full-stall point, the foregoing patterns appeared in reverse order, although the limits of ranges of succeeding patterns occurred at larger flow rates than

FIG. 6   RADIAL DISTRIBUTION OF VELOCITY FLUCTUATION-AMPLITUDE RATIOS

(Three-stage free-vortex blading; behind third rotor row; 750 rpm.)
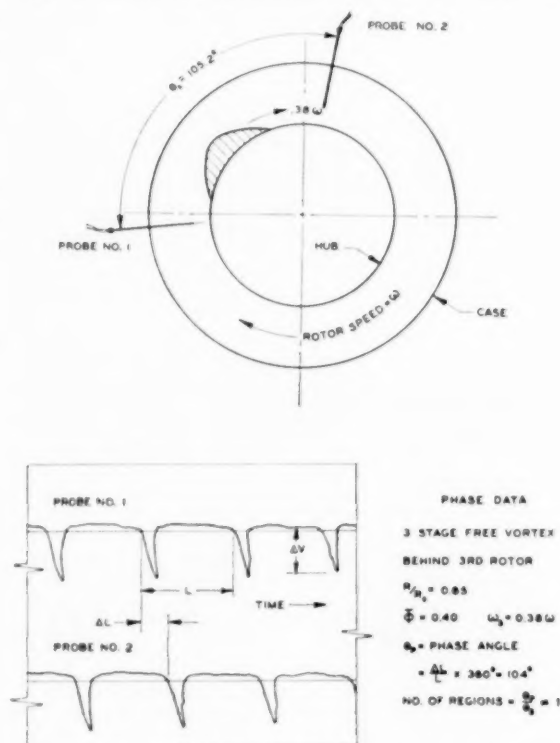
FIG. 7   PHASE MEASUREMENT FOR DETERMINATION OF NUMBER OF STALLED REGIONS
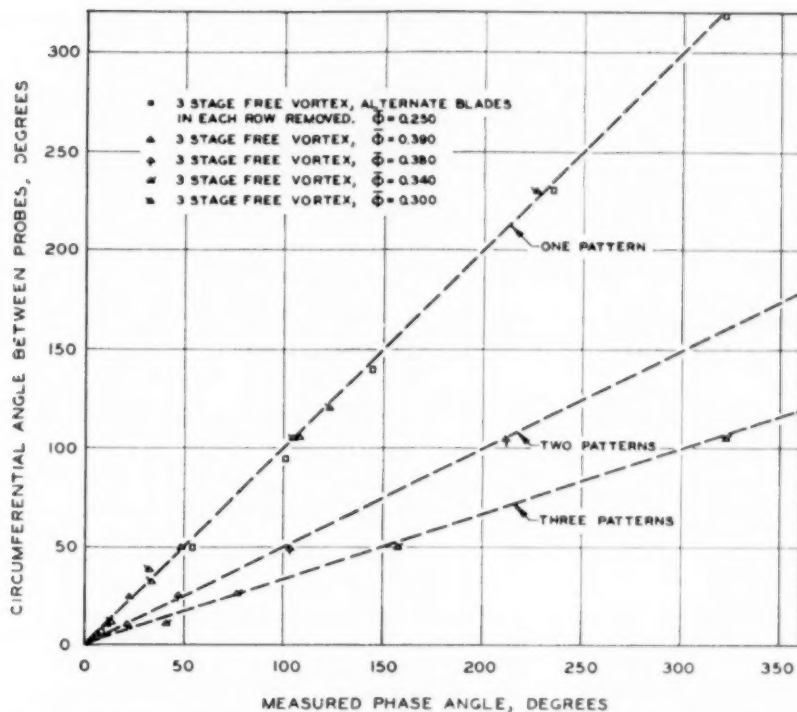
FIG. 8   RESULTS OF HOT-WIRE PHASE-ANGLE MEASUREMENTS FOR DETERMINATION OF NUMBER OF STALLED REGIONS
(Three-stage free-vortex blading.)

on closing throttle.   The three-region pattern appeared at $\bar{\phi} \cong$ 0.34 and the one-region pattern disappeared at $\bar{\phi} \cong 0.41$.   In one instance, four symmetrical propagating-stall regions appeared on opening the throttle from the full stall.   Although well-defined, the pattern was soon replaced by the three-region pattern without touching the throttle.

The blades tended to stall near the hub first as the throttle was closed.   Apparently an alternating pattern of stall is more stable than an axially symmetric stall.   The strong retardation of the flow in the stalled region causes an increased flow rate and hence an unstalling tendency over the remainder of the annulus. It might be thought that further throttling would simply increase the size of the stalled region.   However, the circumferential pressure distribution behind the stalled blade row must be controlled largely by the unstalled axially symmetric flow beyond the mid-radius, and this one would expect to be nearly uniform around the circumference.

Unrestricted growth of the single partial-stalled region would lead to a strong asymmetry incompatible with the symmetry of the flow beyond mid-radius.   Hence the increased area of the region of stall appeared as two equal regions symmetrically placed as if in an effort to keep the pressure as uniform as possible.   Further throttling caused three symmetrically placed patterns to appear for similar reasons.   Evidently a completely axially symmetric stall is unstable compared with alternating stalled regions, and the minimum width for a single stalled region corresponds to 4 or 5 rotor-blade channels.   As long as the outer portion of the annulus is unstalled, the area of the single stalled region cannot grow indefinitely, but multiple patterns of the minimum-area stalled region can arise, tending to keep the over-all flow and, in particular, the pressure as symmetrical as possible.

The stalled regions were sharply defined and demonstrated
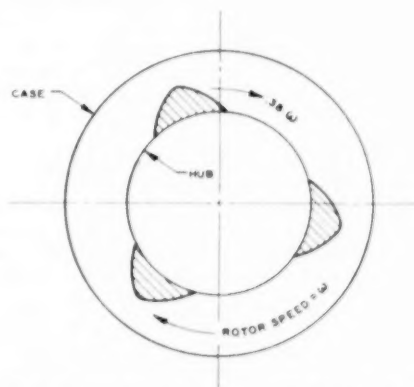
FIG. 9   THREE-REGION PROPAGATING-STALL PATTERN
(Three-stage free-vortex blading; $\phi = 0.363$; behind third rotor row; 750 rpm.)

characteristics of certain types of nonlinear oscillations.   A given throttle setting allowed two alternative patterns and very slight disturbances caused one or the other to appear.   Closing or opening the throttle a small amount eliminated one or the other completely.

FULL STALL.

As the compressor was throttled, a sharp transition occurred at a flow coefficient of $\bar{\phi} \cong 0.30$ from partial stall to full stall. Full stall is characterized by a propagating-stall region that extends over the entire blade height.   The average exit-duct pressure showed no significant change from this point to complete
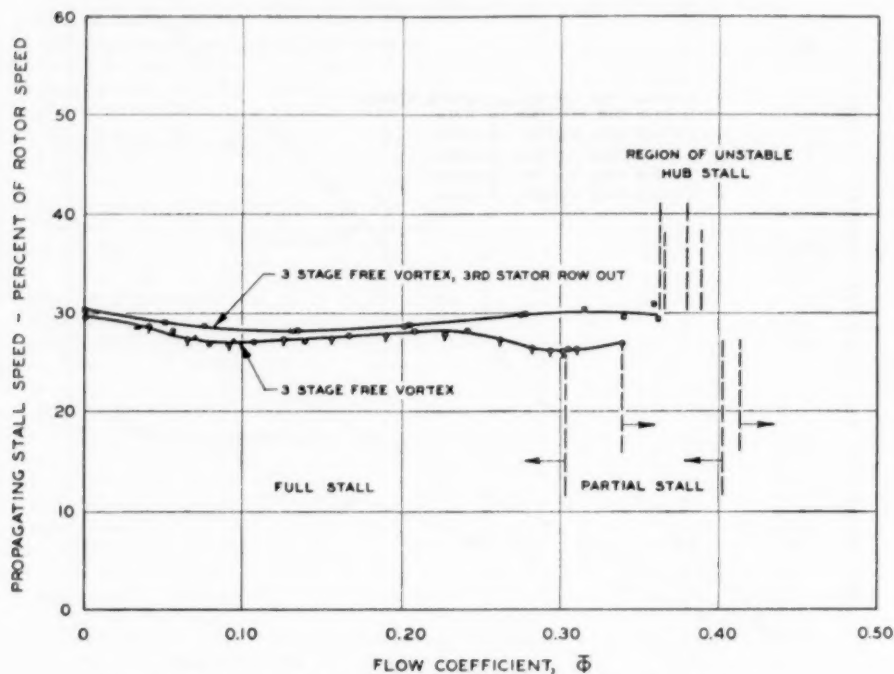
FIG. 10 VARIATION OF FULL-STALL PROPAGATION SPEED WITH FLOW COEFFICIENT
(Three-stage free-vortex blading; 750 rpm.)

shutoff while the torque continued to decrease slightly and then increased uniformly to shutoff. The propagating speed of the full stall did not change significantly, ranging from 26 per cent of the rotor speed at the initiation of full stall to 30 per cent of the rotor speed at shutoff. At any given flow coefficient in the full-stall region, the propagating speed was the same whether the flow rate was reached by opening the throttle or by closing the throttle, Fig. 10.

The extent of the region of retarded flow in full stall at a flow coefficient $\bar{\phi} = 0.323$ (throttle opening) is shown in Fig. 11. The region is widest at the hub where it occupies about 12 rotor-blade-channel widths and its width decreases toward the tip where it occupies 2 rotor-blade-channel widths. The growth of the re-tarded-flow region at mid-blade height as the flow coefficient is decreased is traced in Fig. 12. The width of the stall region increases from about 7 rotor-blade-channel widths at the begin-ning of full stall to almost 26 channel widths at shutoff.

The magnitudes of the velocity fluctuations in full stall were nearly constant over the entire blade length as contrasted with the situation in partial stall, where the velocity fluctuations de-creased in magnitude radially from the hub, Fig. 6. The velocity fluctuations in full stall at mid-blade behind the first and the third rotors are compared in Fig. 13. The magnitude of the peak velocity fluctuation-amplitude ratio, $\Delta V/V$, was larger behind the third rotor than behind the first rotor, indicating a more severe disturbance in the rear stages. Undoubtedly, reverse flow oc-curred in the full-stall regime, particularly at low flow rates. The hot-wire records do not show this clearly since velocity magni-tudes alone were measured. Visual observations of cotton tufts inserted in the compressor air stream showed the presence of re-versed flow at low over-all flow rates, mostly toward the hub.

An investigation of the influence of the volume of ducting was made in early tests. Blocking off the rear of the compressor an-nulus increased the full-stall propagating velocity from 30 per
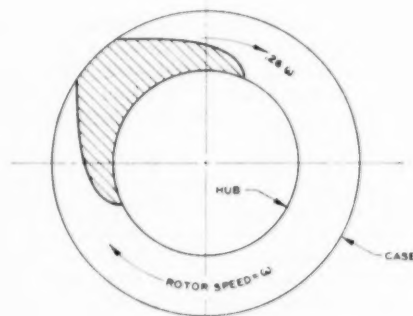
FIG. 11 FULL-STALL PATTERN AT $\phi = 0.323$, OPENING THROTTLE
(Three-stage free-vortex blading; behind third rotor row; 750 rpm.)

cent of the rotor speed to about 40 per cent. Blocking off both front and rear of the compressor annulus so as to eliminate all effects of ducting resulted in a propagation velocity of about 45 per cent of the rotor speed. Although these drastic restrictions have some influence, it is evident that the propagating stall is primarily a characteristic of the blading and its occurrence is inde-pendent of the presence of ducts.

If surging occurred, the frequency would be expected to be high, that is, 20 or 30 cps, corresponding to the resonator fre-quencies of the ducting and much higher than the frequencies of passage of the propagating stall at the rotor speeds used. No surging was recognized in any of the flow regimes mentioned, although there is a possibility that surging occurred in some of the configurations discussed later in the paper.
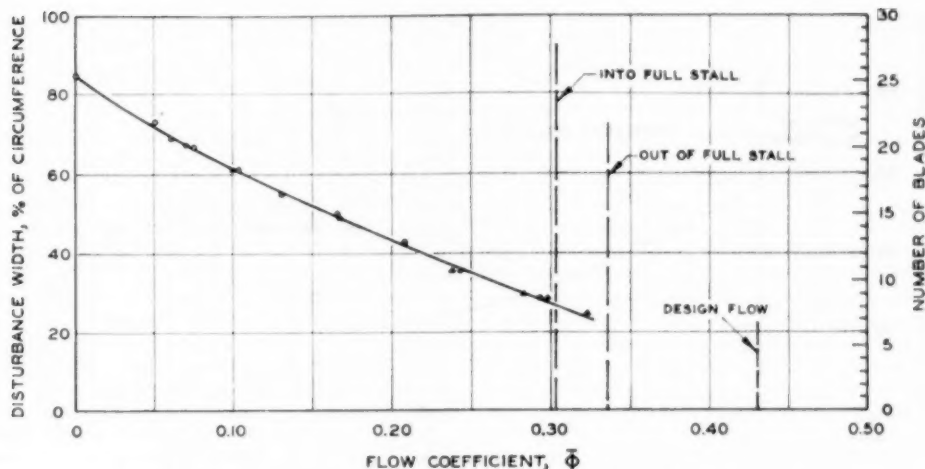
FIG. 12 VARIATION OF RETARDED-FLOW-REGION WIDTH WITH FLOW COEFFICIENT
(Three-stage free-vortex blading; full stall; behind third rotor row; 750 rpm; $R/R_0 = 0.8$.)
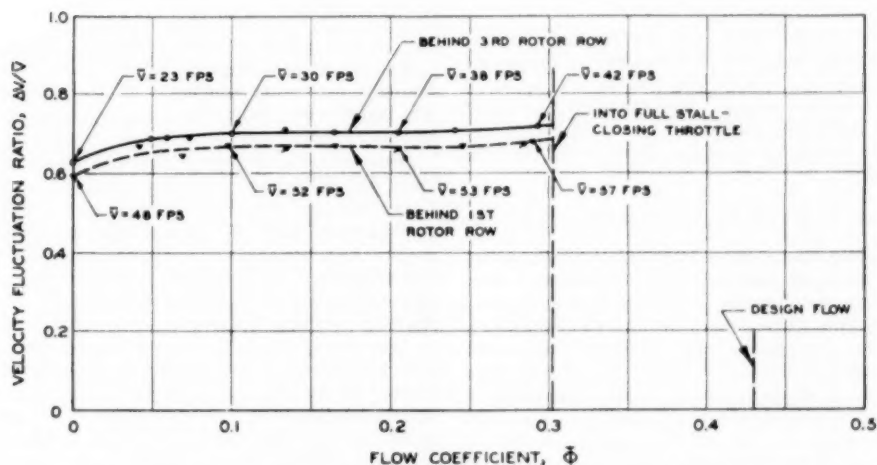
FIG. 13 COMPARISON OF VELOCITY FLUCTUATION-AMPLITUDE RATIOS BEHIND FIRST AND THIRD ROTOR
ROWS AT MID-BLADE HEIGHT; THREE-STAGE FREE-VORTEX BLADING; FULL STALL, 750 RPM

EFFECT OF REMOVING THE THIRD STATOR ROW

Upon removing the blades of the third stator row, that is, the last row of the three-stage free-vortex blading, the most significant effect was that no multiple partial-stall patterns occurred. A single rather unstable partial-stall region appeared at the hub at a flow coefficient $\bar{\phi} \cong 0.38$ on closing the throttle. This flow coefficient was smaller than that marking the beginning of partial stall with the third stator in place. Full stall commenced at $\bar{\phi} \cong 0.36$, a higher flow coefficient than with the third stator. The propagation velocity of both partial and full-stall regimes were nearly equal and both slightly greater than the full-stall velocity with the stator, Fig. 10.

EFFECT OF SOLIDITY

By removing alternate blades from each blade row in the three-stage free-vortex compressor, it was possible to observe the effect of a change in solidity on the stall propagation. Partial stall of the multiple type was not found although a region of small irregular velocity fluctuations was observed on throttling. Full stall

commenced at $\bar{\phi} \cong 0.33$ with one stalled region propagating in the direction of compressor rotation at 27 per cent of the rotor speed. The propagation speed decreased with throttling until $\bar{\phi} \cong 0.29$, from which point the propagation speed remained constant at slightly under 20 per cent of rotor speed. At $\bar{\phi} \cong 0.07$, the one region propagating full stall deteriorated into a rather irregular type of disturbance. Comparison of the propagating-stall speed at $\bar{\phi} = 0.200$ (midway in the stall regime) with that for a full complement of blades showed that decreasing the solidity by one half decreased the propagation speed from 28 per cent to 20 per cent of the rotor speed.

Fig. 14 shows how the stall-region width at mid-radius increased from 3 rotor-blade-channel widths at the start of stall to about 8 blade channels at the lower limit of propagating stall. At $\bar{\phi} = 0.253$, the width of the stalled region is a maximum at the hub and is equivalent to the width of about 7 rotor-blade channels, and a minimum at the outer radius where it is equivalent to about 3 rotor-blade-channel widths. Under these conditions, the width at mid-blade height is approximately equal to 4 blade
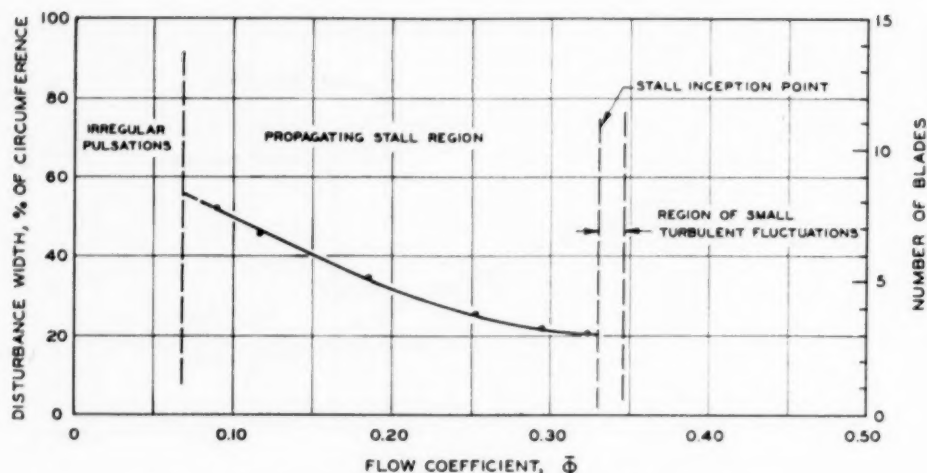
Fig. 14 Variation of Stalled-Region Width With Flow Coefficient

(Three-stage free-vortex blading with one-half normal complement of blades—half solidity mid-blade height, behind third rotor row; 750 rpm.)

channels. Removal of the third stator row resulted in an increase in speed of propagating stall at $\bar\phi = 0.20$ from 20 per cent to 22 per cent of the rotor speed. This increase was similar to that observed with the full solidity. With full solidity for stator blades, one-half solidity for rotor blades, and the third stator row in place, the propagating-stall speed was 23 per cent of the rotor speed (at $\bar\phi \cong 0.20$).

One-Stage Free-Vortex Blading

In tests of the compressor with one stage of free-vortex blading alone, the initial stall with closing throttle appeared in the form of a single propagating-stall region at the outside of the annulus rather than at the hub. This pattern commenced at $\bar\phi \cong 0.31$, with the maximum width of the region of retarded flow corresponding to two rotor-blade-channel widths, and extended from the outer radius to about the mid-blade height, propagating at 48 per cent of the rotor speed. Further throttling to $\bar\phi = 0.303$ resulted in the formation of two stalled regions placed 180 deg apart, propagating with the same speed as the single region. At $\bar\phi = 0.298$, a single-region stall pattern again appeared with a lower propagation speed equal to about 36 per cent of the rotor speed. The velocity fluctuations for this flow pattern were largest near the tip and gradually decreased with radius to zero at a point near the hub.

In all of the foregoing patterns, the maximum value of the velocity-fluctuation ratio, $\Delta V/\bar V$, was about 0.6. On further throttling to the flow coefficient range $0.26 > \bar\phi > 0.11$, irregular velocity fluctuations were observed in the outer part of the annulus.

Full stall did not occur until $\bar\phi \cong 0.11$ where a single region of retarded but fluctuating flow disturbance extending over the entire blade height appeared with the very low propagation speed of about 10 per cent of the rotor speed. At this flow rate the region of retarded flow had a width of about 6 rotor-blade channels at the hub and increased in width with radius to cover the entire annulus at the tip. Closing the throttle further increased the width of the region of retarded flow at the hub from 6 rotor-blade-channel widths to about 22 channel widths at $\bar\phi \cong 0.075$, below which irregular flow seemed to occur over the entire annulus. A small hysteresis loop was observed in the transition between full stall and the irregular partial stall.

One-Stage Solid-Body Blading

With one stage of solid-body blading, the stall occurred first in the outer part of the annulus as the compressor was throttled. The hot-wire records indicated unstable patterns of stalled flow so that consistent determinations of frequency were impossible.

Apparently, the propagating speed of initial stall first appearing at $\bar\phi \cong 0.31$ tended to be about 45 per cent of the rotor speed. Upon closing the throttle to the flow coefficient $\bar\phi \cong 0.30$, no very stable pattern appeared although there was some evidence of a pattern with two regions of retarded flow. Further throttling beyond the flow coefficient $\bar\phi \cong 0.27$ gave only irregular fluctuations of the flow velocities, concentrated for the most part in the outer portion of the annulus. This behavior was quite similar to that observed with one stage of free-vortex blading. With closing throttle, full stall occurred at $\bar\phi \cong 0.13$ with one region of retarded fluctuating flow propagating in the direction of compressor rotation with a speed of about 12 per cent of the rotor speed. A hysteresis loop was observed at the transition as for the vortex blading. The width of the region of retarded flow near the hub in the full stall increased on closing the throttle from nine rotor-blade-channel widths to extend over the entire circumference at $\phi \cong 0.050$. At smaller coefficients, the flow was very irregular everywhere in the annulus and determination of definite flow patterns was impossible.

Discussion of the Experiments

The extreme complexity of the various propagating-stall patterns makes detailed explanation impossible at the present time. Sears[6] and Marble[7] have recently made theoretical studies of propagating disturbances in two-dimensional cascades. Sears assumed an infinite number of blades and, although Marble treated the case of a finite number of blades, the effect of the finite number amounted to only a small correction. Both of these investigations were based on perfect fluid flow, but they had different assumptions concerning the lift-coefficient behavior with

[6] "On Asymmetric Flow in an Axial-Flow Compressor Stage," by W. R. Sears, Journal of Applied Mechanics, Trans. ASME, vol. 75, 1953, pp. 57–62.

[7] "Propagation of Stall in Compressor Blade Rows," by F. E. Marble, California Institute of Technology, paper presented at Institute of Aeronautical Sciences' 21st Annual Meeting, New York, N. Y., January, 1953.

angle of attack. Sears introduced a phase lag between the fluctuating lift and mean angle of attack, whereas Marble postulated a nonlinear dependence of lift on angle of attack in such a way as to give a hysteresis loop.

The forms for the lift dependence on angle of attack used by Sears and Marble were simplified analytical relations approximating in different ways the known behavior of single airfoils in the stall. In the opinion of the senior author, a more realistic picture of the unsteady flow through the cascade of moderate or high solidity is gained by concentrating attention on the leaving flow angle and the total pressure loss through the cascade. To a first approximation, the mean leaving angle can be considered constant and the loss in total pressure is small and nearly constant over an incidence-angle range of 8 to 10 deg but rises sharply to a high value outside of this range. The total pressure variation then introduces the nonlinearity which will fix the amplitude of stall oscillation. In Marble's analysis the amplitude was determined by the lift relation whereas in Sears' linearized theory the amplitude was undetermined.

The velocity of propagation of disturbances must depend on some characteristic time. It has been suggested that this is the time required for establishment of a complete separated-flow region on a blade or in a channel after a sudden increase of incident-flow angle. Experimental determinations of this characteristic time for oscillating single airfoils have shown that the phase lag between lift and angle of attack is rather insensitive to frequency and is of the right order of magnitude to explain propagating stall. However, some of the results of the compressor experiments do not seem quite consistent with such a characteristic time. In particular, removal of every second blade should result in doubling the propagation speed if this characteristic time were controlling, whereas no such large change was observed. The comparative constancy of the full-stall propagating speed with flow rate over such a wide range requires a characteristic time that is quite insensitive to large changes of mean angle of incidence and even to reversed flow, and this seems rather inconsistent with the time required for establishment of a boundary layer.

All the propagating disturbances observed, of course, involved both rotor and stator-blade rows, but the propagation speeds were such that it was not certain whether the rotor or the stator was primarily responsible. There was some tendency for the width of the regions of retarded flow to be integral multiples of the rotor-blade-channel widths at the hub and blade tip in full stall, and hence it is believed that the disturbances were propagating on the rotor. The stator blades had a marked influence in determining whether or not a given stall pattern occurred, as demonstrated by the striking results of removal of the third stator-blade row. This prevented the multiple partial-stall patterns at the hub from occurring, even five blade rows ahead.

Although the full-stall flow régime was the most stable in so far as range of flow was concerned, at least with more than one stage installed, the partial stalls are in many ways more interesting. The partial stall occurs at the larger flow rates and would occur more frequently in normal compressor operation than the full stall. Further, it is generally agreed that blade failures are more likely to occur at flow rates corresponding to the beginning of stall and hence probably in the partial-stall regimes.

In the past, many believed that blade failure was caused primarily by a stalled flutter with only one mode of vibration excited by the self-induced aerodynamic forces. From the observations of the partial stall it is clear that large aerodynamic excitation can arise without self-induced flutter of individual blades. It seems quite possible that the partial stall may be responsible for blade failure rather than the stalled flutter. What effect blade flexibility would have on partial stall is not known. The various partial-stall patterns observed were of a metastable type and a blade natural frequency in the range of partial-stall frequencies might influence the relative stability of the partial-stall regimes greatly. It is clear that to reduce aerodynamic excitation of rotor blades, it is preferable to have the partial stall occur at the hub rather than the blade tip. The free-vortex rotor blades have constant chord from root to tip although this is not the general practice. In the multistage tests, the partial stall occurred at the hub whereas with the more conventional tapering blades, it might well occur at the tip. The relatively high solidity of the free-vortex blading and even higher solidity of the solid-body blading toward the tip were not sufficient to prevent tip stall in the single-stage configurations.

The effective wave lengths of the partial-stall and even more of the full-stall patterns are so large that the influence of the propagating stall cannot be confined to a single blade row, because the distance between center lines of the blade rows is a small fraction of the pattern wave length. Hence stall on a single blade row can influence rows far ahead as well as far behind. It is difficult at this moment to predict how the knowledge of the propagating stall will influence future compressor design. It may be possible to suppress some of the stall patterns, but it is not even known if this would improve or worsen over-all performance. More experiments on a variety of compressors are required to determine which of the various stall phenomena are characteristics of all compressors and which phenomena are characteristics of particular machines.

Acknowledgments

Basic Compressor Characteristics From Tests of a Two-Stage Axial-Flow Machine

By W. R. NEW,[1] A. H. REDDING,[2] H. B. SALDIN,[3] and K. O. FENTRESS[4]

The attainable pressure ratio per stage and efficiency of axial-flow compressors, working at subsonic gas velocities, may be expected to depend at least upon Mach and Reynolds numbers additionally of all features of blading geometry. The results of a high-speed test program on a two-stage axial-flow compressor, with one easily defined and accurately reproducible choice of blading geometry, are reported in this paper. The tests covered a range of Mach numbers 0.3 to 0.9 and a range of Reynolds numbers 50,000 to 500,000. The relationships among the variables covered by this program are believed generally to be representative of the behavior of axial-flow-compressor stages at subsonic velocities even though absolute values of loading and efficiency are not indicative of the best current design standards. Three-dimensional diagrams showing the dependence of pressure ratio per stage and efficiency upon Mach and Reynolds numbers are included to aid in visualizing these relationships. The results are then condensed into pairs of two-dimensional plots exemplary of types more convenient for extensive use.

NOMENCLATURE

The following nomenclature is used in the paper:

w_a = weight flow rate of air, lb/sec

p_0 = static pressure in large pipe ahead of model, in. Hg or H_2O

p_2 = static pressure at prevailing velocity in blade-entrance annulus, in. Hg or H_2O

p_3 = static-pressure average of inner and outer wall taps in blade-exit annulus, in. Hg or H_2O

p_4 = static pressure in test circuit after blade-exit diffuser, in. Hg or H_2O

p_5 = static pressure in large pipe ahead of flowmeter, in. Hg or H_2O

p_6 = static-pressure average of wall taps in throat of flowmeter, in. Hg or H_2O

T = absolute temperatures, deg F

v = specific volumes, ft^3/lb

a = acoustic velocities, fps

μ = absolute viscosities, lb sec/ft^2

c_m = mean chord length; rotating blade, ft

U = peripheral velocity of blades; subscript m designates mean, t tip, fps

V_z = axial components of air velocity, fps

Numeral subscripts same significance as for pressures

M_R = Mach number relative to blade tips

N_{Re} = Reynolds number based on mean chord length, relative velocity, and kinematic viscosity

ν_m = velocity ratio, quotient of mean axial velocity, and mean peripheral speed

ρ = pressure ratio per stage taken as $\sqrt{p_3/p_2}$

η = internal or group blading efficiency, defined in Fig. 5

η_B = a basic internal efficiency selected for summary curves

ρ_B = a basic stage pressure ratio selected for summary curves

INTRODUCTION

About 12 years ago the authors' Company entered the field of development of turbojet engines under the sponsorship of the Bureau of Aeronautics, United States Navy Department.

Within certain ranges of the possible broad spectra of operation of these machines, one or more of the recognized key variables may exert a major influence on the desired function. In other ranges, these same variables may have small or negligible effect. Attempts to design a "limit machine" for specified service clearly indicated the fragmentary nature of the most comprehensive experimental results available to the authors at that time.

Among the more important matters, it was felt that a much better basic understanding of the effects of Mach and Reynolds numbers on the performance of axial-flow-compressor stages was needed. Support of this viewpoint by the Bureau of Aeronautics resulted in funds being made available for the conduct of tests upon which this paper is based.

PROBLEM OUTLINED AND EQUIPMENT AVAILABLE

The general problem was resolved most simply into a question of how to obtain accurate determination of the effects of Mach and Reynolds numbers on the performance of any representative axial-flow-compressor stage. This was considered a more attractive way to start than investigation of the many aspects of geometry of the stage selected. To this end a simple type of stage with a nominal efficiency level was chosen, comprising axial entry without any inlet guide vanes, and with most of the work of compression done in the rotating blades. In order to generate sufficient pressure to overcome the resistance of the test system, and still have a reasonably wide operating range, it was necessary to use a two-stage assembly in the tests.

Fig. 1 shows the compressor-testing equipment, available in 1942, looking down from above the driving end. Fig. 2 is a schematic arrangement of this equipment keyed to the table of nomenclature. A single-stage, compressed-air-driven turbine is in the small cylinder at the lower left of Fig. 1. This turbine furnished the power to drive the experimental compressor. The closed compressor circuit, with large rectangular cooler in the right rear, occupies most of the picture. An Amsler torsiometer

[1] Manager, Aviation Gas Turbine Laboratories, Technical Operations Department, Aviation Gas Turbine Division, Westinghouse Electric Corporation, Philadelphia, Pa., and Kansas City, Mo. Mem. ASME.

[2] Westinghouse Senior Resident Representative at Rolls-Royce Ltd., Derby, England. Mem. ASME.

[3] Section Manager, Engineering Department, Aviation Gas Turbine Division, Westinghouse Electric Corporation, Kansas City, Mo. Mem. ASME.

[4] Engineering Department, Aviation Gas Turbine Division, Westinghouse Electric Corporation, Philadelphia, Pa.

P₀ AND P₄ WALL TAPS
T₀ AVERAGE OF 3 SHIELDED THERMOCOUPLES
RPM COUNTER AND STOP WATCH
P₃ AVERAGE OF 4 WALL TAPS EACH ON
    INNER AND OUTER DIAMETERS
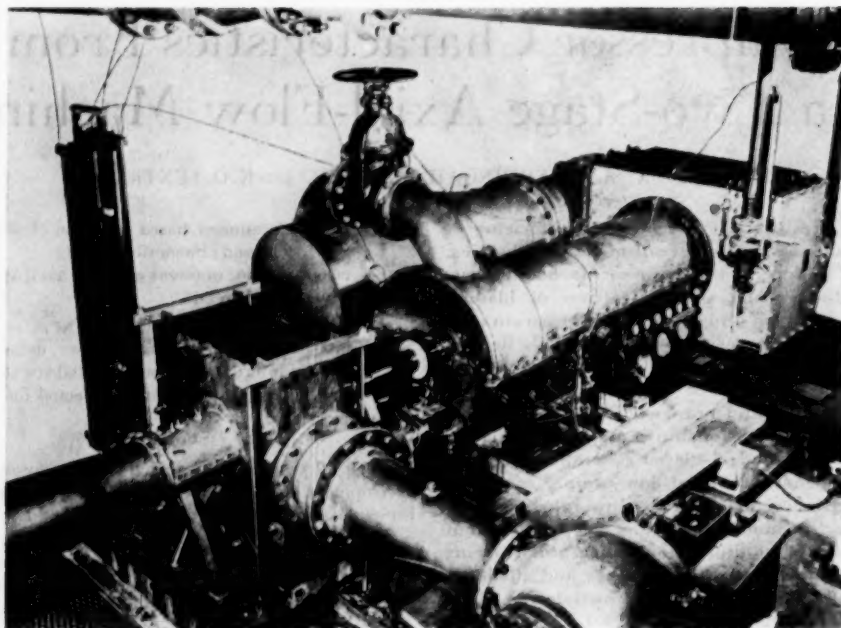P₅ AND P₆ AVERAGE OF 4 WALL TAPS
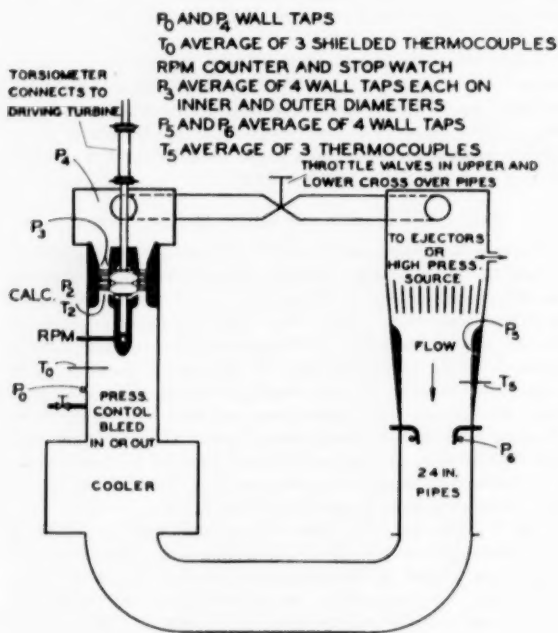T₅ AVERAGE OF 3 THERMOCOUPLES

Fig. 2   Test Circuit Diagram

equipped with calibrated bars for full-scale deflection at 20, 35, 70, and 140 ft-lb connected the turbine and compressor couplings. A manometer board for pressure measurements is at the left, and the potentiometer for temperature measurements is on the stand just behind the turbine throttle valve body at the lower right of Fig. 1. A revolution counter, geared to the shaft, is in the small circular housing at the end of the row of lubrication pres-

sure gages. The bottom of the air-inlet pipe, supplying the driving turbine, frames the top of the picture.

The flow established by the test compressor in the cylinder with horizontal joint forming the right-hand branch of the circuit, is toward the turbine, then through gate valves, in upper and lower crossover connections to the left-hand branch of the circuit containing the flowmeter. Steam ejectors on the roof of the building maintained any desirable partial vacuum in the closed circuit, which could also be pressurized from the shop air supply.

Test Compressor

This is a two-stage axial-flow machine of vortex design, with no tangential component entering the rotating blades. Each row of stationary blades is designed to remove the swirl component of velocity introduced by the preceding rotating row. Fig. 3 is a longitudinal section of the important part of the test compressor showing essential diameters and other dimensions.

The rotating blades, milled from alloy steel, have a cross section defined by an arc of a circle and a straight line, with the leading edge rounded. The integral bulb-type root is side-inserted into slots milled at the required angles into the two steel disks shrunk on the shaft. Fig. 4 shows the blade section at the hub, and at a blade height of $2 \, ^5/_8$ in. There are 20 blades on each disk, cut to length to operate at the radial clearance shown in Fig. 3. The blades are oriented in the disk so that the straight side, defining the pressure face, at the hub makes an angle of $40^1/_4$ deg to the axis of rotation in the first row, and 52 deg in the second row.

The stationary blades, which are neither warped nor tapered, are made of steel rolled to NACA Section No. 6512 with chord dimension of 0.875 in. The 45 blades in each row are oriented such that a straightedge tangent to the concave surface makes an angle of 5 deg with the axis of rotation, opposite in sign to the angle of the rotating blades.

Fig. 3 clearly indicates the location of static pressure taps at both the inner and outer diameters of the short straight section of the blade-exit diffuser.
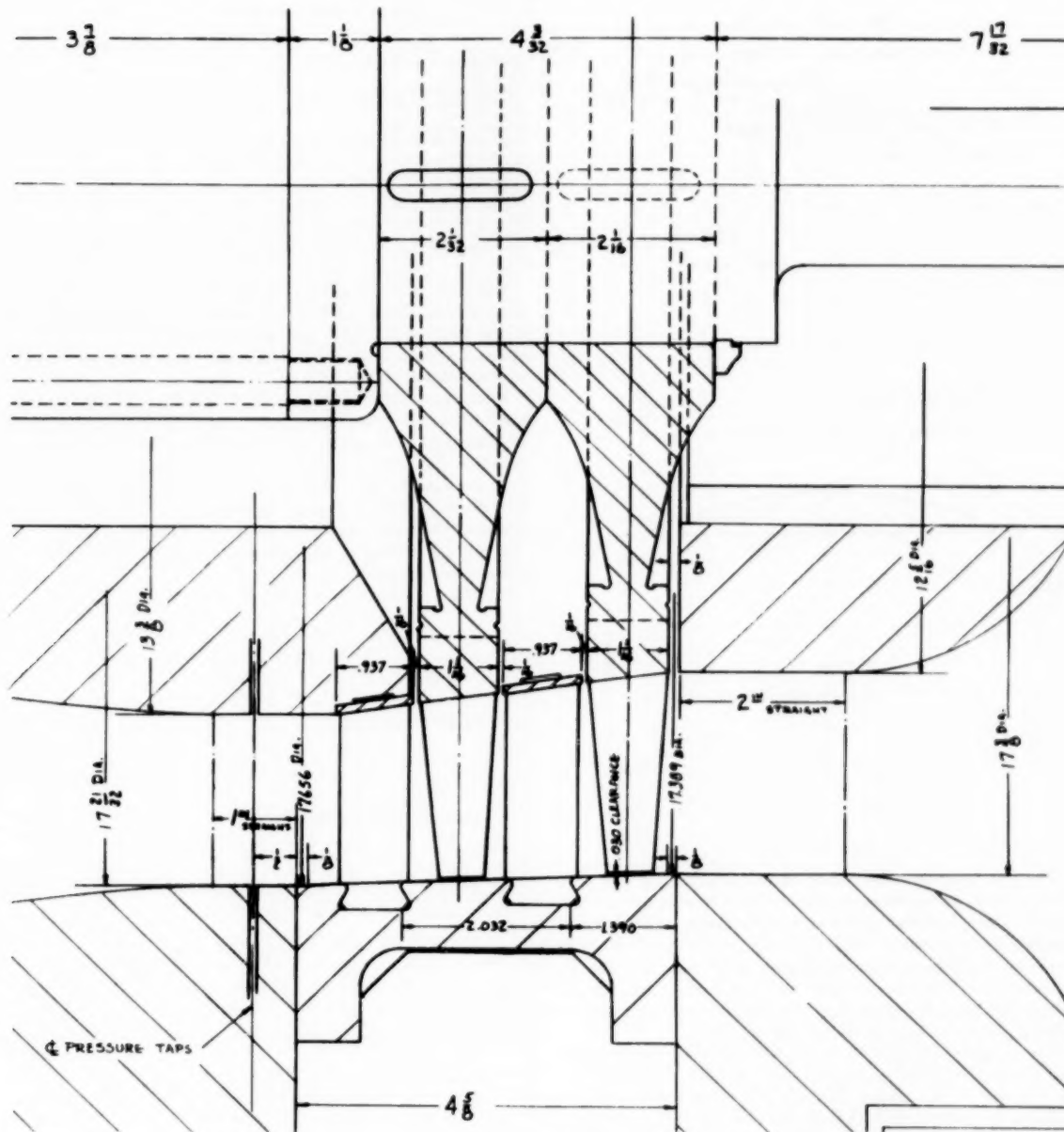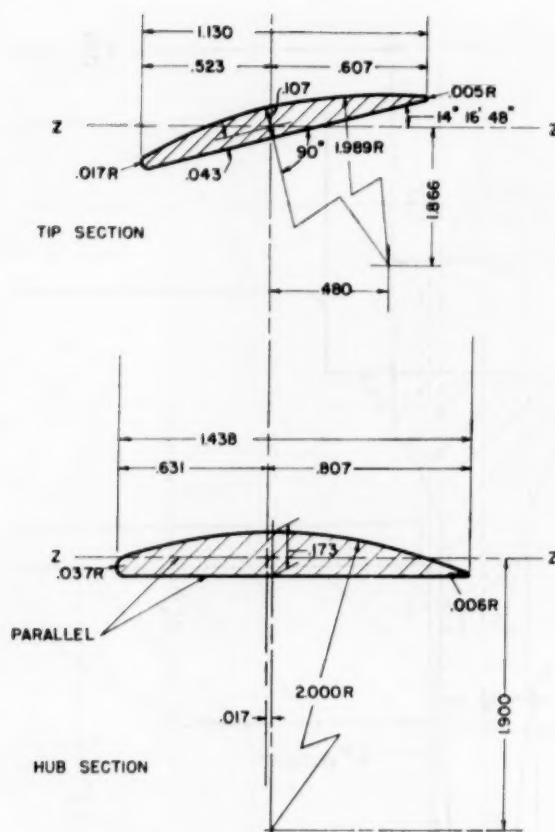
Fig. 3 Compressor Blade Path

FIG. 4   ROTATING BLADE SECTIONS

TABLE 1   RANGE OF TEST VARIABLES

Item	Reynolds numbers				Speeds, rpm
	50000	100000	200000	400000	
Inlet pressure, in. Hg abs......	6.0	12	24	48	
Flow, lb/sec...............	2.25	4.5	9.0	18	5500
Torque-bar limit, ft-lb......	20	20	35	70	
Inlet pressure, in. Hg abs......	3.75	7.5	15	30	
Flow, lb/sec...............	2.25	4.5	9.0	18	8700
Torque-bar limit, ft-lb......	20	35	70	140	
Inlet pressure, in. Hg abs......	3.25	6.5	13.0	26	
Flow, lb/sec...............	2.25	4.5	9.0	18	10000
Torque-bar limit, ft-lb......	20	35	70	140	
Inlet pressure, in. Hg abs......	3.0	6.0	12.0	24	
Flow, lb/sec...............	2.25	4.5	9.0	18	11000
Torque-bar limit, ft-lb......	20	35	70	140	
Inlet pressure, in. Hg abs.....	2.7	5.4	10.8	21.6	
Flow, lb/sec...............	2.25	4.5	9.0	18	12000
Torque-bar limit, ft-lb........	20	35	70	140	

Using the area of the large pipe ahead of the model with measured-state condition (p_0, T_0), the annular area immediately ahead of the first rotating row, and assuming isentropic conversion, a uniform average axial velocity V_{a2} and state condition (p_2, T_2) were calculated.

From the annular area immediately following the second stage, weight flow rate of air, net power input to the blading, static pressure (p_3), and assuming uniform flow, the average axial velocity (V_{a3}) and temperature (T_3) were calculated.

In addition to the foregoing, $V_{a2.1}$, $T_{2.1}$, and $p_{2.1}$, representing conditions at the interstage location, were calculated as the arithmetic averages of similar quantities at stations 2 and 3.

From the foregoing quantities, the following numbers and ratios were calculated:

1   Mach number relative to blade tips

$$M_R = \frac{\sqrt{\dfrac{U_{t2}^2 + V_{a2}^2}{gkRT_2}} + \sqrt{\dfrac{U_{t2.1}^2 + V_{a2.1}^2}{gkRT_{2.1}}}}{2}$$

2   Mean velocity ratio

$$\nu_m = \frac{V_{a2.1}}{U_m}$$

3   Pressure ratio per stage

$$\rho = \sqrt{p_3/p_2}$$

4   Reynolds number based on mean chord length, relative velocity, and kinematic viscosity

$$N_{Re} = \frac{\sqrt{U_m^2 + \left[\dfrac{V_{a2} + V_{a2.1}}{2}\right]^2} \, (c_m) \, \dfrac{1}{4}\left[\dfrac{3p_2}{RgT_2} + \dfrac{p_3}{RgT_3}\right]}{\mu}$$

5   Internal or group-blading efficiency

$$\eta = \frac{T_2 c_p \left[\left(\dfrac{p_3}{p_2}\right)^{\frac{k-1}{k}} - 1\right]}{\dfrac{550\,(hp)}{Jw_a} + \dfrac{V_{a2}^2}{2gJ} - \dfrac{V_{a2}^2}{2gJ}}$$

The calculations just outlined are detailed in Table 2 for one of the 20 basic test runs. In Fig. 6 the results of the sample calculation comprising Mach number relative to the tip of each rotating row, stage efficiency, pressure ratio, and Reynolds number are plotted as functions of mean velocity ratio. The contour maps, isometric diagrams, and summary curves, were prepared from the 20 detailed curves of which Fig. 6 is a sample.

RESULTS AND CONCLUSIONS

The test results of the entire program are summarized on four contour maps of the Reynolds-Mach number plane with velocity ratio as a parameter. Four isometric diagrams each, of

TEST PROGRAM

The test program consisted of obtaining efficiency and compression ratio as functions of velocity ratio from wide-open discharge to incipient stalling for each combination of five rotative speeds (Mach number) and four flow rates (Reynolds number) as shown in Table 1, wherein numbers have been rounded for convenience. The scope of the tests was limited only by the permissible vibration of the long, slender rotor assembly and the driving power available at the chosen speeds.

The quantity of oil flow to each of the two compressor bearings and the temperature rise therein were obtained for every test. At the end of the stated program the compressor rotor was replaced by a simple shaft through the bearings and a correlation established between speed and torque measurements and the quantity of oil flow and temperature rise. Mechanical losses corrected back to actual loss torque and speed by means of this correlation were used in evaluating net power input to the blading. Other tests in addition to calculations revealed no appreciable disk friction, coupling-nut windage, or other source of mechanical loss to contaminate the net power input.

CALCULATION PROCEDURE

The data taken during each run consisted of a rotative speed, weight flow rate of air, power input less calibrated bearing losses, initial state point (p_0, T_0) in the large pipe ahead of the model, and the average static pressure at inner and outer-wall taps in the annulus immediately after the model.

TABLE 2 TEST CALCULATION SHEET FOR TWO-STAGE AXIAL FLOW COMPRESSOR

$c_p = 0.240$; $k = 1.4$; $R = 53.35$ ft/°F.; $g = 32.17$ ft/sec²;
$A_0 = 3.546$ ft²; $A_2 = 0.822$ ft²; $A_3 = 0.725$ ft²; $J = 778.26$ ft-lb/Btu
$C_1 = 10.29$ $C_2 = 29.5 \times 10^{-6}$ $C_3 = 37.25 \times 10^{-6}$ $C_4 = 0.707$

I $T_0/T_2 = (P_0/P_2)^{(k-1)/k}$ II $\left(\frac{V_0}{P_0}\right)^2 T_0 - \frac{A_2^2}{R} \frac{2k}{k-1} \frac{P_0/P_2 \frac{k-1}{k} - 1}{P_0/P_2 \left[(P_0/P_2)^{2/k} (A_0/A_2)^2 - 1\right]}$

Date 4/8/43

	TIME: A.M.	10:32	10:43	10:52	11:01	11:10	11:20	11:31	11:41
1	Speed rpm	11100	10960	10810	10722	10650	10640	10610	10610
2	Flow W_a lb/sec	4.150	3.985	3.885	3.770	3.650	3.550	3.398	3.217
3	Net power hp	53.38	54.90	54.90	56.77	57.03	57.91	58.53	58.99
4	p_2 in H2O	74.567	73.617	74.160	73.617	71.753	73.751	74.098	73.549
5	P_3 in H2O	82.487	93.907	96.618	87.732	89.138	90.508	92.912	92.797
6	T_0 °F abs.	522.61	520.63	520.55	520.20	519.58	519.46	519.30	518.00
7	$(W_a/P_0) T_0$	1.619	1.527	1.430	1.365	1.273	1.205	1.086	.990
8	P_0/P_2 from I	1.0821	1.0766	1.0710	1.0673	1.0620	1.0583	1.0519	1.0469
9	T_0/T_2 from II	1.0228	1.0213	1.0198	1.0188	1.0174	1.0163	1.0146	1.0130
10	$P_2 = P_0/$ ⑧	.98.91	.68.38	69.24	66.97	69.45	69.69	70.44	70.25
11	$T_2 = T_0/$ ⑨	511.0	509.8	510.4	510.6	510.7	511.1	511.8	511.3
12	$V_2 = C_1(T_2/T_2)$	76.15	76.65	75.90	76.28	75.75	75.50	74.77	74.90
13	$V_2 W_a$	317.0	305.7	295.2	287.7	276.4	268.0	253.8	240.8
14	$V_2^2/2gJ = C_2$⑬²	2.961	2.756	2.570	2.440	2.256	2.120	1.900	1.711
15	$(P_3/P_2)^{(k-1)/k} - 1$	1.1970	1.2271	1.2510	1.2720	1.2843	1.2987	1.3091	1.3210
16	$(P_3/P_2)^{(k-1)/k} - 1$	.0627	.0602	.0660	.0711	.07405	.0775	.07995	.08275
17	Assumed Eff. η °	.8	.8	.8	.8	.8	.8	.8	.8
18	$16/\eta$ ° + 1	1.0659	1.0753	1.0825	1.0890	1.0927	1.0970	1.1000	1.1035
19	$T'_3 = T_2$ ⑱	544.7	548.2	552.5	556.0	558.0	560.7	563.0	564.2
20	$V'_3 = C_1 T'_3/P_3$	67.95	67.27	65.60	65.25	64.40	63.77	62.85	62.55
21	$V'_3 W_a$	282.0	268.3	255.0	246.0	235.2	226.3	213.3	201.0
22	$V_3^2/2gJ = C_2$⑳²	2.962	2.685	2.424	2.257	2.061	1.910	1.696	1.510
23	C_4⑬ W_a Btu/lb	9.09	9.72	10.15	10.65	11.05	11.51	12.20	12.95
24	㉓ + ㉑ - ㉒	9.216	10.021	10.516	11.043	11.475	11.992	12.664	13.411
25	C_p⑲ Btu/lb	6.46	7.36	8.095	8.725	9.09	9.505	9.825	10.16
26	T' = ㉔ / ㉕	.694	.735	.7695	.7900	.7920	.7935	.776	.7575
27	㉖η/η ° + 1	1.0760	1.0820	1.0858	1.0900	1.0935	1.0977	1.1030	1.1021
28	$T_3 = T_2$ ㉗	549.8	551.6	554.2	556.6	558.5	561.0	564.5	567.2
29	$V_3 = C_1 T_3/P_3$	68.60	67.70	65.77	65.3	64.47	63.78	63.00	62.87
30	$V_3 W_a$	284.7	270.0	255.8	246.3	235.3	226.4	213.6	202.2
31	$V_3^2/2gJ = C_2$㉚²	3.022	2.718	2.439	2.263	2.063	1.912	1.701	1.525
32	㉓ + ㉑ - ㉛	9.031	9.788	10.281	10.827	11.243	11.738	12.399	13.136
33	η = ㉜ / ㉔	.7155	.752	.7865	.805	.8075	.8095	.792	.7725

$C_5 = 49.02$ $C_6 = 0.0758$ $C_7 = 1.215$ $C_8 = 0.0764$
$C_9 = 9.647$ $C_{10} = 0.0664$ $C_{11} = 0.00338$

Date 4/8/43

	Time	10:32	10:43	10:52	11:01	11:10	11:20	11:31	11:41
34	$a_2 = C_5\sqrt{T_2}$	1110	1108	1109	1109	1109	1110	1111	1110
35	$U_{22} = C_6$ (rpm)	841.5	830.5	820.0	813.0	807.0	806.0	804.5	804.5
36	$V_{a2} = C_7 V_2 W_a$	385.0	371.0	358.2	349.2	336.0	325.5	308.1	292.4
37	$\sqrt{㉟² + ㊱²}$	925	910	895	885	874	869.5	861.0	855.5
38	$M_{R2} = ㊲ / ㉞$	.8335	.821	.8075	.798	.788	.7835	.775	.771
39	$T_{2.1} = (T_2 + T_3)/2$	530.4	530.7	532.3	533.6	534.6	536.1	538.2	539.3
40	$a_{2.1} = C_5\sqrt{㊴}$	1130	1130	1132	1134	1135	1137	1139	1140
41	$U_{22.1} = C_8$ (rpm)	847.6	836.5	825.5	819.0	813.5	812.5	810.5	810.5
42	$V_{2.1} = C_9(V_2 + V_3)$	369.5	372.4	356.3	345.3	331.0	319.8	302.2	286.5
43	$\sqrt{㊶² + ㊷²}$	912	915	899	888	878	873.5	864.5	859.5
44	$M_{R2.1} = ㊸ / ㊵$	.825	.8095	.794	.7825	.774	.768	.759	.754
45	$M_R = (M_{R2} + M_{R2.1})/2$	.829	.815	.801	.790	.781	.776	.767	.762
46	$V_3 = (3V_3 + V_2)/4$	74.41	74.41	73.37	73.54	72.93	72.57	71.84	71.89
47	$T_m = (T_2 + T_{2.1})/2$	520.7	520.3	521.4	522.1	522.7	523.6	525.0	525.1
48	U_3' based on ㊻	3.70	3.70	3.70	3.70	3.70	3.73	3.72	3.72
49	$U_m = C_{10}$ (rpm)	736	727	717.5	712	706	705.5	704.5	704.5
50	$V_{2.0} = (V_0 + V_2)/2$	357.8	371.7	357.2	347.2	333.5	322.7	305.2	289.5
51	㊽ $\sqrt{㊹ + ㊺}$	852.5	815.5	801.5	791.5	780.0	776.0	767.0	760.7
52	$N_{Re} = C_{11}$ ㊿	102300	100300	99909	98850	97800	97500	97050	96400
53	$V = V_{a2.1}/U_m$	.5285	.5125	.497	.485	.468	.4525	.429	.407

the efficiencies and pressure ratios per stage, pictorially superior to the contour maps, are included to assist in forming a correct mental picture of the interaction of the variables considered (Figs. 7, 8, and 9).

Finally, it was found possible to consolidate on a single page, Fig. 10, all of the information revealed by the tests. In Fig. 10 a basic efficiency and basic stage-pressure ratio are exhibited as functions of velocity ratio with Reynolds number as parameter; then a Mach-number correction factor is provided for each. In the case of efficiency the correction factor requires only a Reynolds-number parameter, but in the case of pressure ratio both Reynolds number and velocity ratio are involved. Considerable cross plotting preceded construction of Fig. 10, with the inevitable sacrifices in faithful reproduction of the actual test data at some conditions. In spite of this, numerous spot checks of Fig. 10 with the basic measurements show few disparities of 1 per cent or greater.
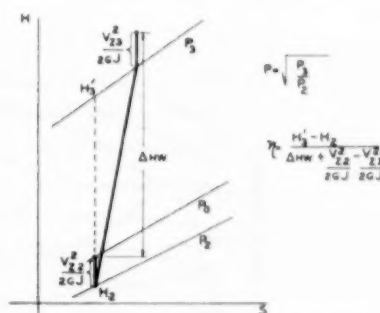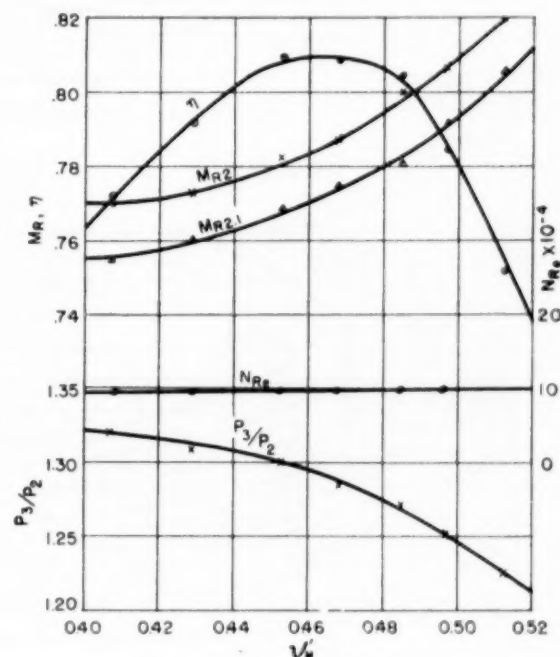

FIG. 5 EFFICIENCY DIAGRAM—H-S PLANE

FIG. 6 SAMPLE TEST CURVE

It was expected that compressor efficiency would fall off with increasing Mach numbers and decreasing Reynolds numbers. This, in fact, proved to be the case. In the model tested it appeared that the critical Reynolds number was in the order of 200,000 to 300,000 while the critical Mach number was approximately 0.64 relative to the tip of the rotating blades. At a constant Mach number of 0.6, efficiency decreased from 86 to 78 per cent as Reynolds number decreased from 250,000 to 60,000. At constant Reynolds number of 250,000, efficiency decreased from 86 to 76 per cent as Mach number increased from about 0.67 to 0.86.

An additional effect was noted particularly at low Reynolds numbers. This was a decrease in efficiency at a constant Reynolds number as Mach number was reduced below the critical value. In this case the dropoff may not exist in fact, but rather may represent experimental error in the range where all measured quantities are small. There is no question that even though all possible precautions were taken (such as using four torque bars in order to get a larger percentage of full-scale torque at low powers
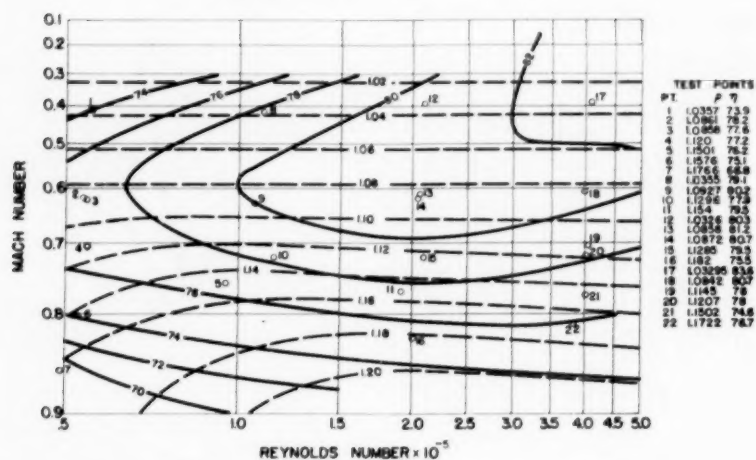
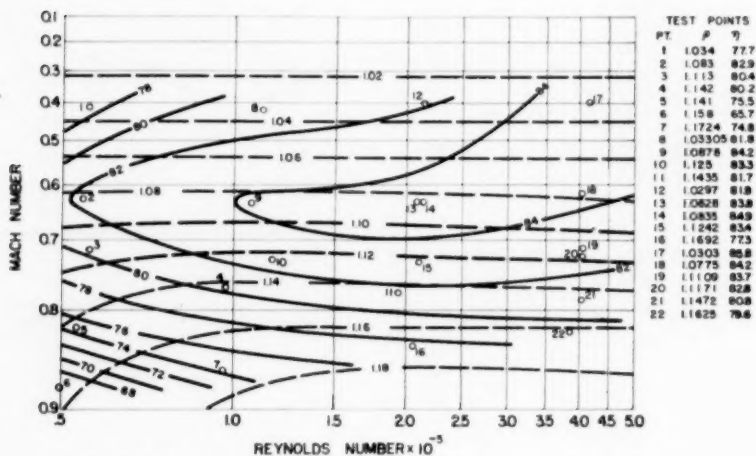FIG. 7(a) PERFORMANCE CONTOUR MAP; MEAN-VELOCITY RATIO = 0.40

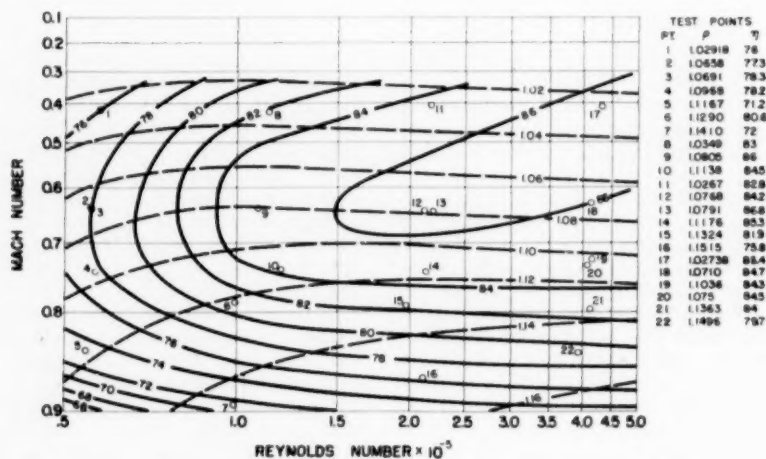FIG. 7(b) PERFORMANCE CONTOUR MAP; MEAN-VELOCITY RATIO = 0.44

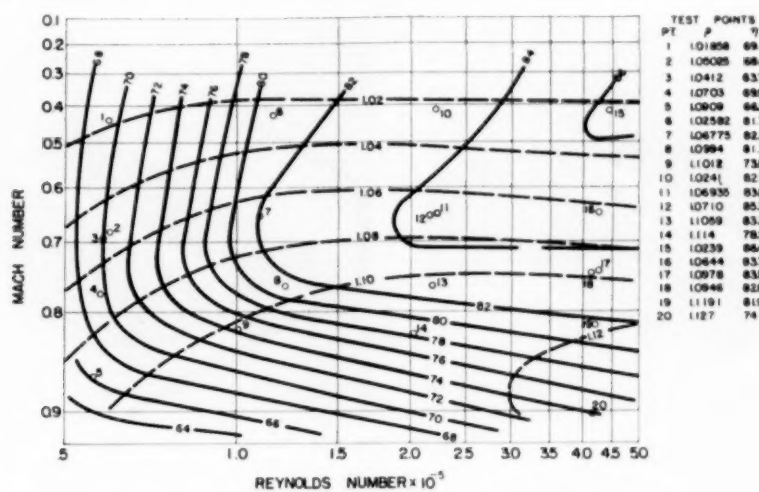FIG. 7(c) PERFORMANCE CONTOUR MAP; MEAN-VELOCITY RATIO = 0.48

FIG. 7(d)   PERFORMANCE CONTOUR MAP; MEAN-VELOCITY RATIO = 0.52
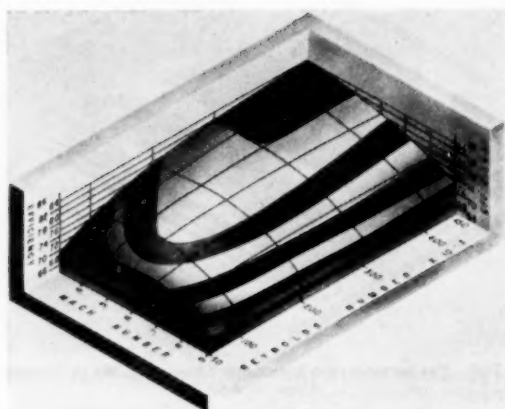

FIG. 8(a)   EFFICIENCY ISOMETRIC DIAGRAM; MEAN-VELOCITY RATIO = 0.40
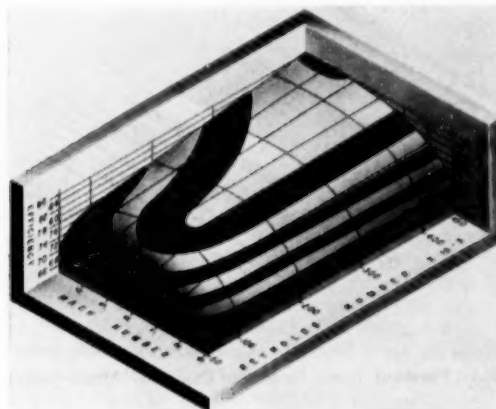

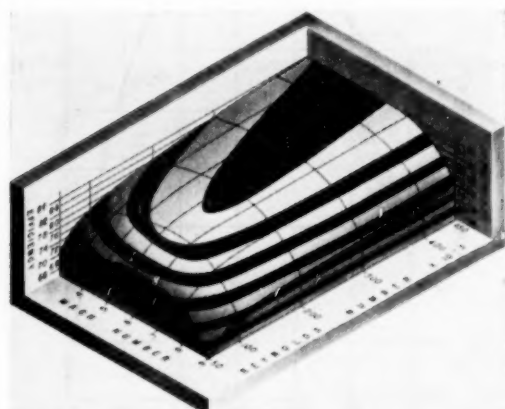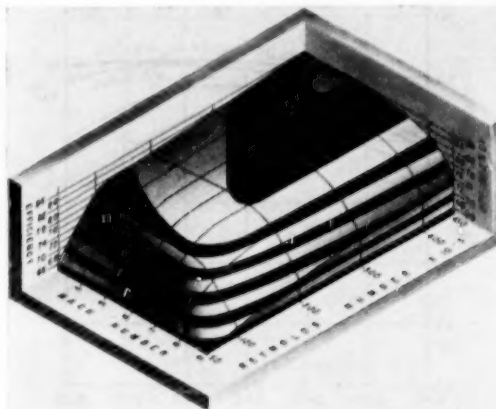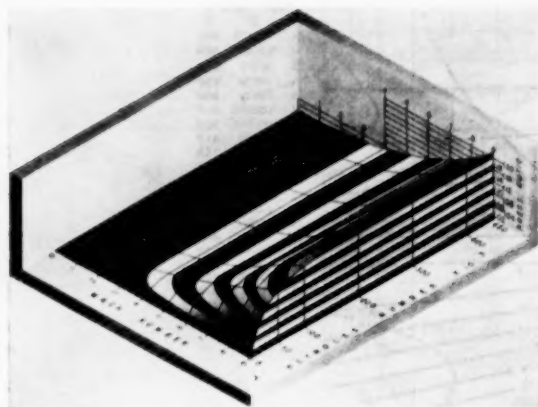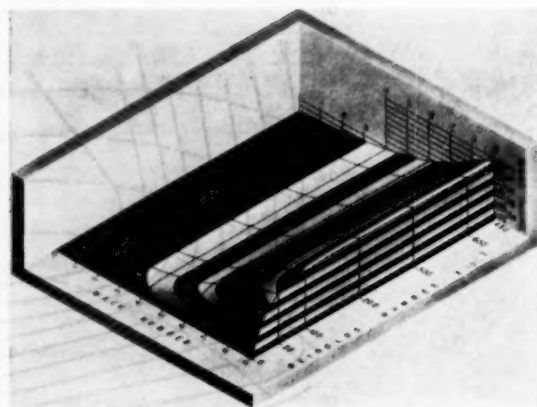FIG. 8(b)   EFFICIENCY ISOMETRIC DIAGRAM; MEAN-VELOCITY RATIO = 0.44

FIG. 8(c)   EFFICIENCY ISOMETRIC DIAGRAM; MEAN-VELOCITY RATIO = 0.48

FIG. 8(d)   EFFICIENCY ISOMETRIC DIAGRAM; MEAN-VELOCITY RATIO = 0.52

FIG. 9(a)   PRESSURE RATIO ISOMETRIC DIAGRAM;   MEAN-VELOCITY
RATIO = 0.40

FIG. 9(b)   PRESSURE RATIO ISOMETRIC DIAGRAM;   MEAN-VELOCITY
RATIO = 0.44
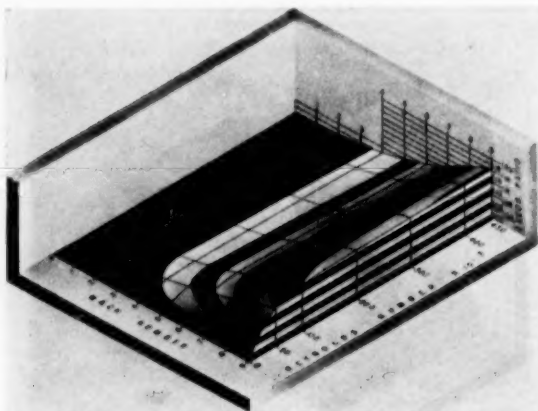
FIG. 9(c)   PRESSURE RATIO ISOMETRIC DIAGRAM;   MEAN-VELOCITY
RATIO = 0.48
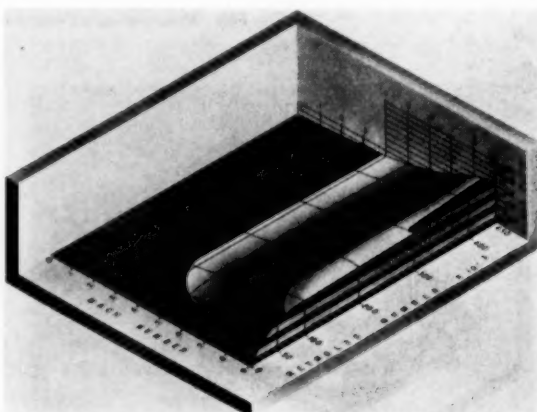
FIG. 9(d)   PRESSURE RATIO ISOMETRIC DIAGRAM;   MEAN-VELOCITY
RATIO = 0.52
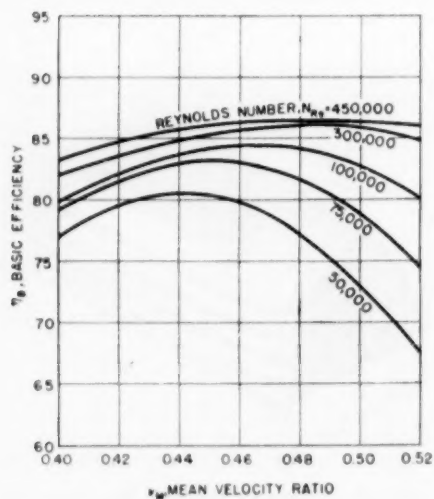
FIG. 10(a)   SUMMARIZED PERFORMANCE;   BASIC EFFICIENCY
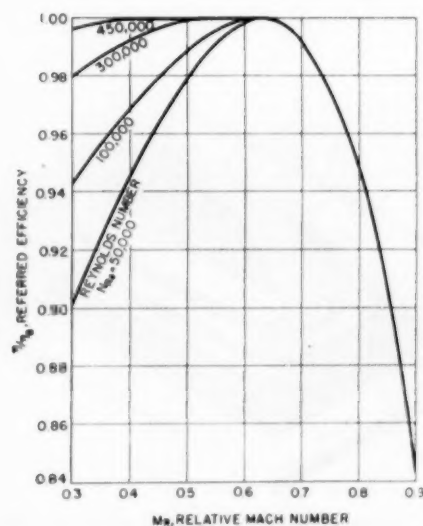
FIG. 10(b)   SUMMARIZED PERFORMANCE;   REFERRED EFFICIENCY
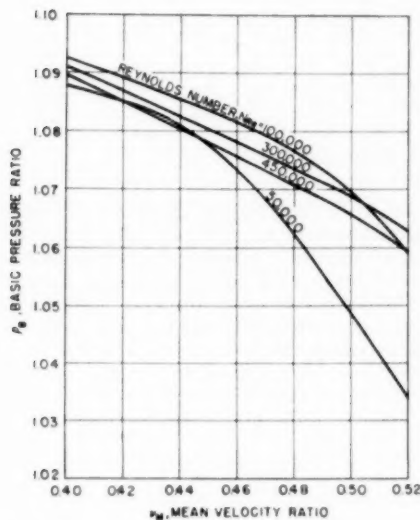
FIG. 10(c) SUMMARIZED PERFORMANCE; BASIC-PRESSURE RATIO

FIG. 10(d) SUMMARIZED PERFORMANCE; REFERRED-PRESSURE RATIO

and shifting from mercury to water manometers) the level of accuracy is poorer in the low Mach-number, low Reynolds-number range. It is still possible however that as Mach number is reduced at low Reynolds number the shock-induced turbulence may be reduced in such a manner that the effective Reynolds number is actually decreasing.

It is also possible that as Mach number decreases, the pressure distribution on the blading is changed in an adverse manner causing laminar separation. At the present time these thoughts represent little more than conjecture, and the question of experimental inaccuracies must not be ignored.

Another matter of interest is the shift in peak efficiency from high to low-velocity ratios as the Reynolds number is decreased. This is shown best in Fig. 10. The losses in compressor blading are made up of secondary losses which increase as velocity ratio

is lowered, irrespective of Reynolds number, and blade-profile losses which decrease as velocity ratio is decreased (at least up to incipient separation). Profile losses increase with decreasing Reynolds numbers. If we assume that the maximum efficiency is obtained where secondary and profile losses are about equal, the shift in peak efficiencies with Reynolds number may be explained.

While the entire program involved only a single choice of blading geometry, it is believed that the effects of Reynolds numbers exhibited apply generally to subsonic axial-flow-compressor stages. The Mach number limiting maximum efficiency is associated most closely with the geometry of the particular blading selected. The choice, however, representative of a design adequate from the viewpoint of mechanical strength, but not conservative, gives a qualitative picture probably not misleading as to order of magnitude.

An Analytical Approach to the Design of Four-Link Mechanisms[1]

By FERDINAND FREUDENSTEIN,[2] NEW YORK, N. Y.

The symmetry inherent in four-link mechanisms has been used in deriving a general analytical expression relating the diagonals of a four-link mechanism by means of a characteristic parameter. The nature of this expression has been analyzed. The particular case obtained by using as a parameter the square root of the sum of the squares of the lengths of the links diminished by the sum of the squares of the diagonals, has been worked out in detail and the results reduced to a form believed to be useful in design work. Design applications have been considered.

NOMENCLATURE

The following nomenclature is used in this paper (units are in inches, radians, and seconds):

O_DO_A = horizontal fixed link, length a, O_A the left pivot, and O_D the right pivot

O_AO_B = driving crank, length b

O_BO_C = connecting rod, length c

O_CO_D = driven crank, length d

$\phi_{ab} = \phi = \angle O_DO_AO_B$, measured counterclockwise from O_AO_D

$\phi_{bc} = \phi' = \angle O_AO_BO_C$, measured counterclockwise from O_BO_A

$\phi_{cd} = \phi'' = \angle O_BO_CO_D$, measured counterclockwise from O_CO_B

$\phi_{da} = \phi''' = \angle O_CO_DO_A$, measured counterclockwise from O_DO_C

Q = point rigidly attached to O_BO_C, M-units from O_B, N-units from O_BO_C

$R = O_AQ$

$\alpha = \angle QO_AO_B$, measured counterclockwise from O_AQ

$\alpha' = \angle O_BQO_A$, measured counterclockwise from QO_A

$w = d\phi/dt$ = angular velocity of driving crank

t = time

v = velocity ratio = $d\phi'''/d\phi$

a = acceleration ratio = $d^2\phi'''/d\phi^2$

$x = O_BO_D^2$

$x' = O_CO_A^2$

INTRODUCTION

Having the minimum number of links required for determinate motion, the four-bar mechanism, Fig. 1, may be regarded as a fundamental mechanism—as a basic building block in terms of which other mechanisms can be analyzed. The four-bar mechanism is used in all types of machinery, ranging from locomotive drives to delicate computing instruments. Its universality is the result of several factors:

(a) Simplicity of the conception and of manufacture.

(b) Flexibility in design as a means of power and motion transmission.

(c) Adaptability to efficient operation at high speeds.

(d) High efficiency as a result of design for minimum backlash and friction.

The versatility of the four-bar mechanism has led to the development of a variety of design techniques. Since the introduction of the basic concepts of Reuleaux (1),[3] much work has been done on
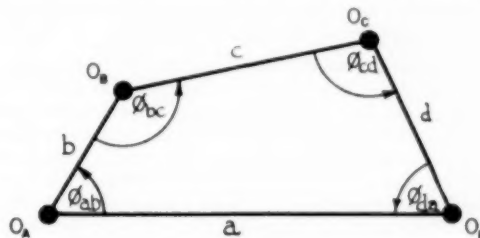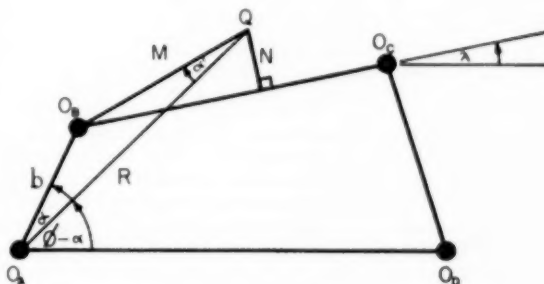

FIG. 1 FOUR-BAR LINKAGE

FIG. 2 FOUR-BAR LINKAGE SHOWING POINT Q RIGIDLY ATTACHED TO CONNECTING ROD

coupler curves (2), on the development of general design methods involving techniques in projective geometry (3), and on the adaptation of a theory of polynomials and other advanced methods to synthesis problems (4).

Advances made in this country during the past decade indicate the increasing importance of kinematical problems in which systematic methods are a prerequisite. Talbourdet (5) has published a mathematical analysis of four-bar linkages; Svoboda (6) has developed graphical methods for the design of computing linkages; and Miller (7) has used the diagonal to facilitate linkage computations. In these investigations, emphasis has been placed on immediate applicability to design rather than on basic analyses, although the need for the latter is realized (8). In the presentation which follows, basic geometry has been used in an attempt to develop an analysis, the results of which are sufficiently simple and direct to be of value in design.

[3] Numbers in parentheses refer to the Bibliography at the end of the paper.

METHODS

Basic Symmetry in a Four-Bar Linkage. The symmetry inherent in a four-bar linkage derives from the fundamental vector equation: $O_AO_B + O_BO_C + O_CO_D + O_DO_A = 0$. This equation remains invariant upon cyclical interchange of the letters A, B, C, D, i.e., $A \to B, B \to C, C \to D, D \to A$. Algebraically, this symmetry is contained in the following observations:

(a) Any equation relating a, b, c, d and $\phi_{ab}, \phi_{bc}, \phi_{cd}, \phi_{da}$ remains valid upon cyclical interchange of the letters a, b, c, d. Thus, for example, $a^2 + b^2 - 2ab\cos\phi_{ab} = c^2 + d^2 - 2cd\cos\phi_{cd}$ $(= O_BO_D{}^2)$; whence $b^2 + c^2 - 2bc\cos\phi_{bc} = d^2 + a^2 - 2da\cos\phi_{da}$ $(= O_CO_A{}^2)$.

(b) There exist parameters which can be expressed as symmetric functions of the sides a, b, c, d and the angles $\phi_{ab}, \phi_{bc}, \phi_{cd}, \phi_{da}$. Thus, for example, the area K, enclosed by the linkage, can be expressed in the form $K = \frac{1}{4}(ab \sin \phi_{ab} + bc \sin \phi_{bc} + cd \sin \phi_{cd} + da \sin \phi_{da})$ so that cyclical interchange of a, b, c, d leaves the numerical value of the area K unaltered. Parameters such as K will be referred to as symmetric parameters.

The nature of geometric configurations is often revealed by parametric rather than by direct equations. Consider the expression $\cos \phi_{ab} = f(a, b, c, d, P)$, where f is a continuous function of a, b, c, d, P, and P is a symmetric parameter which varies with ϕ_{ab}. The foregoing observation (a) states that if such a relation exists, there are three additional similar relations obtained by cyclical interchange of a, b, c, d in the relation $\cos \phi_{ab} = f(a, b, c, d, P)$. The foregoing observation (b) states that the parameter P will appear unchanged in each of these relations. Thus, symbolically, if

then

$$\cos \phi_{ab} = f(a, b, c, d, P)$$
$$\left.\begin{array}{l}\cos \phi_{bc} = f(b, c, d, a, P) \\ \cos \phi_{cd} = f(c, d, a, b, P) \\ \cos \phi_{da} = f(d, a, b, c, P)\end{array}\right\} \quad \ldots\ldots\ldots\ldots [1]$$

The symmetry in a four-bar linkage thus is used in setting up the parametric relationship of Equations [1]. This paper is concerned with the investigation of the functional nature of this relationship. Questions such as the following now may be asked: In what manner does the form of the function $f(a, b, c, d, P)$ depend on the choice of P? Are there any symmetric parameters which can obtain useful expressions for the angles? Can such formulations be reduced to reasonable design procedures? To answer these questions requires the development of some mathematical preliminaries.

Mathematical Development. The questions raised in the preceding paragraph lead to the consideration of functional equations, i.e., equations in which we are interested in the form of a function, rather than in a particular numerical value. The type of functional equation arising in linkage considerations, it is believed, has not been discussed in the mathematical literature. To solve these equations it has been found useful to introduce the idea of regarding cyclical interchange as an operation. A linear operator L can be defined as follows: L, operating on the function $f(a, b, c, d, P)$, yields the function $f(b, c, d, a, P)$. Symbolically, $Lf(a, b, c, d, P) = f(b, c, d, a, P)$. For example, if $f = a - b + c - d + P$, then $Lf = b - c + d - a + P$. A more familiar example of an operator is the differential operator $D = (d/dx)$.

The following notation is employed:

$$H(a, b, c, d, P) = H$$
$$H(b, c, d, a, P) = H' = LH$$
$$H(c, d, a, b, P) = H'' = L^2H$$
$$H(d, a, b, c, P) = H''' = L^3H$$

With the aid of this notation, the investigation of the parametric representation, Equation [1], can be reduced to the problem of solving a functional equation in the following manner:

Let $O_BO_D{}^2 = x = x(a, b, c, d, P)$; then $O_CO_A{}^2 = Lx = x' = x(b, c, d, a, P)$.[4] Furthermore, $x'' = L^2x = O_DO_B{}^2 = x$. As shown in A1[5] of the Appendix, the relationship between the diagonals is

$$(1 + L)\{(Lx)[x(x - \phi_1/2)] + \phi_2 x + \phi_3/2\} = 0 \ldots [2]$$

where

$$x = x(a, b, c, d, P)$$
$$\phi_1 = a^2 + b^2 + c^2 + d^2$$
$$\phi_2 = (a^2 - d^2)(b^2 - c^2)$$
$$\phi_3 = (a^2 - b^2 + c^2 - d^2)(a^2c^2 - b^2d^2)$$

Consider Equation [2] as a functional equation for x in terms of P. The problem then is: With a given choice of P (e.g., the area K, for instance), how is the form of the function $x = x(a, b, c, d, P)$ limited and determined by Equation [2]? Equation [2] is simpler than the direct relation between the angles ϕ_{ab}, ϕ_{da}. Knowing x and x', the angles can be determined from the relations $\cos \phi_{ab} = (a^2 + b^2 - x)/2ab$ and $\cos \phi_{da} = (a^2 + d^2 - x')/2da$.

Equation [2] has been solved by a method adapted from an example by Babbage (9). The general solution can be expressed in the form (A2)

$$C_1x^5 + C_2x^4 + C_3x^3 + C_4x^2 + C_5x + C_6 = 0 \ldots\ldots\ldots\ldots [3]$$

where

$$C_1 = (N - N')(M - \phi_2 N')$$

$$C_2 = \phi_1M(N' - 2N) + (N - N') + NN'(\phi_1\phi_2 - \phi_3) + \phi_2N'^2$$

$$C_3 = \phi_2{}^2N^2 + NN'(\phi_1\phi_3 - \phi_2\phi_2') + \phi_2(2N'M' - 2NM - NM') + \phi_1(N' - 2N) + \phi_2'(2NM - MN') + \phi_2{}^2NM + M^2 - MM'$$

$$C_4 = 2\phi_2\phi_3N^2 - \phi_2'\phi_3NN' + \phi_2(2N'M' - NM' - 2NM) - 2\phi_2N + \phi_1MM' - 2\phi_1\phi_2'NM + \phi_1\phi_2NM' + \phi_2{}^2N + \phi_2'(2N - N') - M' + 2M$$

$$C_5 = (1 - \phi_3N)^2 - \phi_2'MM' + \phi_2M'^2 + \phi_1M' + \phi_2'^2NM - \phi_2\phi_2'NM' - 2\phi_1\phi_2'N + \phi_1\phi_2NM'$$

$$C_6 = (M' - \phi_2'N)(\phi_2M' - \phi_2')$$

M, N = arbitrary functions of a, b, c, d, P

Equation [3] is considered a "solution" because by assigning arbitrary functions for M and N, the functional form of x in terms of a, b, c, d, P is given by Equation [3].

RESULTS

The form of the function $f(a, b, c, d, P)$ varies within certain limits, depending upon the particular choice of P (see A3). Equation [3] can be simplified to a quadratic form in x in two ways only and cannot be reduced further. These forms correspond to the choices $P = xx'$, and $P = \sqrt{a^2 + b^2 + c^2 + d^2 - (x + x')}$ (refer to A4). This paper is limited to a discussion of the latter expression.

THE CASE $P = \sqrt{a^2 + b^2 + c^2 + d^2 - (x + x')}$

Derivations and Interpretations. Table 1 lists displacements, velocity, and acceleration ratios in a four-bar mechanism, in terms of the parameter, $P = \sqrt{a^2 + b^2 + c^2 + d^2 - (x + x')}$. Equations

---

[4] See (a) under "Methods."

[5] Numbers prefaced "A" refer to similarly numbered paragraphs in the Appendix.

[4] to [11] are basic. To use these equations, P is given an arbitrary value and the angles are determined from it.

In the alternate formulations of Equations [16] and [17], the square-root term is symmetric and the sign of the root alternates during cyclical interchange of a, b, c, d (see A5). The significance of these and succeeding equations hinges on the geometrical meaning of P, Fig. 3. P is constructed as follows: Take any two adjacent links and form a parallelogram with these as sides. Draw a straight line joining that vertex of the parallelogram not belonging to the linkage (the M's), to that linkage pivot not already belonging to the parallelogram (the O's). This line segment has the length P. Thus there are four different ways of constructing P (see Fig. 3) as is to be expected from symmetry considerations.

Each of the four auxiliary angles A, B, C, D appears four times in Fig. 3, although for the sake of clarity each is shown just once. The arrow indicates the positive sense of description. From Fig. 3, $A = \angle O_A M_D O_D$, $B = |LA| = \angle O_C O_D M_D$, $C = |L^2 A| = \angle M_D O_D O_A$, $D = |L^3 A| = \angle O_D M_D O_C$. The displacements and velocity ratios listed in Table 1 possess immediate geometrical significance, and similar equations are derivable from each other by cyclical rotation of a, b, c, d.

A number of properties of four-bar mechanisms follow from the geometrical interpretation. These will facilitate use of the formulas in Table 1 in design applications.

1 The range of P is within the intermediate two of the absolute values of $a - c$, $a + c$, $b - d$, $b + d$ (see A6).

2 At extreme values of P, the two cranks are parallel and the connecting rod has zero angular velocity ($P = b \pm d$), or the connecting rod is parallel

TABLE 1   DISPLACEMENT, VELOCITY, AND ACCELERATION RELATIONSHIPS IN A FOUR-BAR LINKAGE

Displacements

$$\cos A = \frac{P^2 + c^2 - a^2}{2cP} \quad\dots\dots\quad [4]$$

$$\cos B = L \cos A = \frac{P^2 + d^2 - b^2}{2dP} \quad\dots\quad [5]$$

$$\cos C = L^2 \cos A \quad\dots\dots\quad [6]$$

$$\cos D = L^3 \cos A \quad\dots\dots\quad [7]$$

$$\phi = D - C \quad\dots\dots\quad [8]$$

$$\phi' = -(A + D) \quad\dots\dots\quad [9]$$

$$\phi'' = -(B - A) \quad\dots\dots\quad [10]$$

$$\phi''' = C + B \quad\dots\dots\quad [11]$$

$$|\phi| = |D - C| \quad\dots\dots\quad [12]$$

$$|\phi'| = |A + D| \quad\dots\dots\quad [13]$$

$$|\phi''| = |B - A| \quad\dots\dots\quad [14]$$

$$|\phi'''| = |C + B| \quad\dots\dots\quad [15]$$

$$\cos \phi_{ab} =$$
$$\frac{(P^2 + a^2 - c^2)(P^2 + b^2 - d^2) \pm \sqrt{[P^2 - (a-c)^2][P^2 - (a+c)^2][P^2 - (b-d)^2][P^2 - (b+d)^2]}}{4abP^2} \dots [16]$$

$$\cos \phi_{bc} =$$
$$\frac{(P^2 + b^2 - d^2)(P^2 + c^2 - a^2) \mp \sqrt{[P^2 - (a-c)^2][P^2 - (a+c)^2][P^2 - (b-d)^2][P^2 - (b+d)^2]}}{4bcP^2} \dots [17]$$

$$\cos \phi_{cd} = L^2 \cos \phi_{ab} \quad\dots\dots\quad [18]$$

$$\cos \phi_{da} = L^3 \cos \phi_{ab} \quad\dots\dots\quad [19]$$

$$P^2 = a^2 + c^2 - 2ac \cos (a, c) \quad\dots\quad [20]$$

$$P^2 = b^2 + d^2 - 2bd \cos (b, d) \quad\dots\quad [21]$$

Velocity Ratios

$$v = \frac{d\phi'''}{d\phi} = \frac{b}{d} \frac{\sin (A + D)}{\sin (A - B)} \quad\dots\dots\quad [22]$$

$$v' \text{ or } Lv = \frac{d\phi}{d\phi'} = \frac{c}{a} \frac{\sin (B - A)}{\sin (B + C)} \quad\dots\quad [23]$$

$$v'' \text{ or } L^2v = d\phi'/d\phi'' \quad\dots\dots\quad [24]$$

$$v''' \text{ or } L^3v = d\phi''/d\phi''' \quad\dots\dots\quad [25]$$

Acceleration Ratios

(*w* is assumed constant)

$$a = \frac{d^2\phi'''}{d\phi^2} = (-v/v') \left[\cot (A + D) - \frac{\cot (A - B)}{v''} \right] \quad\dots\quad [26]$$

$$a' = d^2\phi/d\phi'^2 = La \quad\dots\dots\quad [27]$$

$$a'' = d^2\phi'/d\phi''^2 = L^2a \quad\dots\dots\quad [28]$$

$$a''' = d^2\phi''/d\phi'''^2 = L^3a \quad\dots\dots\quad [29]$$

Motion of Point Rigidly Attached to Connecting Rod

(Fig. 2) *w* = const.

$$v_R = dR/dt = wb \sin \alpha/v' \quad\dots\dots\quad [30]$$

$$w_q = d\phi/dt - d\alpha/dt = w + v_R \cot \alpha'/R \quad\dots\quad [31]$$

$$a_R = d^2R/dt^2 = (wb/v')[(w - w_q)\cos \alpha - v_R a'/bv'] \quad\dots\quad [32]$$

$$a_q = dw_q/dt = \cos \alpha' \left[a_R/R - (v_R^2/R^2) \frac{1 - 2 \cot \alpha}{\sin 2\alpha'} \right] \quad\dots\quad [33]$$

Angular Velocity of Connecting Rod

$$\frac{d\lambda}{d\phi} = 1 + \frac{a}{c} \frac{\sin (B + C)}{\sin (B - A)} \quad\dots\dots\quad [34]$$
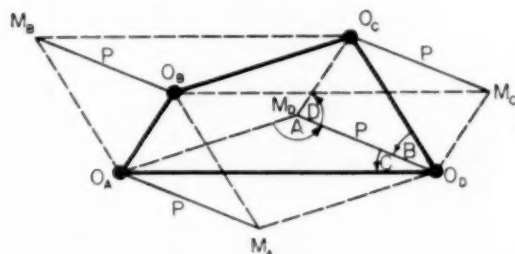

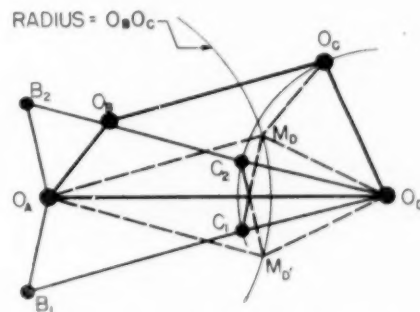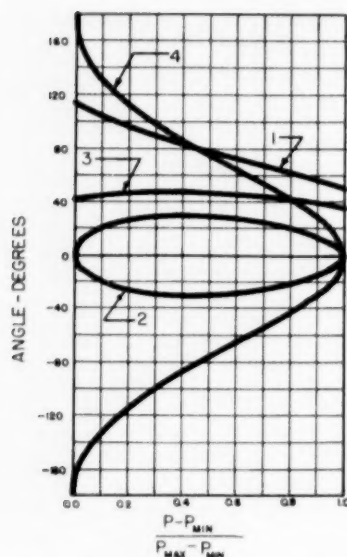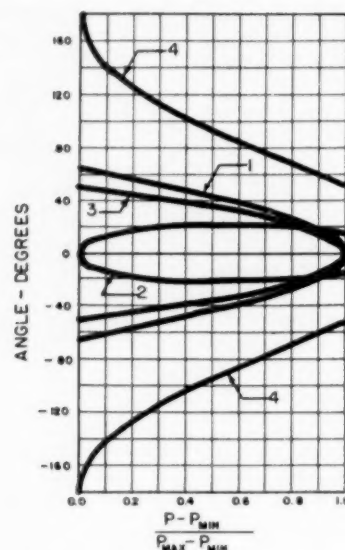FIG. 3   GEOMETRICAL INTERPRETATION OF P

FIG. 4   CONSTRUCTION OF LINKAGES HAVING SAME VALUE OF P

FIG. 5   VARIATION OF AUXILIARY ANGLES WITH P—PURE LIMITS

FIG. 6   VARIATION OF AUXILIARY ANGLES WITH P—MIXED LIMITS

TABLE 2   VARIATION OF AUXILIARY ANGLES WITH P—FOR USE WITH FIGS. 5 AND 6

				Corresponding linkage			
Angle 1	Angle 2	Angle 3	Angle 4	$O_D O_A$	$O_A O_B$	$O_B O_C$	$O_C O_D$
A	B	C	D	a	b	c	d
A	D	C	B	a	d	c	b
C	B	A	D	c	b	a	d
C	D	A	B	c	d	a	b
B	C	D	A	b	c	d	a
B	A	D	C	b	a	d	c
D	C	B	A	d	c	b	a
D	A	B	C	d	a	b	c

TABLE 3   DISPLACEMENTS IN LINKAGES OBTAINED BY PERMUTATION OF LINKS OF A GIVEN LINKAGE

No.	$O_A O_B$	$O_B O_C$	$O_C O_D$	$O_D O_A$	ϕ	ϕ'	ϕ''	ϕ'''	P
1	b	c	d	a	$D - C$	$-(A + D)$	$-(B - A)$	$C + B$	
2	c	d	a	b	$-(A + D)$	$-(B - A)$	$C + B$	$D - C$	$M_D O_D$
3	d	a	b	c	$-(B - A)$	$C + B$	$D - C$	$-(A + D)$	
4	a	b	c	d	$C + B$	$D - C$	$-(A + D)$	$-(B - A)$	
5	b	a	d	c	$D - A$	$-(C + D)$	$-(B - C)$	$A + B$	
6	a	d	c	b	$-(C + D)$	$-(B - C)$	$A + B$	$D - A$	$M_D O_D$
7	d	c	b	a	$-(B - C)$	$A + B$	$D - A$	$-(C + D)$	
8	c	b	a	d	$A + B$	$D - A$	$-(C + D)$	$-(B - C)$	
9	b	d	c	a	$D - C$	$\pi - (B + D)$	$B - A$	$\pi + (A + C)$	
10	d	c	a	b	$\pi - (B + D)$	$B - A$	$\pi + (A + C)$	$D - C$	or
11	c	a	b	d	$B - A$	$\pi + (A + C)$	$D - C$	$\pi - (B + D)$	$O_D O_B$
12	a	b	d	c	$\pi + (A + C)$	$D - C$	$\pi - (B + D)$	$B - A$	
13	b	c	a	d	$\pi + (B + D)$	$-(A + D)$	$\pi + (A + C)$	$-(B + C)$	$O_A O_C$
14	c	a	d	b	$-(A + D)$	$\pi + (A + C)$	$-(B + C)$	$\pi + (B + D)$	or
15	a	d	b	c	$\pi + (A + C)$	$-(B + C)$	$\pi + (B + D)$	$-(A + D)$	$O_D O_B$
16	d	b	c	a	$-(B + C)$	$\pi + (B + D)$	$-(A + D)$	$\pi + (A + C)$	
17	b	a	c	d	$\pi + (B + D)$	$C - D$	$\pi - (A + C)$	$A - B$	$O_A O_C$
18	a	c	d	b	$C - D$	$\pi - (A + C)$	$A - B$	$\pi + (B + D)$	or
19	c	d	b	a	$\pi - (A + C)$	$A - B$	$\pi + (B + D)$	$C - D$	$O_D O_B$
20	d	b	a	c	$A - B$	$\pi + (B + D)$	$C - D$	$\pi - (A + C)$	
21	b	d	a	c	$A + D$	$\pi - (B + D)$	$B + C$	$\pi - (A + C)$	$O_A O_C$
22	d	a	c	b	$\pi - (B + D)$	$B + C$	$\pi - (A + C)$	$A + D$	or
23	a	c	b	d	$B + C$	$\pi - (A + C)$	$A + D$	$\pi - (B + D)$	$O_D O_B$
24	c	b	d	a	$\pi - (A + C)$	$A + D$	$\pi - (B + D)$	$B + C$	

to the fixed link and the cranks have the same angular velocity $(P = a \pm c)$.

3 In general, two linkage configurations exist for each value of P. These two positions have parallel connecting rods or the same angle between cranks.

The locus of P, Fig. 4, can be regarded as that of a vector, one end of which is fixed at O_D and the other end of which is moving on a circle, center O_A, radius c. The two positions having the same value of P can be constructed from the given position in the following way:

(a) $O_C O_D$ and $M_D O_C$ are reflected about $M_D O_D$. The resulting linkage is $O_A B_1 C_1 O_D$ and the connecting rods are parallel.

(b) $M_D O_D$ is reflected about the fixed link. The resulting linkage is $O_A B_2 C_2 O_D$ and $\angle M_D O_C O_D = \angle M_D' C_2 O_D$. Complete reflections are not considered here.

4 An auxiliary angle, as defined by Equations [4] to [7], may be positive or negative, anywhere between -180 deg and $+180$ deg, if the letter denoting the angle appears in the limits for P (as per property 1). If not, only the positive value is permitted.

5 Classification of linkages: In a crank and rocker linkage, $d - b \le P \le d + b$, b is the smallest link, $P(O_D M_D)$ does not cross the line of centers, Fig. 4, and alternate positions having the same value of P are obtained as per 3(a) in the foregoing properties. In a drag link mechanism, $c - a \le P \le c + a$, a is the shortest link, the moving end of $P(M_D)$ generates a complete circle, and alternate positions having the same value of P are obtained as per 3(b). The inversion here is evident. In a double-rocker linkage, the limits of P are either the same as the preceding (pure limits), or involve all four sides (mixed limits). Mixed limits are either $|a - c| \le P \le |b + d|$ or $|b - d| \le P \le |a + c|$.

6 Variation of the auxiliary angles with P: Figs. 5 and 6 show the variation of the auxiliary angles with P of the two basic types of linkages (pure limits and mixed limits). Linkage types other than those shown, can be obtained by interchange and inversion of angles and correspondingly named sides, Table 2.

7 Inversions and permutations of the links: Table 3 lists 24 linkages, displacements of which are obtainable by the knowledge of the values of the auxiliary angles of just one (the given) linkage.

Applications. Applications of the foregoing arise in the fields of machine design and computer design, both in cases where it has been customary to use an analytical approach as well as in cases in which the complexity of an analysis would have rendered such an analysis impractical. Examples will be given.

In the usual type of application, the parameter P is chosen at random; the auxiliary angles then are determined from Equations [4] through [7] and these values are used in the expressions derived for the mechanism under review.

Example: Calculate the displacements of driving and driven cranks in a four-bar linkage in which $a = 1$, $b = 4$, $c = 3$, $d = 5$. From Equations [4] through [7], $\cos A = (P^2 + 8)/6P$; $\cos B = (P^2 + 9)/10P$; $\cos C = (P^2 - 8)/2P$; $\cos D = (P^2 - 9)/8P$. From property 1, $2 \le P \le 4$. From property 4, A, C may be positive or negative, and B, D only positive. From property 5, this is seen to be a drag link mechanism. From Equations [12] and [15], $\phi_{ab} = D - C$ and $\phi_{da} = C + B$.

An intermittent motion mechanism known as the three-gear drive is shown in Fig. 7 (10). It is used in tobacco machinery to obtain a momentary dwell of the output gear, N_3. Gear N_1 is fixed to the drive crank and gears N_2 and N_3 are free to rotate about their centers O_C and O_D. N_1, N_2, N_3 represent the numbers of teeth of each gear as well as serving to identify them. Table 4 lists the pertinent formulas for this mechanism (previously considered too unsuited for analysis) and those which are described in the following.

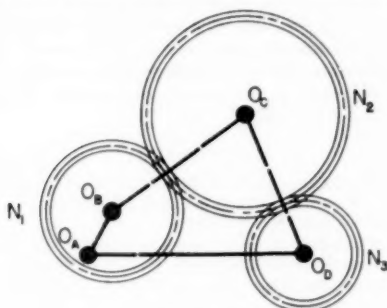Toggle mechanisms, such as the one shown in Fig. 8, are used

FIG. 8 TOGGLE MECHANISM
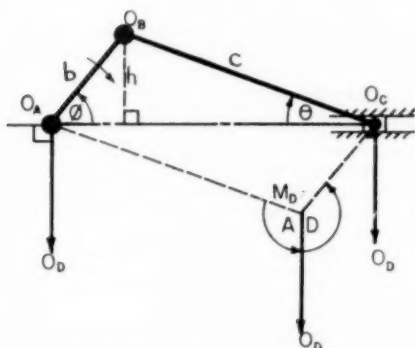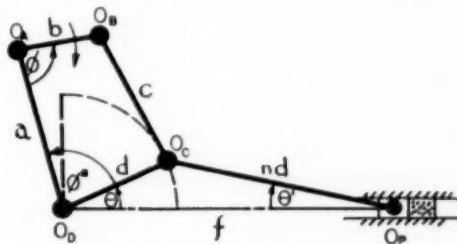

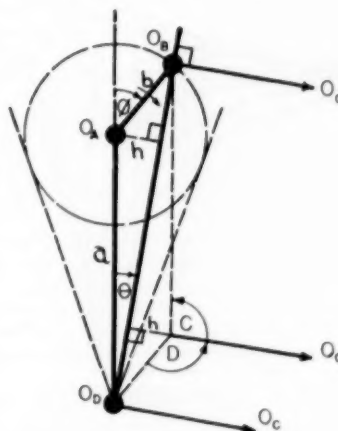FIG. 7 THREE-GEAR DRIVE

FIG. 9 SLIDER-CRANK MECHANISM

FIG. 10 WHITWORTH QUICK-RETURN MECHANISM

TABLE 4   FORMULAS FOR VARIOUS LINKAGE MECHANISMS

4-1 Three-Gear Drive (Fig. 7)

$$\phi = D - C \dotfill [35]$$

Rotation of gear N_3

$$\theta = \frac{N_1 + N_2}{N_3} A - \frac{N_3 + N_2}{N_3} B - C + \frac{N_1}{N_3} D \dotfill [36]$$

$$\text{Velocity ratio} = \frac{d\theta}{d\phi} = N_2/N_3 + \frac{N_1 + N_2}{N_3 v'} + \frac{N_1 + N_3}{N_3} v \dotfill [37]$$

4-2 Toggle Mechanism (Fig. 8)

$$\text{Mechanical advantage} = \cot \theta'/v f \dotfill [38]$$
$$f = d(\cos \theta + n \cos \theta') \dotfill [39]$$
$$\sin \theta = n \sin \theta' \dotfill [40]$$
$$\phi''' + \theta = \text{const} \dotfill [41]$$

4-3 Slider-Crank Mechanism (Fig. 9)

$$a - P = h \dotfill [42]$$
$$\cos B = \cos C = 1 \dotfill [43]$$
$$\sin \phi = - \cos D = h/b \dotfill [44]$$
$$\sin \theta = - \cos A = h/c \text{ as is well known} \dotfill [45]$$

4-4 Whitworth Quick-Return Mechanism (Fig. 10)

$$\cos A = \cos B = 1 \dotfill [46]$$
$$\cos C = -h/a \dotfill [47]$$
$$\cos D = -h/b \dotfill [48]$$
$$\sin \theta = h/a \dotfill [49]$$
$$\phi = C + D - 180° \dotfill [50]$$
$$\text{Velocity ratio} = d\theta/d\phi = 1/(1 + \tan C \cot D) \dotfill [51]$$

4-5 Problems Involving Inclination of Connecting Rod (Fig. 2)   (λ given)

$$P^2 = a^2 + c^2 - 2ac \cos \lambda \dotfill [52]$$

4-6 Equal Crank Linkages $(b = d)$

$$B = D = \cos^{-1}(P/2b) \dotfill [53]$$

4-7 Linkages in Which Fixed Link Has Same Length as Connecting Rod

$$(a = c) \quad A = C = \cos^{-1}(P/2a) \dotfill [54]$$

4-8 Linkages in Which $a^2 - c^2 = \pm(b^2 - d^2)$

If $a^2 - z^2 = +(b^2 - d^2)$

$$\frac{\cos C}{\cos D} = \frac{b}{a} \dotfill [55]$$

$$\frac{\cos A}{\cos B} = \frac{d}{c} \dotfill [56]$$

If $a^2 - c^2 = -(b^2 - d)^2$

$$\frac{\cos C}{\cos B} = \frac{d}{a} \dotfill [57]$$

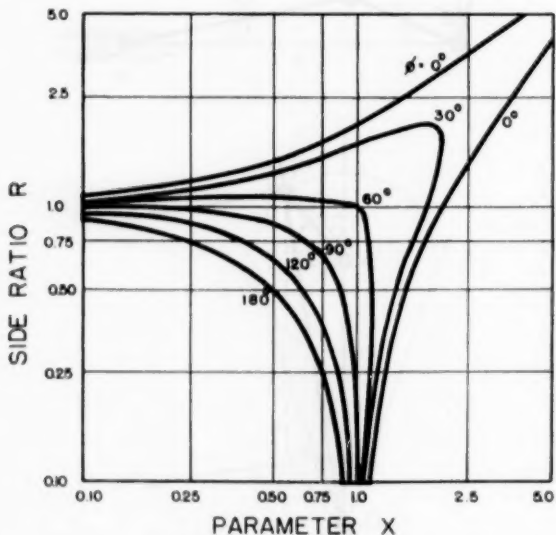$$\frac{\cos A}{\cos D} = \frac{b}{c} \dotfill [58]$$

FIG. 11   GRAPH OF $\phi = \cos^{-1} \dfrac{X^2 + R^2 - 1}{2RX}$ ON LOGARITHMIC CO-ORDINATE PAPER

in crushing and coining operations, where a large mechanical advantage is desired (4-2 in Table 4).

The familiar slider-crank mechanism, Fig. 9 (4-3 in Table 4), and Whitworth quick-return mechanism, Fig. 10 (4-4), can be analyzed. The equations assume a determinate form with the introduction of a new parameter, h.

Certain special problems are suited to this form of analysis. Among these are problems involving the inclination of the connecting rod (4-5), equal crank linkages (4-6), linkages in which the fixed link has the same length as the connecting rod (4-7), and linkages in which $a^2 - c^2 = \pm(b^2 - d^2)$ as noted in (4-8), Table 4.

The symmetry of the formulas in Table 1 is believed to be useful in evaluation by machine methods of computation, such as, for example, those involving punched-card machines.

The auxiliary angles A, B, C, D can be used to simplify the calculations in problems in vibrations, dynamics, and balancing, in which solutions already exist.

Graphical techniques can be developed. Fig. 11, for example, shows a graph of

$$\phi = \cos^{-1} \frac{X^2 + R^2 - 1}{2RX}$$

A transparent overlay, consisting of four points representing one set of corresponding values of A, B, C, D, will generate all corresponding values of these angles if moved across the graph, parallel to the X-axis (A7). An enlarged version of this graph may be used to determine displacements without calculations, or to ascertain the effects of changes in linkage proportions.

BIBLIOGRAPHY

1 "The Kinematics of Machinery," by F. Reuleaux, translated by A. B. W. Kennedy, Macmillan and Company, Ltd., London, England, first English edition, 1876.

2 "On Three-Bar Motion," by A. Cayley, Proceedings of the London Mathematical Society, vol. 7, 1876, pp. 136–166.

3 "Lehrbuch der Kinematik," by L. E. A. Burmester, A. Felix, Leipzig, Germany, 1888.

4 "Are the Russians Ahead in Mechanism Analysis?" by A. E. R. de Jonge, Machine Design, vol. 23, September, 1951, pp. 127, 200–208.

5 "Mathematical Solution of 4-Bar Linkages," by G. J. Talbourdet, Machine Design, vol. 13, May, 1941, pp. 65–68; June, 1941, pp. 81–82; July, 1941, pp. 73–77.

6 "Computing Mechanisms and Linkages," by A. Svoboda, M.I.T. Radiation Series, vol. 27, McGraw-Hill Book Company, Inc., New York, N. Y., first edition, 1948.

7 "Analysis of Quadric-Chain Mechanisms," by H. Miller, Product Engineering, vol. 22, February, 1951, pp. 109–113.

8 "What Is Wrong With Kinematics and Mechanisms?" by A. E. R. de Jonge, Mechanical Engineering, vol. 64, 1942, pp. 273–278.

9 "Examples of the Solutions of Functional Equations," by C. Babbage, London, 1820, published by J. Deighton, and Sons, Cambridge, England, and bound together with "A Collection of Examples of the Applications of the Calculus of Finite Differences," by Sir John F. W. Herschel, London, 1820.

10 "Kinematics of Intermittent Mechanisms, the Three-Gear Drive," by S. Rappaport, Product Engineering, vol. 21, January, 1950, pp. 120–123.

Appendix

A1 From the cosine rule for triangles

$$x = a^2 + b^2 - 2ab \cos \phi_{ab} \dots \dots \dots [59]$$

$$x' = d^2 + a^2 - 2da \cos \phi_{da} \dots \dots \dots [60]$$

Equate for c^2 using Pythagoras' Theorem to combine the projections of c parallel to and perpendicular to a

$$c^2 = (d \sin \phi_{da} - b \sin \phi_{ab})^2 + (a - b \cos \phi_{ab} - d \cos \phi_{da})^2 \dots [61]$$

Substitute x and x' for ϕ_{ab} and ϕ_{da}, using Equations [59] and [60], into Equation [61]. The result after simplification is

$$x^2 x' + x x'^2 - \phi_1 x x' + \phi_2 x + \phi_2' x' + \phi_3 = 0 \dots [62]$$

Equation [2], when expanded, is identical to Equation [62].

A2 Some functional equations can be treated as simultaneous equations by using the operator L, to obtain additional independent equations. Equation [2], however, cannot be solved in this manner. The generalized equation $(Lx)x(Ax + BLx - C) + Dx + ELx + F = 0$ can be set up, where, following the procedure of Babbage,[6] $A = 1 + mA$, $B = 1 + mB$, $C = \phi_1 + mC$, $D = \phi_2 + mD$, $E = \phi_2' + mE$, $F = \phi_3 + mF$; A, B, C, D, E, F, are arbitrary functions of a, b, c, d, P, and m is a number. If $m = 0$, the generalized equation becomes identical to Equation [2]. A second independent equation is now obtainable by operating with L on the generalized equation, so that we now have two simultaneous equations in x and x'. The solution can be obtained by consideration of the limiting case $m = 0$. The first nonvanishing set of terms will be found to be of order m^3.

A shorter method is available. If the two simultaneous equations in x and x' are subtracted from each other, a relation occurs which is independent of m. This relation is, therefore, valid in the limiting case $m = 0$, and can be solved simultaneously with Equation [2]. When this is done, the number of arbitrary functions can be reduced to two, as shown in Equation [3], by means of the substitutions

$$A = 1 \qquad N = \frac{\dfrac{B}{C' - C} + \dfrac{1}{\phi_1}}{\dfrac{\phi_2}{\phi_1} + \dfrac{F - F'}{C' - C}} \qquad M = \frac{\dfrac{\phi_2}{\phi_1} + \dfrac{D - E'}{C' - C}}{\dfrac{\phi_2}{\phi_1} + \dfrac{F - F'}{C' - C}}$$

A3 It can be shown that no representation exists which is rational in P, a, b, c, d. Furthermore, if the value of P at $\phi = 0$ deg is to be the same as the value of P at $\phi = 360$ deg, then f cannot be single-valued.

A4 $N = N'$, $M = \phi_2 N$, $P = \phi_2/\phi_1 - 1/\phi_1 N$ for the former, and $N = 0$, $M = M'$, $P^2 = \phi_1 + 1/M$ for the latter.

A5 This is to be expected, as the root term equals: $x^2 - x'^2 + \phi_1(x' - x) + \phi_2' - \phi_2$.

A6 Properties 1 and 2 are understood easily by considering P as the diagonal of the transposed four-bar linkage with b, c interchanged.

A7 Based on the fact that the expressions for the auxiliary angles assume the form $\phi = \cos^{-1}(X^2 + R^2 - 1)/(2XR)$, by means of the following substitutions:

Angle	Parameter, X	Side ratio, R
A	$(c/a)x$, $x = P/a$	c/a
B	$(a/b)x$	d/b
C	$(a/c)x$	a/c
D	$(a/d)x$	b/d

[6] Reference (9), pp. 10–13.

Discussion

A. E. RICHARD DE JONGE.[7] When the writer in one of his papers, some 12 years ago, drew attention to the very neglected study of kinematics and mechanisms in this country (8)[8] he did so for the purpose of stimulating interest in the study of these sciences. His continued efforts in this direction in the intervening years have caused a number of engineers, educators, and students to take these studies up again. He has had the satisfaction of having been approached and consulted by many on various phases of these sciences. In general, the questions asked and the subjects discussed concerned details, such as how to obtain velocities, accelerations, curvatures, and so on, in relatively simple as well as some very complex mechanisms, or they concerned references to the literature.

While in other countries, as in Germany and Russia, basic work has been done, as the writer has pointed out, for the latter country in an article (4), scarcely any work published in this country has come to his notice, which deals with more fundamental aspects of these sciences, or of parts thereof. References (5, 6, 7) of the author's paper dealing with certain phases of these sciences cannot possibly be called fundamental.

It is, therefore, refreshing to find a paper like the present one written by one of the junior members of the Society. He, too, is one of those who got in touch with the writer, and although we had not met personally until the meeting at which the paper was presented, we had carried on lengthy telephonic conversations on various subjects for several years. The writer's interest in him was aroused, because he, as a student, showed a vivid interest in kinematics and mechanisms.

The author's investigations have not always been plain sailing. At one time it looked as if they might fail. The writer, however, encouraged him not to drop them, and it is a great pleasure to see that they have now been carried to a successful conclusion. His present paper is the first of two submitted to the Society, and the writer hopes that the author will continue his work and submit to this Society in the future the results of further investigations.

The author has treated of four-bar linkages in an analytical and completely new way. While his work uses some of the concepts found in papers by G. J. Talbourdet (5), H. Miller (7), and F. Bowman,[9] the author has not followed their more or less conventional methods, but has invented a completely new method which may be called that of "cyclic interchange of symbols." In adopting this idea, he was forced to develop a new type of "operational calculus" especially suited to the investigation of four-bar mechanisms. While this calculus may not seem to be very complicated, the ideas and their execution are certainly novel, and what their introduction has meant in actual work can be appreciated only by those who will try to repeat it, or even try only to verify the equations presented by the author.

This new method allows one to obtain basic values for four-bar mechanisms in a relatively simple way by calculation, which is necessary when great accuracy is required as, for instance, in computer work or military work. This is now simple when the equations arrived at by the author are known. The method allows one also to obtain, from one such mechanism investigated, immediately, by cyclic interchange of symbols, the same or similar values for all other mechanisms that may be formed with the same four bars even in different sequence. Thus it gives not only the results for the inversions of a specific four-bar linkage, but also those for all other mechanisms that may be composed

[8] Numbers in parentheses refer to the author's bibliography.

[9] "The Plane Four-Bar Linkage," by F. Bowman, Proceedings of the London Mathematical Society, series 2, March, 1952, pp. 135–146.

of the same four bars, but in some other sequence. This yields $4.3.2.1 = 4!$ (factorial) $= 24$ different mechanisms, as shown in the author's Table 3.

The whole method is based on his fundamental Equation [2] which, unfortunately, has not been derived in the paper because of space restrictions. The derivation is only indicated in Appendix (A1) and leads to Equation [62] after very lengthy and cumbersome calculations and transformations. Although differing in form from Equation [2], it is essentially the same, as can be shown readily. Both these equations have been derived independently by the writer and have been found to be accurate.

As stated by the author, the general solution of this symmetrical functional equation has been accomplished by means of a trick used in an old paper by C. Babbage (9) in 1820. It is to the great credit of the author that, by patient searching, he has unearthed this interesting paper on the solution of symmetric functional equations.

The solution leads directly to the fifth degree Equation [3], although the proof has been omitted again because of space limitations. This is particularly regrettable, as it will make the paper difficult to understand by the average engineer.

The author then states that Equation [3] can be reduced to a quadratic form, but no further, that is, not to a linear form. The proof, again, had to be suppressed for the reason stated. The derivation of the quadratic form is based on two particular choices for the symmetric parameter P. How the second form of this parameter, that is, the square root, which is used in the remainder of the paper, can be easily constructed geometrically from Fig. 3, has not been properly explained. It would be very useful if, in his closure, the author could give all of the derivations and proofs and thus make the paper a really valuable contribution to the art.

The interpretations 1 to 7 are all too brief and require further elucidation possibly by accompanying figures, and the same holds for the "classification of linkages" (which should rather read "classification of mechanisms"). Likewise, the necessity for using "auxiliary angles" should be explained more in detail, as should the geometrical interpretation of the symmetric parameter P as a geometrical length, obtainable easily by means of vectors.

The use of parallelograms in Figs. 3 and 4 is not new. Bowman[9] has made use of them, and long ago, in 1908, W. Hartmann, in Germany, used them to obtain the so-called "supplementary mechanisms" which greatly facilitate the derivation of the acceleration components in four-bar linkages.

The "applications," which really form the most important part, certainly require more detailed descriptions and explanations.

In obtaining the auxiliary angles B, C, D from A by means of the first, second, and third cyclic interchange of symbols, it should be pointed out that the cyclic interchange of symbols refers to the cosines of the angles and not to the angles given by three points.

Table 4 requires a good deal of amplification and explanation to make it useful.

In general, it should be stated that the author's new method, although it is difficult to derive, is very much shorter in actual calculations than are the conventional ones, for example, that by Talbourdet.

While the writer considers the new method, as such, praiseworthy, there are a few minor points which have to be criticized adversely.

For example, there are the cumbersome symbols used for the joints and angles. The O's and ϕ's could have been omitted without loss in generality, and the paper would thereby have become easier to read.

Table 3 starts under No. 1 with $b\,c\,d\,a$. This could have been avoided without loss in generality by designating the crank by a, the coupler (or connecting rod) by b, the lever by c, and the frame (or fixed link) by d, thus resulting in a perfectly natural starting mechanism $a\,b\,c\,d$. This would agree with the European method of designation. The writer has said lever and not "driven crank," for a crank is a link that performs a full revolution relative to the adjoining fixed link, which a lever does not.

Highly unfortunate is the author's choice of the symbol L for the new operator, as this conflicts with the symbol L used for the Laplace transform operator used for many years and may lead to confusion.

In Table 1 the author lists "velocity" and "acceleration ratios." He does not mean "linear velocity" and "linear acceleration" ratios, but rather "angular" velocity and acceleration ratios. This should be made perfectly clear.

To sum up, in the writer's opinion the paper is an outstanding contribution to the science of kinematics, and the young author should be highly commended on it.

AUTHOR'S CLOSURE

The author is grateful to Mr. de Jonge for his penetrating and constructive comments. There are as yet few people who are versed in the science of kinematics and the author is therefore particularly appreciative of the interest taken by Mr. de Jonge in this work and the encouragement and advice given by him to the author during the past four years.

It is quite true that in order to conform to ASME regulations, the paper was condensed to the extent that most of the derivations were omitted. The more important of these will be given in this closure. It is noteworthy, however, that all of the results of this paper can be derived using only the geometrical interpretation of P without recourse to previous symmetry considerations or the mathematical development. Indeed, this is the manner in which the results are intended to be used. And now to the derivations:

1   Proof of the geometrical interpretation of P.
Referring to Fig. 3, let

$$\vec{a} = \text{vector } O_D O_A, \text{ length equal to "}a\text{"}$$
$$\vec{b} = \text{vector } O_A O_B, \text{ length equal to "}b\text{"}$$
$$\vec{c} = \text{vector } O_B O_C, \text{ length equal to "}c\text{"}$$
$$\vec{d} = \text{vector } O_C O_D, \text{ length equal to "}d\text{"}$$

$$x = O_B O_D{}^2 = a^2 + b^2 - 2ab\cos(a, b)$$
$$= c^2 + d^2 - 2cd\cos(c, d)$$
$$= \tfrac{1}{2}(a^2 + b^2 + c^2 + d^2) - ab\cos(a, b)$$
$$- cd\cos(c, d)$$

Hence $x' = O_C O_A{}^2 = \tfrac{1}{2}(a^2 + b^2 + c^2 + d^2)$
$$- bc\cos(b, c) - da\cos(d, a)$$

By addition and transposition

$$(a^2 + b^2 + c^2 + d^2) - (x + x') = ab\cos(a, b) + bc\cos(b, c)$$
$$+ cd\cos(c, d) + da\cos(d, a) \quad [i]$$

From Fig. 3, however
$$P^2 = O_D M_D{}^2 = (M_D O_C +\!\!\to O_C O_D) \cdot (M_D O_A +\!\!\to O_A O_D) \text{ where}$$
the $(+\!\!\to)$ sign denotes vector addition and the dot $(\cdot)$ signifies the scalar vector product.

Hence $P^2 = -(\vec{b} +\!\!\to \vec{d}) \cdot (\vec{a} +\!\!\to \vec{c})$
$$= ab\cos(a, b) + bc\cos(b, c) + cd\cos(c, d)$$
$$+ da\cos(d, a)$$

which is identical to the right-hand side of Equation [i].   Q.E.D.

In the section entitled Derivations and Interpretations, properties 1 to 7 are based on visualization and understanding of the geometrical interpretation of P and Figs. 1 to 6.   These properties will now be considered further:

2.   Property 1: Range of P.

The parameter P can be regarded as the diagonal of the transposed linkage in which the connecting rod and the driving link are interchanged.   The range limits of diagonals of a four-bar linkage have been given by Svoboda, reference (6), pp. 108–112.   The limits given in this paper are based on Svoboda's results.   Extreme values of the diagonals occur when links a, c or links b, d are parallel to each other and these are the only possible extreme-value conditions.   Hence we obtain the quantities $|a \pm c|$ and $|b \pm d|$ within the intermediate two of the absolute values of which P must be confined.   Equations [20] and [21] of Table 1 yield the same result when $\cos(a, c)$ or $\cos(b, d)$ is equal to plus or minus unity.

3   Property 2: Extreme Values of P.

When $P = |b \pm d|$, $M_D O_C$ (Fig. 3) must be parallel to $O_C O_D$. The cranks must therefore be parallel.   The instant center of the four-bar linkage is therefore a point at infinity and as a result the connecting rod has zero angular velocity.   Similar reasoning leads to the stated results when $P = |a \pm c|$.   These results can be derived also by means of Equations [20], [21], 22], and [34] of Table 1.

4   Property 3: Linkage Configurations Having the Same Value of P.

The proof of this property can be derived by an examination of the construction given in the paper, with reference to Fig. 4, and is self-explanatory.   Equations [16] and [17] of Table 1 show that the displacements are doubled-valued functions of the parameter P so that at least one of the constructions listed must apply to a given linkage.

5   Properties 4, 5, and 6.

These properties are connected with the fundamental classification of linkage mechanisms stated in property 5.   This classification exhibits the basic nature of the parameter P.   The equivalence of different mechanisms upon inversion, as first pointed out by Reuleaux (1) is brought out by the limits of P in these mechanisms.   In all four-bar linkages, the range limits of P are either pure or mixed.   Every four-bar linkage is kinematically equivalent to one of these types.   Since inversion corresponds to the operation L, it is seen at once that a drag linkage can be inverted into a crank-and-rocker linkage or a double-rocker linkage having pure limits, and that mixed limits can occur only in certain double-rocker linkages.   This fact forms the basis of properties 4, 5 and 6, which will now be discussed with reference to the crank-and-rocker mechanism.   Similar reasoning will enable the reader to derive the results for the other types of four-bar mechanisms.

Inequalities satisfied by crank-and-rocker, drag and double-rocker linkages have been given by Hrones and Nelson ("Analysis of the Four-Bar Linkage," by J. A. Hrones and G. L. Nelson, The Technology Press of M.I.T. and J. Wiley and Sons, N. Y., first edition, p. ix).

A crank-and-rocker mechanism satisfies the following inequalities

$$a + d > b + c$$
$$c + d > a + b$$
$$a - b > d - c$$

From these, it can be deduced that b is the smallest link and that

$$a + c > d + b > d - b > |a - c| \ldots \ldots \ldots [ii]$$

Hence by property 1, the limits of P for a crank-and-rocker

mechanism are $d - b \leqq P \leqq d + b$ as stated in property 4.

The geometrical construction for P (Fig. 3) shows that if P were to cross the line of centers, $P(O_D M_D)$ would have to be equal to $|a \pm c|$.   In virtue of Inequalities [ii], however, this is seen to be impossible.   The motion of P, moreover, is continuous, with continuous motion of the linkage.   The locus of P is, therefore, wholly above or wholly below the line of centers.   According to the comments on proposition 3 in this closure, at least one alternate configuration of the mechanism must be given by one of the constructions shown in Fig. 4.   In construction (b), P would cross the line of centers during motion of the linkage.   Since this is not possible, construction (a) yields the alternate configuration having the same value of P, as stated in proposition 5.   In construction (a), the values of angles B and D change in sign relative to the original configuration, while the values of angles A and C remain unchanged.   The limits of P involve b and d only, and B and D are the only angles which reverse sign, in accordance with proposition 4.   We are at liberty to assume that the values of the angles which do not change sign are positive and less than 180 degrees.   This assumption merely determines whether we are considering a certain linkage or its complete reflection.

Figs. 5 and 6 were drawn for the following particular linkages:

Fig. 5: Pure limits.   This was drawn for a crank-and-rocker mechanism in which $a = 6$, $b = 2.5$, $c = 4.5$, $d = 5$, angle $1 = A$, angle $2 = B$, angle $3 = C$, and angle $4 = D$.

Fig. 6: Mixed limits.   This was drawn for a double-rocker mechanism in which $a = 3.5$, $b = 2$, $c = 3$, $d = 5.5$, angle $1 = A$, angle $2 = B$, angle $3 = C$, and angle $4 = D$.

Any inversions of these mechanisms would merely invert the auxiliary angles so that the identification of curves 1, 2, 3, and 4 with the angles A, B, C, D would change.   For linkages with different proportions, the curves themselves would differ, but would be of similar character.   The extreme points of some curves would remain unchanged.

6   Property 7: Permutations of the sides of a given linkage.

A convenient way of checking this property is to draw a linkage corresponding to a given permutation in such a manner that the vectorial direction of a link is the same as the vectorial direction of the link having the same length in the original linkage. The original angles A, B, C, D, the parameter P can be identified on this drawing and simple addition and subtraction will establish the formulas given.

The auxiliary angles were introduced in order to simplify the formulas of Table 1.   Their geometrical significance is simple and corresponds to the significance of the angles in the triangle notation in which the sides are denoted by a, b, c and the angles opposite to these sides by A, B, C, respectively.   The unabridged Equations [16] and [17] of Table 1 are long and cumbersome and the auxiliary angles reduce them to the far briefer Equations [8] and [9].   If we restrict ourselves to absolute values, as pointed out by Mr. de Jonge, the operator L, when applied to the auxiliary angles yields the "natural" result $L|A| = |B|$, $L^2|A| = |C|$, and $L^3|A| = |D|$.   This fact results in formulas which are easy to derive, check, and remember.   In the equations for velocity ratios and acceleration ratios the inversion of a sum of two auxiliary angles reverses the sign of the second angle.   Thus $L \sin(B - C) = \sin(C + D)$, and this follows from the sign alternation in Equations [16] and [17].

The derivations for Table 4 are based on simple geometrical considerations, but are too lengthy to be given here.   The examples of this table were chosen to illustrate the simplicity of the formulas applied to particular mechanisms.   The main applications are considered to be

(a) for cases where very accurate answers are desired, e.g., in complex and precision mechanisms

(b) for checking of graphical constructions

(c) for use in special applications where the parameter facilitates computation as compared to conventional methods of computation, e.g., when the inclination of the connecting rod is given (Equation [52], Table 4) and the displacements are required.

(d) for punched-card methods and other automatic computational methods where the calculations are sufficiently long and repetitive to warrant use of such methods

(e) for synthesis investigations. The possibilities of Fig. 11 have not yet been explored, but it is believed possible that techniques using this or other graphs of the auxiliary angles may be used in synthesis investigations.

The general solution of the basic functional Equation [2] of the paper was derived using an old paper by Babbage, as stated by Mr. de Jonge. The author would prefer the term "with the aid of" rather than "by means of"; for the operational technique, also used in the derivation of the solution, is believed to be new.

As far as notation and terminology is concerned, the author readily admits the shortcomings of this paper and is grateful to Mr. de Jonge for his authoritative comments. The paper would have been far more readable if they could have been included. The letter "L" was chosen to designate the operator to denote the word "linear"; perhaps the symbol "O" would have been less confusing. The O's and ϕ's should indeed have been omitted and the crank length, rather than the length of the fixed link, should have been designated by the letter "a." In future work the author will undoubtedly use these suggestions, with which he was unacquainted at the time of submission of this paper. The European method of link designation is more logical than the one used in the paper (i.e. "lever" instead of "driven crank," etc.). It would be very desirable to establish some sort of standard kinematical terminology, as proposed by Mr. de Jonge during the 1953 Annual Meeting of The American Society of Mechanical Engineers.

Minimization of Gear-Train Inertia

By E. G. BURGESS, JR.,[1] LONG ISLAND CITY, N. Y.

In the design of a system consisting of a motor driving an inertial load through gearing it is often necessary that the acceleration of the load be a maximum. The gear ratios giving a maximum acceleration are determined here either for a specified over-all train ratio, or for the condition where the over-all ratio must be found. Charts, which embody certain simplifying assumptions, are provided for selecting the optimum number of gear ratios and the ratios of the individual meshes corresponding to maximum load acceleration.

INTRODUCTION

WE are concerned with the utilization of the available motor torque to greatest advantage in accelerating a load; we wish to make the torque-inertia ratio at the load shaft a maximum.

The formulas and charts developed have specific application to the design of high-quality servomechanisms where the response consists of a motor driving various inertial loads by means of gearing. (In order to clarify the principles involved, friction and external-load torques have not been considered.) The principles developed are also applicable to hydraulically driven linear-displacement mechanisms where the connections to the inertial load are made through linkages. Many analogous systems may be treated in a similar manner.

SINGLE-MESH CONNECTION

Consider the system shown schematically in Fig. 1, composed of a motor m driving a load L by means of a gear pair of ratio r
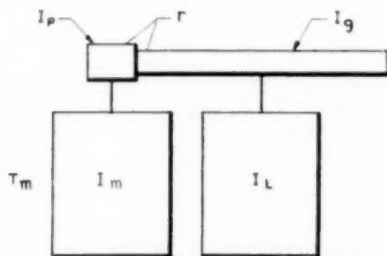

FIG. 1 SINGLE-MESH INERTIA CONNECTION

consisting of a pinion p on the motor drive shaft and a gear g on the load shaft. The motor rotor, pinion, gear and load have the respective moments of inertia I_m, I_p, I_g and I_L in in-oz sec^2.

This simple case is considered in detail since the principles involved apply to the general case of an n-mesh connection. Furthermore the results are useful in obtaining an estimate of the optimum over-all ratio between motor and load when this ratio r is unknown or unspecified.

If the torque applied to the motor rotor is T_m in-oz, then the torque available at the motor shaft for accelerating the load shaft is

$$T_m - (I_m + I_p)a_m = \frac{(I_L + I_g)a_L}{r} \quad \ldots \ldots \ldots [1]$$

where

a_m = angular acceleration of motor shaft, rad/sec^2
a_L = angular acceleration of load shaft, rad/sec^2

and

$$a_m = ra_L \quad \ldots \ldots \ldots \ldots \ldots \ldots [2]$$

due to the gear ratio r. After eliminating a_m from Equation [1] by the Relation [2], we get

$$a_L = \frac{T_m}{(I_m + I_p)r + \dfrac{I_L + I_g}{r}} \quad \ldots \ldots \ldots [3]$$

In order to progress further we now derive an expression for I_g in terms of I_p. It is clear that

$$I_p = \frac{\pi \left(\dfrac{d_p}{2}\right)^2 t_p \omega_p}{g} \frac{1}{2} \left(\frac{d_p}{2}\right)^2 = \frac{\pi \omega_p t_p d_p^4}{32g} \text{ oz in. sec}^2 \ldots [4]$$

$$I_g = \frac{\pi \left(\dfrac{d_g}{2}\right)^2 t_g \omega_g}{g} \frac{1}{2} \left(\frac{d_g}{2}\right)^2 = \frac{\pi \omega_g t_g d_g^4}{32g} \text{ oz in. sec}^2 \ldots [5]$$

where

d_p = pitch diameter of pinion, in.
t_p = thickness of pinion, in.
ω_p = weight of pinion material, oz/in.^{3}
d_g = pitch diameter of gear, in.
t_g = thickness of gear, in.
ω_g = weight of gear material, oz/in.^{3}
g = acceleration of gravity, in./sec^2

From the Relations [4] and [5] we get

$$I_g = \frac{\omega_g t_g d_g^4}{\omega_p t_p d_p^4} I_p = kr^4 I_p \quad \ldots \ldots \ldots \ldots [6]$$

where k is a design constant associated with the meshing gear pair of ratio r.

In Equation [3] I_g may now be replaced by its equivalent expression from Equation [6] with the result that

$$a_L = \frac{T_m}{\dfrac{I_L}{r} + (I_m + I_p)r + kI_p r^3} = \frac{T_m}{D} \quad \ldots \ldots [7]$$

where D equals the expression in the denominator. In this relation I_m and I_L are known quantities. I_p is also known since this quantity is normally made as small as possible. Accordingly for a given T_m the load acceleration will be a maximum when D in Equation [7] is a minimum. Since the magnitude of D depends on r, we can find a minimum value of D by solving the equation

$$\frac{\partial D}{\partial r} = 0 \text{ for } r$$

provided also

$$\frac{\partial^2 D}{\partial r^2} > 0$$

Performing this familiar process on D gives

$$\frac{\partial D}{\partial r} = -\frac{I_L}{r^2} + (I_m + I_p) + 3kI_p r^2 = 0 \quad \ldots \ldots [8]$$

or

$$r^2 = \frac{-(I_m + I_p) + \sqrt{(I_m + I_p)^2 + 12kI_p I_L}}{6kI_p} \quad \ldots \ldots [9]$$

Also

$$\frac{\partial^2 D}{\partial r^2} = \frac{2I_L}{r^2} + 6kI_p r > 0$$

and therefore the value of r given by Equation [9] will give a minimum value for D, and accordingly a maximum value for a_L.

TWO-MESH CONNECTION

In considering the system shown schematically in Fig. 2, the notation is similar to that used previously except that subscripts
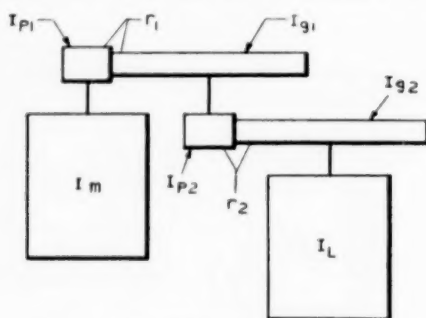

FIG. 2 TWO-MESH INERTIA CONNECTION

are used to denote the elements of a particular mesh counting from the motor mesh. As in the simple single-mesh case, we again would like to make the acceleration a_L of the load, corresponding to a given torque T_m on the rotor, a maximum. There are two situations to consider in treating this two-mesh connection of I_m and I_L. In the first instance we can maximize a_L assuming that we have no knowledge of the over-all gear ratio

$$R = r_1 r_2 \quad \ldots \ldots \ldots [10]$$

In the second instance we can maximize a_L assuming that the over-all ratio R has been determined from consideration of the load-velocity requirements. To treat either one of these problems, an expression for a_L in terms of the system parameters must first be derived.

Let us denote the torque on the shaft carrying g_1 and p_2 by T_i, and the acceleration of this shaft by a_i, then

$$T_i = [T_m - (I_m + I_{p1})a_m]r_1 = (I_{g1} + I_{p2})a_i + \frac{T_L}{r_2} \ldots [11]$$

where

$$T_L = (I_{g2} + I_L)a_L$$
$$a_i = r_2 a_L$$
$$a_m = r_1 r_2 a_L$$

Making these substitutions in Equation [11], and solving for a_L we get

$$a_L = \frac{T_m}{I_m r_1 r_2 + I_{p1} r_1 r_2 (1 + k_1 r_1^2) + \dfrac{I_{p2} r_2 (1 + k_2 r_2^2)}{r_1} + \dfrac{I_L}{r_1 r_2}}$$

$$= \frac{T_m}{D} \ldots \ldots [12]$$

where $D =$ expression in denominator, and

$$I_{g1} = k_1 I_{p1} r_1^4$$
$$I_{g2} = k_2 I_{p2} r_2^4$$

The values of r_1 and r_2 making D a minimum are obtained from the simultaneous solution of the equations

$$\frac{\partial D}{\partial r_1} = 0, \quad \frac{\partial D}{\partial r_2} = 0 \ldots \ldots \ldots \ldots [13]$$

for r_1 and r_2. If we assume that $k_1 = k_2 = k$ and $I_{p1} = I_{p2} = I_p$, then this pair of equations will reduce to the set

$$r_1^8 + \frac{2}{5k}\left(1 + \frac{I_m}{I_p}\right)r_1^6 - \frac{6}{5k}r_1^4 - \frac{2}{5k^2}\left(1 + \frac{I_m}{I_p}\right)r_1^2$$

$$+ \frac{1}{5k^2}\left(1 - 4k\frac{I_L}{I_p}\right) = 0 \ldots \ldots [14]$$

and

$$r_2^2 - \frac{1}{2}\left(r_1^4 - \frac{1}{k}\right) = 0 \ldots \ldots \ldots \ldots [15]$$

Equation [14] can be solved for r_1^2 since k, I_p, I_m, and I_L are known. This value of r_1^2 used in Equation [15] gives r_2. Accordingly, the optimum over-all ratio is given by Equation [10].

In the case where the over-all ratio R is known, reference to Equation [12] indicates that a_L is a maximum when D is a minimum as before. However, in the expression for D we may replace r_2 by its equivalent value

$$r_2 = \frac{R}{r_1} \ldots \ldots \ldots \ldots [16]$$

To find the minimum value of D we then solve the equation

$$\frac{\partial D}{\partial r_1} = 0 \ldots \ldots \ldots \ldots [17]$$

or

$$r_1^4 - \frac{1}{k}r_1^2 - 2R^2 = 0 \ldots \ldots \ldots \ldots [18]$$

for r_1 and substitute this value in D. Equation [18] assumes $k_1 = k_2 = k$ and $I_{p1} = I_{p2} = I_p$.

n-MESH CONNECTION

For a system consisting of a motor having a rotor inertia I_m connected to a load inertia I_L through an n-mesh gear train, the total reflected inertia of the system referred to the motor shaft is

$$I_{lm} = I_m + I_{p1} + \frac{I_{g1} + I_{p2}}{r_1^2} + \frac{I_{g2} + I_{p3}}{r_1^2 r_2^2} + \ldots$$

$$+ \frac{I_{g(n-1)} + I_{pn}}{r_1^2 r_2^2 \ldots r_{n-1}^2} + \frac{I_{gn} + I_L}{r_1^2 r_2^2 \ldots r_n^2} \ldots \ldots [19]$$

where I_{pi}, I_{gi}, and r_i are the inertias and the ratio of the gears in the ith mesh counting from the motor. Since

$$I_{gi} = k_i I_{pi} r_i^4 \ldots \ldots \ldots \ldots [20]$$

Equation [19] may be written

$$I_{tm} = I_m + I_{p1}(1 + k_1 r_1^2) + \frac{I_{p2}(1 + k_2 r_2^2)}{r_1^2} + \frac{I_{p3}(1 + k_3 r_3^2)}{r_1^2 r_2^2}$$

$$+ \ldots + \frac{I_{pn}(1 + k_n r_n^2)}{r_1^2 r_2^2 \ldots r_{n-1}^2} + \frac{I_L}{r_1^2 r_2^2 \ldots r_n^2} \ldots \ldots [21]$$

Similarly the total reflected inertia of the system referred to the load shaft is

$$J_{tL} = I_{tm} r_1^2 r_2^2 \ldots r_n^2 = I_{tm} R^2 \ldots \ldots \ldots [22]$$

where R is the over-all gear-train ratio.

We are interested in making the load acceleration a maximum. The general expression for this acceleration, for a given rotor torque T_m, is

$$a_L = \frac{T_L}{I_{tL}} = \frac{T_m R}{I_{tm} R^2} = \frac{T_m}{I_{tm} R} = \frac{T_m}{D} \ldots \ldots [23]$$

Accordingly a_L will be a maximum when the denominator D is a minimum. Since D is a function of $r_1, r_2, \ldots r_n$, this function will be a minimum when these variables satisfy simultaneously the set of n-equations

$$\frac{\partial D}{\partial r_i} = R \frac{\partial I_{tm}}{\partial r_i} + I_{tm} \frac{\partial R}{\partial r_i} = 0; \quad i = 1, 2, \ldots n \ldots [24]$$

provided also that the complicated criterion[2] insuring that D is actually a minimum is also satisfied, as it is in this case.

After performing the partial differentiations indicated in Equations [24], it becomes apparent that this set of equations may be reduced to a much simpler set by forming the combinations

$$\frac{1}{2} \frac{r_i^2}{R} \frac{\partial D}{\partial r_i} - \frac{1}{2} \frac{r_{i+1}^2}{R} \frac{\partial D}{\partial r_{i+1}} = 0 \ldots \ldots [25]$$

For example, if $i = 1$, we obtain the equation

$$k_1 I_{p1} r_1^4 - I_{p2} - 2k_2 I_{p2} r_2^2 = 0 \ldots \ldots [26]$$

Letting $i = 1, 2, \ldots n - 1$ in turn we get the set of $n - 1$ relations

$$\left.\begin{array}{l} 2k_2 I_{p2} r_2^2 = k_1 I_{p1} r_1^4 - I_{p2} \\ 2k_3 I_{p3} r_3^2 = k_2 I_{p2} r_2^4 - I_{p3} \\ \ldots \quad \ldots \\ 2k_n I_{pn} r_n^2 = k_{n-1} I_{p(n-1)} r_{n-1}^4 - I_{pn} \end{array}\right\} \ldots \ldots [27]$$

By means of these $n - 1$ relations it is possible to eliminate $r_2, r_3, \ldots r_n$ from any one of the Equations [24] and so obtain an equation involving r_1 only. Having solved this for r_1 we may determine $r_2, r_3, \ldots r_n$ in turn from the Set [27]. Accordingly we can solve the problem of determining the individual ratios in an n-mesh train so that for a given motor torque the load acceleration is a maximum, the over-all gear ratio being at first unspecified. It must be admitted, however, that this is a very tedious process unless n is small, say, < 4.

The companion problem of determining the individual ratios for maximum load acceleration when the over-all ratio R is given is much more tractable. The calculations can be made quite simple if it is agreed that all pinions are similar and that all gears differ only in pitch diameter, so that

$$\left.\begin{array}{l} I_{p1} = I_{p2} = \ldots = I_{pn} = I_p \\ k_1 = k_2 = \ldots = k_n = k \end{array}\right\} \ldots \ldots [28]$$

With these assumptions Equations [27] take the form

$$\left.\begin{array}{l} 2k r_2^2 = k r_1^4 - 1 \\ 2k r_3^2 = k r_2^4 - 1 \\ \ldots \quad \ldots \\ 2k r_n^2 = k r_{n-1}^4 - 1 \end{array}\right\} \ldots \ldots [29]$$

---

[2] Smithsonian Miscellaneous Collections, vol. 74, no. 1, publication 2672, 1922, p. 153.
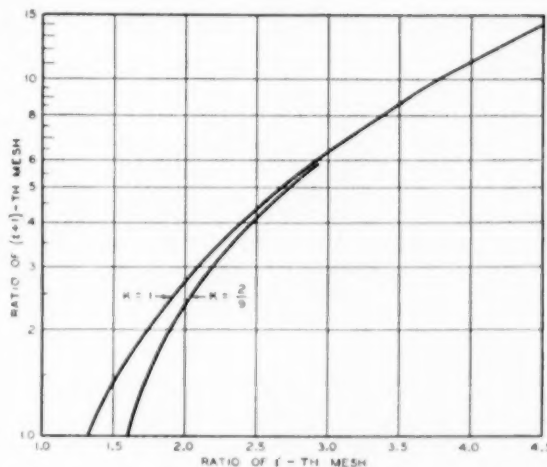

FIG. 3 RELATION BETWEEN SUCCESSIVE MESH RATIOS IN MINIMUM INERTIA TRAIN

This interesting set of recurrence relations can be made the basis of most problems connected with minimization of gear train inertia.

The general relation of Equations [29], namely

$$r_{i+1} = \sqrt{\frac{k r_i^4 - 1}{2k}} \ldots \ldots [30]$$

is plotted in Fig. 3 for $k = 1$ corresponding to pinions and gears of the same material and thickness and for $k = \frac{2}{9}$ corresponding to stainless-steel pinions and aluminum gears of $\frac{2}{3}$ thickness of pinion.

Now having given the over-all ratio R, we have

$$R = r_1 r_2 \ldots r_n \ldots \ldots [31]$$

By means of the Relations [29], we may eliminate $r_n, r_{n-1} \ldots r_2$ in turn from Equation [31] squared. Thus

$$R^2 = r_1^2 r_2^2 \ldots r_{n-1}^2 \left(\frac{k r_{n-1}^4 - 1}{2k}\right)$$

$$= r_1^2 r_2^2 \ldots r_{n-2}^2 \left(\frac{k r_{n-1}^4 - 1}{2k}\right) \left[\frac{k \left(\frac{k r_{n-2}^4 - 1}{2k}\right)^2 - 1}{2k}\right] \ldots [32]$$

and so forth. Finally we reach a relation between R and r_1 from which r_1 may be determined. The formulas connecting R and r_1 are exhibited in Table 1 for small values of n. The relation between R and r_1 has been plotted for $k = 1$ and $n = 1, 2, 3, 4$ in Fig. 4, and for $k = \frac{2}{9}$ and $n = 1, 2, 3, 4$ in Fig. 5.

The expressions in Table 1 have not been expanded in terms of r_1 since the forms given are convenient for the numerical computation of R in terms of r_1. Having given n, k, and R we may determine r_1 from the appropriate curve.

DETERMINATION OF NUMBER OF MESHES

In order to compare the inertia of gear trains containing different numbers of meshes it is convenient to make use of the concept of inertia ratio. The inertia ratio of a gear train is defined by

$$R_I = \frac{\text{Moment of inertia of train referred to motor shaft}}{\text{Moment of inertia of motor pinion}}$$

TABLE 1　FORMULAS GIVING RELATIONSHIP BETWEEN OVER-
ALL RATIO R AND THE RATIO OF THE FIRST MESH r_1 OF GEAR
TRAIN

No. of meshes (n)	Formula
1	$R = r_1$ (trivial)
2	$R^2 = r_1^2 \left(\frac{kr_1^4 - 1}{2k} \right)$
3	$R^2 = r_1^2 \left(\frac{kr_1^4 - 1}{2k} \right) \left[\dfrac{k\left(\frac{kr_1^4 - 1}{2k}\right)^2 - 1}{2k} \right]$
4	$R^2 = r_1^2 \left(\frac{kr_1^4 - 1}{2k} \right) \left(\frac{kr_2^4 - 1}{2k} \right) \left(\frac{kr_3^4 - 1}{2k} \right)$, where $r_2^4 = \left(\frac{kr_1^4 - 1}{2k} \right)^2$, $r_3^4 = \left(\frac{kr_2^4 - 1}{2k} \right)^2$
n	$R^2 = r_1^2 \left(\frac{kr_1^4 - 1}{2k} \right) \left(\frac{kr_2^4 - 1}{2k} \right) \cdots \left(\frac{kr_{n-1}^4 - 1}{2k} \right)$, where $r_2^4 = \left(\frac{kr_1^4 - 1}{2k} \right)^2$, $r_3^4 = \left(\frac{kr_2^4 - 1}{2k} \right)^2$, etc.

Referring to Equation [21] we see that

$$R_I = \frac{I_{tm} - I_m - \dfrac{I_L}{R^2}}{I_p} \quad \dots \quad [33]$$

If the assumptions embodied in Equations [28] are made, it is clear from Equation [21] that

$$R_I = (1 + kr_1^2) + \frac{1 + kr_2^2}{r_1^2} + \frac{1 + kr_3^2}{r_1^2 r_2^2} + \dots + \frac{1 + kr_n^2}{r_1^2 r_2^2 \dots r_{n-1}^2} \quad \dots \quad [34]$$
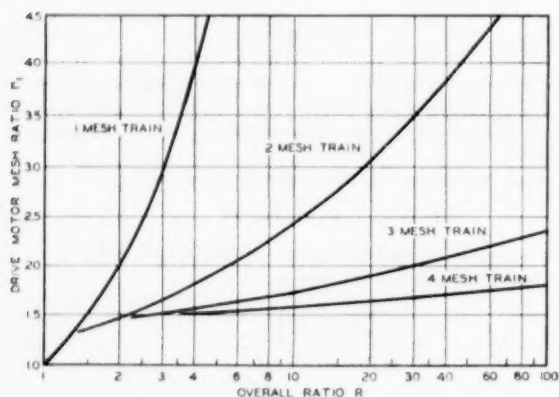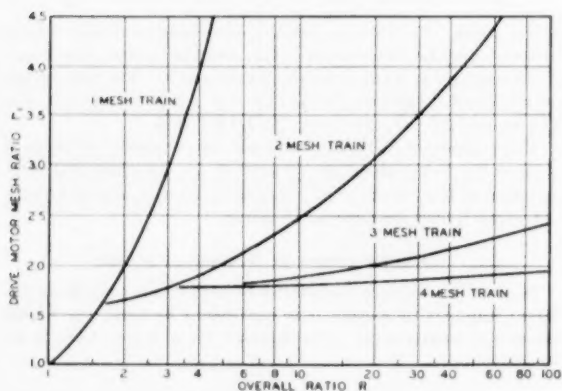
TABLE 2　INERTIA RATIO IN TERMS OF MOTOR MESH GEAR
RATIO FOR DIFFERENT NUMBERS OF GEAR-TRAIN MESHES IN
MINIMUM INERTIA TRAIN

No. of meshes = n	Inertia ratio = $R_I = f(r_1)$
1	$R_I = 1 + kr_1^2$
2	$R_I = 1 + \dfrac{3kr_1^2}{2} + \dfrac{1}{2r_1^2}$
3	$R_I = 1 + \dfrac{7kr_1^2}{4} + \dfrac{1}{4r_1^2} + \dfrac{k}{r_1^2(kr_1^4 - 1)}$
4	$R_I = 1 + \dfrac{15kr_1^2}{8} + \dfrac{1}{8r_1^2} + \dfrac{k}{2r_1^2(kr_1^4 - 1)} + \dfrac{8k^2}{r_1^2(kr_1^4 - 1)[(kr_1^4 - 1)^2 - 4k]}$
n	$R_I \cong \dfrac{2^n - 1}{2^{n-1}} kr_1^2 \quad r_1 > 1.5$

The values of $r_1, r_2, \dots r_n$ which are to be substituted in this general relation are those minimizing D in Equation [23]. In the case where the over-all ratio R is unspecified, these values of r, are given by the simultaneous solution of the set of Equations [29] together with any one equation of the set of Equations [24]. In the case where R is known, the corresponding value of r_1 is found either from the curves of Fig. 4 or 5, or by calculation from Equation [32]. Having r_1, the remaining ratios are found from the set of Equations [29], or from the appropriate curve of Fig. 3.

The expressions for R_I in terms of r_1 for small values of n are given in Table 2. The values of R_I corresponding to a given r_1 are plotted in Fig. 6 for $k = 1$ and $n = 1, 2, 3, 4$; and in Fig. 7 for $k = 2/9$ and $n = 1, 2, 3, 4$.

Fig. 4　Motor Mesh Ratio for $K = 1$
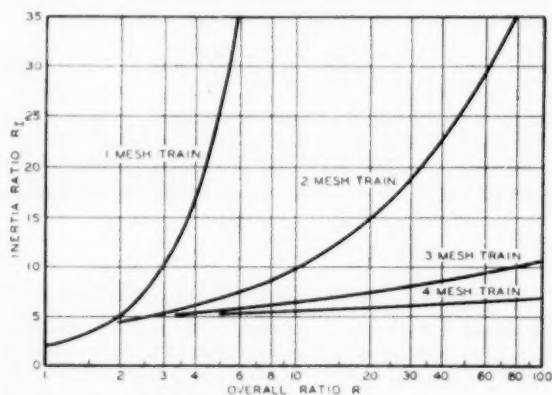
Fig. 6　Selection of Number of Gear Meshes for Minimum
Inertia Train; $K = 1$

Fig. 5　Motor Mesh Ratio for $K = 2/9$
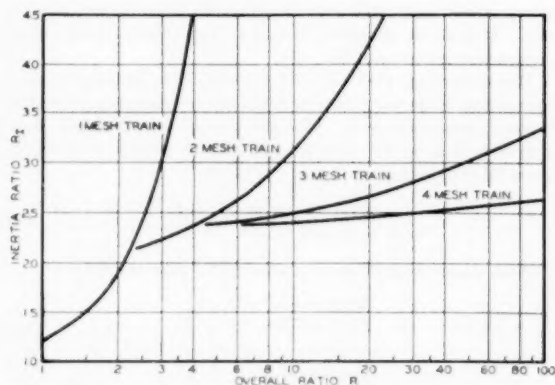
Fig. 7　Selection of Number of Gear Meshes for Minimum
Inertia Train; $K = 2/9$

AN ASME PAPER

Its Preparation, Submission and Publication, and Presentation

To a large degree the papers prepared and presented under the ASME sponsorship are evidence by which its professional standing and leadership are judged. It follows, therefore, that to qualify for ASME sponsorship, a paper must not only present suitable subject matter, but it must be well written and conform to recognized standards of good English and literary style.

The pamphlet on "AN ASME PAPER" is designed to aid authors in meeting these requirements and to acquaint them with rules of the Society relating to the preparation and submission of manuscripts and accompanying illustrations. It also includes suggestions for the presentation of papers before Society meetings.

CONTENTS

Price 40¢. No discount allowed. *A remittance must accompany all orders for $5.00 or less. U. S. Postage Stamps are acceptable.*

THE AMERICAN SOCIETY OF MECHANICAL ENGINEERS
29 West 39th Street, New York 18, N. Y.

ASME ——BOOKS—

ASME TRANSACTIONS FOR 1953

Nowhere else will you find in a single volume so much valuable information on major trends and developments throughout the mechanical-engineering field. Containing 255 papers, this massive reference places at your fingertips the experience of over 400 experts, each a specialist in his field, with significant problems associated with aviation, applied mechanics, boiler feedwater treatment, fuels, gas turbine power, heat transfer, hydraulics, industrial instruments, lubrication, machine design, metal cutting, metal engineering, oil and gas power, production engineering, rubber and plastics, and steam generation. Discussions of the papers provide additional valuable data. Supplementing the text are hundreds of tables, graphs, charts, and photographs.

2250 pages   **Cloth Bound**   **$15.00 ($7.50 to ASME members)**

VISCOSITY OF LUBRICANTS UNDER PRESSURE

This new publication reviews and co-ordinates twelve experimental investigations made in England, Germany, Japan, Russia, and the United States over a period of thirty-five years. The tests were made on 148 lubricants comprising 25 fatty oils, 94 petroleum oils, 17 compounded oils, and 12 other lubricants. Data are co-ordinated by means of sixty tables in which the results originally appearing in diversified units are compared. The methods proposed for correlating viscosity-pressure characteristics of oils with properties determined at atmospheric pressures are reviewed and illustrated. Pertinent aspects such as experimental work on heavily loaded bearings, lubrication calculations, and additional techniques for viscosity are covered. Conclusions and recommendations are presented. Other chapters give the required computation of the temperature coefficients of viscosity, method of computing pressure coefficients, a bibliography of 189 items, and symbols used.

$5.00

METALS ENGINEERING—DESIGN

This first of the four-volume ASME Handbook is the design engineer's own guidebook of vital data on the properties, testing, inspection, and selection of metals. Comprising 48 sections and written by 43 well-known authorities, it provides: Criteria for facing the over-all problems of selection of materials; facts on potential weaknesses of various metals and ways of making the metals strong; details of the specific problems of corrosion and the mechanical factors which influence corrosion; present knowledge of testing by nondestructive methods; special requirements of design and surface finish set up by mass production; modern basic information on the design theory, design practice, experimental design; and the special requirements of aluminum and magnesium. Here, too, are important design data—equations for determining such factors as stress, creep, impact strength; results of such methods as the use of residual stresses to improve fatigue resistance, the use of flame hardening to increase resistance to fatigue failure; methods for making your structure or machine part stronger, such as shot peening, cold working, and case carburizing.

400 pages   **560 Illustrations**   **$10.00**

OTHER TITLES OF THE FOUR-VOLUME ASME HANDBOOK ARE:

METALS PROPERTIES, to be published in June. Price, $11.00.

ENGINEERING TABLES AND METALS ENGINEERING—PROCESSES, in preparation.

GENERAL DISCUSSION ON HEAT TRANSFER

The complete proceedings of the 1951 Heat Transfer Conference, arranged by the IME and ASME, it mirrors a decade's development in heat transfer and in the design of the apparatus relating thereto, offering first-hand information on significant investigations, new discoveries in the field, actual performance of fundamental data, and on new practical applications of known principles. Over 200 specialists have collaborated to present the 93 timely papers in its pages, of which sixteen deal with problems associated with heat transfer with change of state; twenty-three are concerned with problems associated with heat transfer between fluids and surfaces; sixteen treat problems connected with conduction in solids and fluids; eighteen covering convection, radiation, instrumentation, measurement techniques; and twenty discuss special problems, such as, heat transfer in turbine-blade cooling, in liquid metals, in gas engines, in piston engines, mercury boiler, etc. Additionally, there are seventy-five pages of discussions, critical summaries of the papers, and hundreds of bibliographical references. In short, this is a reference of prime importance for those engaged in heat-transfer work.

500 pages   **$10.00**

MANUAL ON CUTTING OF METALS

Look to this book for shop-tested data on metals which are machined commercially...the best cutting practices...the tool shapes which experimental work has shown to be most efficient...and a hundred other helps for cutting costs, stepping up production, and standardizing practice. Specifically it shows how to machine a variety of metals including high-nickel alloys, stainless steels, copper and its alloys, magnesium, cast irons, and plastics; discusses the mechanical characteristics and structures of the materials being worked and the relations of their behavior and properties to microscopic structure; gives detailed consideration to types and sizes of tools, tips, inserts, and holders; to tool materials, grinding and evaluating tool performance. Cutting fluids and their influence on cutting speeds, etc., are covered; also cutting forces for machining a variety of metals. Cutting, idle and loading time, as well as tool changing and grinding costs are analyzed, and the cost per piece formula presented along with an example showing how costs are calculated.

546 pages   **600 Illustrations**   **$10.00**

THE AMERICAN SOCIETY OF MECHANICAL ENGINEERS 29 W. 39th St., New York 18, N.Y.